Electromagnetic waves in loaded cylindrical structures : a radial transmission line approach

Citation for published version (APA):
Addamo, G. (2008). *Electromagnetic waves in loaded cylindrical structures : a radial transmission line approach*. [Phd Thesis 2 (Research NOT TU/e / Graduation TU/e), Electrical Engineering]. Technische Universiteit Eindhoven. https://doi.org/10.6100/IR635237

DOI:
10.6100/IR635237

Document status and date:
Published: 01/01/2008

Document Version:
Publisher's PDF, also known as Version of Record (includes final page, issue and volume numbers)

Please check the document version of this publication:

• A submitted manuscript is the version of the article upon submission and before peer-review. There can be important differences between the submitted version and the official published version of record. People interested in the research are advised to contact the author for the final version of the publication, or visit the DOI to the publisher's website.
• The final author version and the galley proof are versions of the publication after peer review.
• The final published version features the final layout of the paper including the volume, issue and page numbers.

Link to publication

General rights
Copyright and moral rights for the publications made accessible in the public portal are retained by the authors and/or other copyright owners and it is a condition of accessing publications that users recognise and abide by the legal requirements associated with these rights.

- Users may download and print one copy of any publication from the public portal for the purpose of private study or research.
- You may not further distribute the material or use it for any profit-making activity or commercial gain
- You may freely distribute the URL identifying the publication in the public portal.

If the publication is distributed under the terms of Article 25fa of the Dutch Copyright Act, indicated by the "Taverne" license above, please follow below link for the End User Agreement:

www.tue.nl/taverne

Take down policy
If you believe that this document breaches copyright please contact us at:

openaccess@tue.nl

providing details and we will investigate your claim.

Download date: 16. Nov. 2023

Electromagnetic waves in loaded cylindrical structures:

a radial transmission line approach

Electromagnetic waves in loaded cylindrical structures:

a radial transmission line approach

PROEFSCHRIFT

ter verkrijging van de graad van doctor aan de
Technische Universiteit Eindhoven, op gezag van de
Rector Magnificus, prof.dr.ir. C.J. van Duijn, voor een
commissie aangewezen door het College voor
Promoties in het openbaar te verdedigen
op dinsdag 17 juni 2008 om 14.00 uur

door

Giuseppe Addamo

geboren te Messina, Italië

Dit proefschrift is goedgekeurd door de promotoren:

prof.dr. A.G. Tijhuis
en
prof.dr. R. Orta

Copromotor:
dr.ir. B.P. de Hon

CIP-DATA LIBRARY TECHNISCHE UNIVERSITEIT EINDHOVEN

Addamo, Giuseppe

Electromagnetic waves in loaded cylindrical structures : a radial transmission line approach / by Giuseppe Addamo. - Eindhoven : Technische Universiteit Eindhoven, 2008.
Proefschrift. - ISBN 978-90-386-1894-4
NUR 959
Trefw.: elektromagnetisme ; numerieke methoden / integraalvergelijkingen / elektromagnetische verstrooiing / Green-functies.
Subject headings: computational electromagnetics / integral equations / electromagnetic wave scattering / Green's function methods.

Cover design: Giuseppe Addamo
Press: Universiteitsdrukkerij, TU/e

Contents

Chapter 1

Introduction

Transmission lines, used to send telegraph signals over long distance, were introduced in communication technology around the middle of the nineteenth century. William Thomson (Lord Kelvin) in 1855 presented the first mathematical model to describe the propagation of electric current on a submarine cable. It was a diffusion model, where the cable inductance was neglected. A more complete model was set up by Oliver Heaviside in 1885, in the form of telegrapher's equations, a system of two partial differential equations for the voltage and current on the line. About at the same time James C. Maxwell published his fundamental *Treatise*, but this type of formulation can also be developed very simply, by extending lumped circuit theory to the realm of distributed circuits. Later, the term *transmission line* was used to indicate several types of structures supporting the propagation of a TEM mode (or, at least, of a quasi-TEM mode, as in microstrips), hence structures comprising at least two conductors [1], [2], [3] and [4].

However, electromagnetic waves can propagate also inside hollow pipes of various cross sections, although with properties slightly different from plain transmission lines. Lord Rayleigh in 1897 published the first mathematical analysis of a rectangular waveguide.

The key concept is that of *propagation mode*. A mode is a field configuration existing in the waveguide, with the property that in the propagation its shape remains unchanged, while the field itself is multiplied by a number. When this number is complex with unit amplitude (in the case of a lossless waveguide) the mode is said to be above cut-off; when it is real the mode is said to be below cut-off.

Thanks to the work of S. A. Schelkunoff and H. G. Booker the concept of electrical impedance started to be associated also to waves, both guided and in free space, [5]. The following natural step was to extend lumped circuit network theory to the field of waveguide discontinuities. The person who developed in rigorous way this circuit point of view of wave propagation is N. Marcuvitz, first at the M.I.T. Radiation Laboratory during the years of Word War II in collaboration with J. Schwinger, and then at the Polytechnic Institute of Brooklyn. Milestones in this process are [6], [7], [8]. According to this point of view, the field in a straight waveguide, with z and $\underline{\rho}$ as longitudinal and transverse coordinates is represented in the form (in the frequency domain):

$$\begin{aligned}
\underline{E}_t(\underline{\rho}, z) &= \sum_i V_i(z)\underline{e}_i(\underline{\rho}) \\
\underline{H}_t(\underline{\rho}, z) &= \sum_i I_i(z)\underline{h}_i(\underline{\rho}) \\
E_z(\underline{\rho}, z) &= \sum_i I_i(z)Z_{\infty i}e_{zi}(\underline{\rho}) \\
H_z(\underline{\rho}, z) &= \sum_i V_i(z)Y_{\infty i}h_{zi}(\underline{\rho})
\end{aligned}$$

where $\underline{e}_i(\underline{\rho})$, $e_{zi}(\underline{\rho})$, $\underline{h}_i(\underline{\rho})$, $h_{zi}(\underline{\rho})$ are the mode functions and the coefficients $V_i(z)$, $I_i(z)$ satisfy the ODE system

$$\begin{aligned}
-\frac{dV_i}{dz} &= jk_{zi}Z_{\infty i}I_i \\
-\frac{dI_i}{dz} &= jk_{zi}Y_{\infty i}V_i
\end{aligned}$$

Since these are just transmission line equations, it is reasonable to call the coefficients modal voltage and modal current on the i-th modal transmission line, having characteristic impedance $Z_{\infty i}$ and propagation constant k_{zi}. In this way, the transmission line concept has left the concreteness of copper and has become an abstract mathematical concept.

If we reconsider the previous expressions, we realize that the variables $\underline{\rho}$ and z have been separated. This means that modal transmission line theory can also be interpreted as the application to Maxwell's equations of the classical method of separation of variables. The important point (particularly important for engineers) is that a physical meaning has been attached to the various quantities. This characteristic has led A.A. Oliner to state: "…The network formulation of microwave field theory has been fundamental to the rapid progress made by the microwave community" [5].

Once we recognize that transmission line theory is separation of variables in disguise, we are ready for a further step in the generalization. Canonical waveguides have cross sections (circu-

lar, rectangular, elliptical) that allow complete separation of variables. This leads to the idea of a transverse coordinate, such as x or y in the case of rectangular waveguides and ρ or φ in the case of circular ones, as the variable on which voltages and currents depend. In this way the concept of transverse resonance method has been developed, with its many applications in the field of microwaves.
In the case of cylindrical waveguides, the transverse point of view leads to the introduction of radial lines, already described in [7].

In this thesis we study discontinuity problems in a cylindrical waveguide. The approach is rigorous and is based on the deduction and numerical solution of an integral equation. The kernel of the integral equation is the Green's function of the problem and its computation is often not a trivial task. We found very convenient to employ radial transmission line theory for this purpose. Two problems were considered, one is that of leaky coaxial cables, the other is that of ring cavity filters.

Leaky Coaxial Cables (LCX) are cables, in the outer conductor of which series of slots are opened so that the field, originally propagating in the inside, is partially radiated so as to create an area of RF coverage in the neighborhood, which is capable of providing two-way communication. Hence, LCX are antennas, but of a peculiar type, since the user always lies in their near-field region. Indeed LCX are mainly used in tunnels, underground and indoor applications in general. Several types of slot arrangements were proposed in the past, but we will focus only on the case of φ oriented slots, since we want in particular to analyze the potentiality of the numerical method. An example is shown in Figure 1.1.

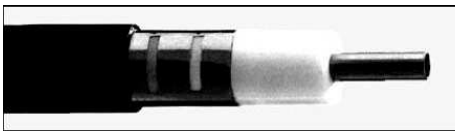

Figure 1.1: Example of slotted coaxial cable

Slotted cables have been studied in several papers in the past, but invariably the method used was the application of periodic structure theory. The analysis can be limited to a single cell, with an obvious advantage in terms of cpu-time requirements. The drawback is that only strictly periodic LCX can be studied and also that the problem of the excitation of the LCX by means of an unslotted cable cannot be attacked. For this reason, our approach is general in the sense that a finite number of slots is assumed, not necessarily identical. This method is powerful but is intrinsically limited to cables with not more than a few hundreds slots, to keep the size of the numerical effort within reasonable limits for a PC. In order to be able to study cables with many more slots, also a longitudinal approach has been developed. The slots are assumed to be identical, but always in a finite number, so that we can analyze the excitation problem. This longitudinal approach is based on Bloch wave theory and is very unconventional since it makes use of the continuous spectrum of an open waveguide. Finally, an eigencurrent approach based on the computation of the approximated eigencurrents of the entire array is discussed.

The second problem we have considered is that of stop-band filters. A possible configuration, typically used in rectangular waveguides, exploits E- or H-plane stubs. Since the capability of double polarization operation was required, the cross section of the waveguide was selected to be circular, so that the stub gets the shape of a disk. To reduce the transverse size of the filter, the stubs are shortened and loaded with a ring shaped cavity, obtaining the structure shown in Figure 1.2. This structure can be studied with a method similar to that used for LCX, but in this case two apertures are present for each cavity and the mathematical formulation consists of a system of two coupled integral equations.

Common to both applications is the necessity of the numerical evaluation of a large number of infinite domain integrals of oscillating, singular and slowly decaying functions. This is really the bottleneck of the method and it was necessary to develop special integration techniques in order to increase the efficiency. In this way it was possible to simulate structures with considerable size.

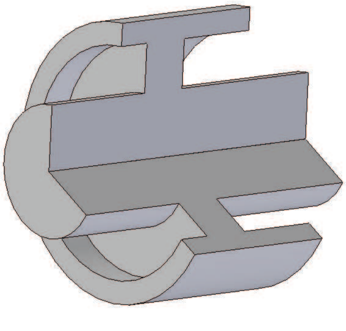

Figure 1.2: Element of a ring cavity filter

Organization of the thesis

The present thesis is organized as follows.

In Chapter 2 we lay the foundations for all the subsequent chapters. Radial transmission line theory is developed starting from Maxwell's equations. All the relevant network concepts are introduced, such as impedances, propagators, scattering matrices, etc.

Chapter 3 is devoted to the analysis of slotted cables with the aid of an integral equation technique. Exploiting an equivalence theorem, the slots are closed with a metal conductor on which an unknown magnetic current is introduced. The integral equation results from the enforcement of the continuity, at the slot locations, of the total magnetic field. Hence, the problem is formulated in terms of a magnetic field integral equation. The numerical solution is carried out via the Galerkin method of moments. Subsequently, the scattering matrix of the slotted cable is determined.

Chapter 4 describes the Bloch wave approach for the analysis of long slotted cables. This involves the development of a suitable mathematical formalism for the computation of the Bloch waves of the structure.

Chapter 5 is devoted to the application of the eigencurrent approach for the analysis of a LCX. First the general idea behind the method is described and then the related computational detail is worked out for its application in a LCX setting. The dependence of the eigencurrents on the geometrical characteristics of the slots is analyzed in detail. Some further approximation techniques are presented and are compared to the standard formulation.

In Chapter 6 the numerical results for slotted coaxial cables are discussed. Their electromagnetic characteristics are analyzed in their dependence on the period and the geometry of the cell. Further, the longitudinal approach is set against the radial one.

Chapter 7 discusses the radiation properties of the slots on a coaxial cable. First a single slot is analyzed. A comparison with finite cylinders demonstrates that results that may appear strange at first sight, may be shown to be related to the infinite length of an LCX. Then, a cable with many slots is considered and the properties of the field radiated in the near-field region are discussed.

Chapter 8 presents a design technique for LCXs with uniform radiation along their length. In particular, we demonstrate how to taper the sizes of the apertures along the cable, in order to compensate for the power decay due to the radiation into the exterior unbounded domain.

Chapter 9 is devoted to the analysis of ring cavity filters. It is shown that a combination of the radial approach and the traditional longitudinal one allows us to generate a very efficient numerical code for the design of ring cavity filters.

In Chapter 10 we describe the numerical integration techniques, used in the implementation of the methods. In particular, a specific class of transformations of the variables of integration turns out to be very efficient and accurate.

Finally, conclusions are extracted from the analytic and numeric results, and an indication of directions for future research is given.

Chapter 2

Radial Transmission Lines

2.1 Radial transmission line equations

The electric and magnetic fields generated by electric and magnetic sources satisfy the well known Maxwell equations:

$$
\begin{aligned}
\nabla \times \underline{\mathcal{E}} &= - \mu \frac{\partial \underline{\mathcal{H}}}{\partial t} - \underline{\mathcal{J}}_m \\
\nabla \times \underline{\mathcal{H}} &= \varepsilon \frac{\partial \underline{\mathcal{E}}}{\partial t} + \underline{\mathcal{J}}_e
\end{aligned}
$$

in time domain and

$$
\begin{aligned}
\nabla \times \underline{E} &= -j\omega\mu \underline{H} - \underline{J}_m \\
\nabla \times \underline{H} &= +j\omega\varepsilon \underline{E} + \underline{J}_e
\end{aligned}
$$

in frequency domain, with the $\exp(j\omega t)$ time convention.

In the case of cylindrical waveguides of arbitrary cross section and axis $\hat{z}$, it is possible to define transverse vector mode functions, whose amplitudes can be considered as modal voltages and currents and satisfy transmission line equations [8].

Radial waveguides are non uniform cylindrical regions described by a $\rho,\ \varphi,\ z$ coordinate system. The transmission direction is along the radius ρ and the cross sections are the cylindrical surfaces ρ=const. It it well known, [7] page 30, that in this case it is not possible to define transverse vector modes. The representation of transverse fields must be carried out on a scalar basis, *i.e.* in terms of components. It will be found that a convenient matrix formalism and a radial circuit theory can be set up.

To carry out this program, let us start by writing Maxwell's equation a in cylindrical coordinate system (ρ, φ, z):

$$\hat{\rho}\left[\frac{1}{\rho}\frac{\partial E_z}{\partial \varphi} - \frac{\partial E_\varphi}{\partial z}\right] + \hat{\varphi}\left[\frac{\partial E_\rho}{\partial z} - \frac{\partial E_z}{\partial \rho}\right] + \hat{z}\left[\frac{E_\varphi}{\rho} + \frac{\partial E_\varphi}{\partial \rho} - \frac{1}{\rho}\frac{\partial E_\rho}{\partial \varphi}\right] =$$

$$= -j\omega\mu\left[H_\rho\hat{\rho} + H_\varphi\hat{\varphi} + H_z\hat{z}\right] - J_{m\varphi}\hat{\varphi} - J_{m\rho}\hat{\rho} - J_{mz}\hat{z} \tag{2.1}$$

$$\hat{\rho}\left[\frac{1}{\rho}\frac{\partial H_z}{\partial \varphi} - \frac{\partial H_\varphi}{\partial z}\right] + \hat{\varphi}\left[\frac{\partial H_\rho}{\partial z} - \frac{\partial H_z}{\partial \rho}\right] + \hat{z}\left[\frac{H_\varphi}{\rho} + \frac{\partial H_\varphi}{\partial \rho} - \frac{1}{\rho}\frac{\partial H_\rho}{\partial \varphi}\right] = \tag{2.2}$$

$$= j\omega\varepsilon\left[E_\rho\hat{\rho} + E_\varphi\hat{\varphi} + E_z\hat{z}\right] + J_{e\varphi}\hat{\varphi} + J_{e\rho}\hat{\rho} + J_{ez}\hat{z}$$

where $\hat{\rho}$, $\hat{\varphi}$ and $\hat{z}$ represent the three unit vectors of the cylindrical reference systems.

The components of the above equations can be written as:

$$\frac{1}{\rho}\frac{\partial E_z}{\partial \varphi} - \frac{\partial E_\varphi}{\partial z} = -j\omega\mu\, H_\rho - J_{m\rho}$$

$$\frac{\partial E_\rho}{\partial z} - \frac{\partial E_z}{\partial \rho} = -j\omega\mu\, H_\varphi - J_{m\varphi}$$

$$\frac{E_\varphi}{\rho} + \frac{\partial E_\varphi}{\partial \rho} - \frac{1}{\rho}\frac{\partial E_\rho}{\partial \varphi} = -j\omega\mu\, H_z - J_{mz}$$

$$\frac{1}{\rho}\frac{\partial H_z}{\partial \varphi} - \frac{\partial H_\varphi}{\partial z} = j\omega\varepsilon\, E_\rho + J_{e\rho}$$

$$\frac{\partial H_\rho}{\partial z} - \frac{\partial H_z}{\partial \rho} = j\omega\varepsilon\, E_\varphi + J_{e\varphi}$$

$$\frac{H_\varphi}{\rho} + \frac{\partial H_\varphi}{\partial \rho} - \frac{1}{\rho}\frac{\partial H_\rho}{\partial \varphi} = j\omega\varepsilon\, E_z + J_{ez}$$

Let us assume that the structure is infinite in the z direction for $0 \leq \varphi < 2\pi$ and filled with homogeneous dielectric. More general structures will be considered in Section 2.8. In order to derive a circuit formalism to study the propagation of electromagnetic fields in the $\hat{\rho}$ direction, the dependence on the variables φ and z must disappear. To this end, we introduce a spectral representation of fields and sources:

$$\tilde{E}_z(\rho,n,\chi) = \int_0^{2\pi}\int_{-\infty}^{+\infty} E_z(\rho,\varphi,\, z)\,\mathrm{e}^{jn\varphi}\,\mathrm{e}^{j\chi z} dz\, d\varphi \tag{2.3}$$

$$\tag{2.4}$$

$$E_z(\rho,\varphi,z) = \left(\frac{1}{2\pi}\right)^2 \sum_{n=-\infty}^{\infty} \mathrm{e}^{-jn\varphi}\int_{\Re} \tilde{E}_z(\rho,n,\chi)\,\mathrm{e}^{-j\chi z} d\chi \tag{2.5}$$

and similarly for all the other components. Here n is an integer and χ is a real number.
The use of these spectral representations is very convenient because of the symbolic relations

$$\frac{\partial}{\partial z} \longleftrightarrow -j\chi \qquad \frac{\partial}{\partial \varphi} \longleftrightarrow -jn$$

so that only the $\rho-$derivatives survive.
Substituting (2.5) in (2.3) one obtains:

$$\left\{\begin{array}{rcl} -\dfrac{jn}{\rho}\tilde{E}_z + j\chi\tilde{E}_\varphi & = & -j\omega\mu\tilde{H}_\rho - \tilde{J}_{m\rho} \\[2ex] -j\chi\tilde{E}_\rho - \dfrac{\partial\tilde{E}_z}{\partial\rho} & = & -j\omega\mu\tilde{H}_\varphi - \tilde{J}_{m\varphi} \\[2ex] \dfrac{\tilde{E}_\varphi}{\rho} + \dfrac{\partial\tilde{E}_\varphi}{\partial\rho} + \dfrac{jn}{\rho}\tilde{E}_\rho & = & -j\omega\mu\tilde{H}_z - \tilde{J}_{mz} \end{array}\right. \tag{2.6}$$

$$\left\{\begin{array}{rcl} -\dfrac{jn}{\rho}\tilde{H}_z + j\chi\tilde{H}_\varphi & = & j\omega\epsilon\tilde{E}_\rho + \tilde{J}_{e\rho} \\[2ex] -j\chi\tilde{H}_\rho - \dfrac{\partial\tilde{H}_z}{\partial\rho} & = & j\omega\epsilon\tilde{E}_\varphi + \tilde{J}_{e\varphi} \\[2ex] \dfrac{\tilde{H}_\varphi}{\rho} + \dfrac{\partial\tilde{H}_\varphi}{\partial\rho} + \dfrac{jn}{\rho}\tilde{H}_\rho & = & j\omega\epsilon\tilde{E}_z + \tilde{J}_{ez} \end{array}\right. \tag{2.7}$$

By using the same procedure that is generally applied in the standard analysis of cylindrical waveguides, we eliminate the longitudinal field components $\tilde{E}_\rho$, $\tilde{H}_\rho$ in order to develop a set of equations of Marcuvitz-Schwinger type, which contain only the transverse (to $\hat{\rho}$) field components. From the first equations of the (2.6) and (2.7) we obtain:

$$\tilde{H}_\rho = \frac{n}{\omega\mu\rho}\tilde{E}_z - \frac{\chi}{\omega\mu}\tilde{E}_\varphi + \frac{j}{\omega\mu}\tilde{J}_{m\rho} \tag{2.8}$$

$$\tilde{E}_\rho = -\frac{n}{\omega\epsilon\rho}\tilde{H}_z + \frac{\chi}{\omega\epsilon}\tilde{H}_\varphi + \frac{j}{\omega\epsilon}\tilde{J}_{e\rho} \tag{2.9}$$

Notice that $\tilde{E}_{z,\varphi}$ given by (2.5) is a spectral density of electric field per unit spatial bandwidth (with respect to z), hence it is measured in $V/m \cdot \dfrac{1}{m^{-1}} = V$. Likewise, $\tilde{H}_{z,\varphi}$ is measured in $A/m \cdot \dfrac{1}{m^{-1}} = A$.
For this reason we introduce the new symbols:

$$\underline{V} = \underline{V}(\rho, n, \chi) = \begin{pmatrix} V_u \\ V_v \end{pmatrix}(\rho, n, \chi) = \begin{pmatrix} \tilde{E}_z \\ \tilde{E}_\varphi \end{pmatrix}(\rho, n, \chi) \tag{2.10}$$

$$\underline{I} = \underline{I}(\rho, n, \chi) = \begin{pmatrix} I_u \\ I_v \end{pmatrix}(\rho, n, \chi) = \begin{pmatrix} -\tilde{H}_\varphi \\ \tilde{H}_z \end{pmatrix}(\rho, n, \chi) \tag{2.11}$$

and call them (vector) voltage and current. The definition of the vector current $\underline{I}$ is chosen so as to simplify the computation of the power flow in the ρ direction.
Clearly, if voltages and currents are (2×1) vectors, impedances and reflection coefficients are (2×2) matrices, here denoted by a double underline. These vectors belong to an abstract "polarization" space, with unit vectors:

$$\hat{u} = \begin{pmatrix} 1 \\ 0 \end{pmatrix} \qquad \hat{v} = \begin{pmatrix} 0 \\ 1 \end{pmatrix}$$

Substituting now (2.9) and (2.8) into the second and third equations of (2.6) and (2.7) we get:

$$-\frac{d}{d\rho}\begin{bmatrix} \underline{V} \\ \\ \underline{I} \end{bmatrix} = \begin{bmatrix} \underline{\underline{D}}_1 & j\,\underline{\underline{Z}}_1 \\ \\ j\,\underline{\underline{Y}}_2 & \underline{\underline{D}}_2 \end{bmatrix} \cdot \begin{bmatrix} \underline{V} \\ \\ \underline{I} \end{bmatrix} + \begin{bmatrix} \overset{\circ}{\underline{v}} \\ \\ \overset{\circ}{\underline{i}} \end{bmatrix} \tag{2.12}$$

where:

$$\underline{\underline{D}}_1 = \underline{\underline{D}}_1(\rho) = \begin{bmatrix} 0 & 0 \\ \\ 0 & \dfrac{1}{\rho} \end{bmatrix} ; \underline{\underline{D}}_2 = \underline{\underline{D}}_2(\rho) = \begin{bmatrix} \dfrac{1}{\rho} & 0 \\ \\ 0 & 0 \end{bmatrix}$$

$$\underline{\underline{Z}}_1 = \underline{\underline{Z}}_1(\rho) = \begin{bmatrix} \dfrac{\tau^2}{\omega\epsilon} & -\dfrac{n\chi}{\omega\epsilon\rho} \\ \\ -\dfrac{n\chi}{\omega\epsilon\rho} & \dfrac{1}{\omega\epsilon}(k^2 - \dfrac{n^2}{\rho^2}) \end{bmatrix} ; \underline{\underline{Y}}_2 = \underline{\underline{Y}}_2(\rho) = \begin{bmatrix} \dfrac{1}{\omega\mu}(k^2 - \dfrac{n^2}{\rho^2}) & +\dfrac{n\chi}{\omega\mu\rho} \\ \\ +\dfrac{n\chi}{\omega\mu\rho} & \dfrac{\tau^2}{\omega\mu} \end{bmatrix}$$

$$\overset{\circ}{\underline{v}} = \begin{bmatrix} -\dfrac{\chi}{\omega\epsilon} \\ \\ -\dfrac{n}{\omega\epsilon\rho} \end{bmatrix} \cdot \tilde{J}_{e\,\rho} + \begin{bmatrix} -1 & 0 \\ \\ 0 & 1 \end{bmatrix} \cdot \begin{bmatrix} \tilde{J}_{m\varphi} \\ \\ \tilde{J}_{m\,z} \end{bmatrix} \tag{2.13}$$

$$\overset{\circ}{\underline{i}} = \begin{bmatrix} +\dfrac{n}{\omega\mu\rho} \\ \\ -\dfrac{\chi}{\omega\mu} \end{bmatrix} \cdot \tilde{J}_{m\,\rho} + \begin{bmatrix} 0 & 1 \\ \\ 1 & 0 \end{bmatrix} \cdot \begin{bmatrix} \tilde{J}_{e\varphi} \\ \\ \tilde{J}_{e\,z} \end{bmatrix}$$

and $k^2 \triangleq \omega^2\mu\epsilon$ is the wavenumber and $\tau \triangleq \sqrt{k^2 - \chi^2}$ plays the role of a longitudinal propagation constant. Equations 2.12 are the radial transmission line equations. The sign conventions are shown in Fig. 2.1. The evident asymmetry in the definition of the vector current in (2.11)

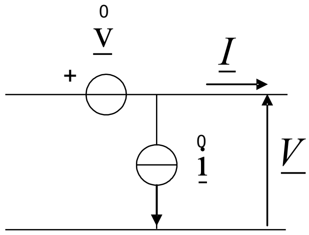

Figure 2.1: Sign conventions for the distributed generators

is explained by the desire of a simple expression for the time-averaged power transmitted across a cylindrical surface of radius $\rho = \rho_0$. As well known, this power is given by the flux of the Poynting vector

$$P = \frac{1}{2}\Re\left\{\int_S \underline{E}(\rho_0, \varphi, z) \times \underline{H}^*(\rho_0, \varphi, z) \cdot \hat{\rho} dS\right\} \tag{2.14}$$

where the superscript "*" stands for complex conjugate. In terms of components[1]:

$$P = \frac{1}{2}\Re\left\{\rho_0 \int_0^{2\pi} \int_{-\infty}^{+\infty} \left[-E_z H_\varphi^* + E_\varphi H_z^*\right] d\varphi dz\right\} =$$
$$= \frac{1}{2}\Re\left\{\frac{\rho_0}{4\pi^2} \int_\chi \sum_n \left[-\tilde{E}_z \tilde{H}_\varphi^* + \tilde{E}_\varphi \tilde{H}_z^*\right] d\chi\right\} \tag{2.15}$$

where Parseval theorem has been applied. Thanks to the definition (2.11), this power is computed as:

$$P = \frac{1}{2}\Re\left\{\frac{\rho_0}{4\pi^2} \int_\chi \sum_n \left[V_u(\rho,\chi,n) I_u^*(\rho,\chi,n) + V_v(\rho,\chi,n) I_v^*(\rho,\chi,n)\right] d\chi\right\}$$

i.e.:

$$P = \frac{1}{2}\Re\left\{\frac{\rho_0}{4\pi^2} \int_\chi \sum_n \underline{V}(\rho,\chi,n) \cdot \underline{I}^*(\rho,\chi,n) d\chi\right\} \tag{2.16}$$

which has a clear circuit flavor. Moreover, the integrand $\rho_0 \underline{V}(\rho,\chi,n) \cdot \underline{I}^*(\rho,\chi,n)$, measured in Wm=W/m^{-1}, can be interpreted as the spectral density of active power per unit spatial bandwidth (with respect to z) associated to a cylindrical wave.

2.2 Solution of radial transmission line equations

In this section we will obtain the solution of the radial transmission line equations (2.12). It is to be remarked that the system matrix is a function of ρ and it can be verified that also its eigenvectors depend on ρ. This implies that no vector mode (in the u, v space) can be introduced for this system. Nevertheless it can be solved analytically .

The (2.12) is a linear system of differential equations which concisely can be written as:

$$\begin{cases} -\dfrac{d}{d\rho}\underline{\psi}(\rho) = \underline{\underline{A}}(\rho)\underline{\psi}(\rho) + \underline{s}(\rho) \\ \\ \underline{\psi}(\rho) = \underline{\psi}_0 \quad \text{given} \end{cases} \tag{2.17}$$

The solution of this initial value problem is is well known in literature [9] and can be written as:

$$\underline{\psi}(\rho) = \underline{\underline{F}}(\rho,\rho_0) \cdot \underline{\psi}(\rho_0) + \int_{\rho_0}^{\rho} \underline{\underline{F}}(\rho,\rho_0) \cdot \underline{\underline{F}}^{-1}(\rho',\rho_0) \cdot \underline{s}(\rho') d\rho' \tag{2.18}$$

---

[1] from here on, where not expressly indicated, the sum are from $-\infty$ to $+\infty$

where $\underline{\underline{F}}(\rho, \rho_0)$ is the fundamental matrix (or matricant) which obeys:

$$\begin{cases} -\dfrac{d}{d\rho}\underline{\underline{F}}(\rho, \rho_0) = \underline{\underline{A}}(\rho)\underline{\underline{F}}(\rho, \rho_0) \\ \\ \underline{\underline{F}}(\rho, \rho_0) = \underline{\underline{U}} \end{cases} \tag{2.19}$$

where $\underline{\underline{U}}$ is the 4×4 identity matrix.
The solution of this equation will be carried out in the next pages and the result will be finally obtained in section 2.5. In the course of the derivation a number of useful circuit concepts will be introduced, such as the wave impedances, the voltage/current propagators, etc.
the equation to be solved is:

$$-\frac{d}{d\rho}\begin{pmatrix} \tilde{E}_z \\ \tilde{E}_\varphi \\ -\tilde{H}_\varphi \\ \tilde{H}_z \end{pmatrix} = \underline{\underline{A}} \cdot \begin{pmatrix} \tilde{E}_z \\ \tilde{E}_\varphi \\ -\tilde{H}_\varphi \\ \tilde{H}_z \end{pmatrix} \tag{2.20}$$

The idea is to eliminate the transverse field components (*i.e.* $\tilde{E}_\varphi$ and $\tilde{H}_\varphi$): the z axis is a symmetry axis for the system and it can be expected that the longitudinal components (*i.e.* $\tilde{E}_z$ and $\tilde{H}_z$) play a special role.
Let us, therefore, consider the homogeneous problem for an infinite radial line, where the voltage and current generators are absent and $0 \le \rho < \infty$. It is convenient to define the two column vectors $\underline{\tilde{L}}$ and $\underline{\tilde{T}}$ to collect the Fourier transforms of the longitudinal and the transverse field components:

$$\underline{\tilde{L}} = \begin{pmatrix} \tilde{E}_z \\ \\ \tilde{H}_z \end{pmatrix}, \qquad \underline{\tilde{T}} = \begin{pmatrix} \tilde{E}_\varphi \\ \\ \tilde{H}_\varphi \end{pmatrix}$$

In terms of these, (2.12) can be rewritten as:

$$\frac{d}{d\rho}\begin{bmatrix} \underline{\tilde{L}} \\ \\ \underline{\tilde{T}} \end{bmatrix} = \begin{bmatrix} \underline{\underline{M}}_{11} & \underline{\underline{M}}_{12} \\ \\ \underline{\underline{M}}_{21} & \underline{\underline{M}}_{22} \end{bmatrix} \cdot \begin{bmatrix} \underline{\tilde{L}} \\ \\ \underline{\tilde{T}} \end{bmatrix} \tag{2.21}$$

where:

$$\underline{\underline{M}}_{11} = \underline{\underline{M}}_{11}(\rho) = \frac{j\chi n}{\omega\rho}\begin{bmatrix} 0 & \dfrac{1}{\epsilon} \\ \\ -\dfrac{1}{\mu} & 0 \end{bmatrix}$$

$$\underline{\underline{M}}_{12} = \underline{\underline{M}}_{12}(\rho) = \frac{j\tau^2}{\omega} \begin{bmatrix} 0 & \dfrac{1}{\epsilon} \\ & \\ -\dfrac{1}{\mu} & 0 \end{bmatrix}$$

$$\underline{\underline{M}}_{21} = \underline{\underline{M}}_{21}(\rho) = \frac{j}{\omega}\left(k^2 - \frac{n^2}{\rho^2}\right) \begin{bmatrix} 0 & \dfrac{1}{\epsilon} \\ & \\ -\dfrac{1}{\mu} & 0 \end{bmatrix}$$

$$\underline{\underline{M}}_{22} = \underline{\underline{M}}_{22}(\rho) = -\frac{1}{\rho}\underline{\underline{U}} - \frac{j\,n\chi}{\omega\rho} \begin{bmatrix} 0 & \dfrac{1}{\epsilon} \\ & \\ -\dfrac{1}{\mu} & 0 \end{bmatrix}$$

where $\underline{\underline{U}}$ is the identity matrix. From the first equation of (2.21) one obtains:

$$\underline{\tilde{T}} = \underline{\underline{M}}_{12}^{-1} \cdot \frac{\partial \underline{\tilde{L}}}{\partial \rho} - \underline{\underline{M}}_{12}^{-1} \cdot \underline{\underline{M}}_{11} \cdot \underline{\tilde{L}} \tag{2.22}$$

then the second equation becomes:

$$\frac{\partial}{\partial \rho}\left(\underline{\underline{M}}_{12}^{-1} \cdot \frac{\partial \underline{\tilde{L}}}{\partial \rho} - \underline{\underline{M}}_{12}^{-1} \cdot \underline{\underline{M}}_{11} \cdot \underline{\tilde{L}}\right) = \underline{\underline{M}}_{21} \cdot \underline{\tilde{L}} + \underline{\underline{M}}_{21} \cdot \left(\underline{\underline{M}}_{12}^{-1} \cdot \frac{\partial \underline{\tilde{L}}}{\partial \rho} - \underline{\underline{M}}_{12}^{-1} \cdot \underline{\underline{M}}_{11} \cdot \underline{\tilde{L}}\right)$$

i.e.

$$\begin{aligned} &\frac{d^2 \underline{\tilde{L}}}{d^2 \rho} - \left(\underline{\underline{M}}_{11} + \underline{\underline{M}}_{12} \cdot \underline{\underline{M}}_{22} \cdot \underline{\underline{M}}_{12}^{-1}\right) \frac{d\underline{\tilde{L}}}{d\rho} + \\ &- \left(\frac{d}{d\rho}\underline{\underline{M}}_{11} + \underline{\underline{M}}_{12} \cdot \underline{\underline{M}}_{21} - \underline{\underline{M}}_{12} \cdot \underline{\underline{M}}_{22} \cdot \underline{\underline{M}}_{12}^{-1} \cdot \underline{\underline{M}}_{11}\right) \underline{\tilde{L}} = 0 \end{aligned} \tag{2.23}$$

From a direct computation of the matrix products, one obtains:

$$\frac{d^2 \underline{\tilde{L}}}{d^2 \rho} + \frac{1}{\rho}\frac{d\underline{\tilde{L}}}{d\rho} + \left(\tau^2 - \frac{n^2}{\rho^2}\right) \underline{\tilde{L}} = 0 \tag{2.24}$$

$$\underline{\tilde{T}} = \frac{\omega}{j\tau^2} \begin{pmatrix} 0 & -\mu \\ \epsilon & 0 \end{pmatrix} \frac{d}{d\rho}\underline{\tilde{L}} - \frac{n\chi}{\rho\tau^2}\underline{\tilde{L}} \tag{2.25}$$

The first expression is recognized as the Bessel equation. In terms of the components V_u, V_v, I_u and I_v we have:

$$\left[\frac{\partial^2}{\partial\rho^2}+\frac{1}{\rho}\frac{\partial}{\partial\rho}+\tau^2-\left(\frac{n}{\rho}\right)^2\right]V_u(\rho)=0 \tag{2.26}$$

$$\left[\frac{\partial^2}{\partial\rho^2}+\frac{1}{\rho}\frac{\partial}{\partial\rho}+\tau^2-\left(\frac{n}{\rho}\right)^2\right]I_v(\rho)=0 \tag{2.27}$$

$$V_v(\rho)=-\frac{n\chi}{\rho\tau^2}V_u(\rho)+\frac{j\omega\mu}{\tau^2}\frac{\partial}{\partial\rho}I_v(\rho) \tag{2.28}$$

$$I_u(\rho)=+\frac{n\chi}{\rho\tau^2}I_v(\rho)+\frac{j\omega\varepsilon}{\tau^2}\frac{\partial}{\partial\rho}V_u(\rho) \tag{2.29}$$

The general solutions of (2.26) and (2.27) can be written in a variety of ways in terms of Bessel functions. We have chosen the following "mixed" form:

$$V_u(\rho,\chi,n)=\overset{\leftrightsquigarrow}{c_E}\,J_n(\tau\rho)+\overset{\rightsquigarrow}{c_E}\,H_n^{(2)}(\tau\rho) \tag{2.30}$$

$$I_v(\rho,\chi,n)=\underbrace{\overset{\leftrightsquigarrow}{c_H}\,J_n(\tau\rho)}_{\text{regularwave}}+\underbrace{\overset{\rightsquigarrow}{c_H}\,H_n^{(2)}(\tau\rho)}_{\text{centrifugalwave}} \tag{2.31}$$

where $\overset{\leftrightsquigarrow}{c}_{E,H}, \overset{\rightsquigarrow}{c}_{E,H}$ are constants that depend on the boundary conditions of the circuit problem. The right arrow indicates that the corresponding solutions propagates outwards, whereas the double arrows indicates that the solution are regular in the interior domain, implying that they consist of both outward and inward propagating constituents. The subscript E in the first line is related to the fact that V_u is the transform of E_z and, hence, describes an E-field configuration (*i.e.* TM). Likewise, the subscript H in the second line denotes an H-field configuration (*i.e.* TE). Moreover, c_E, c_H have dimensions of voltage and current, respectively, and denote the amount of TM and TE contribution to the total wavefield. In order to use a more balanced description, we introduce another set of variables, of the "power wave type", with dimensions $\sqrt{W}$:

$$c_E=a_E\sqrt{Z} \qquad\qquad c_H=a_h\sqrt{Y} \tag{2.32}$$

where $Z=\sqrt{\mu/\varepsilon}$ is the medium wave impedance.

By means of (2.28) and (2.29), we can complete the expressions of the $\underline{V}$ and $\underline{I}$ vectors. We see that the expressions of the total voltage and current decompose naturally into the sum of a regular and a centrifugal wave. Let us highlight their respective characteristics.

–**Regular wave** The voltage and current of this wave can be written as

$$\overset{\leftrightsquigarrow}{\underline{V}}(\rho) = \sqrt{Z} \begin{pmatrix} \overset{\leftrightsquigarrow}{a}_E \, J_n(\tau\rho) \\ \\ -\dfrac{n\chi}{\rho\tau^2}\overset{\leftrightsquigarrow}{a}_E \, J_n(\tau\rho) + \dfrac{j\,k}{\tau}\overset{\leftrightsquigarrow}{a}_H \, J_n'(\tau\rho) \end{pmatrix}$$

and

$$\overset{\leftrightsquigarrow}{\underline{I}}(\rho) = \sqrt{Y} \begin{pmatrix} +\dfrac{n\chi}{\rho\tau^2}\overset{\leftrightsquigarrow}{a}_H \, J_n(\tau\rho) + \dfrac{j\,k}{\tau}\overset{\leftrightsquigarrow}{a}_E \, J_n'(\tau\rho) \\ \\ \overset{\leftrightsquigarrow}{a}_H \, J_n(\tau\rho) \end{pmatrix}$$

where $k = \omega\sqrt{\varepsilon\mu}$ is the medium wavenumber. In a more compact form:

$$\overset{\leftrightsquigarrow}{\underline{V}}(\rho) = \sqrt{Z} \; \overset{\leftrightsquigarrow}{\underline{\underline{M}}}_V(\rho) \cdot \overset{\leftrightsquigarrow}{\underline{a}} \tag{2.33}$$

$$\overset{\leftrightsquigarrow}{\underline{I}}(\rho) = \sqrt{Y} \; \overset{\leftrightsquigarrow}{\underline{\underline{M}}}_I(\rho) \cdot \overset{\leftrightsquigarrow}{\underline{a}} \tag{2.34}$$

where:

$$\overset{\leftrightsquigarrow}{\underline{\underline{M}}}_V(\rho) = \begin{pmatrix} J_n(\tau\rho) & 0 \\ \\ -\dfrac{n\chi}{\tau^2\rho}J_n(\tau\rho) & \dfrac{j\,k}{\tau}J_n'(\tau\rho) \end{pmatrix}$$

$$\overset{\leftrightsquigarrow}{\underline{\underline{M}}}_I(\rho) = \begin{pmatrix} \dfrac{j\,k}{\tau}J_n'(\tau\rho) & \dfrac{n\chi}{\rho\tau^2}J_n(\tau\rho) \\ \\ 0 & J_n(\tau\rho) \end{pmatrix}$$

$$\overset{\leftrightsquigarrow}{\underline{a}} = \begin{pmatrix} \overset{\leftrightsquigarrow}{a}_E \\ \\ \overset{\leftrightsquigarrow}{a}_H \end{pmatrix} \tag{2.35}$$

Notice that the matrices $\overset{\leftrightsquigarrow}{\underline{\underline{M}}}_{V,I}(\rho)$ have a geometrical meaning, since their elements are dimensionless. This wave is called regular because it satisfies the regularity prescription at the endpoint $\rho = 0$. Since the Bessel functions of the first kind are real, it is clearly a stationary wave. It may be of interest to compute the active power carried by this wave:

$$P = \frac{1}{2}\Re\left\{\overset{\leftrightsquigarrow}{\underline{V}}(\rho,\chi,n)\cdot\overset{\leftrightsquigarrow}{\underline{I}}^{*}(\rho,\chi,n)\right\} = \frac{1}{2}\Re\left\{\overset{\leftrightsquigarrow}{\underline{a}}^{T}\cdot\overset{\leftrightsquigarrow}{\underline{\underline{M}}}{}_{V}^{T}(\rho)\cdot\overset{\leftrightsquigarrow}{\underline{\underline{M}}}{}_{I}^{*}(\rho)\cdot\overset{\leftrightsquigarrow}{\underline{a}}^{*}\right\} =$$

$$= \frac{1}{2}\Re\left\{\overset{\leftrightsquigarrow}{\underline{a}}^{T}\cdot\begin{pmatrix} -\dfrac{j\,k}{\tau}J_n(\tau\rho)J_n'(\tau\rho) & 0 \\ & \\ 0 & \dfrac{j\,k}{\tau}J_n(\tau\rho)J_n'(\tau\rho)\end{pmatrix}\cdot\overset{\leftrightsquigarrow}{\underline{a}}^{*}\right\} =$$

$$= \frac{1}{2}\Re\left\{\frac{j\,k}{\tau}J_n(\tau\rho)J_n'(\tau\rho)\left(|\overset{\leftrightsquigarrow}{a_H}|^2 - |\overset{\leftrightsquigarrow}{a_E}|^2\right)\right\} = 0 \tag{2.36}$$

in accordance with the stationary character.

–**Centrifugal wave** The voltage and current of this wave can be written as

$$\overset{\rightsquigarrow}{\underline{V}}(\rho) = \sqrt{Z}\begin{pmatrix} \overset{\rightsquigarrow}{a_E}\,H_n^{(2)}(\tau\rho) \\ \\ -\dfrac{n\chi}{\rho\tau^2}\overset{\rightsquigarrow}{a_E}\,H_n^{(2)}(\tau\rho) + \dfrac{j\,k}{\tau}\overset{\rightsquigarrow}{a_H}\,H_n'^{(2)}(\tau\rho)\end{pmatrix}$$

and

$$\overset{\rightsquigarrow}{\underline{I}}(\rho) = \sqrt{Y}\begin{pmatrix} +\dfrac{n\chi}{\rho\tau^2}\overset{\rightsquigarrow}{a_H}\,H_n^{(2)}(\tau\rho) + \dfrac{j\,k}{\tau}\overset{\rightsquigarrow}{a_E}\,H_n'^{(2)}(\tau\rho) \\ \\ \overset{\rightsquigarrow}{a_H}\,H_n^{(2)}(\tau\rho)\end{pmatrix}$$

or in a more compact form:

$$\overset{\rightsquigarrow}{\underline{V}}(\rho) = \sqrt{Z}\;\overset{\rightsquigarrow}{\underline{\underline{M}}}{}_{V}(\rho)\cdot\overset{\rightsquigarrow}{\underline{a}} \tag{2.37}$$

$$\overset{\rightsquigarrow}{\underline{I}}(\rho) = \sqrt{Y}\;\overset{\rightsquigarrow}{\underline{\underline{M}}}{}_{I}(\rho)\cdot\overset{\rightsquigarrow}{\underline{a}} \tag{2.38}$$

where:

$$\overset{\leadsto}{\underline{\underline{M}}}_V(\rho) = \begin{pmatrix} H_n^{(2)}(\tau\rho) & 0 \\ \\ -\dfrac{n\chi}{\tau^2\rho} H_n^{(2)}(\tau\rho) & \dfrac{j\,k}{\tau} H_n'^{(2)}(\tau\rho) \end{pmatrix}$$

$$\overset{\leadsto}{\underline{\underline{M}}}_I(\rho) = \begin{pmatrix} \dfrac{j\,k}{\tau} H_n'^{(2)}(\tau\rho) & \dfrac{n\chi}{\rho\tau^2} H_n^{(2)}(\tau\rho) \\ \\ 0 & H_n^{(2)}(\tau\rho) \end{pmatrix}$$

$$\overset{\leadsto}{\underline{a}} = \begin{pmatrix} \overset{\leadsto}{a}_E \\ \\ \overset{\leadsto}{a}_H \end{pmatrix}$$

This wave is called centrifugal because it satisfies the radiation condition at $\rho \to \infty$. The asymptotic expansion of Hankel functions shows clearly that, for $\tau\rho \gg n$, this wave has a phase that (apart from constants) approaches $-\tau\rho$, typical of an outward travelling wave. Let us compute the power associated to it:

$$P = \frac{1}{2}\Re\left\{\overset{\leadsto}{\underline{V}}(\rho,\chi,n) \cdot \overset{\leadsto}{\underline{I}}^*(\rho,\chi,n)\right\} = \frac{1}{2}\Re\left\{\overset{\leadsto}{\underline{a}}^T \cdot \overset{\leadsto}{\underline{\underline{M}}}{}_V^T(\rho) \cdot \overset{\leadsto}{\underline{\underline{M}}}{}_I^*(\rho) \cdot \overset{\leadsto}{\underline{a}}^*\right\} =$$

$$= \frac{1}{2}\Re\left\{\overset{\leadsto}{\underline{a}}^T \cdot \begin{pmatrix} -\dfrac{j\,k}{\tau} H_n^{(2)}(\tau\rho) H_n'^{(2)*}(\tau\rho) & 0 \\ \\ 0 & \dfrac{j\,k}{\tau} H_n'^{(2)}(\tau\rho) H_n^{(2)*}(\tau\rho) \end{pmatrix} \cdot \overset{\leadsto}{\underline{a}}^*\right\} \tag{2.39}$$

To simplify this expression, recall that

$$\begin{aligned} H_n^{(2)} H_n'^{(2)*} &= (J_n - jY_n)(J_n' + jY_n') \\ &= (J_n J_n' + Y_n Y_n') + j(J_n Y_n' - J_n' Y_n) \\ &= (J_n J_n' + Y_n Y_n') + j\frac{2}{\pi\tau\rho} \end{aligned} \tag{2.40}$$

where the Wronskian relation of Bessel functions has been used. In conclusion, noting that the first term gives no contribution when the real part is taken,

$$P = \frac{1}{\pi\tau\rho}\frac{k}{\tau}\left(|\overset{\leadsto}{a}_E|^2 + |\overset{\leadsto}{a}_H|^2\right) \tag{2.41}$$

This equation shows clearly that the TM and TE field portions are power-orthogonal. By comparison with (2.16), this quantity is 2π times the power per unit spatial bandwidth and per unit length along a circular arc of radius ρ. This explains why it is measured in Watt, but is inversely proportional to ρ. If we want to compute the power per unit spatial bandwidth crossing the surface of a cylinder of radius ρ we must multiply P by this radius ρ, obtaining a value, expressed in W/m^{-1}=Wm, independent of ρ.

It is possible to note that the structure matrices $\underline{\underline{M}}_V(\rho)$ and $\underline{\underline{M}}_I(\rho)$ for each wave type are closely related. In particular we note the following relations

$$\underline{\underline{M}}_V(\rho) = \underline{\underline{R}}^{-1} \cdot \underline{\underline{M}}_I(\rho) \cdot \underline{\underline{R}} \tag{2.42}$$

$$\underline{\underline{M}}_I(\rho) = \underline{\underline{R}}^{-1} \cdot \underline{\underline{M}}_V(\rho) \cdot \underline{\underline{R}} \tag{2.43}$$

where the matrix $\underline{\underline{R}}$ is

$$\underline{\underline{R}} = \begin{pmatrix} 0 & 1 \\ \\ -1 & 0 \end{pmatrix}$$

which has the properties

$$\underline{\underline{R}}^{-1} = -\underline{\underline{R}} \qquad\qquad \underline{\underline{R}}^2 = -\underline{\underline{U}}$$

Instead of the general solution in mixed form (2.31) one could have chosen

$$V_u(\rho,\chi,n) = \overleftarrow{c}_E\, H_n^{(1)}(\tau\rho) + \overset{\rightsquigarrow}{c}_E\, H_n^{(2)}(\tau\rho) \tag{2.44}$$

$$I_v(\rho,\chi,n) = \underbrace{\overleftarrow{c}_H\, H_n^{(1)}(\tau\rho)}_{\text{centripetalwave}} + \underbrace{\overset{\rightsquigarrow}{c}_H\, H_n^{(2)}(\tau\rho)}_{\text{centrifugalwave}} \tag{2.45}$$

The first term in this case is a centripetal wave, *i.e.* it carries power toward the origin and, for $\tau\rho \gg n$ the phase (apart from constants) approaches $\tau\rho$. This wave cannot exist alone in a neighborhood of the origin, because it is singular at $\rho = 0$. In other words, the origin has a nonzero reflection coefficient. In the following we will always use the decomposition into regular and centrifugal wave.

2.3 Impedance relations

In this paragraph we will derive the matrix operators that relate voltages and currents in a particular section $\rho = \rho_0$, for the regular and the centrifugal wave. In other words, their impedance relations will be deduced.

In the case of an ordinary (uniform) transmission line this concept tends to be confused with that of line impedance, which coincides with the forward wave impedance. To be precise, the backward wave has an opposite impedance, but usually the appropriate sign is used directly in the equations. In the case of a radial line, instead, the impedances of the regular and the centrifugal wave are completely different and neither can be adopted as “line impedance”. Moreover, they are functions of ρ due to the intrinsic non uniformity of radial lines.

–Regular wave

The relevant wave impedance $\overset{\leftrightsquigarrow}{\underline{\underline{Z}}}(\rho)$ and admittance $\overset{\leftrightsquigarrow}{\underline{\underline{Y}}}(\rho)$ are defined by:

$$\overset{\leftrightsquigarrow}{\underline{I}} = \overset{\leftrightsquigarrow}{\underline{\underline{Y}}}(\rho) \cdot \overset{\leftrightsquigarrow}{\underline{V}} \tag{2.46}$$

$$\overset{\leftrightsquigarrow}{\underline{V}} = \overset{\leftrightsquigarrow}{\underline{\underline{Z}}}(\rho) \cdot \overset{\leftrightsquigarrow}{\underline{I}} \tag{2.47}$$

Their explicit form can be deduced combining (2.33) and (2.34):

$$\overset{\leftrightsquigarrow}{\underline{\underline{Z}}}(\rho) = Z\, \overset{\leftrightsquigarrow}{\underline{\underline{M}}}_V(\rho) \cdot \overset{\leftrightsquigarrow}{\underline{\underline{M}}}{}_I^{-1}(\rho) \tag{2.48}$$

$$\overset{\leftrightsquigarrow}{\underline{\underline{Y}}}(\rho) = Y\, \overset{\leftrightsquigarrow}{\underline{\underline{M}}}_I(\rho) \cdot \overset{\leftrightsquigarrow}{\underline{\underline{M}}}{}_V^{-1}(\rho) \tag{2.49}$$

i.e.:

$$\overset{\leftrightsquigarrow}{\underline{\underline{Z}}}(\rho) = Z \begin{pmatrix} -\dfrac{j\tau}{k}\dfrac{J_n(\tau\rho)}{J'_n(\tau\rho)} & +\dfrac{j\chi\, n}{k\tau\rho}\dfrac{J_n(\tau\rho)}{J'_n(\tau\rho)} \\ +\dfrac{j\chi\, n}{k\tau\rho}\dfrac{J_n(\tau\rho)}{J'_n(\tau\rho)} & +\dfrac{j\, k}{\tau}\dfrac{J'_n(\tau\rho)}{J_n(\tau\rho)} - \dfrac{j\chi^2 n^2}{k\tau^3\rho^2}\dfrac{J_n(\tau\rho)}{J'_n(\tau\rho)} \end{pmatrix} \tag{2.50}$$

$$\overset{\leftrightsquigarrow}{\underline{\underline{Y}}}(\rho) = Y \begin{pmatrix} \dfrac{j\, k}{\tau}\dfrac{J'_n(\tau\rho)}{J_n(\tau\rho)} - \dfrac{j\chi^2 n^2}{k\tau^3\rho^2}\dfrac{J_n(\tau\rho)}{J'_n(\tau\rho)} & -\dfrac{j\chi\, n}{k\tau\rho}\dfrac{J_n(\tau\rho)}{J'_n(\tau\rho)} \\ -\dfrac{j\chi\, n}{k\tau\rho}\dfrac{J_n(\tau\rho)}{J'_n(\tau\rho)} & -\dfrac{j\tau}{k}\dfrac{J_n(\tau\rho)}{J'_n(\tau\rho)} \end{pmatrix} \tag{2.51}$$

Since the matrices $\overset{\leftrightsquigarrow}{\underline{\underline{M}}}_V$ and $\overset{\leftrightsquigarrow}{\underline{\underline{M}}}_I$ have the same determinant (see (2.42)), the matrices appearing in the expressions of $\overset{\leftrightsquigarrow}{\underline{\underline{Z}}}$ and $\overset{\leftrightsquigarrow}{\underline{\underline{Y}}}$ have determinant equal to one. This explains why one can be obtained from the other by simple element exchanges.

Notice that the regular wave impedance is pure imaginary (for real τ), in accordance with the fact that this wave carries no active power. Moreover the origin is a singular point:

$$\lim_{\rho\to 0}\overset{\leftrightsquigarrow}{\underline{\underline{Z}}}(\rho) = -Z \begin{pmatrix} 0 & -\dfrac{j\chi}{k} \\ -\dfrac{j\chi}{k} & \infty \end{pmatrix} \qquad \text{for } n \neq 0 \tag{2.52}$$

$$= -Z \begin{pmatrix} \infty & 0 \\ 0 & 0 \end{pmatrix} \qquad \text{for } n = 0 \tag{2.53}$$

–Centrifugal wave

The relevant wave impedance $\overset{\rightsquigarrow}{\underline{\underline{Z}}}(\rho)$ and admittance $\overset{\rightsquigarrow}{\underline{\underline{Y}}}(\rho)$ are defined by:

$$\overset{\rightsquigarrow}{\underline{I}} = \overset{\rightsquigarrow}{\underline{\underline{Y}}}(\rho)\cdot\overset{\rightsquigarrow}{\underline{V}} \tag{2.54}$$

$$\overset{\rightsquigarrow}{\underline{V}} = \overset{\rightsquigarrow}{\underline{\underline{Z}}}(\rho)\cdot\overset{\rightsquigarrow}{\underline{I}} \tag{2.55}$$

As done before, one obtains from (2.37) and (2.38):

$$\overset{\rightsquigarrow}{\underline{\underline{Z}}}(\rho) = Z\,\overset{\rightsquigarrow}{\underline{\underline{M}}}_V\cdot\overset{\rightsquigarrow}{\underline{\underline{M}}}{}_I^{-1} \tag{2.56}$$

$$\overset{\rightsquigarrow}{\underline{\underline{Y}}}(\rho) = Y\,\overset{\rightsquigarrow}{\underline{\underline{M}}}_I\cdot\overset{\rightsquigarrow}{\underline{\underline{M}}}{}_V^{-1} \tag{2.57}$$

i.e.:

$$\overset{\rightsquigarrow}{\underline{\underline{Z}}}(\rho) = Z \begin{pmatrix} -\dfrac{j\tau}{k}\dfrac{H_n^{(2)}(\tau\rho)}{H_n'^{(2)}(\tau\rho)} & \dfrac{j\chi\,n}{k\tau\rho}\dfrac{H_n^{(2)}(\tau\rho)}{H_n'^{(2)}(\tau\rho)} \\ \dfrac{j\chi\,n}{k\tau\rho}\dfrac{H_n^{(2)}(\tau\rho)}{H_n'^{(2)}(\tau\rho)} & \dfrac{j\,k}{\tau}\dfrac{H_n'^{(2)}(\tau\rho)}{H_n^{(2)}(\tau\rho)} - \dfrac{j\chi^2n^2}{k\tau^3\rho^2}\dfrac{H_n^{(2)}(\tau\rho)}{H_n'^{(2)}(\tau\rho)} \end{pmatrix} \tag{2.58}$$

$$\overset{\rightsquigarrow}{\underline{\underline{Y}}}(\rho) = Y \begin{pmatrix} \dfrac{jk}{\tau}\dfrac{H_n'^{(2)}(\tau\rho)}{H_n^{(2)}(\tau\rho)} - \dfrac{j\chi^2n^2}{k\tau^3\rho^2}\dfrac{H_n^{(2)}(\tau\rho)}{H_n'^{(2)}(\tau\rho)} & -\dfrac{j\chi\,n}{k\tau\rho}\dfrac{H_n^{(2)}(\tau\rho)}{H_n'^{(2)}(\tau\rho)} \\ -\dfrac{j\chi\,n}{k\tau\rho}\dfrac{H_n^{(2)}(\tau\rho)}{H_n'^{(2)}(\tau\rho)} & -\dfrac{j\tau}{k}\dfrac{H_n^{(2)}(\tau\rho)}{H_n'^{(2)}(\tau\rho)} \end{pmatrix} \tag{2.59}$$

The centrifugal wave impedance is complex in general, but

$$\lim_{\rho\to\infty} \overset{\rightsquigarrow}{\underline{\underline{Z}}}(\rho) = Z \begin{pmatrix} \dfrac{\tau}{k} & 0 \\ & \\ 0 & \dfrac{k}{\tau} \end{pmatrix} \tag{2.60}$$

and hence it is real (for real τ), in accordance with the fact that this wave carries active power toward infinity. Notice that the impedance matrices are symmetrical (as a consequence of reciprocity). Due to the usual sign conventions for voltages and currents, see Figure 2.2, the input

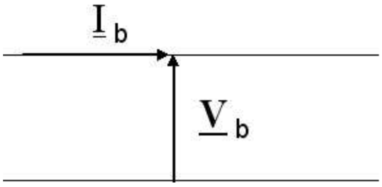

Figure 2.2: Sign convention for radial lines

impedance of an infinite radial line starting at $\rho = \rho_0$ is $\overset{\rightsquigarrow}{\underline{\underline{Z}}}(\rho_0)$, while the input impedance of a length of radial line between the origin and $\rho = \rho_0$ is $-\overset{\leftrightsquigarrow}{\underline{\underline{Z}}}(\rho_0)$. The two are obviously completely different.

2.4 Voltage and current propagators

In this section the propagation operators for regular and centrifugal waves are derived. The corresponding operators in the case of travelling waves on an ordinary transmission line are just exponentials.

–Regular wave

Voltage and current propagators are defined by

$$\overset{\leftrightsquigarrow}{\underline{V}}(\rho) = \overset{\leftrightsquigarrow}{\underline{\underline{P}}}_V(\rho, \rho_0) \cdot \overset{\leftrightsquigarrow}{\underline{V}}(\rho_0) \tag{2.61}$$

$$\overset{\leftrightsquigarrow}{\underline{I}}(\rho) = \overset{\leftrightsquigarrow}{\underline{\underline{P}}}_I(\rho, \rho_0) \cdot \overset{\leftrightsquigarrow}{\underline{I}}(\rho_0) \tag{2.62}$$

To obtain their explicit expressions, let us recall (2.35) and (2.35) written for the section ρ_0, from which we get:

$$\begin{aligned}\overset{\leftrightsquigarrow}{\underline{a}} &= \sqrt{Y}\;\overset{\leftrightsquigarrow}{\underline{\underline{M}}}{}_V^{-1}(\rho_0)\cdot\overset{\leftrightsquigarrow}{\underline{V}}(\rho_0)\\ \overset{\leftrightsquigarrow}{\underline{a}} &= \sqrt{Z}\;\overset{\leftrightsquigarrow}{\underline{\underline{M}}}{}_I^{-1}(\rho_0)\cdot\overset{\leftrightsquigarrow}{\underline{I}}(\rho_0)\end{aligned}$$

Substituting the values $\overset{\leftrightsquigarrow}{\underline{a}}$ in (2.35) and (2.35) written for the section ρ we obtain:

$$\overset{\leftrightsquigarrow}{\underline{V}}(\rho) = \overset{\leftrightsquigarrow}{\underline{\underline{M}}}{}_V(\rho)\cdot\overset{\leftrightsquigarrow}{\underline{\underline{M}}}{}_V^{-1}(\rho_0)\cdot\overset{\leftrightsquigarrow}{\underline{V}}(\rho_0) \tag{2.63}$$

$$\overset{\leftrightsquigarrow}{\underline{I}}(\rho) = \overset{\leftrightsquigarrow}{\underline{\underline{M}}}{}_I(\rho)\cdot\overset{\leftrightsquigarrow}{\underline{\underline{M}}}{}_I^{-1}(\rho_0)\cdot\overset{\leftrightsquigarrow}{\underline{I}}(\rho_0) \tag{2.64}$$

From comparison with (2.62) we derive

$$\overset{\leftrightsquigarrow}{\underline{\underline{P}}}{}_V(\rho,\,\rho_0) = \overset{\leftrightsquigarrow}{\underline{\underline{M}}}{}_V(\rho)\cdot\overset{\leftrightsquigarrow}{\underline{\underline{M}}}{}_V^{-1}(\rho_0) \tag{2.65}$$

$$\overset{\leftrightsquigarrow}{\underline{\underline{P}}}{}_I(\rho,\,\rho_0) = \overset{\leftrightsquigarrow}{\underline{\underline{M}}}{}_I(\rho)\cdot\overset{\leftrightsquigarrow}{\underline{\underline{M}}}{}_I^{-1}(\rho_0) \tag{2.66}$$

Carrying out the matrix multiplications,

$$\overset{\leftrightsquigarrow}{\underline{\underline{P}}}{}_V(\rho,\,\rho_0) = \begin{pmatrix} \dfrac{J_n(\tau\rho)}{J_n(\tau\rho_0)} & 0 \\[3ex] \dfrac{n\chi}{\tau^2}\left[\dfrac{J_n'(\tau\rho)}{\rho_0\,J_n'(\tau\rho_0)} - \dfrac{J_n(\tau\rho)}{\rho\,J_n(\tau\rho_0)}\right] & \dfrac{J_n'(\tau\rho)}{J_n'(\tau\rho_0)} \end{pmatrix} \tag{2.67}$$

$$\overset{\leftrightsquigarrow}{\underline{\underline{P}}}{}_I(\rho,\,\rho_0) = \begin{pmatrix} \dfrac{J_n'(\tau\rho)}{J_n'(\tau\rho_0)} & -\dfrac{n\chi}{\tau^2}\left[\dfrac{J_n'(\tau\rho)}{\rho_0\,J_n'(\tau\rho_0)} - \dfrac{J_n(\tau\rho)}{\rho\,J_n(\tau\rho_0)}\right] \\[3ex] 0 & \dfrac{J_n(\tau\rho)}{J_n(\tau\rho_0)} \end{pmatrix} \tag{2.68}$$

–Centrifugal wave

Operating in the same way as before, we obtain:

$$\overset{\rightsquigarrow}{\underline{\underline{P}}}{}_V(\rho,\,\rho_0) = \overset{\rightsquigarrow}{\underline{\underline{M}}}{}_V(\rho)\cdot\overset{\rightsquigarrow}{\underline{\underline{M}}}{}_V^{-1}(\rho_0) \tag{2.69}$$

$$\overset{\rightsquigarrow}{\underline{\underline{P}}}{}_I(\rho,\,\rho_0) = \overset{\rightsquigarrow}{\underline{\underline{M}}}{}_I(\rho)\cdot\overset{\rightsquigarrow}{\underline{\underline{M}}}{}_I^{-1}(\rho_0) \tag{2.70}$$

with the explicit expressions:

$$\overset{\rightsquigarrow}{\underline{\underline{P}}}_V(\rho,\,\rho_0) = \begin{pmatrix} \dfrac{H_n^{(2)}(\tau\rho)}{H_n^{(2)}(\tau\rho_0)} & 0 \\ \\ \dfrac{n\chi}{\tau^2}\left[\dfrac{H_n'^{(2)}(\tau\rho)}{\rho_0\, H_n'^{(2)}(\tau\rho_0)} - \dfrac{H_n^{(2)}(\tau\rho)}{\rho\, H_n^{(2)}(\tau\rho_0)}\right] & \dfrac{H_n'^{(2)}(\tau\rho)}{H_n'^{(2)}(\tau\rho_0)} \end{pmatrix} \tag{2.71}$$

$$\overset{\rightsquigarrow}{\underline{\underline{P}}}_I(\rho,\,\rho_0) = \begin{pmatrix} \dfrac{H_n'^{(2)}(\tau\rho)}{H_n'^{(2)}(\tau\rho_0)} & -\dfrac{n\chi}{\tau^2}\left[\dfrac{H_n'^{(2)}(\tau\rho)}{\rho_0\, H_n'^{(2)}(\tau\rho_0)} - \dfrac{H_n^{(2)}(\tau\rho)}{\rho\, H_n^{(2)}(\tau\rho_0)}\right] \\ \\ 0 & \dfrac{H_n^{(2)}(\tau\rho)}{H_n^{(2)}(\tau\rho_0)} \end{pmatrix} \tag{2.72}$$

It is quite useful and interesting to notice that all the propagators satisfy, as one can expect, the semigroup property:

$$\underline{\underline{P}}(\rho_2,\,\rho_0) = \underline{\underline{P}}(\rho_2,\,\rho_1)\cdot\underline{\underline{P}}(\rho_1,\,\rho_0) \tag{2.73}$$

where $\rho_2 < \rho_1 < \rho_0$.

Moreover it is simple to explain why $\underline{\underline{P}}_V$ and $\underline{\underline{P}}_i$ can be obtained one from the other by simple element exchange. In fact, recalling (2.42),

$$\underline{\underline{P}}_V(\rho,\,\rho_0) = \underline{\underline{M}}_V(\rho)\cdot\underline{\underline{M}}_V^{-1}(\rho_0) =$$

$$\left(\underline{\underline{T}}^{-1}\cdot\underline{\underline{M}}_V(\rho)\cdot\underline{\underline{T}}\right)\left(\underline{\underline{T}}^{-1}\cdot\underline{\underline{M}}_V(\rho_0)\cdot\underline{\underline{T}}\right)^{-1} =$$

$$\underline{\underline{T}}^{-1}\cdot\underline{\underline{M}}_I(\rho)\cdot\underline{\underline{M}}_I(\rho_0)\cdot\underline{\underline{T}} = \underline{\underline{T}}^{-1}\cdot\underline{\underline{P}}_I(\rho,\,\rho_0)\cdot\underline{\underline{T}} \tag{2.74}$$

These properties hold for both the regular and the centrifugal wave, hence the arrows have been omitted.

2.5 Transmission matrix for voltages and currents

At this point we are finally ready to obtain the explicit expression of the fundamental matrix $\underline{\underline{F}}(\rho_1, \rho_2)$ introduced in section 2.2. Notice that in circuit theory, the fundamental matrix is known as the ABCD matrix of a piece of transmission line comprised between $\rho = \rho_1$ and $\rho = \rho_2$, i.e.

$$\begin{pmatrix} \underline{V}(\rho_1) \\ \\ \underline{I}(\rho_1) \end{pmatrix} = \begin{pmatrix} \underline{\underline{A}}(\rho_1,\, \rho_2) & \underline{\underline{B}}(\rho_1,\, \rho_2) \\ \\ \underline{\underline{C}}(\rho_1,\, \rho_2) & \underline{\underline{D}}(\rho_1,\, \rho_2) \end{pmatrix} \begin{pmatrix} \underline{V}(\rho_2) \\ \\ \underline{I}(\rho_2) \end{pmatrix} \tag{2.75}$$

Recalling (2.33), (2.34), (2.37), (2.38), let us write the electrical state, expressed in terms of total voltage and total current, at $\rho = \rho_1$

$$\begin{pmatrix} \underline{V}(\rho_1) \\ \\ \underline{I}(\rho_1) \end{pmatrix} = \begin{pmatrix} \sqrt{Z} & 0 \\ \\ 0 & \sqrt{Y} \end{pmatrix} \begin{pmatrix} \overset{\leftrightsquigarrow}{\underline{\underline{M}}}_V(\rho_1) & \overset{\rightsquigarrow}{\underline{\underline{M}}}_V(\rho_1) \\ \\ \overset{\leftrightsquigarrow}{\underline{\underline{M}}}_I(\rho_1) & \overset{\rightsquigarrow}{\underline{\underline{M}}}_I(\rho_1) \end{pmatrix} \begin{pmatrix} \overset{\leftrightsquigarrow}{\underline{a}} \\ \\ \overset{\rightsquigarrow}{\underline{a}} \end{pmatrix} \tag{2.76}$$

and at $\rho = \rho_2$

$$\begin{pmatrix} \underline{V}(\rho_2) \\ \\ \underline{I}(\rho_2) \end{pmatrix} = \begin{pmatrix} \sqrt{Z} & 0 \\ \\ 0 & \sqrt{Y} \end{pmatrix} \begin{pmatrix} \overset{\leftrightsquigarrow}{\underline{\underline{M}}}_V(\rho_2) & \overset{\rightsquigarrow}{\underline{\underline{M}}}_V(\rho_2) \\ \\ \overset{\leftrightsquigarrow}{\underline{\underline{M}}}_I(\rho_2) & \overset{\rightsquigarrow}{\underline{\underline{M}}}_I(\rho_2) \end{pmatrix} \begin{pmatrix} \overset{\leftrightsquigarrow}{\underline{a}} \\ \\ \overset{\rightsquigarrow}{\underline{a}} \end{pmatrix} \tag{2.77}$$

Solving (2.77) with respect to $(\overset{\leftrightsquigarrow}{\underline{a}} \;\; \overset{\rightsquigarrow}{\underline{a}})^T$ and substituting into (2.76) we get

$$\begin{pmatrix} \underline{V}(\rho_1) \\ \\ \underline{I}(\rho_1) \end{pmatrix} = \underline{\underline{D}} \begin{pmatrix} \overset{\leftrightsquigarrow}{\underline{\underline{M}}}_V(\rho_1) & \overset{\rightsquigarrow}{\underline{\underline{M}}}_V(\rho_1) \\ \\ \overset{\leftrightsquigarrow}{\underline{\underline{M}}}_I(\rho_1) & \overset{\rightsquigarrow}{\underline{\underline{M}}}_I(\rho_1) \end{pmatrix} \begin{pmatrix} \overset{\leftrightsquigarrow}{\underline{\underline{M}}}_V(\rho_2) & \overset{\rightsquigarrow}{\underline{\underline{M}}}_V(\rho_2) \\ \\ \overset{\leftrightsquigarrow}{\underline{\underline{M}}}_I(\rho_2) & \overset{\rightsquigarrow}{\underline{\underline{M}}}_I(\rho_2) \end{pmatrix}^{-1} \underline{\underline{D}}^{-1} \begin{pmatrix} \underline{V}(\rho_2) \\ \\ \underline{I}(\rho_2) \end{pmatrix} \tag{2.78}$$

where the diagonal matrix $\underline{\underline{D}}$ is

$$\underline{\underline{D}} = \begin{pmatrix} \sqrt{Z} & 0 \\ \\ 0 & \sqrt{Y} \end{pmatrix} \tag{2.79}$$

From this equation, the expression of the ABCD matrix is readily identified.

By carrying out a considerable amount of algebraic manipulations, the following result is obtained:

$$\underline{\underline{A}}(\rho_1,\,\rho_2)=\frac{j\pi\tau\rho_2}{4}\begin{bmatrix}-R_n(\rho_1,\rho_2) & 0\\ \frac{n\chi}{\rho_1\tau^2}R_n(\rho_1,\rho_2)+\frac{n\chi}{\rho_2\tau^2}Q_n(\rho_1,\rho_2) & Q_n(\rho_1,\rho_2)\end{bmatrix}$$

$$\underline{\underline{B}}(\rho_1,\,\rho_2)=\frac{j\pi\tau\rho_2}{4}\begin{bmatrix}\frac{\tau}{j\omega\varepsilon}P_n(\rho_1,\rho_2) & -\frac{n\chi}{j\omega\varepsilon\tau\rho_2}P_n(\rho_1,\rho_2)\\ -\frac{n\chi}{j\omega\varepsilon\rho_1\tau}P_n(\rho_1,\rho_2) & \frac{n^2\chi^2}{j\omega\varepsilon\tau^3\rho_1\rho_2}P_n(\rho_1,\rho_2)-\frac{j\omega\mu}{\tau}S_n(\rho_1,\rho_2)\end{bmatrix}$$

$$\underline{\underline{C}}(\rho_1,\,\rho_2)=\frac{j\pi\tau\rho_2}{4}\begin{bmatrix}\frac{n^2\chi^2}{j\omega\mu\tau^3\rho_1\rho_2}P_n(\rho_1,\rho_2)-\frac{j\omega\varepsilon}{\tau}S_n(\rho_1,\rho_2) & -\frac{n\chi}{j\omega\mu\tau\rho_2}P_n(\rho_1,\rho_2)\\ -\frac{n\chi}{j\omega\mu\rho_1\tau}P_n(\rho_1,\rho_2) & \frac{\tau}{j\omega\mu}P_n(\rho_1,\rho_2))\end{bmatrix} \tag{2.80}$$

$$\underline{\underline{D}}(\rho_1,\,\rho_2)=\frac{j\pi\tau\rho_2}{4}\begin{bmatrix}Q_n(\rho_1,\rho_2) & -\frac{n\chi}{\rho_1\tau^2}R_n(\rho_1,\rho_2)+\frac{n\chi}{\rho_2\tau^2}Q_n(\rho_1,\rho_2)\\ 0 & -R_n(\rho_1,\rho_2)\end{bmatrix}$$

The terms P_n, Q_n, R_n, S_n are combinations of Bessel functions and their derivatives, defined by [10]:

$$P_n(\rho_1,\rho_2)=2j\left[J_n(\tau\rho_1)Y_n(\tau\rho_2)-J_n(\tau\rho_2)Y_n(\tau\rho_1)\right] \tag{2.81}$$

$$Q_n(\rho_1,\rho_2)=2j\left[J_n'(\tau\rho_1)Y_n(\tau\rho_2)-J_n(\tau\rho_2)Y_n'(\tau\rho_1)\right] \tag{2.82}$$

$$R_n(\rho_1,\rho_2)=2j\left[J_n(\tau\rho_1)Y_n'(\tau\rho_2)-J_n'(\tau\rho_2)Y_n(\tau\rho_1)\right] \tag{2.83}$$

$$S_n(\rho_1,\rho_2)=2j\left[J_n'(\tau\rho_1)Y_n'(\tau\rho_2)-J_n'(\tau\rho_2)Y_n'(\tau\rho_1)\right] \tag{2.84}$$

Taking (2.78) into account, it is straightforward to derive the following obvious property of the ABCD matrix:

$$\begin{pmatrix} \underline{\underline{A}}(\rho_1,\,\rho_2) & \underline{\underline{B}}(\rho_1,\,\rho_2) \\ \\ \underline{\underline{C}}(\rho_1,\,\rho_2) & \underline{\underline{D}}(\rho_1,\,\rho_2) \end{pmatrix} = \begin{pmatrix} \underline{\underline{A}}(\rho_2,\,\rho_1) & \underline{\underline{B}}(\rho_2,\,\rho_1) \\ \\ \underline{\underline{C}}(\rho_2,\,\rho_1) & \underline{\underline{D}}(\rho_2,\,\rho_1) \end{pmatrix}^{-1}$$

This property can be used to simplify (2.18). Indeed:

$$\underline{\underline{F}}(\rho,\rho_0)\cdot\underline{\underline{F}}^{-1}(\rho',\rho_0) = \underline{\underline{F}}(\rho,\rho_0)\cdot\underline{\underline{F}}(\rho_0,\rho') = \underline{\underline{F}}(\rho,\rho') \tag{2.85}$$

so that

$$\underline{\psi}(\rho) = \underline{\underline{F}}(\rho,\rho_0)\cdot\underline{\psi}(\rho_0) + \int_{\rho_0}^{\rho}\underline{\underline{F}}(\rho,\rho')\cdot\underline{s}(\rho')d\rho' \tag{2.86}$$

2.6 Examples of radial line theory

In this section we consider some basic problems in radial transmission line theory. Their solution, which illustrates the concepts introduced in the preceding sections, is useful for the construction of the Green's functions required in the formulation of the electromagnetic problems described further on.

2.6.1 Short circuited line

Consider a radial line comprised between $\rho = \rho_1$ and $\rho = \rho_2$, loaded by a short circuit in $\rho = \rho_1$, as shown in Figure 2.3. The input admittance $\underline{\underline{Y}}_{in}$ is required.

Using the transmission matrix (2.75) we can write:

$$\begin{pmatrix} \underline{V}(\rho_1) \\ \\ \underline{I}(\rho_1) \end{pmatrix} = \begin{pmatrix} 0 \\ \\ \underline{I}(\rho_1) \end{pmatrix} = \begin{pmatrix} \underline{\underline{A}}(\rho_1,\,\rho_2) & \underline{\underline{B}}(\rho_1,\,\rho_2) \\ \\ \underline{\underline{C}}(\rho_1,\,\rho_2) & \underline{\underline{D}}(\rho_1,\,\rho_2) \end{pmatrix}\cdot\begin{pmatrix} \underline{V}(\rho_2) \\ \\ \underline{I}(\rho_2) \end{pmatrix} \tag{2.87}$$

where $\underline{V}(a)$ is equal to zero because it is the voltage on the short-circuit. From the first line of the above relation we obtain

$$\underline{I}(\rho_2) = -\underline{\underline{B}}^{-1}(\rho_1,\rho_2)\cdot\underline{\underline{A}}(\rho_1,\rho_2)\,\underline{V}(\rho_2) \tag{2.88}$$

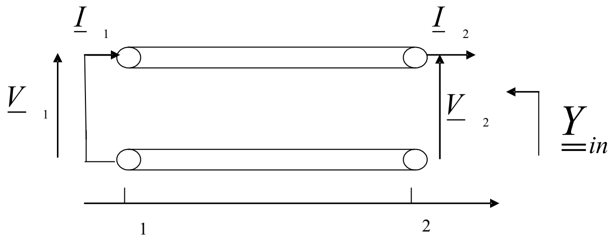

Figure 2.3: Short circuited radial line: case 1

Then the input admittance (*i.e.* looking toward the origin) at $\rho = \rho_2$ is:

$$\underline{\underline{Y}}_{in} = \underline{\underline{B}}^{-1}(\rho_1, \rho_2) \cdot \underline{\underline{A}}(\rho_1, \rho_2) \tag{2.89}$$

that is, explicitly:

$$\underline{\underline{Y}}_{in} = Y \begin{bmatrix} -\dfrac{jk}{\tau}\dfrac{R_n(\rho_1,\rho_2)}{P_n(\rho_1,\rho_2)} + \dfrac{j\chi^2 n^2}{k\tau^3\rho_2^2}\dfrac{Q_n(\rho_1,\rho_2)}{S_n(\rho_1,\rho_2)} & \dfrac{j\,n\chi}{k\tau\,\rho_2}\dfrac{Q_n(\rho_1,\rho_2)}{S_n(\rho_1,\rho_2)} \\ & \\ \dfrac{j\,n\chi}{k\tau\,\rho_2}\dfrac{Q_n(\rho_1,\rho_2)}{S_n(\rho_1,\rho_2)} & \dfrac{j\tau}{k}\dfrac{Q_n(\rho_1,\rho_2)}{S_n(\rho_1,\rho_2)} \end{bmatrix} \tag{2.90}$$

We recall that $Y = \sqrt{\varepsilon/\mu}$ is the medium wave admittance.

If the short circuit is located at $\rho = \rho_2$, as in Figure 2.4, we can proceed as before, obtaining

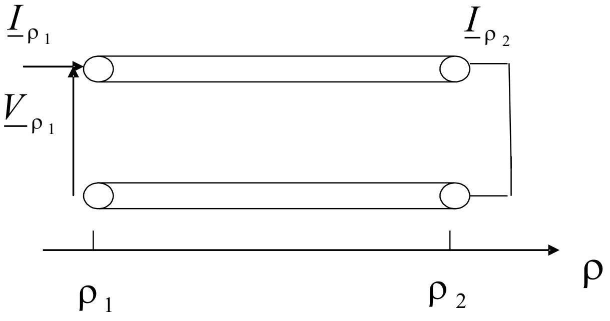

Figure 2.4: Short circuited radial line: case 2

$$\underline{\underline{Y}}_{in} = Y \begin{bmatrix} \dfrac{jk}{\tau}\dfrac{R_n(\rho_2,\rho_1)}{P_n(\rho_2,\rho_1)} - \dfrac{j\chi^2 n^2}{k\tau^3 b^2}\dfrac{Q_n(\rho_2,\rho_1)}{S_n(\rho_2,\rho_1)} & -\dfrac{j\,n\chi}{k\tau\,a}\dfrac{Q_n(\rho_2,\rho_1)}{S_n(\rho_2,\rho_1)} \\ & \\ -\dfrac{j\,n\chi}{k\tau\,a}\dfrac{Q_n(\rho_2,\rho_1)}{S_n(\rho_2,\rho_1)} & -\dfrac{j\tau}{k}\dfrac{Q_n(\rho_2,\rho_1)}{S_n(\rho_2,\rho_1)} \end{bmatrix} \tag{2.91}$$

Note the minus sign at the beginning and the exchange $\rho_1 \longleftrightarrow \rho_2$ in the quantities P_n etc.

2.6.2 Junction between different lines

Consider the junction between the two radial lines of Figure 2.5. The first, between $\rho = \rho_2$ and $\rho = \rho_3$ refers to a dielectric medium with permittivity ε_{r2}; the second is of infinite length and refers to a dielectric medium with permittivity ε_{r3}. The input admittance $\underline{\underline{Y}}_{in}$ is required.

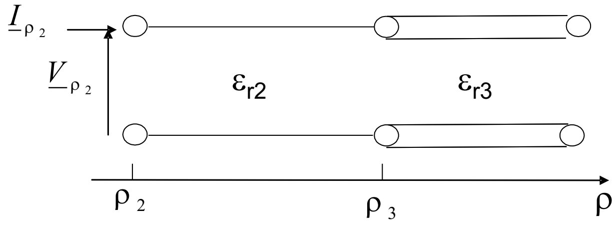

Figure 2.5: Junction between different lines

The circuit can be modified as shown in Figure 2.6. The first transmission line length is described

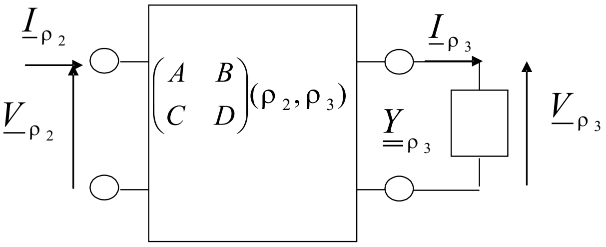

Figure 2.6: Equivalent description of the circuit of fig.2.5

via its ABCD matrix, which is given by (2.80) with $\varepsilon_r = \varepsilon_{r2}$. The second line is represented by its input admittance $\underline{\underline{Y}}_{\rho_3}$. On this line, only the centrifugal wave is present, so $\underline{\underline{Y}}_{\rho_3}$ can be obtained from (2.59) with $\rho = \rho_3$ and $\varepsilon_r = \varepsilon_{r3}$.

The electrical state at $\rho = \rho_2$ can by obtained by

$$\begin{pmatrix} \underline{V}_{\rho_2} \\ \\ \underline{I}_{\rho_2} \end{pmatrix} = \begin{pmatrix} \underline{\underline{A}}(\rho_2, \rho_3) & \underline{\underline{B}}(\rho_2, \rho_3) \\ \\ \underline{\underline{C}}(\rho_2, \rho_3) & \underline{\underline{D}}(\rho_2, \rho_3) \end{pmatrix} \cdot \begin{pmatrix} \underline{V}_{\rho_3} \\ \\ \underline{I}_{\rho_3} \end{pmatrix} \tag{2.92}$$

with:

$$\underline{I}_{\rho_3} = \underline{\underline{Y}}_{\rho_3} \cdot \underline{V}_{\rho_3} \tag{2.93}$$

By eliminating $\underline{V}_{\rho_3}$ between the two equations above, we obtain:

$$\underline{I}_{\rho_2} = \left[\underline{\underline{C}}(\rho_2, \rho_3) + \underline{\underline{D}}(\rho_2, \rho_3)\right] \cdot \left[\underline{\underline{A}}(\rho_2, \rho_3) + \underline{\underline{B}}(\rho_2, \rho_3)\right]^{-1} \cdot \underline{V}_{\rho_2} \tag{2.94}$$

i.e.

$$\underline{\underline{Y}}_{in} = \left[\underline{\underline{C}}(\rho_2, \rho_3) + \underline{\underline{D}}(\rho_2, \rho_3)\right] \cdot \left[\underline{\underline{A}}(\rho_2, \rho_3) + \underline{\underline{B}}(\rho_2, \rho_3)\right]^{-1} \tag{2.95}$$

2.7 Properties of the admittance matrix

In this section some symmetry and electromagnetic properties of the admittance matrix (2.90) will be deduced. It can be shown that also the other admittances of the preceding paragraph have the same characteristics.

For the reader's convenience, the explicit expression of (2.90) is here reported:

$$\underline{\underline{Y}}(\chi, n) = \sqrt{\frac{\varepsilon_{r1}}{\mu}} \begin{bmatrix} Y_{uu} & Y_{uv} \\ Y_{vu} & Y_{vv} \end{bmatrix}$$

where

$$\begin{aligned}
Y_{uu} &= -\frac{j\,k}{\tau}\frac{J_n(\tau\rho_1)Y_n'(\tau\rho_2) - J_n'(\tau\rho_2)Y_n(\tau\rho_1)}{J_n(\tau\rho_1)Y_n(\tau\rho_2) - J_n(\tau\rho_2)Y_n(\tau\rho_1)} + \frac{j\chi^2 n^2}{k\rho_2^2\tau^3}\frac{J_n'(\tau\rho_1)Y_n(\tau\rho_2) - J_n(\tau\rho_2)Y_n'(\tau\rho_1)}{J_n'(\tau\rho_1)Y_n'(\tau\rho_2) - J_n'(\tau\rho_2)Y_n'(\tau\rho_1)} \\
Y_{uv} &= Y_{vu} = \frac{jn\chi}{k\rho_2\tau}\frac{J_n'(\tau\rho_1)Y_n(\tau\rho_2) - J_n(\tau\rho_2)Y_n'(\tau\rho_1)}{J_n'(\tau\rho_1)Y_n'(\tau\rho_2) - J_n'(\tau\rho_2)Y_n'(\tau\rho_1)} \\
Y_{vv} &= \frac{j\tau}{k}\frac{J_n'(\tau\rho_1)Y_n(\tau\rho_2) - J_n(\tau\rho_2)Y_n'(\tau\rho_1)}{J_n'(\tau\rho_1)Y_n'(\tau\rho_2) - J_n'(\tau\rho_2)Y_n'(\tau\rho_2)}
\end{aligned}$$

From the above equations, one notes that the diagonal elements of $\underline{\underline{Y}}(\chi, n)$ are even functions of χ and n, while the off-diagonal ones are odd functions of χ and n.

Moreover from a direct computation one obtains the following behavior for $\chi\rho_1 \gg n$:

$$Y_{uu}(\chi, n) \sim \frac{1}{\chi}\left(j\omega\varepsilon_{r1} - \frac{j\,n^2}{\omega\mu\,\rho_2^2}\right) \tag{2.96}$$

$$Y_{uv}(\chi, n) \sim \frac{2}{\omega\mu\,\rho_2} \tag{2.97}$$

$$Y_{vv}(\chi, n) \sim \frac{-2j}{\omega\mu\chi} \tag{2.98}$$

and for $n \gg \tau\rho_2$:

$$Y_{uu}(\chi, n) \sim n\left(\frac{j\omega\varepsilon_{r1}}{\tau} - \frac{j}{\omega\mu\,\rho_2^2}\right) \tag{2.99}$$

$$Y_{uv}(\chi, n) \sim \frac{j\beta}{\omega\mu\,\rho_2\tau} \tag{2.100}$$

$$Y_{vv}(\chi, n) \sim \frac{j\tau}{\omega\mu\,n} \tag{2.101}$$

It is known from circuit theory that the imaginary part of the eigenvalues of the impedance matrix of any reactive load is an increasing monotone function of frequency, [11]. It is interesting to note that this law is still valid for this particular kind of transmission lines, this fact enhances the circuit interpretation carried on until now. To illustrate the property, Figure 2.7 shows a plot of the imaginary part of the eigenvalues of Z_{uu} in the case $\rho_1 = 8$ mm, $\rho_2 = 20.65$ mm and $\chi = 0$ for $n = 0$.

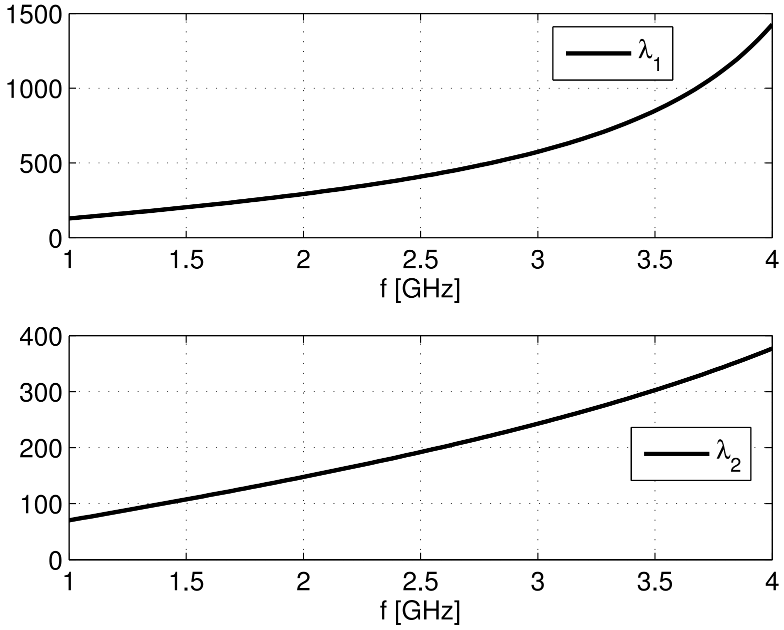

Figure 2.7: Imaginary part of the eigenvalues λ_1 and λ_2 of $Z(\chi = 0, n)$ versus frequency for $n = 0$

2.8 Limited cross-section radial waveguides

In this chapter we have developed the radial transmission line theory in the case of a radial waveguide with unlimited cross-section $(\varphi, z) \in [0, 2\pi) \times (-\infty, \infty)$. We have seen in Section 2.2 that voltage and current are essentially the Fourier transform of the transverse (with respect to $\hat{\rho}$) electric and magnetic fields.
The relationship can be written in vector form as

$$\underline{E}_t(\rho, \varphi, z) = \sum_n \int_{\Re} \underline{\underline{K}}_\infty(\varphi, z; n, \chi) \cdot \underline{\underline{B}}^T \cdot \underline{V}(\rho, n, \chi) d\chi \tag{2.102}$$

$$\underline{H}_t(\rho, \varphi, z) \times \hat{\rho} = \sum_n \int_{\Re} \underline{\underline{K}}_\infty(\varphi, z; n, \chi) \cdot \underline{\underline{B}}^T \cdot \underline{I}(\rho, n, \chi) d\chi \tag{2.103}$$

with the inverses

$$\underline{V}(\rho, n, \chi) = \int_0^{2\pi} \int_{\Re} \underline{\underline{K}}^*_\infty(\varphi, z; n, \chi) \cdot \underline{\underline{B}} \cdot \underline{E}_t(\rho, \varphi, z) dz d\varphi \tag{2.104}$$

$$\underline{I}(\rho, n, \chi) = \int_0^{2\pi} \int_{\Re} \underline{\underline{K}}^*_\infty(\varphi, z; n, \chi) \cdot \underline{\underline{B}} \cdot \left(\underline{H}_t(\rho, \varphi, z) \times \hat{\rho}\right) dz d\varphi \tag{2.105}$$

where the matrix B performs the base change from $\hat{z}$, $\hat{\varphi}$ to $\hat{u}$, $\hat{v}$ and is given by

$$\underline{\underline{B}} = (\hat{u}\hat{z} + \hat{v}\hat{\varphi}) \tag{2.106}$$

The kernel is

$$\underline{\underline{K}}_\infty(\varphi, z; n, \chi) = \frac{1}{4\pi^2} \mathrm{e}^{-jn\varphi} \mathrm{e}^{-j\chi z} (\hat{\varphi}\hat{\varphi} + \hat{z}\hat{z}) \tag{2.107}$$

with the subscript making reference to the unlimited cross section. The constants have been chosen so that

$$\sum_n \int_{\Re} \underline{\underline{K}}_\infty(\varphi, z; n, \chi) \cdot \underline{\underline{K}}^*_\infty(\varphi', z'; n, \chi) d\chi = \frac{1}{4\pi^2} \delta(\varphi - \varphi') \delta(z - z') (\hat{\varphi}\hat{\varphi} + \hat{z}\hat{z}) \tag{2.108}$$

Radial waveguides may have limited cross section $-s/2 < z < s/2$ and $-\frac{\alpha}{2} < \varphi < \frac{\alpha}{2}$ because suitable perfectly conducting planes, parallel to coordinate planes, have been introduced. It is well known that the consequence of the introduced limitations is just a quantization of the spectral variables, with slight changes in the kernels, while the transmission line theory developed in this chapter does not require any modification. In the following, we show that exploiting (2.107) we can deduce the relevant kernels.

2.8.1 Half-space waveguide

The domain of this waveguide is defined by

$$\begin{aligned} z & \geq 0 && (2.109)\\ 0 \leq \quad \alpha & < 2\pi && (2.110) \end{aligned}$$

The presence of a metal plate in $z = 0$ introduces the boundary conditions:

$$E_\varphi(\rho, \varphi, 0) = 0 \qquad \left(\underline{H}_t(\rho, \varphi, 0) \times \hat{\rho}\right)_\varphi = 0 \tag{2.111}$$

$$\frac{\partial}{\partial z} E_z(\rho, \varphi, 0) = 0 \qquad \frac{\partial}{\partial z} \left(\underline{H}_t(\rho, \varphi, 0) \times \hat{\rho}\right)_z = 0 \tag{2.112}$$

In general, the relation between E_φ and V_v must be of the form

$$E_\varphi(\rho, \varphi, z) = \sum_n \int_{\Re} K_{\varphi\varphi}(\varphi, z; n, \chi) V_v(\rho, n, \chi) d\chi \tag{2.113}$$

The boundary condition (2.112) is certainly satisfied if

$$K_{\varphi\varphi}(\varphi, 0; n, \chi) = 0 \tag{2.114}$$

Exploiting (2.107) we find that the χ variable is limited to positive values. Moreover, we construct $K_{\varphi\varphi}$ in terms of $K_\infty(\varphi, z; n, \pm\chi)$ as

$$K_{\varphi\varphi}(\varphi, z; n, m) = C \sin(\chi z)\, \mathrm{e}^{-jn\varphi} \tag{2.115}$$

In view of (2.108) we find $C = 2/\pi$.
As for $K_{zz}(\varphi, z; n, \chi)$, we proceed in a similar way and find that the complete kernel is:

$$\underline{\underline{K}}(\varphi, z; n, m) = \frac{\mathrm{e}^{-j\,n\,\varphi}}{4\pi^2} \cdot \left[\sin(\chi z)\, \hat{\varphi}\hat{\varphi} + \cos(\chi z)\, \hat{z}\hat{z}\right] \tag{2.116}$$

2.8.2 Parallel plate waveguide

The domain of this waveguide is defined by

$$\begin{aligned} -\frac{s}{2} < \quad z & < \frac{s}{2} && (2.117)\\ 0 \leq \quad \alpha & < 2\pi && (2.118) \end{aligned}$$

This is the type of radial waveguide that will be used in Chapter 9.

The presence of two metal plates in $z = \pm s/2$ introduces the boundary conditions:

$$E_\varphi(\rho,\varphi,\pm\frac{s}{2}) \;=\; 0 \qquad \left(\underline{H}_t(\rho,\varphi,\pm\frac{s}{2})\times\hat{\rho}\right)\cdot\hat{z}=0 \tag{2.119}$$

$$\frac{\partial}{\partial z}E_z(\rho,\varphi,\pm\frac{s}{2}) \;=\; 0 \qquad \frac{\partial}{\partial z}\left(\underline{H}_t(\rho,\varphi,\pm\frac{s}{2})\times\hat{\rho}\right)\cdot\hat{\varphi}=0 \tag{2.120}$$

In general, the relation between E_φ and V_v must be of the form

$$E_\varphi(\rho,\varphi,z)=\sum_n\int_{\Re}K_{\varphi\varphi}(\varphi,z;n,\chi)V_v(\rho,n,\chi)d\chi \tag{2.121}$$

The boundary condition (2.120) is certainly satisfied if

$$K_{\varphi\varphi}(\varphi,\pm\frac{s}{2};n,\chi)=0 \tag{2.122}$$

Exploiting (2.107) we find that the χ variable is discretized and can take on only the values

$$\chi_m=\frac{m\pi}{s}$$

with $m = 0, 1, 3, \ldots$. Moreover, we construct $K_{\varphi\varphi}$ in terms of $K_\infty(\varphi, z; n, \pm\chi_m)$ as

$$K_{\varphi\varphi}(\varphi,z;n,\chi_m)=C\sin\left(\frac{m\pi z}{s}+\frac{m\pi}{2}\right) \tag{2.123}$$

In view of (2.108) we find $C = 1/(\pi s)$.

As for $K_{zz}(\varphi, z; n, \chi)$, we proceed in a similar way and find that the complete kernel is

$$\underline{\underline{K}}(\varphi,z;n,\chi_m)=\frac{\mathrm{e}^{-j\,n\,\varphi}}{\pi\,s\,\epsilon_m}\cdot\left[\sin\left(\frac{m\pi\,z}{s}+\frac{m\pi}{2}\right)\hat{\varphi}\hat{\varphi}+\cos\left(\frac{m\pi\,z}{s}+\frac{m\pi}{2}\right)\hat{z}\hat{z}\right] \tag{2.124}$$

where ε_m is the Neumann symbol.

2.8.3 Wedge waveguide

The domain of this waveguide is defined by

$$-\infty < \; z \; < \infty \tag{2.125}$$

$$-\frac{\alpha}{2} < \; \varphi \; < \frac{\alpha}{2} \tag{2.126}$$

The presence of two metal plates in $\varphi = \pm\alpha/2$ implies the boundary conditions:

$$\frac{\partial}{\partial\varphi}E_\varphi(\rho,\pm\frac{\alpha}{2},z) \;=\; 0 \qquad \frac{\partial}{\partial\varphi}\left(\underline{H}_t(\rho,\pm\frac{\alpha}{2},z)\times\hat{\rho}\right)\cdot\hat{z}=0 \tag{2.127}$$

$$E_z(\rho,\varphi,z) \;=\; 0 \qquad \left(\underline{H}_t(\rho,\varphi,\pm\frac{s}{2})\times\hat{\rho}\right)\cdot\hat{\varphi}=0 \tag{2.128}$$

In general, the relation between E_z and V_u must be of the form

$$E_z(\rho, \varphi, z) = \sum_n \int_{\Re} K_{zz}(\varphi, z; n, \chi) V_u(\rho, n, \chi) d\chi \tag{2.129}$$

The boundary condition (2.128) is certainly satisfied if

$$K_{zz}(\pm\frac{\alpha}{2}, z; n, \chi) = 0 \tag{2.130}$$

Exploiting (2.107), it is convenient to turn n into the continuous variable ν, which becomes discrete on enforcing the boundary conditions and can take on only the values (generally non integer)

$$\nu_n = \frac{n\pi}{\alpha}$$

with $n = 0, 1, 3, \ldots$. Moreover, using $K_\infty(\varphi, z; \pm\nu_n, \chi)$, we construct

$$K_{zz}(\varphi, z; n, \chi) = C \sin\left(\frac{n\pi\varphi}{\alpha} + \frac{n\pi}{2}\right) e^{-j\chi z} \tag{2.131}$$

The constant C is fixed by (2.108): $C = 1/(\pi\alpha)$.
As for $K_{\varphi\varphi}(\varphi, z; n, \chi)$, we proceed in a similar way and find that the complete kernel is

$$\underline{\underline{K}}(\varphi, z; n, \chi) = \frac{\mathrm{e}^{-j\chi z}}{\pi\,\alpha\,\epsilon_n} \cdot \left[\sin\left(\frac{n\pi\,\varphi}{\alpha} + \frac{n\pi}{2}\right)\hat{z}\hat{z} + \cos\left(\frac{n\pi\,\varphi}{\alpha} + \frac{n\pi}{2}\right)\hat{\varphi}\hat{\varphi}\right] \tag{2.132}$$

where ε_n is the Neumann symbol.

2.8.4 “Rectangular” waveguide

The domain of this waveguide is defined by

$$-\frac{s}{2} < \quad z \quad < \frac{s}{2} \tag{2.133}$$

$$-\frac{\alpha}{2} < \quad \varphi \quad < \frac{\alpha}{2} \tag{2.134}$$

The term “rectangular waveguide” is to be interpreted, in the context of the radial setting. The geometry is separable and the kernel can be written down by inspection on the basis of the cases previously considered:

$$\begin{aligned}\underline{\underline{K}}(\varphi, z; n, m) \;&=\; \frac{4}{s\,\alpha\,\epsilon_m\,\epsilon_n} \cdot \left[\sin\left(\frac{n\pi\,\varphi}{\alpha} + \frac{n\pi}{2}\right)\cos\left(\frac{m\pi\,z}{s} + \frac{m\pi}{2}\right)\hat{z}\hat{z} + \right.\\ &+\; \left.\cos\left(\frac{n\pi\,\varphi}{\alpha} + \frac{n\pi}{2}\right)\sin\left(\frac{m\pi\,z}{s} + \frac{m\pi}{2}\right)\hat{\varphi}\hat{\varphi}\right]\end{aligned} \tag{2.135}$$

2.8.5 Phase Shift Wall (PSW) waveguide

The domain of this waveguide is defined by

$$\begin{aligned} -\frac{L}{2} < \quad z \quad &< \frac{L}{2} && (2.136) \\ 0 \le \quad \alpha \quad &< 2\pi && (2.137) \end{aligned}$$

In this case, the planes in $z = \pm L/2$ are not actual metal plates but geometrical surfaces for which the boundary conditions are

$$\begin{aligned} \underline{E}(\rho, \varphi, L/2) &= \mathrm{e}^{-jk_{z0}L}\underline{E}(\rho, \varphi, -L/2) \\ \underline{H}(\rho, \varphi, L/2) &= \mathrm{e}^{-jk_{z0}L}\underline{H}(\rho, \varphi, -L/2) \end{aligned} \qquad (2.138)$$

where k_{z0} is an arbitrary real or complex constant. This is a standard method to reduce the study of an infinite periodic structure to the central cell only. In this case the kernel $\underline{\underline{K}}(\varphi, z; n, \chi)$ has to pseudoperiodic, *i.e.*

$$\underline{\underline{K}}(\varphi, L/2; n, \chi) = \mathrm{e}^{-jk_{z0}L}\ \underline{\underline{K}}(\varphi, -L/2; n, \chi) \qquad (2.139)$$

Floquet theorem [12] implies that the χ spectral variable is discretized and the allowed values are

$$\chi_m = k_{z0} + m\frac{2\pi}{L}$$

The kernel is given in this case by

$$\underline{\underline{K}}(\varphi, z; n, m) = \frac{1}{4\pi^2}\mathrm{e}^{-jn\varphi}\mathrm{e}^{-j\chi_m z}(\hat{\varphi}\hat{\varphi} + \hat{z}\hat{z}) \qquad (2.140)$$

The modes of the PSW waveguide are known as Floquet modes.

2.9 Conclusions

In the next chapters two scattering problems in cylindrical geometry will be addressed: a leaky coaxial cable (chapter 3, 4 and 5) and a ring-loaded stop-band filter (chapter 9). They may seem very different at first sight, but they will be attacked by the same method, *i.e.* magnetic field integral equation. The kernel of that is the Green's function of the structure and the radial transmission line theory will be extensively employed in its construction. Moreover, since this theory permits to give an integral representation of the field radiated by conformal slots, it will be employed (chapter 7) to derive the electromagnetic properties of the far field of these slots and of the near field of the relevant array.

Chapter 3

Slotted Coaxial Cables: Transverse Approach

3.1 Introduction

The idea of controlled energy exchange between the interior of a coaxial cable located in a tunnel and the surrounding external space through an annular slot in the outer conductor originated from P. Delogne in 1968 [13]. At that time, the intention was to convey communication signals with a low specific attenuation inside the cable, and to release the minimum required energy in the tunnel space by a few slots located at discrete places along the cable, in order to provide communication to mobile receivers located therein. As the radiation process involved is reciprocal, two-way communications can be established between a base station connected to the cable and mobile transceivers.

From that time, this idea has been extended in order to provide communication links in many places, such as subways, underground shops and generally indoor environment. The applications range from telephone to WiFi and WLAN systems. Also, the operating frequency range has changed during these years, nowadays there is an increasing interest in the application of this technology in the GSM and UMTS bands.

Currently available slotted coaxial cables fall mainly in two groups. One is the surface-wave type, and the other is the leaky-wave type. The former is usually called radiative coaxial cable (RCX), the latter leaky coaxial cable (LCX). Both RCX and LCX are periodically slotted, the most significant difference between them is their pitch, *i.e.* the separation between adjacent slots. The pitch of RCX is quite small, so that a guided surface wave is supported on the outside of the cable. The link is established by a coupling of the receiving antenna to this reactive field. The pitch of LCX is larger and no surface wave is guided on the outside of the cable. On the contrary a real radiation takes place, which is conveniently described in terms of a leaky wave.

Slotted coaxial cables have been studied by several researchers. Wait, Hill and Siedel studied the characteristics of guided waves on helical wire shielded coaxial cables and braided cables within tunnels [14]. These types of cables are now less attractive because of the large longitudinal attenuation.

Hassan, Delogne and Laloux [15] analyzed axially slotted coaxial cables, which are also known to have relatively large longitudinal attenuation but are easier to fabricate than the periodically slotted cables.

Hill and Wait [14], Richmond, Wang and Tran [16] studied coaxial cables with vertical periodic slots.

Kim, Yun, Park and Yoon [17] analyzed the propagation and radiation properties of coaxial cables with multi-angle multi-slot configuration.

The analysis techniques employed in these studies have various degrees of accuracy. Some of them are based on Bethe's small aperture theory, others adopt some form of mode matching or exploit the FDTD method. Without exceptions, only the infinite periodically slotted cable is analyzed, and no consideration is given to the problem of the junction between a closed and a slotted cable.

As discussed above, a standard application of an LCX is to convey the incident electromagnetic signals along a tunnel in order to obtain a uniform coverage.

If a cylindrical frame of reference is introduced, where z is the tunnel axis, one is interested in the properties of the radiated field for specific values of ρ as function of z for an angular sector φ (see Figure 3.1). Certainly, the field in a specific point depends both on the LCX and on the tunnel characteristics, so that it would seem necessary to model accurately both of them. Actually, some work has been done along this line [18].

On the other hand, we should realize that the tunnel walls are rough and lossy, and the tunnel environment itself has a high degree of randomness related, for instance, to the presence of moving vehicles. For these reasons, it is reasonable to expect that the reaction of the tunnel environment on the slotted cable is very weak, so that the two parts of the problem can be decoupled. First, the radiation of the cable is modeled assuming it is placed in free space; then the presence of the actual environment is taken into account only on the radiated field, assuming that the slot

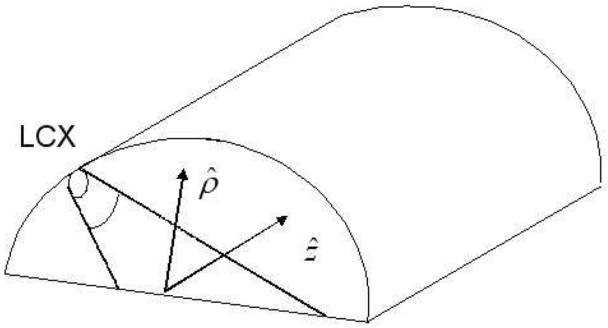

Figure 3.1: Schematic representation of a tunnel with an LCX

excitation is not changed by it. In this thesis, only the first issue is studied.

In this chapter, the problem is attacked by an integral equation technique, and the relevant Green's function is constructed by exploiting the radial transmission line theory developed in Chapter 2. The solution is carried out by the Galerkin method of moments and the slot array is characterized in terms of its scattering matrix. The formulation is general, and can be applied also to the case of large slots.
In practical applications, the slots are very thin and the formulation can be simplified.
The numerical solution is carried out by the method of moments, applied directly in the spectral domain. Suitable basis functions are chosen to expand the magnetic current, which describe accurately the field behavior in the neighborhood of the edges. The results of a convergence study are described and indications are given for the choice of the parameters of the numerical method.

3.2 Magnetic Field Integral Equation (HFIE) and its solution

Let us consider a coaxial cable with N_{slot} rectangular apertures on the external conductor, orthogonal to the cable axis, as shown in Figure 3.2. The radii of the inner, outer conductor and of the external dielectric cover, are denoted by ρ_1, ρ_2 and ρ_3, respectively; ε_{r1} and ε_{r2} are the relative dielectric permittivities (in general complex) of the internal and external dielectric media; the width and the angular aperture of the q-th slot (with $q = 1, .., N_{slot}$), are s_q and α_q; the longitudinal distance between the first slot and the q-th one is L_q. The ohmic losses in the cable are described by an equivalent loss tangent, which takes approximately into account both dielectric

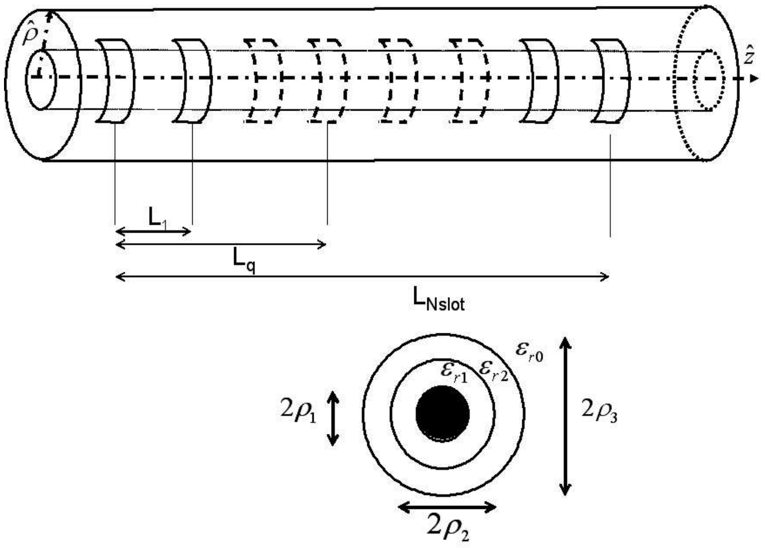

Figure 3.2: Slotted coaxial cable

and copper losses.

The scattering problem under consideration is solved by the domain decomposition method. For this purpose, applying an Equivalence Theorem [19], the apertures are closed by perfect electric conductors and two magnetic equivalent current distributions $\underline{\mathbb{J}}_{m1}$ and $\underline{\mathbb{J}}_{m2}$ are placed in $\rho = \rho_2^-$ and $\rho = \rho_2^+$, respectively. The support Σ_{slots} of these currents coincides with the apertures. The conductor thickness is assumed negligible, so that the tangential electric field is continuous. By denoting by $\underline{E}_0$ the electric field in the slots, the magnetic currents $\underline{\mathbb{J}}_{m1}$ and $\underline{\mathbb{J}}_{m2}$ are equal in magnitude but opposite:

$$\begin{aligned}
\underline{\mathbb{J}}_{m1}(\rho,\varphi,z) &= (\underline{E}_0(\varphi,z)\times\hat{\rho})\,\frac{\delta(\rho-\rho_2)}{\rho} \\
\underline{\mathbb{J}}_{m2}(\rho,\varphi,z) &= (\underline{E}_0(\varphi,z)\times(-\hat{\rho}))\,\frac{\delta(\rho-\rho_2)}{\rho}
\end{aligned}$$

Enforcing the tangential magnetic field continuity in the slots, we obtain the Magnetic Field Integral Equation (HFIE) of the problem:

$$\underline{H}^{\mathrm{inc}}(\rho_2,\varphi,z)+\underline{H}^{\mathrm{scat}}_{\mathrm{int}}\{\underline{\mathbb{J}}_m\}(\rho_2,\varphi,z)=\underline{H}^{\mathrm{scat}}_{\mathrm{ext}}\{-\underline{\mathbb{J}}_m\}(\rho_2,\varphi,z)\quad \text{for } (\varphi,z)\in\Sigma_{slots} \tag{3.1}$$

where $\underline{H}^{\mathrm{scat}}_{\mathrm{ext}}$ ($\underline{H}^{\mathrm{scat}}_{\mathrm{int}}$) is the scattered tangential magnetic field in the external (internal) region. $\underline{H}^{\mathrm{inc}}$ is the incident magnetic field, *i.e.* the one that propagates in the un-slotted cable.

To make (3.1) explicit, we must determine the relation between the magnetic current distribution

$\underline{\mathbb{J}}_m$ and the scattered fields ($\underline{H}^{\mathrm{scat}}_{\mathrm{int}}$, $\underline{H}^{\mathrm{scat}}_{\mathrm{ext}}$), which is in the form of a double convolution integral due to the invariance of the structure with respect to $\varphi-$ and $z-$translations (see below). The kernel of the integral operator, which is the Green's function of the problem, will be computed employing the radial transmission line theory developed in Chapter 2.

By adopting the radial point of view, the slotted outer conductor has the form of a grid that couples two possibly different waveguides. Since, in this case, the inner and the outer part of the cable are radially represented by identical waveguides (both have no boundaries in the φ and z direction), the scattering problem is of iris type and its equivalent radial circuit is shown in Figure 3.3.

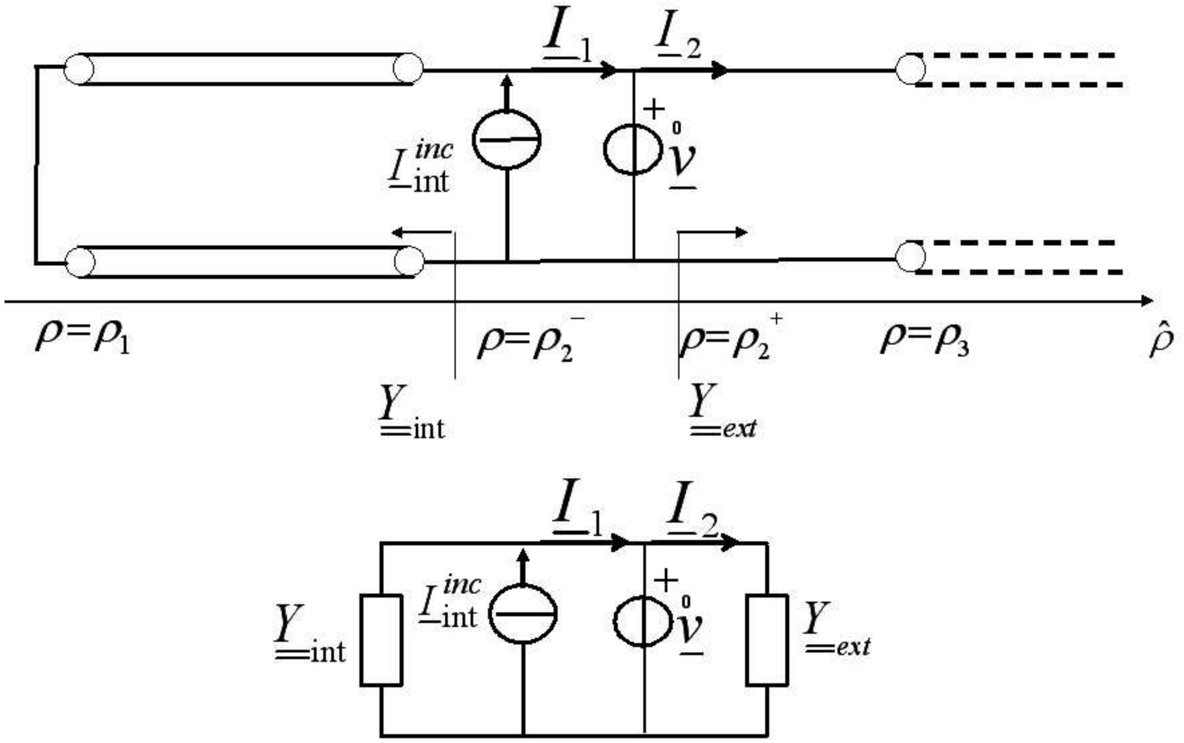

Figure 3.3: Equivalent radial circuit of the slotted cable

Here, $\underline{\mathring{v}}(\chi, n)$ is the voltage generator representing the Fourier transform of the magnetic current $\underline{\mathbb{J}}_m(\varphi, z)$, $\underline{\underline{Y}}_{\mathrm{int}}(\chi, n)$ and $\underline{\underline{Y}}_{\mathrm{ext}}(\chi, n)$ are the equivalent admittance matrices of the internal and external region of the cable, respectively. The vector currents $\underline{I}_1(\chi, n)$ and $\underline{I}_2(\chi, n)$ are the Fourier transforms of the scattered magnetic fields. Finally, the current generator $\underline{I}^{\mathrm{inc}}(\chi, n)$ is the Fourier transform of the incident magnetic field in $\rho = \rho_2^-$.

Let us compute the current flowing through the voltage generator. By inspection of the circuit:

$$\begin{aligned}\Delta\underline{I}(\chi,n) &= \underline{I}_1(\chi,n)-\underline{I}_2(\chi,n)= \\ &= \underline{I}^{\mathrm{inc}}(\rho_2,\chi,n)-\left(\underline{\underline{Y}}^{\mathrm{int}}(\rho_2,\chi,n)+\underline{\underline{Y}}^{\mathrm{ext}}(\rho_2,\chi,n)\right)\cdot\underline{\mathring{v}}(\chi,n)\end{aligned}$$

This is a typical equation of Wiener-Hopf type. It contains two unknowns, one ($\underline{\mathring{v}}(\chi,n)$) is the Fourier transform of a function ($\underline{\mathbb{J}}_m(\varphi,z)$) with support on the apertures, the other ($\Delta\underline{I}(\chi,n)$) is the Fourier transform of a function ($\Delta\underline{H}(\varphi,z)$) with complementary support. The two functions are obviously orthogonal in the natural domain, but also in the spectral domain, by Parseval's theorem. In conclusion, the complete formulation of the scattering problem in the spectral domain is

$$\begin{cases}\Delta\underline{I}(\chi,n) = \underline{I}^{\mathrm{inc}}(\chi,n)-(\underline{\underline{Y}}^{\mathrm{int}}(\rho_2,\chi,n)+\underline{\underline{Y}}^{\mathrm{ext}}(\rho_2,\chi,n))\cdot\underline{\mathring{v}}(\chi,n) \\ \\ 0 = \dfrac{1}{4\pi^2}\displaystyle\sum_n\int_{-\infty}^{+\infty}\Delta\underline{I}(\chi,n)\cdot\underline{\mathring{v}}(\chi,n)d\chi\end{cases} \tag{3.2}$$

Now we take the inverse Fourier transform with respect to χ and n and get

$$\begin{cases}\underline{H}^{\mathrm{inc}}(rho_2,\varphi,z)\times\hat{\rho}=\dfrac{1}{4\pi^2}\displaystyle\sum_n\int_{-\infty}^{+\infty}\underline{\underline{B}}^T\cdot\underline{\underline{Y}}^{tot}(\rho_2,\chi,n)\cdot\underline{\mathring{v}}(\chi,n)\cdot\,\mathrm{e}^{-jn\varphi}\,\mathrm{e}^{-j\chi z}d\chi \\ \\ \text{for } \rho=\rho_2 \text{ and } (\varphi,z)\in\Sigma_{slots}\end{cases} \tag{3.3}$$

where $\underline{\underline{B}}=(\hat{u}\hat{z}+\hat{v}\hat{\varphi})$ and $\underline{\underline{Y}}^{tot}(\rho_2,\chi,n)=\underline{\underline{Y}}^{\mathrm{int}}(\rho_2,\chi,n)+\underline{\underline{Y}}^{\mathrm{ext}}(\rho_2,\chi,n)$ is the total load admittance of the voltage generator.

Let us consider a general multimode field in the coaxial cable, incident on the slots from the left and from the right. The tangential magnetic field on the wall can be expressed as[1]:

$$\underline{H}_{tg}^{\mathrm{inc}}(\rho_2,z,\varphi)=\underline{\check{H}}_{tg}^{\mathrm{inc}}(\rho_2,z,\varphi)+\underline{\hat{H}}_{tg}^{\mathrm{inc}}(\rho_2,z,\varphi) \tag{3.4}$$

with

$$\underline{\check{H}}_{tg}^{\mathrm{inc}}(\rho_2,z,\varphi) = \sum_i Y_{\infty i}\check{V}_i^{\mathrm{inc}}(z_1)\mathrm{e}^{-j\,k_{z\,i}(z-z_1)}\underline{\check{h}}_i^{tg}(\rho_2)\mathrm{e}^{j\,m(i)\varphi} \tag{3.5}$$

$$\underline{\hat{H}}_{tg}^{\mathrm{inc}}(\rho_2,z,\varphi) = -\sum_i Y_{\infty i}\hat{V}_i^{\mathrm{inc}}(z_2)\mathrm{e}^{j\,k_{z\,i}(z-z_2)}\underline{\hat{h}}_i^{tg}(\rho_2)\mathrm{e}^{j\,m(i)\varphi} \tag{3.6}$$

---

[1] the subscript"i" is used from here as an index for the i-th mode of the coaxial cable, the azimuthal mode index m depends on i and therefore it is indicated as $m=m(i)$

and

$$\check{\underline{h}}_i^{tg}(\rho_2) = h_{\varphi i}(\rho_2)\hat{\varphi} + h_{zi}(\rho_2)\hat{z} \tag{3.7}$$

$$\hat{\underline{h}}_i^{tg}(\rho_2) = h_{\varphi i}(\rho_2)\hat{\varphi} - h_{zi}(\rho_2)\hat{z} \tag{3.8}$$

where $k_{z\,i}$, $Y_{\infty\, i}$, are the propagation constant and modal admittance of the i-th mode of the coaxial cable. $\check{V}_i^{\mathrm{inc}}(z_1)$ and $\hat{V}_i^{\mathrm{inc}}(z_2)$ are incident voltages on the left ($z = z_1$) and on the right ($z = z_2$) reference planes of the structure.[2]

The relation between the magnetic current and the voltage generator can be written as

$$\mathring{\underline{v}}(\chi, n) = \int_{-\infty}^{+\infty} \int_0^{2\pi} \underline{\underline{B}} \cdot \underline{\mathbb{J}}_m(\varphi, z) \times \hat{\rho}\, \mathrm{e}^{j\,n\varphi}\, \mathrm{e}^{j\chi\, z} d\varphi\, dz \tag{3.9}$$

Substituting into (3.3) and performing first the summation over n and the integration over χ, we obtain the explicit integral equation of the problem under consideration:

$$\left\{ \begin{array}{l} \underline{H}^{\mathrm{inc}}(\rho_2, \varphi, z) \times \hat{\rho} = \displaystyle\int_{-\infty}^{+\infty} \int_0^{2\pi} \underline{\underline{\mathcal{Y}}}^{tot}(\rho_2, \varphi - \varphi', z - z') \cdot \underline{\mathbb{J}}_m(\varphi', z') d\varphi' dz' \\ \\ \text{for } \rho = b \text{ and } (\varphi, z) \in \Sigma_{slots} \end{array} \right. \tag{3.10}$$

where the Green's function is given by

$$\underline{\underline{\mathcal{Y}}}^{tot}(\rho_2, \varphi - \varphi', z - z') = \frac{1}{4\pi^2} \sum_n \int_{-\infty}^{+\infty} \underline{\underline{B}}^T \cdot \underline{\underline{Y}}^{tot}(\rho_2, \chi, n) \cdot \underline{\underline{B}}\, \mathrm{e}^{-jn(\varphi - \varphi')}\, \mathrm{e}^{-j\chi\,(z - z')} d\chi \tag{3.11}$$

Actually, what is relatively simple to determine is the spectral representation $\underline{\underline{Y}}^{tot}(\rho_2, \chi, n)$. On the contrary, the computation of the Green's function is numerically very problematic because of the infinite summation and of the infinite domain integral, both very slowly convergent. However, the integral equation (3.10) can be solved by the Method of Moments applied directly in the spectral domain, so that the computation of the Green's function is not necessary. For this purpose we introduce a set $\{\underline{u}_c(z, \varphi)\}$ of vector basis functions in order to expand the unknown magnetic current distribution:

$$\underline{\mathbb{J}}_m(z, \varphi) = \sum_{c=1}^{N_f} x_c \underline{u}_c(z, \varphi) \tag{3.12}$$

---

[2] From here on the superscripts ˇ and ˆ are related to the left and right reference plane of the structure under consideration, respectively. Except, of course, for the unit vector

At this point we do not want to be specific about the details of these basis functions. They could be defined on the complete slotted cable, or on each slot or else they could be of subdomain type. This subject will be discussed in Section 3.4. The equations below are valid for each choice. Combining (3.12) with (3.3) and (3.9) we obtain:

$$\underline{H}^{\mathrm{inc}} \times \hat{\rho} = \sum_{c=1}^{N_f} x_c \sum_n \int_{-\infty}^{+\infty} \mathrm{e}^{-j\chi z} \mathrm{e}^{-jn\varphi} \underline{\underline{B}}^T \cdot \underline{\underline{Y}}^{tot}(\rho_2, \chi, n) \cdot \underline{\underline{B}} \cdot \underline{\tilde{u}}_c(\chi, n) d\chi \tag{3.13}$$

where $\underline{\tilde{u}}_c(\chi, n)$ is the double Fourier transform of $\underline{u}_c(z, \varphi)$.
Applying the Galerkin version of the Method of Moment, we project (3.13) on $\underline{u}_r(z, \varphi)$, $r = 1, \ldots, N_f$, obtaining:

$$< \left(\underline{H}^{\mathrm{inc}} \times \hat{\rho}\right), \underline{u}_r >= \sum_{c=1}^{N_f} x_c \sum_n \int_{-\infty}^{+\infty} (\underline{\tilde{u}}_r^*(\chi, n))^T \cdot \underline{\underline{B}}^T \cdot \underline{\underline{Y}}^{tot}(\rho_2, \chi, n) \cdot \underline{\underline{B}} \cdot \underline{\tilde{u}}_c(\chi, n) d\chi \tag{3.14}$$

where, clearly, the inner product is defined in the φ, z domain and the exponential kernel on the right hand side gives rise to the Fourier transform of the test function. It is convenient to write this linear system in matrix form:

$$\underline{\underline{A}} \cdot \underline{x} = \left[\underline{\check{B}} + \underline{\hat{B}}\right] \Rightarrow \underline{x} = \underline{\underline{A}}^{-1} \left[\underline{\check{B}} + \underline{\hat{B}}\right] \tag{3.15}$$

where, the right hand side shows explicitly the contributions of the field incident from the left and from the right. The moment matrix $\underline{\underline{A}}$ has elements

$$A_{rc} = \sum_n \int_{-\infty}^{+\infty} \underline{\tilde{u}}_r^*(\chi, n) \cdot \underline{\underline{B}}^T \cdot \underline{\underline{Y}}^{tot}(\rho_2, \chi, n) \cdot \underline{\underline{B}} \cdot \underline{\tilde{u}}_c(\chi, n) d\chi \tag{3.16}$$

The two terms on the right hand side are given by

$$\begin{aligned}
\check{B}_r &= < \left(\underline{\check{H}}^{\mathrm{inc}} \times \hat{\rho}\right), \underline{u}_r >= \\
&= < \sum_{i=1}^{N_i} Y_{\infty i} \check{V}_i^{\mathrm{inc}}(z_1) \mathrm{e}^{-j\,k_{z\,i}(z - z_1)} \left(\underline{\check{h}}_i^{tg}(\rho_2) \times \hat{\rho}\right) \mathrm{e}^{j\,m(i)\varphi}, \underline{u}_r >= \\
&= \sum_{i=1}^{N_i} Y_{\infty i} \check{V}_i^{\mathrm{inc}}(z_1) \mathrm{e}^{j\,k_{z\,i} z_1} \left(\underline{\check{h}}_i^{tg}(\rho_2) \times \hat{\rho}\right) \cdot \underline{\tilde{u}}_r^*(-k_{zi}, m(i))
\end{aligned} \tag{3.17}$$

and likewise

$$\begin{aligned}
\hat{B}_r &= < \left(\underline{\hat{H}}^{\text{inc}} \times \hat{\rho}\right), \underline{u}_r >= \\
&= < \sum_{i=1}^{N_i} Y_{\infty\, i} \hat{V}_i^{\text{inc}}(z_2) \mathrm{e}^{-j\, k_{z\, i}(z-z_2)} \left(\underline{\hat{h}}_i^{tg}(\rho_2) \times \hat{\rho}\right) \mathrm{e}^{j\, m(i) \varphi}, \underline{u}_r >= \\
&= \sum_{i=1}^{N_i} Y_{\infty\, i} \hat{V}_i^{\text{inc}}(z_2) \mathrm{e}^{-j\, k_{z\, i} z_2} \left(\underline{\hat{h}}_i^{tg}(\rho_2) \times \hat{\rho}\right) \cdot \underline{\tilde{u}}_r^*(k_{zi}, m(i)) \qquad (3.18)
\end{aligned}$$

These expressions can be written more concisely by introducing a matrix formalism. Let us define the $N_i \times N_i$ diagonal matrices

$$\underline{\underline{D}}_1 = \text{diag}\left\{\mathrm{e}^{+j\, k_{z\, i} z_1}\right\} \qquad (3.19)$$

$$\underline{\underline{D}}_2 = \text{diag}\left\{\mathrm{e}^{+j\, k_{z\, i} z_2}\right\} \qquad (3.20)$$

$$\underline{\underline{Y}}_\infty = \text{diag}\left\{Y_{\infty\, i}\right\} \qquad (3.21)$$

$$\underline{\underline{\check{h}}} = \text{diag}\left\{\underline{\check{h}}_i^{tg}(\rho_2) \times \hat{\rho}\right\} \qquad (3.22)$$

$$\underline{\underline{\hat{h}}} = \text{diag}\left\{\underline{\hat{h}}_i^{tg}(\rho_2) \times \hat{\rho}\right\} \qquad (3.23)$$

and the $N_i \times N_f$ full matrices $\underline{\underline{U}}^{-+}$, $\underline{\underline{U}}^{++}$ with elements:

$$U^{-+}|_{r,c} = \underline{\tilde{u}}_r(-k_{z\, c}, +m(c))$$

$$U^{++}|_{r,c} = \underline{\tilde{u}}_r(+k_{z\, c}, +m(c))$$

Some of these matrices are abstract in the sense that their elements are vectors. With these notations, the known term of the linear system is expressed as:

$$\underline{\check{B}} = \left(\underline{\underline{U}}^{-+}\right)^* \cdot \underline{\underline{\check{h}}} \cdot \underline{\underline{Y}}_\infty \cdot \underline{\underline{D}}_1 \cdot \underline{\check{V}}^{\text{inc}} \qquad (3.24)$$

$$\underline{\hat{B}} = \left(\underline{\underline{U}}^{++}\right)^* \cdot \underline{\underline{\hat{h}}} \cdot \underline{\underline{Y}}_\infty \cdot \underline{\underline{D}}_2^{-1} \cdot \underline{\hat{V}}^{\text{inc}} \qquad (3.25)$$

where the amplitudes of the incident modes (TE and TM) have been grouped in the vectors $\underline{\hat{V}}^{\text{inc}}$, $\underline{\check{V}}^{\text{inc}}$. In Section 3.3 it will be useful to exploit a direct relation between the incident voltages and the magnetic current coefficients. This is easily derived from (3.15) and (3.25):

$$\underline{x} = \underline{\underline{A}}^{-1} \cdot \left[\underline{\check{B}} + \underline{\hat{B}}\right] \tag{3.26}$$

$$= \underline{\underline{\check{C}}} \cdot \underline{\check{V}}^{\text{inc}} + \underline{\underline{\hat{C}}} \cdot \underline{\hat{V}}^{\text{inc}} = \underline{\underline{C}} \cdot \begin{pmatrix} \underline{\check{V}}^{\text{inc}} \\ \underline{\hat{V}}^{\text{inc}} \end{pmatrix} \tag{3.27}$$

where the matrix $\underline{\underline{C}}$ has size $N_f \times 2N_i$.

3.3 Array scattering matrix

Once the linear system is solved, *i.e.* an approximation of the equivalent magnetic current $\underline{\mathbb{J}}_m$ in the subspace spanned by the basis functions is obtained, it is possible to compute the field scattered both inside the cable and outside of it. In this section we will derive the scattering matrix of the structure for all the modes of the coaxial cable, as well as the power radiated from the slots.
The equivalent circuit of the slotted cable for the i-th mode is shown in Figure 3.4 where:

$$\overline{v}_i(z) = <\underline{\mathbb{J}}_m, h_{\varphi i}> = \sum_{c=1}^{N_f} x_c < \hat{\varphi} \cdot \underline{u}_c, h_{\varphi i}> \tag{3.28}$$

$$\overline{i}_i(z) = Y^*_{\infty i} <\underline{\mathbb{J}}_m, h_{z i}> = Y^*_{\infty i} \sum_{c=1}^{N_f} x_c < \hat{z} \cdot \underline{u}_c, h_{zi}> \tag{3.29}$$

These inner products are integrals defined on the cable cross section. However, since the magnetic current support is the wall $\rho = b$, only the φ integral remains. We will first compute the voltages produced by the generators. Consider the couple of a voltage and a current generator, located in the point z'. Applying the superposition principle, the partial voltages at the two terminal planes z_1, z_2 are given by

$$\check{V}_i^{\text{scat}}(z_1, z') = \frac{1}{2}\left(\overline{v}_i(z') - Z_{\infty i}\overline{i}_i(z')\right) \mathrm{e}^{-j\,k_{z\,i}\,(z'-z_1)} \tag{3.30}$$

$$\hat{V}_i^{\text{scat}}(z_2, z') = -\frac{1}{2}\left(\overline{v}_i(z') + Z_{\infty i}\overline{i}_i(z')\right) \mathrm{e}^{-j\,k_{z\,i}\,(z_2-z')} \tag{3.31}$$

By substituting the expression of the generators (3.29), integrating with respect to z' over the support of the slots, and recognizing the exponentials

$$\exp(\pm j k_{zi} z' \pm j m(i) \varphi)$$

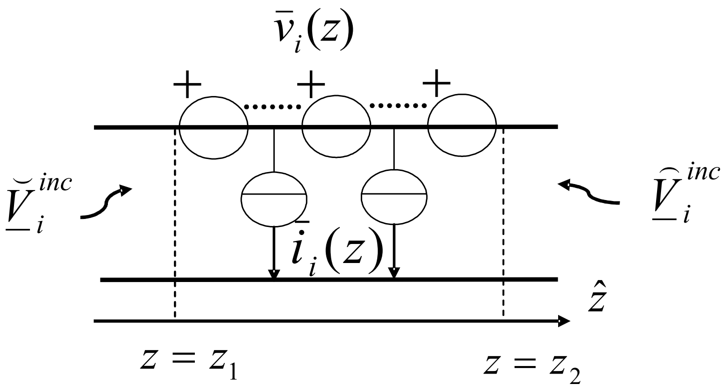

Figure 3.4: Equivalent circuit for the i-th mode of the coaxial cable

as Fourier kernels, we get the total scattered voltages:

$$\check{V}_i^{\text{scat}}(z_1) = \frac{1}{2}\,\mathrm{e}^{+j\,k_{z\,i}\,z_1}\sum_{c=1}^{N_f} x_c\left[h^*_{\varphi\,i}(\rho_2)\hat{\varphi}\cdot\underline{\tilde{u}}_c(-k_{z\,i},-m(i)) - Z_{\infty\,i}Y^*_{\infty\,i}\,h^*_{z\,i}(\rho_2)\,\hat{z}\cdot\underline{\tilde{u}}_c(-k_{z\,i},-m(i))\right]$$

$$\hat{V}_i^{\text{scat}}(z_2) = -\frac{1}{2}\,\mathrm{e}^{-j\,k_{z\,i}\,z_2}\sum_{c=1}^{N_f} x_c\left[-h^*_{\varphi\,i}(\rho_2)\hat{\varphi}\cdot\underline{\tilde{u}}_c(k_{z\,i},-m(i)) + Z_{\infty\,i}Y^*_{\infty\,i}\,h^*_{z\,i}(\rho_2)\hat{z}\cdot\underline{\tilde{u}}_c(+k_{z\,i},m(i))\right]$$

Using the definition (3.8), this expression simplifies in

$$\check{V}_i^{\text{scat}}(z_1) = \frac{1}{2}\,\mathrm{e}^{+j\,k_{z\,i}\,z_1}\sum_{c=1}^{N_f} x_c\left[\underline{\hat{h}}_i^{tg*}(\rho_2)\cdot\underline{\underline{W}}_i\cdot\underline{\tilde{u}}_c(-k_{z\,i},-m(i))\right]$$

$$\hat{V}_i^{\text{scat}}(z_2) = -\frac{1}{2}\,\mathrm{e}^{-j\,k_{z\,i}\,z_2}\sum_{c=1}^{N_f} x_c\left[\underline{\check{h}}_i^{tg*}(\rho_2)\cdot\underline{\underline{W}}_i\cdot\underline{\tilde{u}}_c(-k_{z\,i},-m(i))\right]$$

where the dyadic $\underline{\underline{W}}_i$ is defined by

$$\underline{\underline{W}}_i = \hat{\varphi}\hat{\varphi} + (Z_{\infty\,i}Y^*_{\infty\,i})\,\hat{z}\hat{z} = \hat{\varphi}\hat{\varphi} + \left(\frac{k^*_{z\,i}}{k_{z\,i}}\right)\hat{z}\hat{z} \tag{3.32}$$

Note that $\underline{\underline{W}}_i$ is the identity in the tangent plane to the cable $\hat{\varphi}, \hat{z}$ for above cut-off modes (in the lossless case). Note also that only the TE mode expression of the modal impedance has been used: indeed, if the incident i mode is TM, the vector $\underline{\check{h}}_i^{tg}(\rho_2)$ has only the φ component.
We write now this expression in matrix form. Define the diagonal matrix $\underline{\underline{W}}$, with dyadic elements:

$$\underline{\underline{W}} = \text{diag}\{\underline{\underline{W}}_i\}$$

Then the vectors of the scattered voltages are given by:

$$\check{\underline{V}}^{\text{scat}} = \frac{1}{2}\underline{\underline{D}}_1 \cdot \hat{\underline{\underline{h}}}^* \cdot \underline{\underline{W}} \cdot (\underline{\underline{U}}^{--})^T \cdot \underline{x} = \check{\underline{\underline{M}}}_{\text{int}} \cdot \underline{x} \tag{3.33}$$

$$\hat{\underline{V}}^{\text{scat}} = -\frac{1}{2}\underline{\underline{D}}_2^{-1} \cdot \check{\underline{\underline{h}}}^* \cdot \underline{\underline{W}} \cdot (\underline{\underline{U}}^{--})^T \cdot \underline{x} = \hat{\underline{\underline{M}}}_{\text{int}} \cdot \underline{x} \tag{3.34}$$

where the $N_i \times N_f$ matrices $\check{\underline{\underline{M}}}_{\text{int}}$ and $\hat{\underline{\underline{M}}}_{\text{int}}$ represent the operators which relate the magnetic current on the slot to the scattered voltages.

Combining Eqs. (3.33), (3.34) and (3.27) we obtain the scattered voltages as a functions of the incident ones:

$$\check{\underline{V}}^{\text{scat}} = \check{\underline{\underline{M}}}_i \cdot \left(\check{\underline{\underline{C}}} \cdot \check{\underline{V}}^{\text{inc}} + \hat{\underline{\underline{C}}} \cdot \hat{\underline{V}}^{\text{inc}} \right) \tag{3.35}$$

$$\hat{\underline{V}}^{\text{scat}} = \hat{\underline{\underline{M}}}_i \cdot \left(\check{\underline{\underline{C}}} \cdot \check{\underline{V}}^{\text{inc}} + \hat{\underline{\underline{C}}} \cdot \hat{\underline{V}}^{\text{inc}} \right) \tag{3.36}$$

By introducing power waves to describe the incident and scattered mode amplitudes via the usual normalizations:

$$\begin{aligned} \underline{a}_1 &= \underline{\underline{Y}}_\infty^{-1/2} \cdot \check{\underline{V}}^{\text{inc}} & \qquad \underline{a}_2 &= \underline{\underline{Y}}_\infty^{-1/2} \cdot \hat{\underline{V}}^{\text{inc}} \\ \underline{b}_1 &= \underline{\underline{Y}}_\infty^{-1/2} \cdot \check{\underline{V}}^{\text{scat}} & \qquad \underline{b}_2 &= \underline{\underline{Y}}_\infty^{-1/2} \cdot \hat{\underline{V}}^{\text{scat}} \end{aligned} \tag{3.37}$$

we can obtain the scattering matrix of the slotted cable (with respect to the cable modes):

$$\begin{pmatrix} \underline{b}_1 \\ \underline{b}_2 \end{pmatrix} = \begin{pmatrix} \underline{\underline{S}}_{11} & \underline{\underline{S}}_{12} \\ \underline{\underline{S}}_{21} & \underline{\underline{S}}_{22} \end{pmatrix} \cdot \begin{pmatrix} \underline{a}_1 \\ \underline{a}_2 \end{pmatrix} \tag{3.38}$$

where the submatrices have the expressions:

$$\underline{\underline{S}}_{11} = \underline{\underline{Y}}_\infty^{1/2} \cdot \check{\underline{\underline{M}}}_{\text{int}} \cdot \check{\underline{\underline{C}}} \cdot \underline{\underline{Y}}_\infty^{-1/2} \tag{3.39}$$

$$\underline{\underline{S}}_{12} = \underline{\underline{Y}}_\infty^{1/2} \cdot \check{\underline{\underline{M}}}_{\text{int}} \cdot \hat{\underline{\underline{C}}} \cdot \underline{\underline{Y}}_\infty^{-1/2} + \underline{\underline{D}}_2^{-1} \cdot \underline{\underline{D}}_1 \tag{3.40}$$

$$\underline{\underline{S}}_{21} = \underline{\underline{Y}}_\infty^{1/2} \cdot \hat{\underline{\underline{M}}}_{\text{int}} \cdot \check{\underline{\underline{C}}} \cdot \underline{\underline{Y}}_\infty^{-1/2} + \underline{\underline{D}}_2^{-1} \cdot \underline{\underline{D}}_1 \tag{3.41}$$

$$\underline{\underline{S}}_{22} = \underline{\underline{Y}}_\infty^{1/2} \cdot \hat{\underline{\underline{M}}}_{\text{int}} \cdot \hat{\underline{\underline{C}}} \cdot \underline{\underline{Y}}_\infty^{-1/2} \tag{3.42}$$

The term $\underline{\underline{D}}_2^{-1} \cdot \underline{\underline{D}}_1$, present in $\underline{\underline{S}}_{12}$ and $\underline{\underline{S}}_{21}$ accounts for the direct contribution of the incident voltages.

Even if the dielectric media are lossless, the scattering matrix $\underline{\underline{S}}$ is not unitary due to the power P_{rad} radiated from the slots, which is “lost” from the point of view of the coaxial cable modes.

The matrix is, however, symmetric because the structure is reciprocal.

To complete the global characterization of the slotted cable, we compute the total radiated power. To this end we apply the Poynting theorem:

$$\begin{aligned} P_{rad} &= \frac{1}{2}\int_{\Sigma} \Re\{\underline{E} \times \underline{H}^* \cdot \hat{\rho}\} d\Sigma = \frac{b}{8\pi^2}\Re\left\{\sum_n \int_{\Re} \underline{V}(\rho_2,\chi,n)\cdot \underline{I}^*(\rho_2,\chi,n) d\chi\right\} = \\ &= \frac{b}{8\pi^2}\sum_n \int_{-k_0}^{k_0} \mathring{\underline{v}}^*(\chi,n)\cdot\Re\{\underline{\underline{Y}}^{ext}(\rho_2,\chi,n)\}\cdot\mathring{\underline{v}}(\chi,n)\, d\chi = \\ &= \frac{b}{8\pi^2}\sum_{c,r} x_r^* x_c \sum_n \int_{-k_0}^{k_0} \tilde{\underline{u}}_r^*(\chi,n)\cdot\underline{\underline{B}}^T\cdot\Re\{\underline{\underline{Y}}^{ext}(\rho_2,\chi,n)\}\cdot\underline{\underline{B}}\cdot\tilde{\underline{u}}_c(\chi,n) d\chi \end{aligned} \tag{3.43}$$

where Σ is a cylindrical surface flush with the outer conductor $\rho = b$ and k_0 is the free space wavenumber. Parseval theorem has been exploited to convert the surface integral to the spectral domain.

Note that the integration interval is limited to the visible range, because it is the only one that gives contribution to the real part. It is to be remarked that the integrals in this equation are the same occurring in the computation of the Moment matrix $\underline{\underline{A}}$.

3.4 Expansion functions for the magnetic current

The choice of a good set of basis functions is a decisive and delicate step in the numerical solution of any integral equation by the Method of Moments. It is well known, indeed, that a poor selection can create various problems (*e.g.* slow convergence of the numerical solution or ill conditioning of the Moment Matrix). Moreover, in the problem under consideration, only an appropriate choice of this set can keep the number of unknowns within reasonable limits.

The type of discontinuity considered (*i.e.* complete or incomplete rectangular apertures) has a canonical geometrical shape. This fact suggests the use of entire domain expansion functions, defined on each slot, instead of sub-domain ones (such as Rao-Wilton-Glisson (RWG), rooftops, piecewise ones, etc.).

Each slot may have a different width s_q and angular dimension α_q, in general, but the same basis functions will be used for all them. The set of basis functions can be generated in the following way. First, one introduces a set of functions $\{\underline{u}_t(\overline{z},\overline{\varphi})\}$ where $\overline{z}$ and $\overline{\varphi}$ are normalized variables belonging to the interval $[-1,+1]$. Since metallic losses are neglected in this study, it is convenient to employ a set of basis functions that satisfy the Meixner edge conditions [20]. Hence, we assume:

$$\underline{u}_t(\overline{z},\overline{\varphi}) = f_{m(t)}(\overline{z})g_{l(t)}(\overline{\varphi})\hat{\varphi} + g_{l(t)}(\overline{z})f_{m(t)}(\overline{\varphi})\hat{z} \tag{3.44}$$

where $m(t)$ and $l(t)$ are suitable index mapping functions. In particular:

$$f_m(\overline{z}) = T_m(\overline{z})\frac{1}{\sqrt{1-(\overline{z})^2}} \tag{3.45}$$

$$g_l(\overline{\varphi}) = U_l(\overline{\varphi})\sqrt{1-(\overline{\varphi})^2} \tag{3.46}$$

where $T_m(\overline{z})$ and $U_l(\overline{\varphi})$ are Tchebychev polynomials of first and second kind, respectively. Some of these functions are plotted in Figures 3.5 and 3.6. The f_m functions have a square root divergence at the domain limits and are therefore useful to expand a current component parallel to the edge. On the contrary the g_l functions go to zero as a square root and are appropriate to represent current components normal to the edge.

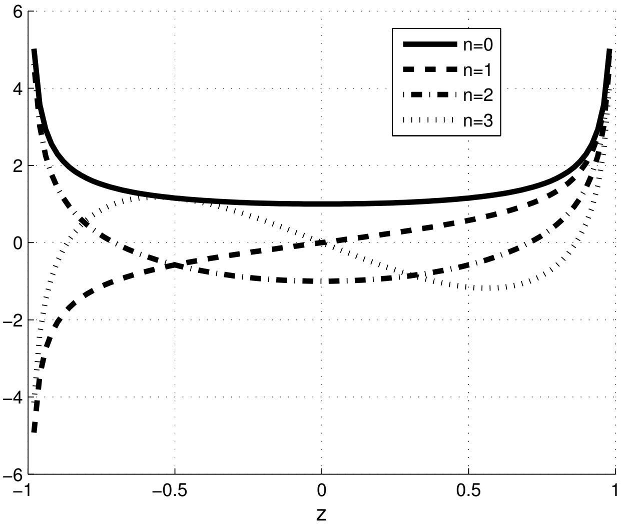

Figure 3.5: Plot of $f_n(\overline{z})$ for $n = 0, 1, 2, 3$

The Fourier transforms of these functions can be evaluated in closed form as [10]

$$\tilde{f}_m(\chi) = \pi j^m J_m(\chi)$$

$$\tilde{g}_l(n) = \frac{\pi\,(l+1)j^l}{n}J_l(n)$$

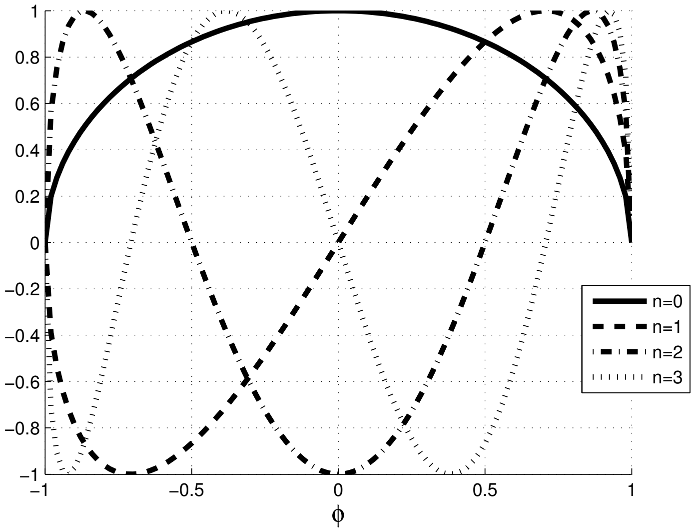

Figure 3.6: Plot of $g_n(\overline{\varphi})$ for $n = 0, 1, 2, 3$

Note that $f_m(\overline{z})$ and $g_l(\overline{\varphi})$ are alternatively even and odd real functions, which implies that their Fourier transforms are real even or imaginary odd functions, respectively.

Some of these transforms are plotted in Figures 3.7 and 3.8.

Then, for the q-th slot, one defines the specific subset $\mathbb{U}_q$:

$$\mathbb{U}_q = \bigcup_{t=1}^{N_{tot}} \{\underline{u}_t(2z_q/s_q, 2\varphi/\alpha_q)\} \tag{3.47}$$

where z_q is defined with respect to the local reference system, centered on the q-th slot and $N_{tot} = 2N_{f\varphi}N_{fz}$, where $N_{f\varphi}$, N_{fz} denote the numbers of functions used to expand the two components. If the origin of the global reference system is centered on the first slot, then $z_q = z - L_q$ and the total set $\mathbb{U}$ of basis functions is defined as [21]:

$$\mathbb{U} = \bigcup_{q=1}^{N_{slot}} \mathbb{U}_q = \bigcup_{q=1}^{N_{slot}} \bigcup_{t=1}^{N_{tot}} \{\underline{u}_t(2(z - L_q)/s_q, 2\varphi/\alpha_q)\} \tag{3.48}$$

In section 5.5 the eigenfunctions of the admittance operator related to one slot are numerically computed using as basis functions, for the φ-dependence, weighted Chebyshev polynomials of the second kind and piecewise linear functions. For the sake of completeness the relevant ex-

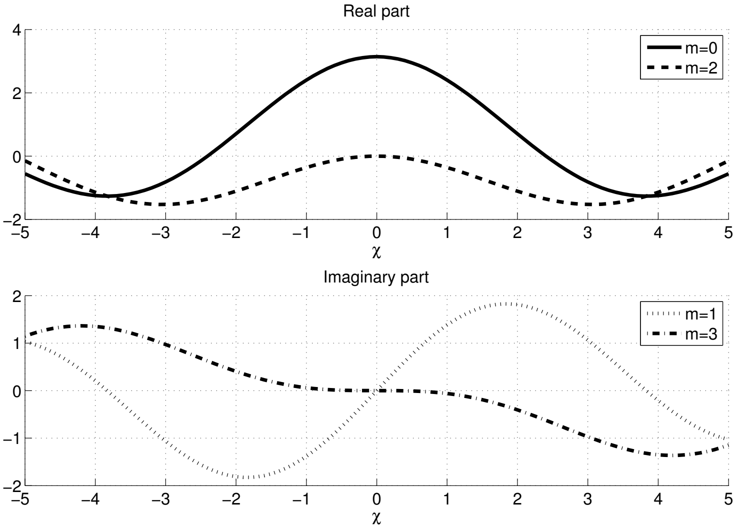

Figure 3.7: Plot of $\tilde{f}_m(\chi)$ for $m = 0, 1, 2, 3$

pressions of the elements of this last set are here reported:

$$g_l(\varphi) = \begin{cases} 1 + \frac{\varphi - \varphi_l}{\Delta} & -\Delta \leq \varphi - \varphi_l \leq 0 \\ \\ 1 - \frac{\varphi + \varphi_l}{\Delta} & 0 \leq \varphi + \varphi_l \leq \Delta \end{cases} \qquad \text{with } l = 1, \ldots, N_{f\varphi} \tag{3.49}$$

where the centers of the triangles are $\varphi_l = \frac{l\alpha}{1+N_{f\varphi}} - \frac{\alpha}{2}$ and the semi-width $\Delta = \frac{\alpha}{N_{f\varphi}+1}$. The Fourier Transform of $g_l(\varphi)$ is:

$$\tilde{g}_l(n) = e^{\jmath n\varphi_l} \frac{2}{n^2\Delta}(1 - \cos n\Delta) \tag{3.50}$$

3.5 Simplifying assumptions

Slotted cables are always designed to be single mode in the frequency band of interest, then the incident field on each slot can be assumed to be TEM only:

$$\underline{H}^{\text{inc}}(\rho_2, \varphi, z) = I^{\text{inc}}(z) h_\varphi(\rho_2, \varphi)\hat{\varphi} = I^{\text{inc}}(z) \frac{1}{\rho_2\sqrt{2\pi \ln(\rho_1/\rho_2)}}\hat{\varphi}$$

Also, in the standard application of this kind of antennas, the slots are very narrow in comparison with the free-space wavelength λ_0 (*i.e.* $s_q < \lambda_0/10$ with $q = 1, .., N_{slot}$). This fact suggests a

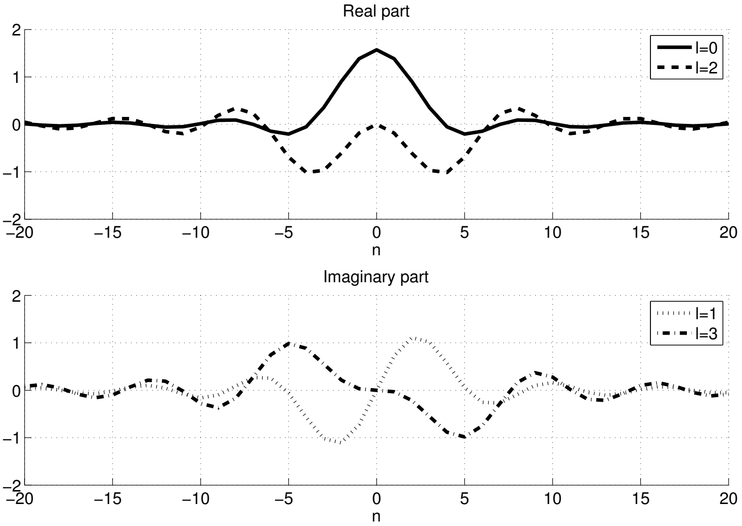

Figure 3.8: Plot of $\tilde{g}_l(n)$ for $l = 0, 1, 2, 3$

simplification in (3.14), *i.e.* we can assume that the equivalent magnetic current distribution $\underline{\mathbb{J}}_m$ has a negligible z-component:

$$\underline{\mathbb{J}}_m \simeq J_{m\varphi}\hat{\varphi} \Longleftrightarrow \underline{\mathring{v}}(\chi, n) \simeq \mathring{v}_u(\chi, n)\hat{u} \tag{3.51}$$

This assumption, widely employed in literature, has been also numerically verified by means of numerical experiments.

Hence,only $\hat{\varphi}$ directed vector basis functions are used. Equation 3.14 assumes the following form:

$$\begin{aligned} < H_\varphi^{\rm inc}, u_{\varphi r} > &= \sum_c x_c \sum_n \int_{-\infty}^{+\infty} u_{\varphi r}^*(\chi, n) Y_{uu}^{tot}(\chi, n) \tilde{u}_{\varphi c}(\chi, n) d\chi \\ < H_z^{\rm inc}, u_{z r} > = 0 &= \sum_c x_c \sum_n \int_{-\infty}^{+\infty} u_{z r}^*(\chi, n) Y_{vu}^{tot}(\chi, n) \tilde{u}_{\varphi c}(\chi, n) d\chi \end{aligned} \tag{3.52}$$

where it has been taken into account that the incident field has no $\hat{z}$ component. For the reader's convenience we report here the explicit expressions of Y_{uu}^{tot} and Y_{vu}^{tot}, in the case the dielectric cover is neglected, as computed in Section 2.7:

$$
\begin{aligned}
Y_{uu}^{int} &= -\frac{j\omega\varepsilon_1}{\tau_1}\frac{J_n(\tau_1\rho_1)Y_n'(\tau_1\rho_2)-J_n'(\tau_1\rho_2)Y_n(\tau_1\rho_1)}{J_n(\tau_1\rho_1)Y_n(\tau_1\rho_2)-J_n(\tau b)Y_n(\tau_1\rho_1)}+\frac{j\chi^2n^2}{\omega\mu_0\rho_2^2\tau_1^3}\frac{J_n'(\tau_1\rho_1)Y_n(\tau_1\rho_2)-J_n(\tau_1\rho_2)Y_n'(\tau_1\rho_1)}{J_n'(\tau\rho_1)Y_n'(\tau_1\rho_2)-J_n'(\tau_1\rho_2)Y_n'(\tau_1\rho_1)}\\
Y_{uv}^{int} &= \frac{j\,n\chi}{\omega\mu_0\rho_2\tau_1}\frac{J_n'(\tau_1\rho_1)Y_n(\tau_1\rho_2)-J_n(\tau_1\rho_2)Y_n'(\tau_1\rho_1)}{J_n'(\tau_1\rho_1)Y_n'(\tau_1\rho_2)-J_n'(\tau_1\rho_2)Y_n'(\tau_1\rho_1)}\\
Y_{uu}^{ext} &= \frac{j\omega\epsilon_0}{\tau}\frac{H_n'^{(2)}(\tau\rho_2)}{H_n^{(2)}(\tau\rho_2)}-\frac{j\chi^2n^2}{\omega\mu\tau^3\rho_2^2}\frac{H_n^{(2)}(\tau\rho_2)}{H_n'^{(2)}(\tau\rho_2)}\\
Y_{vu}^{ext} &= -\frac{j\chi\,n}{\omega\mu\tau\rho_2}\frac{H_n^{(2)}(\tau\rho_2)}{H_n'^{(2)}(\tau\rho_2)}
\end{aligned}
$$

where:

$$
\begin{aligned}
\tau_1 &= \sqrt{k_0^2\varepsilon_{r1}-\chi^2}\\
\tau &= \sqrt{k_0^2-\chi^2}
\end{aligned}
$$

are the radial propagation constants.
For the case of complete slots, since the incidence is φ-independent, the basis functions $u_\varphi(\varphi,z)$ do not depend on φ, then the relevant Fourier transforms are different from zero only for n equal to zero. Since Y_{uv}^{tot} is proportional to n, the second equation of (3.52) is automatically satisfied and the problem is not over-determined. On the contrary, in the general case of incomplete slots, the second equation is not automatically satisfied, because the transform of the basis functions $\tilde{u}_\varphi(\chi,n)$ is non-zero for all n and the problem is over-determined. This fact depends on the hypothesis that the magnetic current $\underline{\mathbb{J}}_m$ has only a φ component. The usual approach, when the slot width is very small as in this case, is just to neglect the second equation. Indeed if one should solve the complete problem, would find that the z component of the unknown magnetic current distribution is negligible.

It can be useful to write here the expressions of the moment matrix and of the right hand side of the linear system, in the case of the simplified approach:

$$
\begin{aligned}
A_{\,r,c} &= \sum_n\int_{-\infty}^{+\infty}\tilde{u}_{t(r)}^*(\chi,n;s_{q(r)},\alpha_{q(r)})Y_{uu}^{tot}(\chi,n)\tilde{u}_{t(c)}(\chi,n;s_{q(c)},\alpha_{q(c)})\,\mathrm{e}^{-j\,\chi(L_{q(c)}-L_{q(r)})}\,d\chi\\
B_{\,r,1} &= -4\pi^2\,Y_\infty h_{\,\varphi}(\rho_2)\tilde{u}_{t(r)}^*(-k_{\,1},\,0;s_{\,q(r)},\alpha_{\,q(r)})\,\mathrm{e}^{-j\,k_{\,1}(L_{\,q(r)}-z_{\,1})}\\
B_{\,r,2} &= +4\pi^2\,Y_\infty h_{\,\varphi}(\rho_2)\tilde{u}_{t(r)}^*(+k_{\,1},\,0;s_{\,q(r)},\alpha_{\,q(r)})\,\mathrm{e}^{-j\,k_{\,1}(z_{\,2}-L_{\,q(r)})}
\end{aligned}
\qquad (3.53)
$$

Here, $\tilde{u}_{\,t}(\chi,n;s_{\,q},\alpha_{\,q})$ is the double Fourier Transform of the basis function $u_{\,t}(z,\varphi;s_{\,q},\alpha_{\,q})$, constructed as explained in section 3.4.

3.6 Convergence study for a single slot

In order to study the convergence of the numerical scheme that has been developed up to now, a LCX with a single slot will be considered. The geometrical and electric characteristics of this cable are: inner conductor radius $a = 3.4$ mm, outer conductor radius $b = 8.8$ mm, slot width $s = 3$ mm, relative permittivity $\varepsilon_{r1} = 1.26$ and frequency $f = 1$ GHz. To distinguish the different convergence rates of the subsets $f_r(z)$ and $g_r(\varphi)$, the best strategy consists in treating first the particular case of a complete slot, in order to deduce the appropriate number of basis functions for the $z-$dependence and subsequently the general case.

Even if the actual unknown of the integral equation is $\underline{J}_m$, from an engineering point of view it is more interesting to study the convergence of the real design parameters, *i.e.* the scattering coefficients and the radiated power. They allow an immediate understanding of the electromagnetic characteristics of these antennas and have also a faster convergence due to their stationary character (see [22] and [23]).

In Figures 3.9 and 3.10, the reflection and transmission coefficients (in dB) versus N_f are shown for a LCX with a complete aperture.

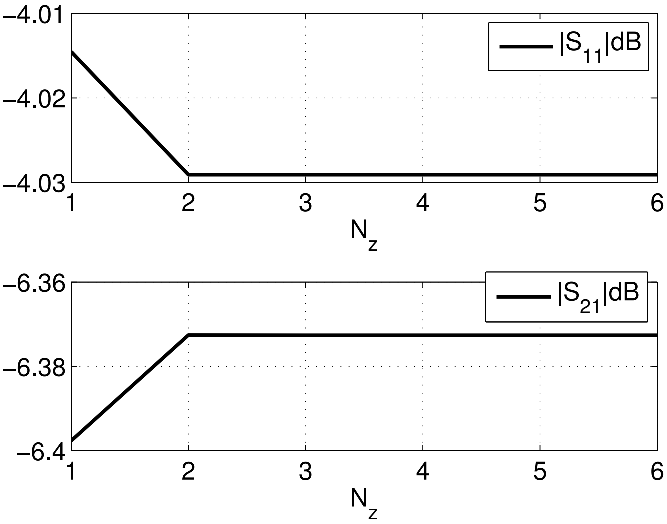

Figure 3.9: Reflection and transmission coefficients versus the number of basis functions for a complete slot

From the pictures we note that, as it can be expected since $k_0 s \ll 1$, one basis function is suffi-

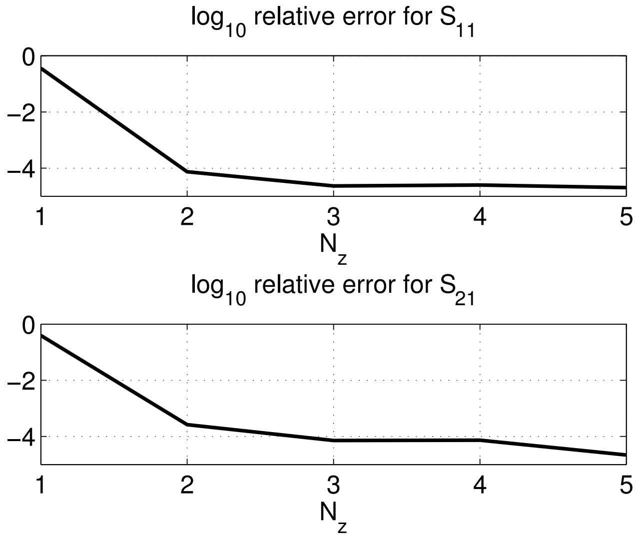

Figure 3.10: $\log_{10}$ of the relative error of the reflection and transmission coefficients versus the number of basis functions for a complete slot

cient to guarantee a good accuracy. This fact fixes the value of N_z to be equal to one. Now, we must determine N_φ and the truncation criterion of the n series in (3.53).

For symmetry reasons, the upper and lower limit of the series (3.53) are chosen equal and opposite, *i.e.* $\pm N_{max}$. In order to take into account the well known relative convergence phenomenon [24] N_{max} and N_φ have to be chosen together. From an accurate convergence analysis, it has been shown that an excellent compromise between the number of basis functions N_φ and the value of N_{max} can be obtained, for not too small values of α, with $N_\varphi = 3$ and $N_{max} = \lceil 50/\alpha \rceil$ (with α expressed in radians). It can be shown [25] that, N_{max} should be about three times the value of the first zero after the absolute maximum of $\tilde{g}_3(n)$. As an example, Figures 3.11 and 3.12 show the reflection and transmission coefficients (in dB) versus N_{max} with $N_\varphi = 3$, for a slot of aperture $\alpha = 180°$.

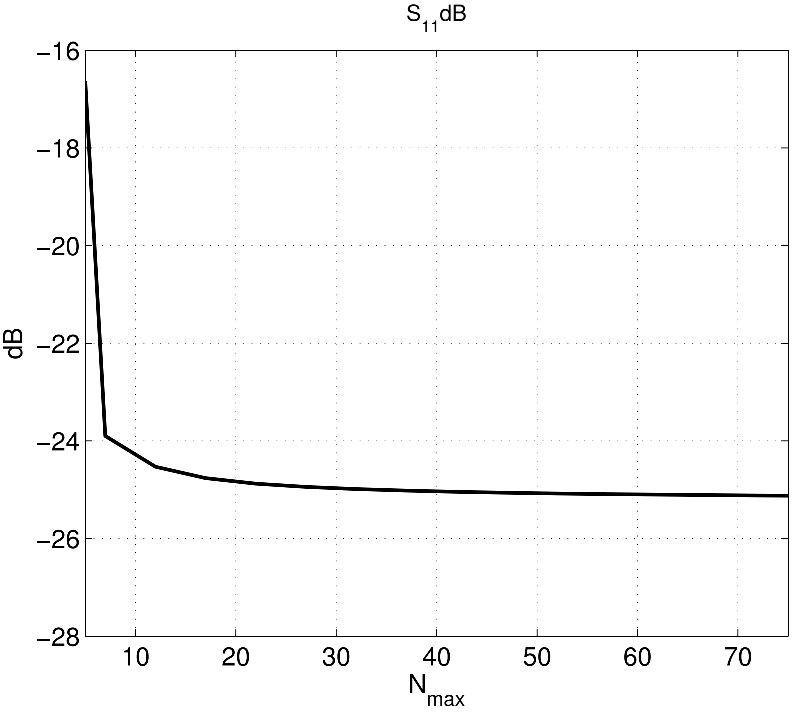

Figure 3.11: Reflection coefficient of an incomplete slot ($\alpha = 180°$) versus the number of terms of the azimuthal series. $N_\varphi = 3$

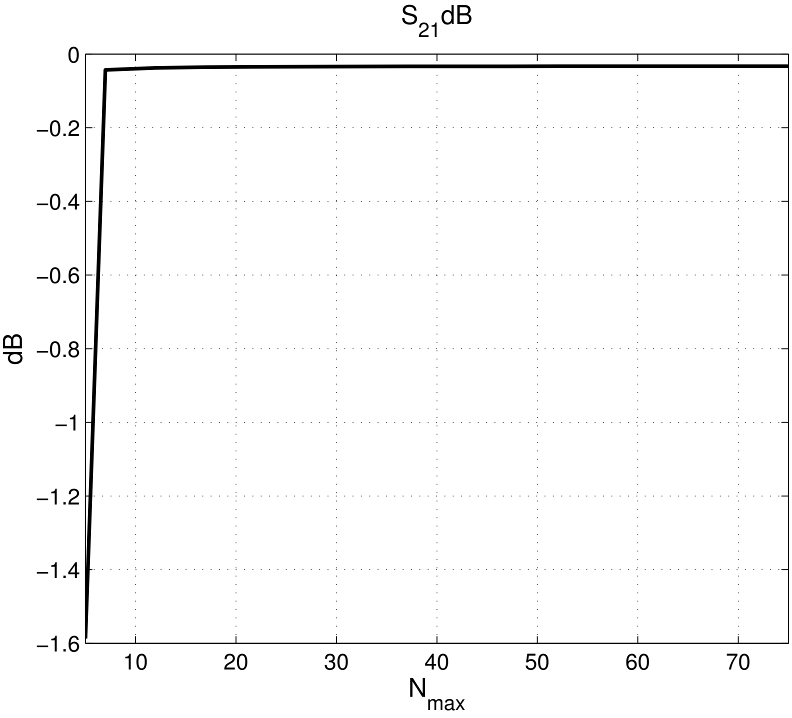

Figure 3.12: Transmission coefficient of an incomplete slot ($\alpha = 180°$) versus the number of terms of the azimuthal series. $N_\varphi = 3$

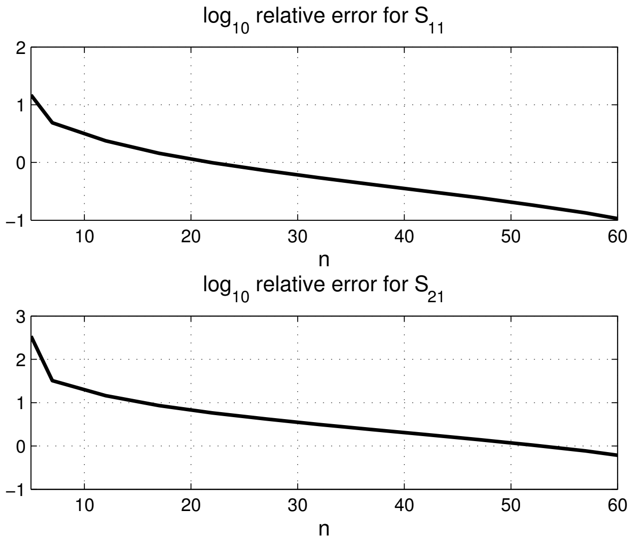

Figure 3.13: $\log_{10}$ of the relative error of the reflection and transmission coefficients versus the number of terms of the azimuthal series. $N_\varphi = 3$

Chapter 4

Slotted Coaxial Cables: Longitudinal Approach

4.1 Introduction

In chapter 3 an integral equation technique for the computation of the radiated and scattered electromagnetic field of a generic LCX has been developed. That formulation is rigorous and the solution is obtained by the Method of Moments in the Galerkin's form directly in the spectral domain where the relative Green function is known in closed form.

One of the main limitation of this technique lies in the size of the linear system needed for a proper representation of the HFIE, which increases linearly with the number of slots. This aspect represents an obstacle to the application of this method to real LCXs, which often cover wide zones and contain thousands of slots. On the other hand, the fact that almost always the slots are identical and arranged in a periodic lattice suggests the use of Bloch wave theory.

The standard approach [26] for the determination of Bloch waves in a periodically loaded closed waveguide consists first in the computation of the scattering matrix $\underline{\underline{S}}$ of the unit cell (see Fig. 4.1 where a and b denote the incident and scattered power waves at the left (port "1") and right (port "2") reference planes of the cell, respectively). Then, the transmission matrix, whose definition is recalled in Fig. 4.2, is computed from $\underline{\underline{S}}$ via the relations:

$$\underline{\underline{T}}_{11} = \underline{\underline{S}}_{21}^{-1} \tag{4.1}$$

$$\underline{\underline{T}}_{12} = -\underline{\underline{S}}_{21}^{-1} \cdot \underline{\underline{S}}_{22} \tag{4.2}$$

$$\underline{\underline{T}}_{21} = \underline{\underline{S}}_{11} \cdot \underline{\underline{S}}_{21}^{-1} \tag{4.3}$$

$$\underline{\underline{T}}_{22} = \underline{\underline{S}}_{12} - \underline{\underline{S}}_{11} \cdot \underline{\underline{S}}_{21}^{-1} \cdot \underline{\underline{S}}_{22} \tag{4.4}$$

Finally, Bloch waves are determined, in the basis of the waveguide modes, as eigenvectors of $\underline{\underline{T}}$,

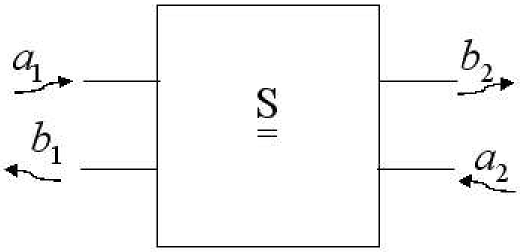

$$\begin{pmatrix} b_1 \\ b_2 \end{pmatrix} = \underline{\underline{S}} \cdot \begin{pmatrix} a_1 \\ a_2 \end{pmatrix} = \begin{pmatrix} S_{11} & S_{12} \\ S_{21} & S_{22} \end{pmatrix} \cdot \begin{pmatrix} a_1 \\ a_2 \end{pmatrix}$$

Figure 4.1: Unit cell of a periodic structure described by the generalized scattering matrix. The standard notation for the power wave amplitudes has been used

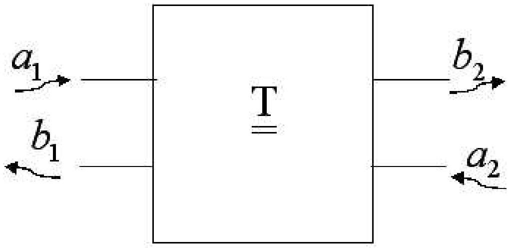

$$\begin{pmatrix} a_1 \\ b_1 \end{pmatrix} = \underline{\underline{T}} \cdot \begin{pmatrix} b_2 \\ a_2 \end{pmatrix} = \begin{pmatrix} T_{11} & T_{12} \\ T_{21} & T_{22} \end{pmatrix} \cdot \begin{pmatrix} b_2 \\ a_2 \end{pmatrix}$$

Figure 4.2: Unit cell of a periodic structure described by the transmission matrix. The standard notation for the power wave amplitudes has been used

whereas the eigenvalues yield the associated phase shifts per cell. This standard approach is not trivial in our case since the discontinuities are inserted in an open waveguide and the modal spectrum of the free space region around the cable is continuous. The unit cell behavior, therefore can not be described by a matrix relation but requires a scattering operator and the computation of the transmission operator requires, as it is evident from (4.1), the inversion of the operator corresponding to $\underline{\underline{S}}_{21}$ and this aspect, as well known, is in general not trivial. The solution of this problem is discussed in this chapter.

In order to simplify the exposition, we will proceed in two steps. First, we will address a problem that is similar to that of LCX but simpler. Essentially, the outer region does not extend to infinity, but is closed by a metal cylinder. In this way the complete modal spectrum is discrete and the difficulty is just that several modes may be above cut-off in the two guides. The goal is to compute the generalized scattering matrix (GSM) of a slot cut in the common wall, for all the modes of interest and not just for those of the (inner) coaxial cable, as in Section 3.3.

Next, the actual problem of an LCX with a single slot is treated. Also in this case the GSM of the slot is computed. As mentioned above, the spectrum of the outer waveguide is continuous and this implies that we have to do with a scattering operator instead of a matrix. Nevertheless, its computation goes more or less along the same lines as in the case of Section 4.2. However, if we want to study the simultaneous presence of two or more slots it becomes computationally necessary to discretize the spectrum of the outer waveguide.

The first idea that comes to mind is just to select a discrete subset of the modal spectrum, composed by a finite number of elements. The method that is actually employed is more refined and is based on the introduction of a set of expansion functions (of the modal index) to represent the modal amplitudes. In this way it becomes possible to compute the GSM of the slot and to exploit the same technique as in Section 4.2. In particular, the Bloch waves of a periodic arrangement of slots are determined and their characteristics analyzed in detail. Once the Bloch spectrum is available, we determine the scattering matrix of the junction between an ordinary coaxial cable and a semi-infinite LCX. This is a result of direct interest also in the case of very long LCX.

Finally, in order to compute the scattering matrix of an LCX consisting of a finite number of periodic cells, we view the structure as a kind of Fabry-Perot interferometer, consisting of two junctions, the first unslotted/slotted, the second slotted/unslotted, separated by a number of cells.

The Bloch wave analysis yields in a natural way the generalized scattering matrix of the array. Two methods can be used for the computation of the radiated field: one is the direct exploitation of the Bloch wave representation, the other passes through the determination of the magnetic currents. Both techniques are discussed in the last section.

4.2 GSM of the coupling slot between two coaxial cables

As an introductory example, let us consider a rectangular aperture which couples two concentric coaxial cables, as shown in Figure 4.3. The radii of the cylinders are denoted by r_1, ρ_2 and r_3. The intermediate cylinder is assumed of negligible thickness and serves as the outer conductor of the inner coaxial and inner conductor of the outer coaxial. The relative permittivities of the two cables are $\varepsilon_{r\,int}$ and $\varepsilon_{r\,ext}$; the width and the angular aperture of the slot are s and α, respectively. Finally, let $z = z_1$ and $z = z_2$ be the left (port "1") and right (port "2") reference planes of the GSM. In this case we have to consider the multimode field incident on the slot along the two different waveguides:

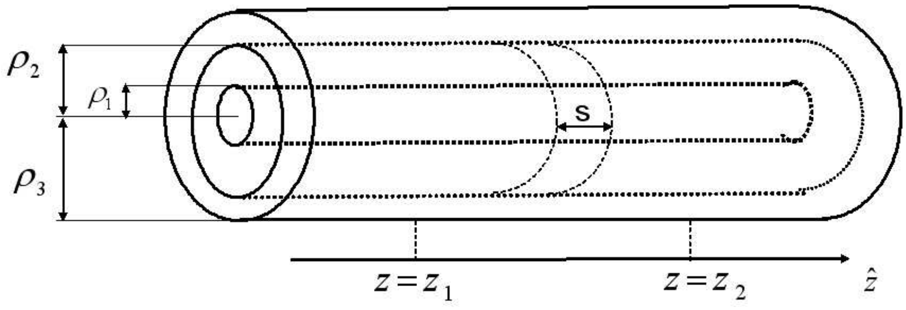

Figure 4.3: Two coaxial cables coupled by an aperture in the common conductor

$$\underline{H}^{\text{inc}}_{tg\,\text{int}}(\rho_2, z, \varphi) = \check{\underline{H}}^{\text{inc}}_{tg\,\text{int}}(\rho_2, z, \varphi) + \hat{\underline{H}}^{\text{inc}}_{tg\,\text{int}}(\rho_2, z, \varphi) \tag{4.5}$$

$$\underline{H}^{\text{inc}}_{tg\,\text{ext}}(\rho_2, z, \varphi) = \check{\underline{H}}^{\text{inc}}_{tg\,\text{ext}}(\rho_2, z, \varphi) + \hat{\underline{H}}^{\text{inc}}_{tg\,\text{ext}}(\rho_2, z, \varphi) \tag{4.6}$$

The subscripts *int* and *ext* will be used to denote the parameters of the internal and external waveguides. This scattering problem can be solved by slightly modifying the formalism developed in chapter 3.

In particular, the expression of the kernel $\underline{\underline{Y}}^{tot}$ of the moment matrix $\underline{\underline{A}}$ is changed since the term $\underline{\underline{Y}}^{ext}$ has to be replaced by the input admittance of a radial line between $\rho = \rho_2$ and $\rho = \rho_3$, loaded by a short circuit in $\rho = \rho_3$, which has already been computed in Section 2.6. The vectors $\check{\underline{B}}$ and $\hat{\underline{B}}$ have to be generalized in order to take into account the fields incident along the two waveguides:

$$\underline{\check{B}} = \underline{\check{B}}_{\,\mathrm{int}} + \underline{\check{B}}_{\,\mathrm{ext}} \tag{4.7}$$

$$\underline{\hat{B}} = \underline{\hat{B}}_{\,\mathrm{int}} + \underline{\hat{B}}_{\,\mathrm{ext}} \tag{4.8}$$

The elements of these vectors are given by expressions identical to (3.17) and (3.18), where the suitable propagation constant, modal admittance and mode eigenfunctions of the two waveguides are used. In compact form, as it has been done in Section 3.2, we obtain:

$$\underline{\check{B}}_{\,\mathrm{int}} = \underline{\underline{U}}^{-+}_{\mathrm{int}} \cdot \underline{\underline{\check{h}}}_{\,\mathrm{int}} \cdot \underline{\underline{Y}}_{\,\infty\ \mathrm{int}} \cdot \underline{\underline{D}}_{\,1\ \mathrm{int}} \cdot \underline{\check{V}}^{\mathrm{inc}}_{\mathrm{int}} \tag{4.9}$$

$$\underline{\hat{B}}_{\,\mathrm{int}} = \underline{\underline{U}}^{++}_{\mathrm{int}} \cdot \underline{\underline{\hat{h}}}_{\,\mathrm{int}} \cdot \underline{\underline{Y}}_{\,\infty\ \mathrm{int}} \cdot \underline{\underline{D}}^{-1}_{2\ \mathrm{int}} \cdot \underline{\hat{V}}^{\mathrm{inc}}_{\mathrm{int}} \tag{4.10}$$

$$\underline{\check{B}}_{\,\mathrm{ext}} = \underline{\underline{U}}^{-+}_{\mathrm{ext}} \cdot \underline{\underline{\check{h}}}_{\,\mathrm{ext}} \cdot \underline{\underline{Y}}_{\,\infty\ \mathrm{ext}} \cdot \underline{\underline{D}}_{\,1\ \mathrm{ext}} \cdot \underline{\check{V}}^{\mathrm{inc}}_{\mathrm{ext}} \tag{4.11}$$

$$\underline{\hat{B}}_{\,\mathrm{ext}} = \underline{\underline{U}}^{++}_{\mathrm{ext}} \cdot \underline{\underline{\hat{h}}}_{\,\mathrm{ext}} \cdot \underline{\underline{Y}}_{\,\infty\ \mathrm{ext}} \cdot \underline{\underline{D}}^{-1}_{2\ \mathrm{ext}} \cdot \underline{\hat{V}}^{\mathrm{inc}}_{\mathrm{ext}} \tag{4.12}$$

Finally, the unknown coefficient vector $\underline{x}$ is given by:

$$\begin{aligned}
\underline{x} &= \underline{\underline{A}}^{-1} \cdot \left[\underline{\check{B}}_{\,\mathrm{int}} + \underline{\check{B}}_{\,\mathrm{ext}} + \underline{\hat{B}}_{\,\mathrm{int}} + \underline{\hat{B}}_{\,\mathrm{ext}}\right] = && (4.13)\\
&= \underline{\underline{\check{C}}}_{\,\mathrm{int}} \cdot \underline{\check{V}}^{\mathrm{inc}}_{\mathrm{int}} + \underline{\underline{\hat{C}}}_{\,\mathrm{int}} \cdot \underline{\hat{V}}^{\mathrm{inc}}_{\mathrm{int}} + \underline{\underline{\check{C}}}_{\,\mathrm{ext}} \cdot \underline{\check{V}}^{\mathrm{inc}}_{\mathrm{ext}} + \underline{\underline{\hat{C}}}_{\,\mathrm{ext}} \cdot \underline{\hat{V}}^{\mathrm{inc}}_{\mathrm{ext}} = \underline{\underline{C}} \cdot \begin{pmatrix} \underline{\check{V}}^{\mathrm{inc}}_{\mathrm{int}} \\ \underline{\check{V}}^{\mathrm{inc}}_{\mathrm{ext}} \\ \underline{\hat{V}}^{\mathrm{inc}}_{\mathrm{int}} \\ \underline{\hat{V}}^{\mathrm{inc}}_{\mathrm{ext}} \end{pmatrix} && (4.14)
\end{aligned}$$

Now the matrix $\underline{\underline{C}}$ has size $2N_f \times 4N_i$ if N_i is the number of modes considered in each waveguide. The scattered voltages can be computed as shown in Section 3.3, the only modification being the sign of the terms, since the magnetic current distributions $\underline{\mathbb{J}}_m$ are equal and opposite in the two wave-guides. The scattered voltages for all the modes (TE and TM), can be written in vector form as:

$$\begin{aligned}
\underline{\check{V}}^{scat}_{\mathrm{int}} &= \frac{1}{2}\underline{\underline{D}}_{\,1\ \mathrm{int}} \cdot \underline{\underline{\hat{h}}}^{*}_{\,\mathrm{int}} \cdot \underline{\underline{W}}_{\mathrm{int}} \cdot (\underline{\underline{U}}^{--}_{\mathrm{int}})^T \cdot \underline{x} = \underline{\underline{\check{M}}}_{\,\mathrm{int}} \cdot \underline{x} && (4.15)\\
\underline{\hat{V}}^{scat}_{\mathrm{int}} &= -\frac{1}{2}\underline{\underline{D}}^{-1}_{2\ \mathrm{int}} \cdot \underline{\underline{\check{h}}}^{*}_{\,\mathrm{int}} \cdot \underline{\underline{W}}_{\mathrm{int}} \cdot (\underline{\underline{U}}^{--}_{\mathrm{int}})^T \cdot \underline{x} = \underline{\underline{\hat{M}}}_{\,\mathrm{int}} \cdot \underline{x} && (4.16)\\
\underline{\check{V}}^{scat}_{\mathrm{ext}} &= -\frac{1}{2}\underline{\underline{D}}_{\,1\ \mathrm{ext}} \cdot \underline{\underline{\hat{h}}}^{*}_{\,\mathrm{ext}} \cdot \underline{\underline{W}}_{\mathrm{ext}} \cdot (\underline{\underline{U}}^{--}_{\mathrm{ext}})^T \cdot \underline{x} = \underline{\underline{\check{M}}}_{\,\mathrm{ext}} \cdot \underline{x} && (4.17)\\
\underline{\hat{V}}^{scat}_{\mathrm{ext}} &= \frac{1}{2}\underline{\underline{D}}^{-1}_{2\ \mathrm{ext}} \cdot \underline{\underline{\check{h}}}^{*}_{\,\mathrm{ext}} \cdot \underline{\underline{W}}_{\mathrm{ext}} \cdot (\underline{\underline{U}}^{--}_{\mathrm{ext}})^T \cdot \underline{x} = \underline{\underline{\hat{M}}}_{\,\mathrm{ext}} \cdot \underline{x} && (4.18)
\end{aligned}$$

where the $N_{\,\mathrm{int}} \times N_f$ matrices $\underline{\underline{\check{M}}}_{\,\mathrm{int}}$, $\underline{\underline{\hat{M}}}_{\,\mathrm{int}}$, $\underline{\underline{\check{M}}}_{\,\mathrm{ext}}$ and $\underline{\underline{\hat{M}}}_{\,\mathrm{ext}}$ represent the operator which relates the magnetic current on the slot to the scattered voltages. Furthermore, the dyadics $\underline{\underline{W}}_{\mathrm{int}}$ and $\underline{\underline{W}}_{\mathrm{ext}}$ are defined by

$$\begin{aligned}\underline{\underline{W}}^{\,\mathrm{int}} &= \mathrm{diag}\{W_r^{\,\mathrm{int}}\}\\ \underline{\underline{W}}^{\,\mathrm{ext}} &= \mathrm{diag}\{W_r^{\,\mathrm{ext}}\}\end{aligned}$$

where:

$$\begin{aligned}W^{\,\mathrm{int}}|_r &= \hat{\varphi}\hat{\varphi} + \left(\frac{k^*_{z\,\mathrm{int}}(r)}{k_{z\,\mathrm{int}}(r)}\right)\hat{z}\hat{z}\\ W^{\,\mathrm{ext}}|_r &= \hat{\varphi}\hat{\varphi} + \left(\frac{k^*_{z\,\mathrm{ext}}(r)}{k_{z\,\mathrm{ext}}(r)}\right)\hat{z}\hat{z}\end{aligned}$$

By introducing power waves to describe the incident and scattered mode amplitudes via the usual normalization:

$$\begin{aligned}\underline{a}_1 &= \begin{pmatrix}\underline{\underline{Y}}^{-1/2}_{\infty\ \mathrm{int}} \cdot \underline{\check{V}}^{\mathrm{inc}}_{\mathrm{int}}\\ \underline{\underline{Y}}^{-1/2}_{\infty\ \mathrm{ext}} \cdot \underline{\check{V}}^{\mathrm{inc}}_{\mathrm{ext}}\end{pmatrix} & \underline{a}_2 &= \begin{pmatrix}\underline{\underline{Y}}^{-1/2}_{\infty\ \mathrm{int}} \cdot \underline{\hat{V}}^{\mathrm{inc}}_{\mathrm{int}}\\ \underline{\underline{Y}}^{-1/2}_{\infty\ \mathrm{ext}} \cdot \underline{\hat{V}}^{\mathrm{inc}}_{\mathrm{ext}}\end{pmatrix}\\ \underline{b}_1 &= \begin{pmatrix}\underline{\underline{Y}}^{-1/2}_{\infty\ \mathrm{int}} \cdot \underline{\check{V}}^{scat}_{\mathrm{int}}\\ \underline{\underline{Y}}^{-1/2}_{\infty\ \mathrm{ext}} \cdot \underline{\check{V}}^{scat}_{\mathrm{ext}}\end{pmatrix} & \underline{b}_2 &= \begin{pmatrix}\underline{\underline{Y}}^{-1/2}_{\infty\ \mathrm{int}} \cdot \underline{\hat{V}}^{scat}_{\mathrm{int}}\\ \underline{\underline{Y}}^{-1/2}_{\infty\ \mathrm{ext}} \cdot \underline{\hat{V}}^{scat}_{\mathrm{ext}}\end{pmatrix}\end{aligned} \tag{4.19}$$

we obtain the scattering matrix of the device (with respect to the cable modes):

$$\begin{pmatrix}\underline{b}_1\\ \underline{b}_2\end{pmatrix} = \begin{pmatrix}\underline{\underline{S}}_{\,11} & \underline{\underline{S}}_{\,12}\\ \underline{\underline{S}}_{\,21} & \underline{\underline{S}}_{\,22}\end{pmatrix} \cdot \begin{pmatrix}\underline{a}_1\\ \underline{a}_2\end{pmatrix} \tag{4.20}$$

where the submatrices have the following expressions:

$$\underline{\underline{S}}_{11} = \begin{pmatrix} \underline{\underline{Y}}^{1/2}_{\infty\,\mathrm{int}} \cdot \underline{\underline{\check{M}}}_{\mathrm{int}} \cdot \underline{\underline{\check{C}}}_{\mathrm{int}} \cdot \underline{\underline{Y}}^{-1/2}_{\infty\,\mathrm{int}} & \underline{\underline{Y}}^{1/2}_{\infty\,\mathrm{int}} \cdot \underline{\underline{\check{M}}}_{\mathrm{int}} \cdot \underline{\underline{\check{C}}}_{\mathrm{ext}} \cdot \underline{\underline{Y}}^{-1/2}_{\infty\,\mathrm{ext}} \\ \underline{\underline{Y}}^{1/2}_{\infty\,\mathrm{ext}} \cdot \underline{\underline{\check{M}}}_{\mathrm{ext}} \cdot \underline{\underline{\check{C}}}_{\mathrm{int}} \cdot \underline{\underline{Y}}^{-1/2}_{\infty\,\mathrm{int}} & \underline{\underline{Y}}^{1/2}_{\infty\,\mathrm{ext}} \cdot \underline{\underline{\check{M}}}_{\mathrm{ext}} \cdot \underline{\underline{\check{C}}}_{\mathrm{ext}} \cdot \underline{\underline{Y}}^{-1/2}_{\infty\,\mathrm{ext}} \end{pmatrix}$$

$$\underline{\underline{S}}_{12} = \begin{pmatrix} \underline{\underline{Y}}^{1/2}_{\infty\,\mathrm{int}} \cdot \underline{\underline{\check{M}}}_{\mathrm{int}} \cdot \underline{\underline{\hat{C}}}_{\mathrm{int}} \cdot \underline{\underline{Y}}^{-1/2}_{\infty\,\mathrm{int}} + \underline{\underline{F}}_{\mathrm{int}} & \underline{\underline{Y}}^{1/2}_{\infty\,\mathrm{int}} \cdot \underline{\underline{\check{M}}}_{\mathrm{int}} \cdot \underline{\underline{\hat{C}}}_{\mathrm{ext}} \cdot \underline{\underline{Y}}^{-1/2}_{\infty\,\mathrm{ext}} \\ \underline{\underline{Y}}^{1/2}_{\infty\,\mathrm{ext}} \cdot \underline{\underline{\check{M}}}_{\mathrm{ext}} \cdot \underline{\underline{\hat{C}}}_{\mathrm{int}} \cdot \underline{\underline{Y}}^{-1/2}_{\infty\,\mathrm{int}} & \underline{\underline{Y}}^{1/2}_{\infty\,\mathrm{ext}} \cdot \underline{\underline{\check{M}}}_{\mathrm{ext}} \cdot \underline{\underline{Y}}^{-1/2}_{\infty\,\mathrm{ext}} + \underline{\underline{F}}_{\mathrm{ext}} \end{pmatrix}$$

$$\underline{\underline{S}}_{21} = \begin{pmatrix} \underline{\underline{Y}}^{1/2}_{\infty\,\mathrm{int}} \cdot \underline{\underline{\hat{M}}}_{\mathrm{int}} \cdot \underline{\underline{\check{C}}}_{\mathrm{int}} \cdot \underline{\underline{Y}}^{-1/2}_{\infty\,\mathrm{int}} + \underline{\underline{F}}_{\mathrm{int}} & \underline{\underline{Y}}^{1/2}_{\infty\,\mathrm{int}} \cdot \underline{\underline{\hat{M}}}_{\mathrm{int}} \cdot \underline{\underline{\check{C}}}_{\mathrm{ext}} \cdot \underline{\underline{Y}}^{-1/2}_{\infty\,\mathrm{ext}} \\ \underline{\underline{Y}}^{1/2}_{\infty\,\mathrm{ext}} \cdot \underline{\underline{\hat{M}}}_{\mathrm{ext}} \cdot \underline{\underline{\check{C}}}_{\mathrm{int}} \cdot \underline{\underline{Y}}^{-1/2}_{\infty\,\mathrm{int}} & \underline{\underline{Y}}^{1/2}_{\infty\,\mathrm{ext}} \cdot \underline{\underline{\hat{M}}}_{\mathrm{ext}} \cdot \underline{\underline{\check{C}}}_{\mathrm{ext}} \cdot \underline{\underline{Y}}^{-1/2}_{\infty\,\mathrm{ext}} + \underline{\underline{F}}_{\mathrm{ext}} \end{pmatrix}$$

$$\underline{\underline{S}}_{22} = \begin{pmatrix} \underline{\underline{Y}}^{1/2}_{\infty\,\mathrm{int}} \cdot \underline{\underline{\hat{M}}}_{\mathrm{int}} \cdot \underline{\underline{\hat{C}}}_{\mathrm{int}} \cdot \underline{\underline{Y}}^{-1/2}_{\infty\,\mathrm{int}} & \underline{\underline{Y}}^{1/2}_{\infty\,\mathrm{int}} \cdot \underline{\underline{\hat{M}}}_{\mathrm{int}} \cdot \underline{\underline{\hat{C}}}_{\mathrm{ext}} \cdot \underline{\underline{Y}}^{-1/2}_{\infty\,\mathrm{ext}} \\ \underline{\underline{Y}}^{1/2}_{\infty\,\mathrm{ext}} \cdot \underline{\underline{\hat{M}}}_{\mathrm{ext}} \cdot \underline{\underline{\hat{C}}}_{\mathrm{int}} \cdot \underline{\underline{Y}}^{-1/2}_{\infty\,\mathrm{int}} & \underline{\underline{Y}}^{1/2}_{\infty\,\mathrm{ext}} \cdot \underline{\underline{\hat{M}}}_{\mathrm{ext}} \cdot \underline{\underline{\hat{C}}}_{\mathrm{ext}} \cdot \underline{\underline{Y}}^{-1/2}_{\infty\,\mathrm{ext}} \end{pmatrix}$$

The $N_{\mathrm{int}} \times N_{\mathrm{int}}$ matrices $\underline{\underline{F}}_{\mathrm{int}}$ and $\underline{\underline{F}}_{\mathrm{ext}}$ represent the direct contribution of the incident voltages:

$$\underline{\underline{F}}_{\mathrm{int}} = \underline{\underline{D}}^{-1}_{2\,\mathrm{int}} \cdot \underline{\underline{D}}_{1\,\mathrm{int}}$$

$$\underline{\underline{F}}_{\mathrm{ext}} = \underline{\underline{D}}^{-1}_{2\,\mathrm{ext}} \cdot \underline{\underline{D}}_{1\,\mathrm{ext}}$$

It can be proved algebraically that, if the metallic and dielectric losses are neglected, the scattering matrix referring to the above-cut-off modes in the two waveguides (possibly only the two TEM modes) is unitary. This property depends neither on the number of expansion functions used nor on the number of azimuthal harmonics taken into account. Moreover, the scattering matrix is symmetric since the structure is reciprocal and the mode eigenfunctions are real.

Suppose now that the two coaxial cables are coupled through N_{slot} apertures. Since the scattering matrix of each slot can be computed as described above, the response of the complete structure can be obtained by the well known cascading procedure [12]. In the application of this method it is useful to recall the concept of localized and accessible modes [27]: when two discontinuities in a waveguide are cascaded, they interact via propagating and evanescent modes. The modes whose attenuation over the distance between the two discontinuities is smaller than a predefined threshold are called *accessible*, the others *localized*. Clearly, only the accessible modes are considered in the cascading, which implies that fairly small matrices need to be manipulated.

4.3 GSM of a radiating slot in a coaxial cable

Let us consider now the case of a slotted coaxial cable with a single aperture. The dielectric cover of the coaxial outer conductor will be neglected for simplicity. For the reader convenience a picture of the structure is shown in Fig. 4.4 where s is the slot width, L is the period of the unit cell and the radii of the inner and outer conductor are denoted by ρ_1 and ρ_2, respectively. The left and right reference planes of the unit cell are $z = -L/2$ and $z = L/2$, respectively.

Applying the same approach of the preceding paragraph the aperture is considered as coupling element between two coaxial waveguides. The first one is the actual coaxial cable, the second one is the free space region surrounding the outer conductor of the cable. This is an open waveguide, *i.e.* its cross section Σ is infinite[1]. Since the dielectric is homogeneous, its modal spectrum is continuous [8], and the expressions of the mode eigenfunctions are listed in Table 4.1 where the modes are labelled by the continuous index $\tau \in (0, \infty)$ and the integer m.

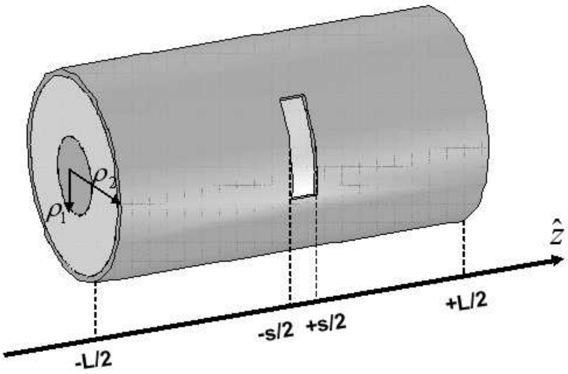

Figure 4.4: Unit cell of a periodic structure of period L, the slot width is s

---

[1] $\Sigma = \{(\rho, \varphi)$ with $\rho > \rho_2$ and $\varphi \in [0, 2\pi]\}$

Clearly these modes satisfy the orthonormality condition which, in this case, assumes the following form:

$$< \underline{e}(\tau, m),\, \underline{h}(\tau', m') \times \hat{z} >= \int_0^{2\pi} \int_{\rho_2}^{\infty} \underline{e}(\rho, \varphi; \tau, m) \cdot \underline{h}^*(\rho, \varphi; \tau', m') \times \hat{z}\, \rho d\rho d\varphi = \delta(\tau - \tau')\delta_{mm'} \tag{4.21}$$

In order to distinguish the modes of the two different waveguides we will use the subscripts " int" and " ext", for the internal and external ones, respectively. It is important to remark that, since the modes of the external guide have a continuous spectrum, the total field for $\rho > \rho_2$ is given by an integral superposition instead of a standard sum. For example, the φ component of the magnetic field is given by:

$$H_\varphi(\rho > \rho_2, \varphi, z) = \sum_{m=-\infty}^{\infty} \int_0^{\infty} I_{\,\mathrm{ext}}(z; \tau,\, m)\, h_{\varphi\,\mathrm{ext}}(\rho, \varphi; \tau, m) d\tau$$

where $I_{\,\mathrm{ext}}(z; \tau,\, m)$ is the current coefficient in the section z for the $(\tau,\, m)$ mode.

We derive now the scattering characteristics of the slot, generalizing the formalism developed in Sections 3.2 and 4.2. Due to the symmetry of the structure, here we consider only the incidence from the left reference plane. Moreover since the incidence from the cable has already been discussed in Section 4.2, here we will focus on the multimode field of the external waveguide incident on the slot.

The tangential incident magnetic field on the wall can be expressed as:

$$\underline{H}^{inc}_{\mathrm{ext}\,tg}(\rho_2, z, \varphi) = \int_0^{\infty} \sum_{m'} Y_{\infty\,\mathrm{ext}}(\tau', m')\, \check{V}^{inc}_{\mathrm{ext}}(\,\tau', m')\, \mathrm{e}^{-j\beta(\tau')(z+L/2)}\, \check{\underline{h}}^{tg}_{\mathrm{ext}}(b; \tau', m') \mathrm{e}^{j\, m'\varphi} d\tau' \tag{4.22}$$

where $\beta(\tau') = \sqrt{k_0^2 - \tau'^2}$ and $Y_{\infty\,\mathrm{ext}}(\tau', m')$, are the propagation constant and modal admittance of the mode (τ', m') of the external waveguide, while $\check{V}^{inc}_{\mathrm{ext}}(z = -L/2; \tau', m')$ is the corresponding incident voltage on the left ($z = -L/2$) reference plane of the structure.

Let us compute the right hand side of the linear system and in particular the matrix $\hat{\underline{B}}_{\,\mathrm{ext}}$ of (4.14), while, obviously, the terms $\underline{B}_{\,\mathrm{int}}$ coincide with (3.17) and (3.18). The explicit expression of the r-th element of $\hat{\underline{B}}_{\,\mathrm{ext}}$ is:

$$\begin{aligned}
\check{B}_{\,\mathrm{ext}}\big|_{\,r} &= < \left(\check{\underline{H}}^{inc}_{\mathrm{ext}} \times \hat{\rho}\right), \underline{u}_r >= \\
&= \int_0^{\infty} \sum_{m'} Y_{\infty\,\mathrm{ext}}(\tau', m') \check{V}^{inc}_{\mathrm{ext}}(z_1; \tau', m') \mathrm{e}^{j\beta(\tau')z_1} \left(\check{\underline{h}}^{tg}_{\mathrm{ext}}(b; \tau', m') \times \hat{\rho}\right) \cdot \tilde{\underline{u}}^*_r(-\beta(\tau'), m') d\tau'
\end{aligned}$$

This expression can be written more concisely applying a matrix formalism as it has been done for the internal ones. In fact, define the $N_m \times N_m$ diagonal matrices:

$$\underline{\underline{D}}_{\,\mathrm{ext}}(\tau) = \mathrm{diag}\left\{\mathrm{e}^{-j\,\beta(\tau)\,L/2}\right\} \tag{4.23}$$

$$\underline{\underline{Y}}_{\,\infty\,\mathrm{ext}}(\tau) = \mathrm{diag}\left\{Y_{\infty\,\mathrm{ext}}(\tau, m)\right\} \tag{4.24}$$

$$\underline{\underline{\check{h}}}_{\,\mathrm{ext}}(\tau) = \mathrm{diag}\left\{\underline{\check{h}}^{tg}_{\mathrm{ext}}(b; \tau, m) \times \hat{\rho}\right\} \tag{4.25}$$

and the $N_m \times N_f$ full matrices $\underline{\underline{U}}^{-+}$, $\underline{\underline{U}}^{++}$ with elements:

$$U^{--}_{\mathrm{ext}}|_{\,r,c}(\tau) = \underline{\tilde{u}}_r(-\beta(\tau), -m(c)) \tag{4.26}$$

$$U^{-+}_{\mathrm{ext}}|_{\,r,c}(\tau) = \underline{\tilde{u}}_r(-\beta(\tau), +m(c)) \tag{4.27}$$

$$U^{+-}_{\mathrm{ext}}|_{\,r,c}(\tau) = \underline{\tilde{u}}_r(+\beta(\tau), -m(c)) \tag{4.28}$$

$$U^{++}_{\mathrm{ext}}|_{\,r,c}(\tau) = \underline{\tilde{u}}_r(+\beta(\tau), +m(c)) \tag{4.29}$$

where N_m represents the number of azimuthal harmonics[2]. Note that the elements of these matrices are not numbers but functions of the variable τ. The addressing function $m(c)$ is necessary because $m \in \mathbb{Z}$ and c is used both for modal and column index. Using this notation, the known term of the linear system can be expressed as:

$$\underline{\check{B}}_{\mathrm{ext}} = \int_0^{\infty} \left(\underline{\underline{U}}^{-+}_{\mathrm{ext}}(\tau')\right)^{*} \cdot \underline{\underline{\check{h}}}_{\,\mathrm{ext}}(\tau') \cdot \underline{\underline{Y}}_{\,\infty\,\mathrm{ext}}(\tau') \cdot \underline{\underline{D}}_{\,\mathrm{ext}}(\tau') \cdot \underline{\check{V}}_{\mathrm{ext}}(\tau')\, d\tau' \tag{4.30}$$

The amplitudes of the incident modes (TE and TM) have been grouped in the vector $\underline{\check{V}}_{\,\mathrm{ext}}(\tau')$. The vector $\underline{x}$ of unknown coefficients, solution of the linear system, is given by:

$$\underline{x} = \underline{\underline{A}}^{-1} \cdot \left[\underline{\check{B}}_{\mathrm{int}} + \underline{\check{B}}_{\mathrm{ext}}\right] = \underline{\underline{\check{C}}}_{\mathrm{int}} \cdot \underline{\check{V}}^{inc}_{\mathrm{int}} + \int_0^{\infty} \underline{\underline{\check{C}}}_{\mathrm{ext}}(\tau') \cdot \underline{\check{V}}^{inc}_{\mathrm{ext}}(\tau') d\tau' \tag{4.31}$$

The size of $\underline{\underline{\check{C}}}_{\mathrm{int}}$ is $N_f \times N_i$, while that of $\underline{\underline{\check{C}}}_{\mathrm{ext}}(\tau')$ is $N_f \times N_m$.

Once the linear system is solved, the scattered voltages at the reference planes can be computed as shown in the Sections 3.3 and 4.2. In this case, one obtains:

---

[2] i.e. $m = [-N_m/2 + 1, N_m/2]$

$$\begin{aligned}
\check{V}^{scat}_{\text{ext}}(\tau,\, m) \;&=\; -\frac{1}{2}\,\mathrm{e}^{-j\beta(\tau)\,L/2}\sum_{c=1}^{N_f} x_c\left[h^*_{\varphi\,\text{ext}}(b;\tau,\, m)\hat{\varphi}\cdot\underline{\tilde{u}}_c(-\beta(\tau),-m)+\right.\\
&\left.-Z_{\infty\,\text{ext}}(\tau,m)Y^*_{\infty\,\text{ext}}(\tau,m)\,h^*_{z\,\text{ext}}(b;\tau,\, m)\,\hat{z}\cdot\underline{\tilde{u}}_c(-\beta(\tau),-m)\right]
\end{aligned}$$

$$\begin{aligned}
\hat{V}^{scat}_{\text{ext}}(\tau,\, m) \;&=\; +\frac{1}{2}\mathrm{e}^{-j\beta(\tau)L/2}\sum_{c=1}^{N_f} x_c\left[-h^*_{\varphi\,\text{ext}}(b;\tau,\, m)\hat{\varphi}\cdot\underline{\tilde{u}}_c(+\beta(\tau),-m)+\right.\\
&\left.+Z_{\infty\,\text{ext}}(\tau,m)Y^*_{\infty\,\text{ext}}(\tau,m)\,h^*_{z\,\text{ext}}(b;\tau,\, m)\hat{z}\cdot\underline{\tilde{u}}_c(+\beta(\tau),-m)\right]
\end{aligned}$$

In matrix form:

$$\underline{\check{V}}^{scat}_{\text{ext}}(\tau) \;=\; -\frac{1}{2}\,\underline{\underline{D}}_{\text{ext}}(\tau)\cdot\underline{\underline{\hat{h}}}^*_{\text{ext}}(\tau)\cdot\underline{\underline{W}}_{\text{ext}}(\tau)\cdot(\underline{\underline{U}}^{--}_{\text{ext}}(\tau))^T\cdot\underline{x} \tag{4.32}$$

$$\underline{\hat{V}}^{scat}_{\text{ext}}(\tau) \;=\; +\frac{1}{2}\,\underline{\underline{D}}_{\text{ext}}(\tau)\cdot\underline{\underline{\check{h}}}^*_{\text{ext}}(\tau)\cdot\underline{\underline{W}}_{\text{ext}}(\tau)\cdot(\underline{\underline{U}}^{+-}_{\text{ext}}(\tau))^T\cdot\underline{x} \tag{4.33}$$

where the dyadic $\underline{\underline{W}}_{\text{ext}}$ is defined by

$$\underline{\underline{W}}_{\text{ext}}(\tau) \;=\; \hat{\varphi}\hat{\varphi}+\left(\frac{\beta(\tau)^*}{\beta(\tau)}\right)\hat{z}\hat{z}$$

Combining (3.33), (3.34), (4.31), (4.32) and (4.33) we obtain the scattered voltages as a function of the incident ones:

$$\begin{aligned}
\underline{\check{V}}^{scat}_{\text{int}} \;&=\; \underline{\underline{\check{M}}}_{\text{int}}\cdot\left[\underline{\underline{\check{C}}}_{\text{int}}\cdot\underline{\check{V}}^{inc}_{\text{int}}+\int_0^\infty\underline{\underline{\check{C}}}_{\text{ext}}(\tau')\cdot\underline{\check{V}}^{inc}_{\text{ext}}(\tau')\,d\tau'\right]\\
\underline{\hat{V}}^{scat}_{\text{int}} \;&=\; \underline{\underline{\hat{M}}}_{\text{int}}\cdot\left[\underline{\underline{\check{C}}}_{\text{int}}\cdot\underline{\check{V}}^{inc}_{\text{int}}+\int_0^\infty\underline{\underline{\check{C}}}_{\text{ext}}(\tau')\cdot\underline{\check{V}}^{inc}_{\text{ext}}(\tau')\,d\tau'\right]\\
\underline{\check{V}}^{scat}_{\text{ext}}(\tau) \;&=\; \underline{\underline{\check{M}}}_{\text{ext}}(\tau)\cdot\left[\underline{\underline{\check{C}}}_{\text{int}}\cdot\underline{\check{V}}^{inc}_{\text{int}}+\int_0^\infty\underline{\underline{\check{C}}}_{\text{ext}}(\tau')\cdot\underline{\check{V}}^{inc}_{\text{ext}}(\tau')\,d\tau'\right]\\
\underline{\hat{V}}^{scat}_{\text{ext}}(\tau) \;&=\; \underline{\underline{\hat{M}}}_{\text{ext}}(\tau)\cdot\left[\underline{\underline{\check{C}}}_{\text{int}}\cdot\underline{\check{V}}^{inc}_{\text{int}}+\int_0^\infty\underline{\underline{\check{C}}}_{\text{ext}}(\tau')\cdot\underline{\check{V}}^{inc}_{\text{ext}}(\tau')\,d\tau'\right]
\end{aligned}$$

where the matrices:

$$\underline{\underline{\check{M}}}_{\text{int}} \;=\; \frac{1}{2}\,\underline{\underline{D}}_{\text{int}}\cdot\underline{\underline{\check{h}}}^*_{\text{int}}\cdot\underline{\underline{W}}_{\text{int}}\cdot(\underline{\underline{U}}^{--}_{\text{int}})^T \tag{4.34}$$

$$\underline{\underline{\hat{M}}}_{\text{int}} \;=\; -\frac{1}{2}\,\underline{\underline{D}}^{-1}_{\text{int}}\cdot\underline{\underline{\hat{h}}}^*_{\text{int}}\cdot\underline{\underline{W}}_{\text{int}}\cdot(\underline{\underline{U}}^{+-}_{\text{int}})^T \tag{4.35}$$

$$\underline{\underline{\check{M}}}_{\text{ext}}(\tau) \;=\; -\frac{1}{2}\underline{\underline{D}}_{\text{ext}}(\tau)\cdot\underline{\underline{\check{h}}}^*_{\text{ext}}(\tau)\cdot\underline{\underline{W}}_{\text{ext}}(\tau)\cdot(\underline{\underline{U}}^{--}_{\text{ext}}(\tau))^T \tag{4.36}$$

$$\underline{\underline{\hat{M}}}_{\text{ext}}(\tau) \;=\; \frac{1}{2}\underline{\underline{D}}_{\text{ext}}(\tau)\cdot\underline{\underline{\hat{h}}}^*_{\text{ext}}(\tau)\cdot\underline{\underline{W}}_{\text{ext}}(\tau)\cdot(\underline{\underline{U}}^{+-}_{\text{ext}}(\tau))^T \tag{4.37}$$

represent, physically, the linear operators that relate the equivalent magnetic current distributions to the scattered mode voltages. Their dimensions are $N_i \times N_f$ and $N_m \times N_f$ for $\check{\underline{\underline{M}}}_{\text{int}}$, $\hat{\underline{\underline{M}}}_{\text{int}}$ and $\check{\underline{\underline{M}}}_{\text{ext}}(\tau)$, $\hat{\underline{\underline{M}}}_{\text{ext}}(\tau)$, respectively.

By introducing power waves to describe the incident and scattered mode amplitudes via the usual normalization:

$$\begin{array}{ll} \check{\underline{a}}_{\text{int}} = \underline{\underline{Y}}^{1/2}_{\infty\,\text{int}} \cdot \check{\underline{V}}^{\text{inc}}_{\text{int}} & \check{\underline{a}}_{\text{ext}}(\tau) = \underline{\underline{Y}}^{1/2}_{\infty\,\text{ext}}(\tau) \cdot \check{\underline{V}}^{\text{inc}}_{\text{ext}}(\tau) \\ \check{\underline{b}}_{\text{int}} = \underline{\underline{Y}}^{1/2}_{\infty\,\text{int}} \cdot \check{\underline{V}}^{\text{scat}}_{\text{int}} & \hat{\underline{b}}_{\text{int}} = \underline{\underline{Y}}^{1/2}_{\infty\,\text{int}} \cdot \hat{\underline{V}}^{\text{scat}}_{\text{int}} \\ \check{\underline{b}}_{\text{ext}}(\tau) = \underline{\underline{Y}}^{1/2}_{\infty\,\text{ext}}(\tau) \cdot \check{\underline{V}}^{\text{scat}}_{\text{ext}}(\tau) & \hat{\underline{b}}_{\text{ext}}(\tau) = \underline{\underline{Y}}^{1/2}_{\infty\,\text{ext}}(\tau) \cdot \hat{\underline{V}}^{\text{scat}}_{\text{ext}}(\tau) \end{array} \tag{4.38}$$

we obtain:

$$\check{\underline{b}}_{\text{int}} = \check{\underline{\underline{M}}}_{\text{int}} \cdot \check{\underline{\underline{C}}}_{\text{int}} \cdot \check{\underline{a}}_{\text{int}} + \underline{\underline{Y}}^{1/2}_{\infty\,\text{int}} \cdot \check{\underline{\underline{M}}}_{\text{int}} \cdot \int_0^\infty \check{\underline{\underline{C}}}_{\text{ext}}(\tau') \cdot \underline{\underline{Y}}^{-1/2}_{\infty\,\text{ext}}(\tau') \cdot \check{\underline{a}}_{\text{ext}}(\tau')\, d\tau' \tag{4.39}$$

$$\hat{\underline{b}}_{\text{int}} = \left(\hat{\underline{\underline{M}}}_{\text{int}} \cdot \check{\underline{\underline{C}}}_{\text{int}} + \underline{\underline{F}}_{\text{int}}\right) \cdot \check{\underline{a}}_{\text{int}} + \underline{\underline{Y}}^{1/2}_{\infty\,\text{int}} \cdot \hat{\underline{\underline{M}}}_{\text{int}} \cdot \int_0^\infty \check{\underline{\underline{C}}}_{\text{ext}}(\tau') \cdot \underline{\underline{Y}}^{-1/2}_{\infty\,\text{ext}}(\tau') \cdot \check{\underline{a}}_{\text{ext}}(\tau')\, d\tau' \tag{4.40}$$

$$\check{\underline{b}}_{\text{ext}}(\tau) = \underline{\underline{Y}}^{1/2}_{\infty\,\text{ext}}(\tau) \cdot \check{\underline{\underline{M}}}_{\text{ext}}(\tau) \cdot \left(\check{\underline{\underline{C}}}_{\text{int}} \cdot \underline{\underline{Y}}^{-1/2}_{\infty\,\text{int}} \cdot \check{\underline{a}}_{\text{int}} + \int_0^\infty \check{\underline{\underline{C}}}_{\text{ext}}(\tau') \cdot \underline{\underline{Y}}^{-1/2}_{\infty\,\text{ext}}(\tau') \check{\underline{a}}_{\text{ext}}(\tau')\, d\tau'\right) \tag{4.41}$$

$$\begin{aligned} \hat{\underline{b}}_{\text{ext}}(\tau) &= \underline{\underline{Y}}^{1/2}_{\infty\,\text{ext}}(\tau) \cdot \hat{\underline{\underline{M}}}_{\text{ext}}(\tau) \cdot \left(\check{\underline{\underline{C}}}_{\text{int}} \cdot \underline{\underline{Y}}^{-1/2}_{\infty\,\text{int}} \cdot \check{\underline{a}}_{\text{int}} + \int_0^\infty \check{\underline{\underline{C}}}_{\text{ext}}(\tau') \cdot \underline{\underline{Y}}^{-1/2}_{\infty\,\text{ext}}(\tau') \cdot \check{\underline{a}}_{\text{ext}}(\tau')\, d\tau'\right) + \\ &+ \underline{\underline{F}}_{\text{ext}}(\tau) \cdot \check{\underline{a}}_{\text{ext}}(\tau) \end{aligned} \tag{4.42}$$

where the matrices $\underline{\underline{F}}_{\text{int}}$ (with size $N_{\text{int}} \times N_{\text{int}}$) and $\underline{\underline{F}}_{\text{ext}}(\tau)$ (with size $N_m \times N_m$) take into account the direct contribution of the incident voltages and are defined by:

$$\begin{aligned} \underline{\underline{F}}_{\text{int}} &= \text{diag}\{e^{-jk_{z\,\text{int}}(c)L}\} \\ \underline{\underline{F}}_{\text{ext}}(\tau) &= \text{diag}\{e^{-j\beta(\tau)L}\} \end{aligned}$$

It can be noted from (4.39), (4.40), (4.41) and (4.42) that, due to the continuous spectrum of the external modes, the incident and scattered power waves are not related by a matrix relation, but by an integral operator. Hence, even the determination of the transmission operator is complicated because it requires the solution of an integral equation. It is clearly necessary to adopt a numerical technique, based on a discretization of the spectrum.

The easiest approach could be to define a grid of points τ_q in the range $0 < \tau_q < \infty$ and then to consider only the corresponding modes. To give a sounder physical background, we could select the τ_q coincident with the cut-off wave-numbers of a virtual coaxial cable, with inner conductor of radius b and outer conductor of very large radius R. It is clear, however, that it is contradictory to model free-space by a box, and moreover, the number of modes to be taken into account could be impractical if the outer radius R is very large.

We follow therefore another approach, more in line with the usual solution of integral equations by the Method of Moments, which was already suggested in [28] and [29] to study waveguide gratings for optical applications. In order to have a clear idea of the method, let us first analyze the simple case of the scalar relation

$$b(\tau) = \int_0^\infty \Gamma(\tau, \tau')a(\tau')d\tau' \tag{4.43}$$

This equation models, for instance, the plane wave reflection from a 2D rough surface, with τ' and τ denoting the transverse wavevectors of the incident and scattered plane wave. To discretize this relation and define a scattering matrix, let us introduce an orthonormal set of basis functions $\{l_c(\tau)\}$, with $c = 1, \ldots, N_\tau$ to represent, in weak form, the power wave amplitudes of the continuous spectrum modes:

$$a(\tau) \simeq \sum_{c=1}^{N_c} a_c\, l_c(\tau) = \underline{l}(\tau) \cdot \underline{a} \tag{4.44}$$

$$b(\tau) \simeq \sum_{c=1}^{N_c} b_c\, l_c(\tau) = \underline{l}(\tau) \cdot \underline{b} \tag{4.45}$$

where the expansion functions have been collected in the $1 \times N_\tau$ row vector $\underline{l}(\tau)$

$$\underline{l}(\tau) = \begin{pmatrix} l_1(\tau) & l_2(\tau) & \ldots & l_{N_\tau}(\tau) \end{pmatrix}$$

and the expansion coefficients have been collected in the $N_\tau \times 1$ column vectors $\underline{a}$, $\underline{b}$. Also, the same symbol is used on the left hand side to denote a function of τ and on the right hand side to denote the associated set of coefficients.

Note that we use the same basis $\{l_n(\tau)\}$ for the incident and scattered waves. This fact is not imperative, but is useful in order to simplify the notation.

Besides the expansion functions we introduce also a set of test functions $\{h_r(\tau)\}$, with $r = 1, \ldots, N_\tau$ and the corresponding $1 \times N_\tau$ row vector $\underline{h}(\tau)$

$$\underline{h}(\tau) = \begin{pmatrix} h_1(\tau) & h_2(\tau) & \ldots & h_{N_\tau}(\tau) \end{pmatrix}$$

Next we denote the projection operation by

$$< f(\tau),\, g(\tau) >= \int_0^\infty f(\tau) g^*(\tau) d\tau$$

Now we substitute the expansions of (4.45) into (4.43) and take projections of both sides onto $\underline{h}(\tau)$:

$$< \underline{h}^T,\, \underline{l} > \cdot \underline{b} = \int_0^\infty < \underline{h}^T(\tau),\, \Gamma(\tau,\tau')\underline{l}(\tau') > d\tau' \cdot \underline{a} \tag{4.46}$$

Our goal is reached if we define the $N_\tau \times N_\tau$ square matrices $\underline{\underline{K}}$ and $\underline{\underline{\Gamma}}$

$$\underline{\underline{K}} =< \underline{h}^T,\, \underline{l} >= \int_0^\infty \underline{h}^{*T}(\tau)\underline{l}(\tau) d\tau$$

and

$$\underline{\underline{\Gamma}} =< \underline{h}^T(\tau),\, \Gamma(\tau,\tau')\underline{l}(\tau') >= \int_0^\infty \int_0^\infty \underline{h}^{*T}(\tau)\Gamma(\tau,\tau')\underline{l}(\tau') d\tau\, d\tau'$$

so that

$$\underline{b} = \underline{\underline{K}}^{-1} \cdot \underline{\underline{\Gamma}} \cdot \underline{a} = \underline{\underline{S}} \cdot \underline{a}$$

We may say that the scattering matrix $\underline{\underline{S}}$ represents the operator (4.43) in the subspace spanned by $\{l_c(\tau)\}$ and $\{h_r(\tau)\}$. It is useful to remark that if the sets $\{h_n(\tau)\}$ and $\{l_n(\tau)\}$ are bi-orthonormal, then the matrix $\underline{\underline{K}}$ reduces to the identity matrix.

Now we are prepared to apply the discretization method to the case of (4.39), (4.40), (4.41) and (4.42). This is more complicated because there are two waveguides. Moreover, the modes of the free space region surrounding the outer conductor are labelled not only by the continuous variable τ, but also by the discrete index m. The index m does not appear explicitly in (4.39), (4.40), (4.41) and (4.42) but is taken into account via the vector notation.

Let us start by representing the power wave amplitudes of the continuous spectrum modes in the basis $\{l_c(\tau)\}$:

$$\check{\underline{b}}_{\text{ext}}(\tau)|_q = \sum_n \check{b}_{\text{ext}}|_{q,n}\, l_n(\tau) \tag{4.47}$$

$$\hat{\underline{b}}_{\text{ext}}(\tau)|_q = \sum_n \hat{b}_{\text{ext}}|_{q,n}\, l_n(\tau) \tag{4.48}$$

$$\check{\underline{a}}_{\text{ext}}(\tau)|_q = \sum_n \check{a}_{\text{ext}}|_{q,n}\, l_n(\tau) \tag{4.49}$$

These equations can be written in compact form as:

$$\check{\underline{b}}_{\text{ext}}(\tau) = \underline{\underline{L}}(\tau) \cdot \check{\underline{b}}_{\text{ext}} \tag{4.50}$$

$$\hat{\underline{b}}_{\text{ext}}(\tau) = \underline{\underline{L}}(\tau) \cdot \hat{\underline{b}}_{\text{ext}} \tag{4.51}$$

$$\check{\underline{a}}_{\text{ext}}(\tau) = \underline{\underline{L}}(\tau) \cdot \check{\underline{a}}_{\text{ext}} \tag{4.52}$$

with the definition of the $N_m \times N_m N_\tau$ matrix

$$\underline{\underline{L}}(\tau) = \begin{pmatrix} \underline{l}(\tau) & \dots & 0 \\ \vdots & \ddots & \vdots \\ 0 & \dots & \underline{l}(\tau) \end{pmatrix}$$

Substituting these expansions into (4.39), (4.40), (4.41) and (4.42) we obtain:

$$\begin{aligned}
\underline{\check{b}}_{\text{int}} &= \underline{\underline{\check{M}}}_{\text{int}} \cdot \underline{\underline{\check{C}}}_{\text{int}} \cdot \underline{\check{a}}_{\text{int}} + \underline{\underline{Y}}^{1/2}_{\infty\,\text{int}} \cdot \underline{\underline{\check{M}}}_{\text{int}} \cdot \int_0^\infty \underline{\underline{\check{C}}}_{\text{ext}}(\tau') \cdot \underline{\underline{Y}}^{-1/2}_{\infty\,\text{ext}}(\tau') \cdot \underline{\underline{L}}(\tau') \cdot \underline{\check{a}}_{\text{ext}}\, d\tau' \\
\underline{\hat{b}}_{\text{int}} &= \left(\underline{\underline{\hat{M}}}_{\text{int}} \cdot \underline{\underline{\check{C}}}_{\text{int}} + \underline{\underline{F}}_{\text{int}}\right) \cdot \underline{\check{a}}_{\text{int}} + \underline{\underline{Y}}^{1/2}_{\infty\,\text{int}} \cdot \underline{\underline{\hat{M}}}_{\text{int}} \cdot \int_0^\infty \underline{\underline{\check{C}}}_{\text{ext}}(\tau') \cdot \underline{\underline{Y}}^{-1/2}_{\infty\,\text{ext}}(\tau') \cdot \underline{\underline{L}}(\tau') \cdot \underline{\check{a}}_{\text{ext}}\, d\tau' \\
\underline{\underline{L}}(\tau) \cdot \underline{\check{b}}_{\text{ext}} &= \underline{\underline{Y}}^{1/2}_{\infty\,\text{ext}}(\tau) \cdot \underline{\underline{\hat{M}}}_{\text{ext}}(\tau) \cdot \underline{\underline{\check{C}}}_{\text{int}} \cdot \underline{\underline{Y}}^{-1/2}_{\infty\,\text{int}} \cdot \underline{\check{a}}_{\text{int}} + \\
&\quad + \underline{\underline{Y}}^{1/2}_{\infty\,\text{ext}}(\tau) \cdot \underline{\underline{\check{M}}}_{\text{ext}}(\tau) \cdot \int_0^\infty \underline{\underline{\check{C}}}_{\text{ext}}(\tau') \cdot \underline{\underline{Y}}^{-1/2}_{\infty\,\text{ext}}(\tau') \cdot \underline{\underline{L}}(\tau') \cdot \underline{\check{a}}_{\text{ext}}\, d\tau' \\
\underline{\underline{L}}(\tau) \cdot \underline{\hat{b}}_{\text{ext}} &= \underline{\underline{Y}}^{1/2}_{\infty\,\text{ext}}(\tau) \cdot \underline{\underline{\hat{M}}}_{\text{ext}}(\tau) \cdot \underline{\underline{\check{C}}}_{\text{int}} \cdot \underline{\underline{Y}}^{-1/2}_{\infty\,\text{int}} \cdot \underline{\check{a}}_{\text{int}} + \\
&\quad + \underline{\underline{Y}}^{1/2}_{\infty\,\text{ext}}(\tau) \cdot \underline{\underline{\hat{M}}}_{\text{ext}}(\tau) \cdot \int_0^\infty \underline{\underline{\check{C}}}_{\text{ext}}(\tau') \cdot \underline{\underline{Y}}^{-1/2}_{\infty\,\text{ext}}(\tau') \cdot \underline{\underline{L}}(\tau') \cdot \underline{\check{a}}_{\text{ext}}\, d\tau' + \underline{\underline{F}}_{\text{ext}}(\tau) \cdot \underline{\underline{L}}(\tau) \cdot \underline{\check{a}}_{\text{ext}}
\end{aligned} \tag{4.53}$$

In order to obtain a matrix relation from the third and fourth equation of (4.53), we take projections on the set $\{h_r(\tau)\}$. Formally, this operation can be performed directly in compact form. Define the $N_m \times N_m N_\tau$ matrix

$$\underline{\underline{H}}(\tau) = \begin{pmatrix} \underline{h}^*(\tau) & \dots & 0 \\ \vdots & \ddots & \vdots \\ 0 & \dots & \underline{h}^*(\tau) \end{pmatrix}$$

At this point we project the third and fourth equations of (4.53) on $\underline{\underline{H}}^T(\tau)$. To simplify the notation, we define the $N_\tau N_m \times N_m$ matrices:

$$\begin{aligned}
\underline{\underline{\check{E}}} &= < \underline{\underline{H}}^T, \underline{\underline{Y}}^{1/2}_{\infty\,\text{ext}} \cdot \underline{\underline{\check{M}}}_{\text{ext}} > \\
\underline{\underline{\hat{E}}} &= < \underline{\underline{H}}^T, \underline{\underline{Y}}^{1/2}_{\infty\,\text{ext}} \cdot \underline{\underline{\hat{M}}}_{\text{ext}} > \\
\underline{\underline{J}} &= < \underline{\underline{H}}^T, \underline{\underline{F}}_{\text{ext}} \cdot \underline{\underline{L}} >
\end{aligned}$$

the $N_f \times N_m N_\tau$ matrices $\underline{\underline{\check{G}}}$ and $\underline{\underline{\hat{G}}}$:

$$\begin{aligned}
\underline{\underline{\check{G}}} &= \int_0^\infty \underline{\underline{\check{C}}}_{\text{ext}}(\tau') \cdot \underline{\underline{Y}}_{\infty\,\text{ext}}^{-1/2}(\tau') \cdot \underline{\underline{L}}(\tau')\, d\tau' \\
\underline{\underline{\hat{G}}} &= \int_0^\infty \underline{\underline{\hat{C}}}_{\text{ext}}(\tau') \cdot \underline{\underline{Y}}_{\infty\,\text{ext}}^{-1/2}(\tau') \cdot \underline{\underline{L}}(\tau')\, d\tau' \qquad (4.54)
\end{aligned}$$

and the $N_m N_\tau \times N_m N_\tau$ block diagonal matrix $\underline{\underline{K}}$:

$$\underline{\underline{K}} = < \underline{\underline{H}}^T, \underline{\underline{L}} > \qquad (4.55)$$

The discretized form of (4.53) can be written:

$$\begin{aligned}
&\underline{\check{b}}_{\text{int}} = \underline{\underline{\check{M}}}_{\text{int}} \cdot \underline{\underline{\check{C}}}_{\text{int}} \cdot \underline{\check{a}}_{\text{int}} + \underline{\underline{Y}}_{\infty\,\text{int}}^{1/2} \cdot \underline{\underline{\check{M}}}_{\text{int}} \cdot \underline{\underline{\check{G}}} \cdot \underline{\check{a}}_{\text{ext}} \\
&\underline{\hat{b}}_{\text{int}} = \left(\underline{\underline{\hat{M}}}_{\text{int}} \cdot \underline{\underline{\check{C}}}_{\text{int}} + \underline{\underline{F}}_{\text{int}}\right) \cdot \underline{\check{a}}_{\text{int}} + \underline{\underline{Y}}_{\infty\,\text{int}}^{1/2} \cdot \underline{\underline{\hat{M}}}_{\text{int}} \cdot \underline{\underline{\check{G}}} \cdot \underline{\check{a}}_{\text{ext}} \\
&\underline{\underline{K}} \cdot \underline{\check{b}}_{\text{ext}} = \underline{\underline{\check{E}}} \cdot \underline{\underline{\check{C}}}_{\text{int}} \cdot \underline{\underline{Y}}_{\infty\,\text{int}}^{-1/2} \cdot \underline{\check{a}}_{\text{int}} + \underline{\underline{\check{E}}} \cdot \underline{\underline{\check{G}}} \cdot \underline{\check{a}}_{\text{ext}} \qquad (4.56) \\
&\underline{\underline{K}} \cdot \underline{\hat{b}}_{\text{ext}} = \underline{\underline{\hat{E}}} \cdot \underline{\underline{\check{C}}}_{\text{int}} \cdot \underline{\underline{Y}}_{\infty\,\text{int}}^{-1/2} \cdot \underline{\check{a}}_{\text{int}} + \underline{\underline{\hat{E}\check{G}}} \cdot \underline{\check{a}}_{\text{ext}} + \underline{\underline{J}} \cdot \underline{\hat{a}}_{\text{ext}}
\end{aligned}$$

Moreover, note that the matrix $\underline{\underline{J}}$ represents the direct contribution of the incident composite mode voltages to the scattered one. Finally, if one defines the vectors $\underline{b}_1$, $\underline{b}_2$ and $\underline{a}_1$ as:

$$\underline{a}_1 = \begin{pmatrix} \underline{\check{a}}_{\text{int}} \\ \underline{\check{a}}_{\text{ext}} \end{pmatrix} \qquad \underline{b}_1 = \begin{pmatrix} \underline{\check{b}}_{\text{int}} \\ \underline{\check{b}}_{\text{ext}} \end{pmatrix} \qquad \underline{b}_2 = \begin{pmatrix} \underline{\hat{b}}_{\text{int}} \\ \underline{\hat{b}}_{\text{ext}} \end{pmatrix} \qquad (4.57)$$

we obtain the relevant terms of the Generalized Scattering Matrix of the cell as:

$$\begin{aligned}
\underline{b}_1 &= \underline{\underline{S}}_{11} \cdot \underline{a}_1 \\
\underline{b}_2 &= \underline{\underline{S}}_{21} \cdot \underline{a}_1
\end{aligned}$$

where the sub-matrices have the expression:

$$\begin{aligned}
\underline{\underline{S}}_{11} &= \begin{pmatrix} \underline{\underline{\check{M}}}_{\text{int}} \cdot \underline{\underline{\check{C}}}_{\text{int}} & \underline{\underline{Y}}_{\infty\,\text{int}}^{1/2} \cdot \underline{\underline{\check{M}}}_{\text{int}} \cdot \underline{\underline{\check{G}}} \\ \underline{\underline{K}}^{-1} \cdot \underline{\underline{\check{E}}} \cdot \underline{\underline{Y}}_{\infty\,\text{int}}^{-1/2} \cdot \underline{\underline{\check{C}}}_{\text{int}} & \underline{\underline{K}}^{-1} \cdot \underline{\underline{\check{E}}} \cdot \underline{\underline{\check{G}}} \end{pmatrix} \\
\underline{\underline{S}}_{21} &= \begin{pmatrix} \underline{\underline{\hat{M}}}_{\text{int}} \cdot \underline{\underline{\check{C}}}_{\text{int}} + \underline{\underline{F}}_{\text{int}} & \underline{\underline{Y}}_{\infty\,\text{int}}^{1/2} \cdot \underline{\underline{\hat{M}}}_{\text{int}} \cdot \underline{\underline{\check{G}}} \\ \underline{\underline{K}}^{-1} \cdot \underline{\underline{\hat{E}}} \cdot \underline{\underline{Y}}_{\infty\,\text{int}}^{-1/2} \cdot \underline{\underline{\check{C}}}_{\text{int}} & \underline{\underline{K}}^{-1} \cdot \left(\underline{\underline{\hat{E}}} \cdot \underline{\underline{\check{G}}} + \underline{\underline{J}}\right) \end{pmatrix}
\end{aligned}$$

It is also useful, for the computation that will be carried out in Section 4.7, to write (4.31) in matrix form. By recalling the definitions (4.54), we find:

$$\underline{x} = \underline{\underline{\check{C}}}_{\text{int}} \cdot \underline{\underline{Y}}_{\infty\,\text{int}}^{-1/2} \cdot \underline{\check{a}}_{\text{int}} + \underline{\underline{\check{G}}} \cdot \underline{\check{a}}_{\text{ext}} \tag{4.58}$$

In this way it is straightforward to compute the representation of the magnetic current in terms of the incident voltages on the slot.

From a physical point of view, the introduction of the set $\{l_n(\tau)\}$ to expand the modal amplitudes amounts to grouping the continuous spectrum modes into a discrete set of "spectral composite modes" [28]. Indeed

$$\underline{E}_t(\rho,\varphi,z) = \sum_m \int_0^\infty V_m(z;\tau)\underline{e}_m(\rho,\varphi;\tau)d\tau = \sum_m \sum_n (a_{mn} + b_{mn})\tilde{\underline{e}}_{mn}(\rho,\varphi) \tag{4.59}$$

$$\underline{H}_t(\rho,\varphi,z) = \sum_m \int_0^\infty I_m(z;\tau)\underline{h}_m(\rho,\varphi;\tau)d\tau = \sum_m \sum_n (a_{mn} - b_{mn})\tilde{\underline{h}}_{mn}(\rho,\varphi) \tag{4.60}$$

where the spectral composite mode functions are defined by

$$\begin{pmatrix} \tilde{\underline{e}}_{mn}(\rho,\varphi) \\ \tilde{\underline{h}}_{mn}(\rho,\varphi) \end{pmatrix} = \int \begin{pmatrix} Y_{\infty\,\text{ext}}^{-1/2}(\tau,m)\underline{e}_m(\rho,\varphi;\tau) \\ Y_{\infty\,\text{ext}}^{1/2}(\tau,m)\underline{h}_m(\rho,\varphi;\tau) \end{pmatrix} l_n(\tau)d\tau \tag{4.61}$$

The ports, in the external waveguide, where the scattering matrix $\underline{\underline{S}}$ is defined, are associated to the spectral composite modes. These composite waves have useful characteristics, such as that of forming an orthonormal basis, each element carrying a finite power. However, the evolution law of their amplitudes is very complicated, because they are all coupled, even in a uniform waveguide.

The discretization of the continuous spectrum and the computation of the GSM has been carried out by using different sets of basis functions, more details can be found in the next sections. The evaluation of the integrals has been performed using special numerical techniques see Section 10.5.

Finally, even if the structure is reciprocal, the scattering matrix is not symmetrical because the mode eigenfunctions of the external waveguide are neither real nor imaginary [26].

At this point, an LCX consisting of N_{slot} apertures can be analyzed by cascading the scattering matrices of each aperture. The procedure is not efficient, since in general N_{slot} is very large. However, the apertures are generally all equal, so that Bloch theory can be very useful to increase the efficiency of the method. This subject will be discussed in the next section.

4.4 Expansion functions for the mode amplitudes

In the preceding sections, in order to derive a matrix representation of the scattering and transmission operator, sets of expansion and testing functions, $\{l_c(\tau)\}$ and $\{h_r(\tau)\}$, have been introduced. Unfortunately, differently from the case of HFIE, this discretization procedure is far from being standard, and it is difficult to select good sets of functions. The simplest choice could be a point matching scheme, but a Galerkin procedure usually gives better results.
Moreover, since the waves scattered form a slot are incident on another one, it appears reasonable to employ the same set to expand both incident and scattered waves amplitudes. In order to define this set of expansion functions, it is useful to consider the explicit expression of the scattered power wave in the right reference plane in $z = L/2$ for the simplest case of a complete slot, only the TEM mode in the cable and one expansion function to represent the magnetic current on the aperture. Note that, since the slot is complete, only φ-independent TM modes are excited in the cable and in the external waveguide. According to (4.39), (4.40), (4.41) and (4.42), the scattered power wave $\check{b}_e(\tau)$ is given by:

$$\hat{b}_e(\tau) = \frac{\hat{M}_e(\tau)}{\sqrt{Z_{\infty e}(\tau)}} \left(\int_0^\infty \sqrt{Z_{\infty e}(\tau')} \cdot \hat{C}_e(\tau') \check{a}_e(\tau') d\tau' + \sqrt{Z_{\infty i}} \check{C}_i \check{a}_i + \right) + \check{a}_e(\tau) \mathrm{e}^{-j\beta(\tau)L} \tag{4.62}$$

Note that the term in the parenthesis is not a function of τ but a number B, so that (4.62) can be written as

$$\hat{b}_e(\tau) = \frac{\hat{M}_e(\tau)}{\sqrt{Z_{\infty e}(\tau)}} B + \check{a}_e(\tau) \mathrm{e}^{-j\beta(\tau)L}$$

i.e., using (4.23), (4.24), (4.25), (4.28) and (4.37), more explicitly :

$$\hat{b}_e(\tau) = -\frac{\jmath}{\pi} \sqrt{\frac{\omega\epsilon}{2\pi}} \frac{\tilde{f}(\beta(\tau)) \mathrm{e}^{-j\beta(\tau)L/2}}{\sqrt{\tau}(k_0^2 - \tau^2)^{1/4} H_0^{(1)}(b\tau)} B + \check{a}_e(\tau) \mathrm{e}^{-j\beta(\tau)L} \tag{4.63}$$

The first part of the right hand side of this equation has a fourth root singularity $\tau = k_0$ and a $\sqrt{\tau} \log \tau$ singularity in $\tau = 0$. Moreover, the exponential term in the numerator approaches $\mathrm{e}^{-\tau L/2}$ for $\tau \gg k_0$. It would be useful that also the basis functions had the same characteristics, but it is difficult to find a set that matches the $\tau \to 0$ behavior. According to [28], it is convenient to use different sets in the above-cut-off range $\tau \in (0, k_0]$ and in the below-cut-off range $\tau \in [k_0, \infty)$. We have tried different sets of functions and after numerical experiments we have shown that the following ones guarantee a fast convergence of the desired electromagnetic parameters (i.e. Bloch waves and their propagation constants):

- For the above cut off range:

$$\{l_m(\tau)\} = \left\{T_m\left(\frac{2\tau - k_0}{k_0}\right)/(k_0\tau - \tau^2)^{1/4}\right\}$$

- For the below cut off range:

$$\{l_m(\tau)\} = \left\{\frac{\sqrt{L_d}\,\mathrm{e}^{L_d\,k_0}}{m}\mathrm{e}^{-L_d\tau/2}L_m(L_d\tau - L_d\,k_0)\right\}$$

where $T_m(x)$ and $L_m(x)$ represent the Chebyshev and Laguerre polynomials, respectively and the exponential decay length L_d is equal to $L/2$. Note that these basis functions are orthonormal: this fact implies that the matrix $\underline{\underline{K}}$ introduced in (4.55) reduces to the identity. The functions used to describe the below cut off range do not diverge for $\tau = k_0$ as the elements of the other set. Even if this is not, from a mathematical point of view, strictly correct, from a numerical point of view we have shown that it allows the use of a reduced number of basis functions since they present the correct decay factor for $\tau \gg k_0$.
In order to analyze the convergence of the numerical scheme, we have considered a specific example in which the continuous spectrum of above cut-off modes is discretized by $N_e = 10$ expansion functions and we assume that the first composite mode, $m = 0$, is incident at the frequency $f = 2$ GHz from the left on a complete slot ($\alpha = 360°$, $s = 3$ mm) in a cable with inner conductor radius $a = 8$ mm, outer conductor radius $b = 20.65$ mm, $\varepsilon_{r1} = 1.26$.
First, we have computed the scattered power wave distribution $\check{b}_e(\tau)$, for the TM modes, according to (4.62), by introducing the appropriate incidence. The result is shown by the solid line in Figure 4.5. As an alternative, we have computed $\check{\underline{b}}_e$ according to (4.56), which is the discretized version of (4.62), and then we have obtained the scattered power wave distribution according to (4.47). The curve obtained in this way is plotted as dashed line in Figure 4.5. It can be seen that the difference between the two curves is quite small (error in L_2-norm less than 1%), which confirms that $N_e = 10$ of the selected expansion functions provide an accurate discretization of the continuous spectrum.
All the details related to the computation of the integrals can be found in Section 10.5.

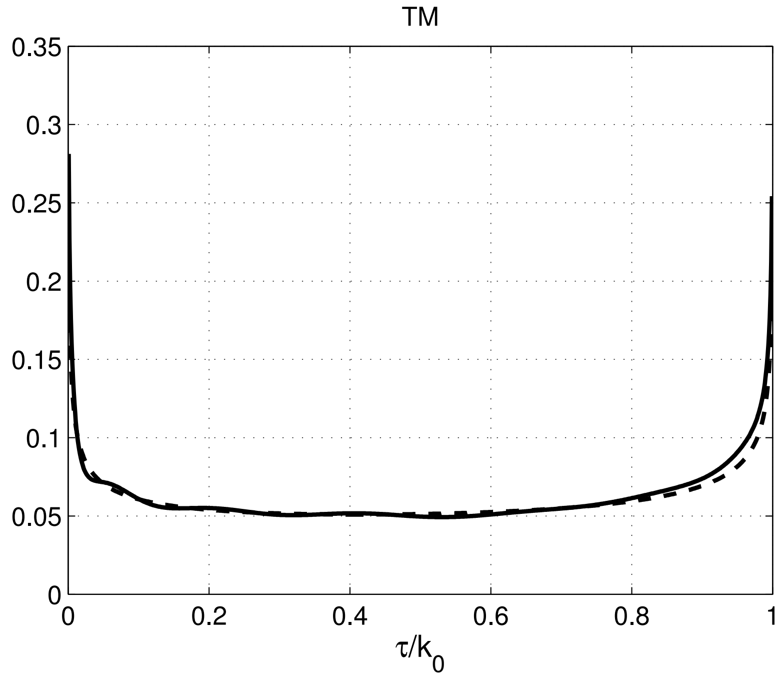

Figure 4.5: Comparison between two ways to compute the scattered power wave distribution. See text

4.5 Bloch waves in a periodically slotted coaxial cable

Once the Generalized Scattering Matrix $\underline{\underline{S}}$ of a section of cable containing a slot is known, the corresponding transmission matrix $\underline{\underline{T}}$ can be computed using the standard relations [12]:

$$\underline{\underline{T}}_{11} = \underline{\underline{S}}_{21}^{-1} \tag{4.64}$$

$$\underline{\underline{T}}_{12} = -\underline{\underline{S}}_{21}^{-1} \cdot \underline{\underline{S}}_{22} \tag{4.65}$$

$$\underline{\underline{T}}_{21} = \underline{\underline{S}}_{11} \cdot \underline{\underline{S}}_{21}^{-1} \tag{4.66}$$

$$\underline{\underline{T}}_{22} = \underline{\underline{S}}_{12} - \underline{\underline{S}}_{11} \cdot \underline{\underline{S}}_{21}^{-1} \cdot \underline{\underline{S}}_{22} \tag{4.67}$$

Note that all the modes with nominal attenuation higher than α_{dB} over the cell length are considered as localized and not used in the computation of the transmission matrix.

In order to study the characteristics of a finite periodic structure, consisting of a number N_{slot} of identical cells, we could simply compute the power N_{slot} of the transmission matrix $\underline{\underline{T}}$ of a single cell. However, it is well known that this procedure suffers from numerical instabilities due to the large dynamic range of the eigenvalues of $\underline{\underline{T}}$ and if N_{slot} is large, as in this application, a different approach is more convenient. In fact, the structure can be seen as a length of periodically slotted cable, inserted between two semi-infinite ordinary cables. As well known, the propagation along the slotted cable, which can be described as a periodically loaded waveguide, is best analyzed by introducing the so called Bloch waves, which play the same role as the modes in a uniform waveguide. Hence, we identify two junctions, between a periodically slotted and an unslotted cable. In circuit terms, each junction is an N-port characterized by a scattering matrix and the two are connected by a number of equivalent transmission lines, relative to the Bloch waves involved. This point of view is illustrated in Figure 4.6. The Bloch wave equivalent transmission lines are shown dotted, to recall that they are a discrete structure, where Bloch wave amplitudes are defined only at the cell reference planes.

Let us recall the basic facts about Bloch waves [12]. The $\underline{\underline{T}}$ matrix expresses the relationship

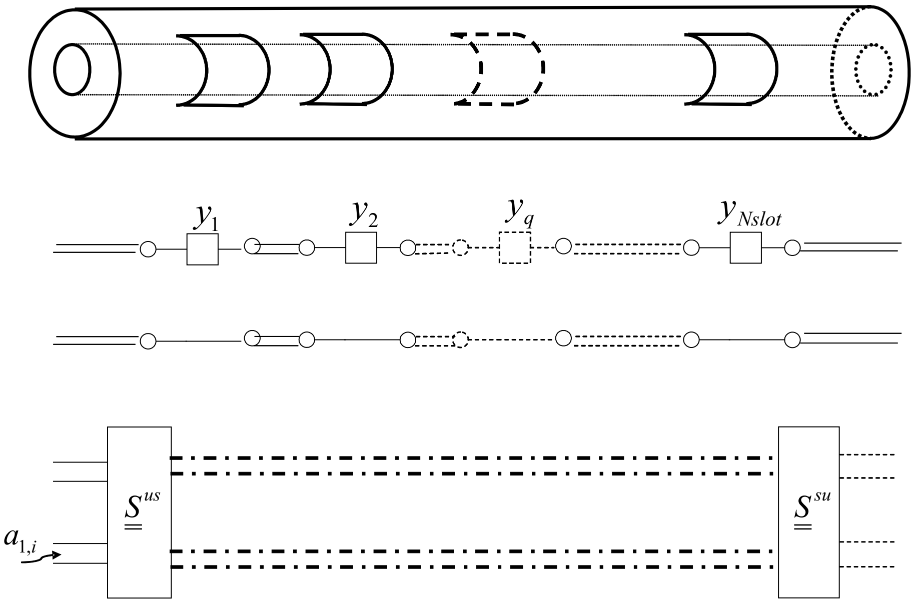

Figure 4.6: Slotted cable with N_{slot} apertures and equivalent circuit in the Bloch domain

between the electrical state at the output and that at the input of the generic cell n:

$$\begin{pmatrix} \underline{p}_n^+ \\ \underline{p}_n^- \end{pmatrix} = \begin{pmatrix} \underline{\underline{T}}_{11} & \underline{\underline{T}}_{12} \\ \underline{\underline{T}}_{21} & \underline{\underline{T}}_{22} \end{pmatrix} \cdot \begin{pmatrix} \underline{p}_{n+1}^+ \\ \underline{p}_{n+1}^- \end{pmatrix} \tag{4.68}$$

where $\underline{p}_n^+$ and $\underline{p}_n^-$ are the vectors of progressive and regressive power waves. They coincide with those of (4.57):

$$\begin{aligned} \underline{p}_n^+ = \underline{a}_1 &= \begin{pmatrix} \check{\underline{a}}_i \\ \check{\underline{a}}_e \end{pmatrix} & \qquad \underline{p}_n^- = \underline{b}_1 &= \begin{pmatrix} \check{\underline{b}}_i \\ \check{\underline{b}}_e \end{pmatrix} \\ \underline{p}_{n+1}^+ = \underline{b}_2 &= \begin{pmatrix} \hat{\underline{b}}_i \\ \hat{\underline{b}}_e \end{pmatrix} & \qquad \underline{p}_{n+1}^- = \underline{a}_2 &= \begin{pmatrix} \hat{\underline{a}}_i \\ \hat{\underline{a}}_e \end{pmatrix} \end{aligned} \tag{4.69}$$

The Bloch waves are defined as the states that satisfy

$$\begin{pmatrix} \underline{p}_{n+1}^+ \\ \underline{p}_{n+1}^- \end{pmatrix} = \exp(-jk_B L) \begin{pmatrix} \underline{p}_n^+ \\ \underline{p}_n^- \end{pmatrix} \tag{4.70}$$

Combining this defining equation with (4.68), we infer that Bloch waves are described, in the basis of the internal cable modes and external composite modes, by the eigenvectors of the transmission matrix $\underline{\underline{T}}$ [26]

$$\begin{pmatrix} \underline{\underline{T}}_{11} & \underline{\underline{T}}_{12} \\ \underline{\underline{T}}_{21} & \underline{\underline{T}}_{22} \end{pmatrix} \cdot \begin{pmatrix} \underline{p}_n^+ \\ \underline{p}_n^- \end{pmatrix} = \lambda \begin{pmatrix} \underline{p}_n^+ \\ \underline{p}_n^- \end{pmatrix} = \exp(jk_B L) \begin{pmatrix} \underline{p}_n^+ \\ \underline{p}_n^- \end{pmatrix}$$

The eigenvalues λ are generally written in exponential form to define a (possibly complex) Bloch wave phase shift per cell ($k_B L$). If N_d and N_e are the number of accessible coaxial cable modes and the number of external composite modes, the vector $((\underline{p}_n^+)^T, (\underline{p}_n^-)^T)$ has dimension $2(N_d + N_e)$. In general, the structure is characterized by $2(N_d + N_e)$ Bloch waves, half forward and half backward propagating. It is to be remarked that the classification has to be done on the following basis. A Bloch wave is progressive if

- k_B is complex and $\mathfrak{Im}\{k_B\} < 0$
- k_B is real and the wave carries active power in the direction of increasing z

The transverse electric and magnetic fields of the j-th Bloch wave at the cell reference planes are given by (the cell label n is dropped):

$$\underline{E}_j(\rho, \varphi) = \sum_{q=1}^{N_d} (p_{qj}^+ + p_{qj}^-) \underline{e}_{d\,q}(\rho, \varphi) + \sum_{q=N_d+1}^{N_e+N_d} (p_{qj}^+ + p_{qj}^-) \underline{e}_{e\,q}(\rho, \varphi) \tag{4.71}$$

$$\underline{H}_j(\rho, \varphi) = \sum_{q=1}^{N_d} Y_{d\,q} (p_{qj}^+ - p_{qj}^-) \underline{h}_{d\,q}(\rho, \varphi) + \sum_{q=N_d+1}^{N_e} (p_{qj}^+ - p_{qj}^-) \underline{h}_{e\,q}(\rho, \varphi) \tag{4.72}$$

where $\underline{e}_{d\,q}$ and $\underline{h}_{d\,q}$ are the transverse electric and magnetic field distributions of the $q-$th mode of the coaxial cable (and $Y_{d\,q}$ the corresponding modal admittance), $\underline{e}_{e\,q}$ and $\underline{h}_{e\,q}$ are the transverse electric and magnetic field distributions of the $q-$th external composite mode. Note that no modal admittance has been introduced for the external composite modes.

If the fields of a Bloch wave are desired at any location z within a cell, the individual constituent modes have to be propagated from the cell boundaries, using the relevant propagation constants $k_{zd\,q}$. As for the external composite modes, the procedure is less straightforward, since they are all coupled even in a uniform waveguide, as noted in the preceding section. Hence, it is necessary to reconstruct the continuous spectrum modes and let them propagate, using the propagation constants $\beta(\tau)$.

Bloch waves have also another useful representation in terms of spatial harmonics. Indeed, it can be proved, [12], that the fields of the j-th Bloch wave satisfy

$$\underline{E}_j(\rho,\varphi,z) = \underline{E}_p(\rho,\varphi,z)\mathrm{e}^{-j\,k_{Bj}z} \tag{4.73}$$

$$\underline{H}_j(\rho,\varphi,z) = \underline{H}_p(\rho,\varphi,z)\mathrm{e}^{-j\,k_{Bj}z} \tag{4.74}$$

where k_{Bj} is the Bloch wave propagation constant and $\underline{E}_p(\rho,\varphi,z)$, $\underline{H}_p(\rho,\varphi,z)$ are periodic functions of z, with period L. This implies that they can be represented by a Fourier series

$$\underline{E}_p(\rho,\varphi,z) = \sum_{m=-\infty}^{\infty} \underline{E}_{pm}(\rho,\varphi)\,\mathrm{e}^{-j\frac{2\pi\,m}{L}z} \tag{4.75}$$

$$\underline{H}_p(\rho,\varphi,z) = \sum_{m=-\infty}^{\infty} \underline{H}_{pm}(\rho,\varphi)\,\mathrm{e}^{-j\frac{2\pi\,m}{L}z} \tag{4.76}$$

(4.73) and (4.74) become

$$\begin{pmatrix} \underline{E}_j(\rho,\varphi,z) \\ \underline{H}_j(\rho,\varphi,z) \end{pmatrix} = \sum_{m=-\infty}^{\infty} \begin{pmatrix} \underline{E}_{pm}(\rho,\varphi) \\ \underline{H}_{pm}(\rho,\varphi) \end{pmatrix} \mathrm{e}^{-jk_{zj\,m}z} \tag{4.77}$$

where the terms of the series are called spatial harmonics and each one has a longitudinal propagation constant

$$k_{zj\,m} = k_{Bj} + \frac{2\pi\,m}{L} \tag{4.78}$$

This is the reason why the Bloch wave propagation constant k_{Bj} is always defined up to an integer multiple of $2\pi/L$. It is to be remarked that each spatial harmonic does not satisfy all the boundary conditions on the slotted cable, so that they do not have independent existence. Spatial harmonics are also called Floquet modes and can be interpreted as modes of a radial waveguide limited by phase shift walls, located at the cell reference planes, [30], see also Section 2.8.5. As such, their longitudinal propagation constants (in the $\hat{\rho}$ direction in this "transverse" picture), in the free space region surrounding the cable, are given by

$$\tau_{jm} = \sqrt{k_0^2 - \left(k_{Bj} + \frac{2\pi\, m}{L}\right)^2} \tag{4.79}$$

The evolution in the radial direction of these Floquet modes is governed by the radial transmission line theory. In particular, the propagation of the centrifugal wave, as discussed in the first chapter, is related to the Hankel function $H_n^{(2)}(\tau_{jm}\rho)$. Owing to the properties of this function, we say that a specific harmonic is radiating if the corresponding τ_{jm} is real or, equivalently, the corresponding $k_{zj\,m}$ lies in the visible range $[-k_0, k_0]$. If no harmonic is radiating, the Bloch wave is of surface type and, in general, a finite number of them (possibly zero) can exist. If at least one harmonic is radiating, the Bloch wave belongs to the continuous spectrum.

We remark that the formulation presented in this section, owing to its longitudinal nature, forces us to view the slotted coaxial cable as an infinite cross section waveguide, in which for convenience two regions are identified, *i.e* the inner and the outer portions of the cable. However, the distinction between the two periodically fails, due to the presence of the slots. The consequence is that only surface Bloch waves and the continuum of radiated Bloch waves can be obtained. Obviously, in the numerical implementation, the continuous spectrum has been discretized and a finite number of radiated Bloch waves is determined.

Of course also a transverse point of view is possible, which exploits the radial transmission line theory of Chapter 1. In this case, surface Bloch waves are related to resonances of the structure, *i.e.* to poles of the Fourier transform of the relevant Green's function. This Green's function is defined on a multi-sheeted Riemann surface, and beyond the possible poles on the proper sheet ($\Im\tau_{jm} < 0$), related to the surface waves, possesses leaky poles on improper sheets. Sometimes, a representation in terms of a single leaky complex Bloch wave instead of a continuum, is possible and very convenient. Notice that this point of view lends itself to a very intuitive description of the radiation phenomenon. In fact, since slots (particularly the ones with limited angular extent) represent a small perturbation of the uniform cable, it is easy to anticipate that the real part of the leaky propagation constant will be close to $k_0\sqrt{\varepsilon_{r1}}$. The imaginary part describes the decay of power in the slotted cable due to radiation, and its value, which depends on the shape, size and arrangement of the slots, is more difficult to estimate, but is typically very small.

On the basis of these considerations, it is possible to identify essentially the following operation conditions (if $\varepsilon_{r1} < 9$):

1. $$L < \frac{\lambda_0}{1 + \sqrt{\varepsilon_{r1}}}$$

   No spatial harmonics in the visible range. We refer to this case as "Surface wave" condition;

2. $$\frac{\lambda_0}{1 + \sqrt{\varepsilon_{r1}}} \leq L < \frac{2\lambda_0}{1 + \sqrt{\varepsilon_{r1}}}$$

   Harmonic "-1" in the visible range. We refer to this case as "Mono Radiation" condition. In this case the propagation direction is identified by

   $$\theta_{-1} = \sin^{-1} \sqrt{\varepsilon_{r1} - \frac{\lambda_0}{L}}$$

   with respect to the z axis;

3. $$L > \frac{2\lambda_0}{1 + \sqrt{\varepsilon_{r1}}}$$

   More than one harmonic is in the visible range. We refer to this case as "Multi-Radiation" condition. Of course there are multiple propagation directions, with angles:

   $$\theta_{-n} = \sin^{-1} \sqrt{\varepsilon_{r1} - n\frac{\lambda_0}{L}}$$

   as long as the square root is real.

4.6 Junction between a uniform and a periodically slotted coaxial cable

Let us compute the scattering matrix of the junction between a semi-infinite periodically slotted cable placed in the region $z > 0$ and a standard cable, located in $z < 0$ (see Figure 4.7). The electric and magnetic fields in the two regions are expressed in terms of the relevant eigenmodes:

the modes of the coaxial cable and the spectral composite waves in the unslotted region; Bloch waves in the periodic structure. Enforcement of the boundary conditions at the junction plane, *i.e.* matching of the transverse field components, yields:

$$\sum_j \left(V_j^{inc} + V_j^{scat}\right) \underline{e}_j = \sum_j \left(c_j^{inc} \underline{E}_j^{inc} + c_j^{scat} \underline{E}_j^{scat}\right) \tag{4.80}$$

$$\sum_j Y_j \left(V_j^{inc} - V_j^{scat}\right) \underline{h}_j = \sum_j \left(c_j^{inc} \underline{H}_j^{inc} + c_j^{scat} \underline{H}_j^{scat}\right) \tag{4.81}$$

where the superscripts inc and $scat$ mean incident and scattered with respect to the junction. $\underline{E}_j(\rho,\varphi)$ and $\underline{H}_j(\rho,\varphi)$ are the transverse electric and magnetic fields of the j-th Bloch wave at the cell reference planes, see (4.71). From 4.80 and 4.81 we derive the Generalized Scattering Matrix of the junction which relates the scattered wave amplitudes $(V_p^{scat},\ c_q^{scat})$ to the incident ones $(V_p^{inc},\ c_q^{inc})$. We may assume that the junction plane coincides with the reference plane of the first cell of the periodic structure.

By substituting (4.71) and (4.72) into (4.80) and (4.81), projecting on the coaxial cables and external composite modes and exploiting the orthonormality properties, we obtain the following set of linear equations for $p = 1, \ldots, N_d + N_e$:

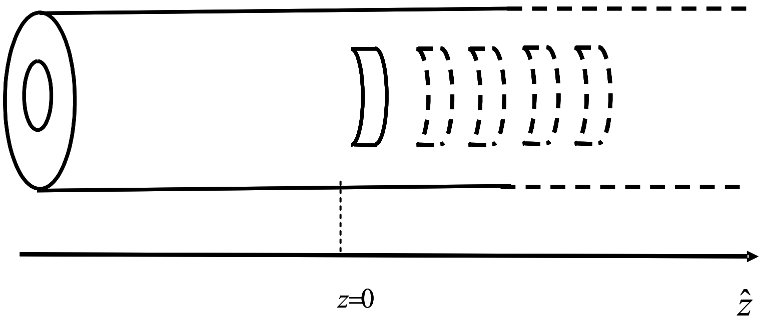

Figure 4.7: junction between an unslotted cable and a slotted one

$$\left\{ \begin{array}{lcl} V_p^{inc} + V_p^{scat} & = & \sum_j \left(p_{qj}^{+\,inc} + p_{qj}^{-\,inc}\right) c_j^{inc} + \left(p_{qj}^{+\,scat} + p_{qj}^{-\,scat}\right) c_j^{scat} \\ \\ V_p^{inc} - V_p^{scat} & = & \sum_j \left(p_{qj}^{+\,inc} - p_{qj}^{-\,inc}\right) c_j^{inc} + \left(p_{qj}^{+\,scat} - p_{qj}^{-\,scat}\right) c_j^{scat} \end{array} \right. \tag{4.82}$$

These equations can be simplified by a matrix formalism. Let us define a matrix $\underline{\underline{U}}$ consisting of the eigenvectors of $\underline{\underline{T}}$ arranged columnwise, first the progressive ones and then the regressive ones

$$\underline{\underline{U}} = \begin{pmatrix} \underline{\underline{U}}_{11} & \underline{\underline{U}}_{12} \\ \underline{\underline{U}}_{21} & \underline{\underline{U}}_{22} \end{pmatrix} = \begin{pmatrix} \ldots p_{qj}^{+\,scat} \ldots & \ldots p_{qj}^{+\,inc} \ldots \\ \ldots p_{qj}^{-\,scat} \ldots & \ldots p_{qj}^{-\,inc} \ldots \end{pmatrix} \tag{4.83}$$

where it has been taken into account that, in the case of this junction, the progressive Bloch waves are the scattered ones. With these notations, the (4.82) becomes

$$\begin{cases} \underline{V}^{inc} + \underline{V}^{scat} = (\underline{\underline{U}}_{12} + \underline{\underline{U}}_{22}) \cdot \underline{c}^{inc} + (\underline{\underline{U}}_{11} + \underline{\underline{U}}_{21}) \cdot \underline{c}^{scat} \\ \\ \underline{V}^{inc} - \underline{V}^{scat} = (\underline{\underline{U}}_{12} - \underline{\underline{U}}_{22}) \cdot \underline{c}^{inc} + (\underline{\underline{U}}_{11} - \underline{\underline{U}}_{21}) \cdot \underline{c}^{scat} \end{cases} \tag{4.84}$$

Solving for $\underline{V}^{scat}$, $\underline{c}^{scat}$ we obtain the GSM $\underline{\underline{S}}^{us}$ of the junction in the form:

$$\begin{pmatrix} \underline{V}^{scat} \\ \underline{c}^{scat} \end{pmatrix} = \begin{pmatrix} \underline{\underline{U}}_{21} \cdot \underline{\underline{U}}_{11}^{-1} & \underline{\underline{U}}_{22} - \underline{\underline{U}}_{21} \cdot \underline{\underline{U}}_{11}^{-1} \underline{\underline{U}}_{12} \\ \\ \underline{\underline{U}}_{11}^{-1} & -\underline{\underline{U}}_{11}^{-1} \cdot \underline{\underline{U}}_{12} \end{pmatrix} \cdot \begin{pmatrix} \underline{V}^{inc} \\ \underline{c}^{inc} \end{pmatrix} = \underline{\underline{S}}^{us} \cdot \begin{pmatrix} \underline{V}^{inc} \\ \underline{c}^{inc} \end{pmatrix} \tag{4.85}$$

It is interesting to note that this result can also be obtained in a simpler way. By a well known theorem of linear algebra, the power N_{slot} of the matrix $\underline{\underline{T}}$ can be computed in the eigenvector basis as

$$\underline{\underline{T}}^{N_{slot}} = \underline{\underline{U}} \cdot \underline{\underline{\lambda}}^{N_{slot}} \cdot \underline{\underline{U}}^{-1} \tag{4.86}$$

with $\underline{\underline{U}}$ defined above and $\underline{\underline{\lambda}} = \mathrm{diag}\{\exp(jk_B L)\}$ the diagonal matrix of the eigenvalues of $\underline{\underline{T}}$. Taking into account the product law of the transmission matrices of cascaded structures, it is easy to recognize from (4.86) that $\underline{\underline{U}}$ is the transmission matrix of the junction between the unslotted and the slotted cable and $\underline{\underline{U}}^{-1}$ is that of the complementary junction. Moreover, $\underline{\underline{\lambda}}^{N_{slot}}$ is the transmission matrix describing the propagation of the Bloch waves across N_{slot} cells. Owing to the ordering of the columns of $\underline{\underline{U}}$, the definition of the transmission matrix of the junction is

$$\begin{pmatrix} \underline{V}^{inc} \\ \underline{V}^{scat} \end{pmatrix} = \begin{pmatrix} \underline{\underline{U}}_{11} & \underline{\underline{U}}_{12} \\ \underline{\underline{U}}_{21} & \underline{\underline{U}}_{22} \end{pmatrix} \cdot \begin{pmatrix} \underline{c}^{scat} \\ \underline{c}^{inc} \end{pmatrix} \tag{4.87}$$

and the expression of the corresponding scattering matrix, already given in (4.85) follows immediately, thanks to the well known transformation formulas dual to (4.64).

The scattering matrix $\underline{\underline{S}}^{su}$ of the complementary junction between the slotted coaxial cable and the unslotted one is simply obtained by applying the operations indicated in (4.85) to the matrix $\underline{\underline{U}}^{-1}$.

In order to cascade the two discontinuities, it is necessary to move the left reference plane of $\underline{\underline{S}}^{su}$ of N_{slot} cells to the left. By taking into account that

$$\underline{c}_{n+1}^{+} = \mathrm{diag}\{1/\lambda^{+}\} \cdot \underline{c}_{n}^{+} \tag{4.88}$$

$$\underline{c}_{n+1}^{-} = \mathrm{diag}\{1/\lambda^{-}\} \cdot \underline{c}_{n}^{-} \tag{4.89}$$

where $\underline{c}_n^+$ is an array of amplitudes of progressive Bloch waves (with eigenvalues $\mathrm{diag}\{\lambda^+\}$), evaluated at the input of cell n and $\underline{c}_n^-$ is an analogous array of regressive Bloch waves (with eigenvalues $\mathrm{diag}\{\lambda^-\}$), the new GSM of the second discontinuity is

$$\begin{pmatrix} \mathrm{diag}\{1/\lambda^{N_{slot}}\} \cdot \underline{\underline{S}}^{su}_{11} \cdot \mathrm{diag}\{1/\lambda^{N_{slot}}\} & \mathrm{diag}\{1/\lambda^{N_{slot}}\} \cdot \underline{\underline{S}}^{su}_{12} \\ \underline{\underline{S}}^{su}_{21} \cdot \mathrm{diag}\{1/\lambda^{N_{slot}}\} & \underline{\underline{S}}^{su}_{22} \end{pmatrix} \tag{4.90}$$

where we denote simply by λ the set of eigenvalues λ^+ of progressive Bloch waves. Notice that the stability of the algorithm originates by the fact that all the eigenvalues appearing in the preceding formula belong to progressive waves, so that $|\lambda| \geq 1$.

At this point the reflection and transmission coefficients of the complete array of slots are computed by the usual cascading formulas as

$$\underline{\underline{S}}^{tot}_{11} = \underline{\underline{S}}^{us}_{11} + \underline{\underline{S}}^{us}_{12} \cdot \mathrm{diag}\{1/\lambda^{N_{slot}}\} \cdot \underline{\underline{S}}^{us}_{22} \cdot \mathrm{diag}\{1/\lambda^{N_{slot}}\} \cdot \underline{\underline{R}} \cdot \underline{\underline{S}}^{us}_{21} \tag{4.91}$$

$$\underline{\underline{S}}^{tot}_{21} = \underline{\underline{S}}^{us}_{12} \cdot \mathrm{diag}\{1/\lambda^{N_{slot}}\} \cdot \underline{\underline{R}} \cdot \underline{\underline{S}}^{us}_{21} \tag{4.92}$$

where $\underline{\underline{R}}$ denotes the resonant denominator

$$\underline{\underline{R}} = \left(\underline{\underline{I}} - \underline{\underline{S}}^{us}_{22} \cdot \mathrm{diag}\{1/\lambda^{N_{slot}}\} \cdot \underline{\underline{S}}^{us}_{22} \cdot \mathrm{diag}\{1/\lambda^{N_{slot}}\}\right)^{-1} \tag{4.93}$$

and $\underline{\underline{I}}$ is the identity matrix. The Bloch wave approach yields in a natural way the scattering matrix of the slotted cable.

Note, anyway, that, due to the finite discretization of the scattering operator and the numerical computation of the integrals, the submatrix of the G.S.M., which refers to the above cut-off modes, $\underline{\underline{S}}_{ac}$ is not exactly unitary. In particular, in Figure 4.8, the eigenvalues of $\underline{\underline{S}}_{ac}\underline{\underline{S}}^H_{ac}$ are shown, the geometry is the same of the preceding example. Note that most of the eigenvalues are exactly one, only four are less than one. The discretization should be sufficiently fine that these modes are not excited. This fact implies that the Bloch wave propagation constants are not exactly real or purely imaginary.

4.7 Computation of the radiated field

In the preceding section we have shown how to compute the scattering matrix of the array of N_{slot} apertures on the basis of Bloch wave theory. For the computation of the radiated field, two alternatives are possible. One is to determine the Bloch wave amplitudes in the slotted part of the cable and from them the magnetic currents. The other is to exploit directly the Bloch wave

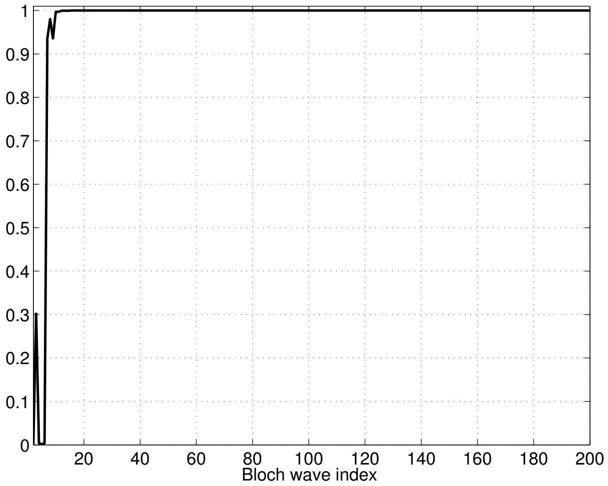

Figure 4.8: Eigenvalues of $\underline{\underline{S}}_{ac}\underline{\underline{S}}_{ac}^{H}$. The matrix $\underline{\underline{S}}_{ac}$ is the part of the GSM that refers to the above cut-off modes

amplitudes.

As for the first method, we recall that the expansion coefficients of the magnetic current on a specific slot are given by (4.31) or, in matrix form, by (4.58). Hence, what is needed first of all are the incident voltages on each slot. According to the theory of scattering matrix connections, we find that

$$\underline{c}_1^+ = \underline{\underline{R}} \cdot \underline{\underline{S}}_{21}^{us} \cdot \underline{a}_1 \tag{4.94}$$

$$\underline{c}_1^- = \text{diag}\{1/\lambda^{N_{slot}}\} \cdot \underline{\underline{S}}_{22}^{us} \cdot \text{diag}\{1/\lambda^{N_{slot}}\} \cdot \underline{c}_1^+ = \tag{4.95}$$

$$= \text{diag}\{1/\lambda^{N_{slot}}\} \cdot \underline{\underline{S}}_{22}^{us} \cdot \text{diag}\{1/\lambda^{N_{slot}}\} \cdot \underline{\underline{R}} \cdot \underline{\underline{S}}_{21}^{us} \cdot \underline{a}_1 \tag{4.96}$$

where $\underline{\underline{R}}$ is the resonant denominator introduced in (4.93). Moreover, $\underline{a}_1$ is an array of amplitudes of unslotted cable modes (discrete and discretized), $\underline{c}_1^+$, $\underline{c}_1^-$ are arrays of progressive and regressive Bloch waves at the left reference plane of the first slot. Consider now the q-th slot. The incident field on its left reference plane is described, in the Bloch wave basis, by $\underline{c}_q^+$, the one incident on its right reference plane by $\underline{c}_{q+1}^-$, given by

$$\underline{c}_q^+ = \text{diag}\{1/\lambda^{q-1}\} \cdot \underline{c}_1^+ \tag{4.97}$$

$$\underline{c}_{q+1}^- = \text{diag}\{\lambda^{q}\} \cdot \underline{c}_1^- \tag{4.98}$$

We need, however, the representations of the incident fields in the basis of the cable modes and, recalling (4.83), these are given by

$$\underline{p}_q^+ = \underline{\underline{U}}_{11} \cdot \underline{c}_q^+ + \underline{\underline{U}}_{12} \cdot \underline{c}_q^- \tag{4.99}$$

$$\underline{p}_{q+1}^- = \underline{\underline{U}}_{21} \cdot \underline{c}_{q+1}^+ + \underline{\underline{U}}_{22} \cdot \underline{c}_{q+1}^- \tag{4.100}$$

We have, in this way, all the data for computing the magnetic current coefficients on the q-th slot via (4.58).
With this formulation it is possible to solve also the canonical problem of a junction between an unslotted and a semi-infinite periodically slotted cable, which obviously cannot be analyzed by the radial technique of the preceding chapter. In this case the equations above simplify drastically, since

$$\underline{c}_1^+ = \underline{\underline{S}}_{21}^{us} \cdot \underline{a}_1 \tag{4.101}$$

$$\underline{c}_1^- = 0 \tag{4.102}$$

so that the incident waves on the q-th slot are

$$\underline{p}_q^+ = \underline{\underline{U}}_{11} \cdot \underline{c}_q^+ \tag{4.103}$$

$$\underline{p}_{q+1}^- = \underline{\underline{U}}_{21} \cdot \underline{c}_{vq+1}^+ \tag{4.104}$$

and, again, we can compute the magnetic current coefficients by (4.58)

Coming to the second method for the field computation, it is to be remarked that it is relatively easy to evaluate the radiated fields, as functions of ρ, φ, only in the reference planes of each cell.

For this purpose we may recall (4.60), which requires only the computation of the progressive and regressive wave amplitudes $\underline{p}_q^\pm$. The formulas of this section are sufficient for this goal. The integrals involved in the definition of the spectral composite modes are to be computed using special numerical schemes, more details are shown in Section 10.5.

The computation of the radiated field in points not lying on the cell reference planes is more involved, since composite modes are all coupled. This means that first the amplitudes of the single radiation modes have to be found. These are then moved to the points where they are needed.

CONTINUOUS SPECTRUM MODE EIGENFUNCTIONS

TM modes:

$$e_{\rho\,\mathrm{ext}}(\rho,\varphi;\tau,m) = -\sqrt{\frac{\tau}{2\pi}}\left[J'_m(\tau\rho) - \frac{J_m(\tau\,\rho_2)}{H_m^{(2)}(\tau\,\rho_2)} H_m'^{(2)}(\tau\rho)\right] \mathrm{e}^{-j\,m\,\varphi}$$

$$e_{\varphi\,\mathrm{ext}}(\rho,\varphi;\tau,m) = -\frac{j\,m}{\rho\sqrt{2\pi\tau}}\left[J_m(\tau\rho) - \frac{J_m(\tau\,\rho_2)}{H_m^{(2)}(\tau\,\rho_2)} H_m^{(2)}(\tau\rho)\right] \mathrm{e}^{-j\,m\,\varphi}$$

$$e_{z\,\mathrm{ext}}(\rho,\varphi;\tau,m) = -\frac{j\tau}{\sqrt{k_0^2-\tau^2}}\left[J_m(\tau\rho) - \frac{J_m(\tau\,\rho_2)}{H_m^{(2)}(\tau\,\rho_2)} H_m^{(2)}(\tau\rho)\right] \mathrm{e}^{-j\,m\,\varphi}$$

$$h_{\rho\,\mathrm{ext}}(\rho,\varphi;\tau,m) = \frac{j\,m}{\rho\sqrt{2\pi\tau}}\left[J_m(\tau\rho) - \frac{J_m(\tau\,\rho_2)}{H_m^{(2)}(\tau\,\rho_2)} H_m^{(2)}(\tau\rho)\right] \mathrm{e}^{-j\,m\,\varphi}$$

$$h_{\varphi\,\mathrm{ext}}(\rho,\varphi;\tau,m) = -\sqrt{\frac{\tau}{2\pi}}\left[J'_m(\tau\rho) - \frac{J_m(\tau\,\rho_2)}{H_m^{(2)}(\tau\,\rho_2)} H_m'^{(2)}(\tau\rho)\right] \mathrm{e}^{-j\,m\,\varphi}$$

$$h_{z\,\mathrm{ext}}(\rho,\varphi;\tau,m) = 0$$

TE modes:

$$e_{\rho\,\mathrm{ext}}(\rho,\varphi;\tau,m) = \frac{j\,m}{\rho\sqrt{2\pi\tau}}\left[J_m(\tau\rho) - \frac{J'_m(\tau\,\rho_2)}{H_m'^{(2)}(\tau\,\rho_2)} H_m^{(2)}(\tau\rho)\right] \mathrm{e}^{-j\,m\,\varphi}$$

$$e_{\varphi\,\mathrm{ext}}(\rho,\varphi;\tau,m) = \sqrt{\frac{\tau}{2\pi}}\left[J'_m(\tau\rho) - \frac{J'_m(\tau\,\rho_2)}{H_m'^{(2)}(\tau\,\rho_2)} H_m'^{(2)}(\tau\rho)\right] \mathrm{e}^{-j\,m\,\varphi}$$

$$e_{z\,\mathrm{ext}}(\rho,\varphi;\tau,m) = 0$$

$$h_{\rho\,\mathrm{ext}}(\rho,\varphi;\tau,m) = -\sqrt{\frac{\tau}{2\pi}}\left[J'_m(\tau\rho) - \frac{J'_m(\tau\,\rho_2)}{H_m'^{(2)}(\tau\,\rho_2)} H_m'^{(2)}(\tau\rho)\right] \mathrm{e}^{-j\,m\,\varphi}$$

$$h_{\varphi\,\mathrm{ext}}(\rho,\varphi;\tau,m) = \frac{j\,m}{\rho\sqrt{2\pi\tau}}\left[J_m(\tau\rho) - \frac{J'_m(\tau\,\rho_2)}{H_m'^{(2)}(\tau\,\rho_2)} H_m^{(2)}(\tau\rho)\right] \mathrm{e}^{-j\,m\,\varphi}$$

$$h_{z\,\mathrm{ext}}(\rho,\varphi;\tau,m) = -\frac{j\tau}{\sqrt{k^2-\tau^2}}\sqrt{\frac{\tau}{2\pi}}\left[J_m(\tau\rho) - \frac{J'_m(\tau\,\rho_2)}{H_m'^{(2)}(\tau\,\rho_2)} H_m^{(2)}(\tau\rho)\right] \mathrm{e}^{-j\,m\,\varphi}$$

with $\tau \in (0,\infty)$ and $m \in \mathbb{Z}$

Table 4.1: Mode eigenfunctions of the free space region around the cable

Chapter 5

The Eigencurrent Approach

5.1 Introduction

In Chapter 3 the scattering problem of a TEM mode incident on a LCX has been formulated in terms of a magnetic field integral equation, which has been solved employing the MoM in the Galerkin form. For this purpose, a suitable set of basis functions has been chosen and the solution has been obtained by inversion of the corresponding moment matrix $\underline{\underline{A}}$. As already outlined, one of the main limitations of this method is related to the size of $\underline{\underline{A}}$, which increases linearly with the number of slots in the array. This point is particularly critical since standard LCXs contain thousands of slots.

To overcome this problem, an alternative approach, based on Bloch Wave Theory, has been presented in Chapter 4. This method requires that all the slots are equal and equally spaced.

Here we describe another method, based on the computation of the approximate eigenvalues and eigenvectors of $\underline{\underline{A}}$ as a linear concatenation of the eigencurrents of a subarray of the entire antenna. In this way, it is possible to obtain the electromagnetic solution avoiding the storage and inversion of a large moment matrix. This method was developed originally in [31] for the analysis of a linear array of patches.

5.2 The Idea of the Eigencurrent Approach

The concept of eigenfunction of a linear operator is so widespread in the mathematical and physical literature that there is no need to recall its importance for an intrinsic characterization of the operator itself [32]. In this section we start describing its application in the numerical solution of the electromagnetic problem under consideration, then the basis idea of Eigencurrent Approach is discussed in detail. Let us consider the HFIE derived in Chapter 3, rewritten here for the reader's convenience:

$$\underline{H}^{inc}(z,\varphi) = \int_{\Sigma} \underline{\underline{\mathcal{Y}}}^{tot}(z-z',\varphi-\varphi') \cdot \underline{\mathbb{J}}_m(z',\varphi')dz'd\varphi' \tag{5.1}$$

For the application of the Galerkin MoM, a set of basis functions $\{\underline{u}_c(z,\varphi)\}$ (with $c = 1,..,N_f$) was introduced and the following linear system was obtained

$$\underline{\underline{A}} \cdot \underline{x} = \underline{b} \tag{5.2}$$

where:

$$\begin{aligned} A_{r,c} &= < \int_{\Sigma} \underline{\underline{\mathcal{Y}}}^{tot}(z-z',\varphi-\varphi') \cdot \underline{u}_c(z',\varphi')dz'd\varphi',\, \underline{u}_r(z,\varphi) > && (5.3)\\ b_r &= < \underline{H}^{inc},\, \underline{u}_r > && (5.4) \end{aligned}$$

and $< \cdot, \cdot >$ is the standard L^2- scalar product. Since the matrix $\underline{\underline{A}}$ is full, the solution can only be obtained numerically.

Let $\{\lambda_n\}$ and $\{\underline{\psi}_n(z,\varphi)\}$, with $n = 1,..,N_f$, be the sets of the eigenvalues and eigenfunctions of the admittance operator. The eigenvalues have the dimension of admittances, the eigenfunctions of magnetic currents: for this reason, they will also be called eigencurrents. If we use these eigenfunctions as MoM expansion functions, the left hand side of (5.1) reduces to:

$$\begin{aligned} &\int_{\Sigma} \underline{\underline{\mathcal{Y}}}^{tot}(z-z',\varphi-\varphi') \cdot \underline{\mathbb{J}}_m(z',\varphi')dz'd\varphi' = \\ &= \sum_c \tilde{x}_c \int_{\Sigma} \underline{\underline{\mathcal{Y}}}^{tot}(z-z',\varphi-\varphi') \cdot \underline{\psi}_c(z',\varphi')dz'd\varphi' = \sum_c \lambda_c \tilde{x}_c \underline{\psi}_c(z,\varphi) \end{aligned} \tag{5.5}$$

and (5.2) becomes

$$\underline{\underline{\tilde{A}}} \cdot \underline{\tilde{x}} = \underline{\tilde{b}} \tag{5.6}$$

where:

$$\begin{aligned} \tilde{A}_{r,c} &= \lambda_c < \underline{\psi}_c, \underline{\psi}_r > && (5.7)\\ \tilde{b}_r &= < \underline{H}^{inc}, \underline{\psi}_r > && (5.8) \end{aligned}$$

In general the eigenfunctions $\underline{\psi}_r(z,\varphi)$ are not orthonormal with respect to the standard L^2-scalar product, so that the moment matrix $\underline{\underline{\tilde{A}}}$ is still full and this choice of basis functions is not more advantageous than that of Chapter 3. However, if we define a new scalar product $< \cdot, \cdot >_s$ such that the eigenfunctions are orthonormal[1], the new moment matrix is diagonal:

$$\tilde{A}^{new}_{r,c} = \lambda_c < \underline{\psi}_c, \underline{\psi}_r >_s = \lambda_c \, \delta_{r,c} \tag{5.9}$$

$$\tilde{b}^{new}_r = < \underline{H}^{inc}, \underline{\psi}_r >_s \tag{5.10}$$

and the solution of the linear system is straightforward. In particular, the $r-$th component of the unknown vector $\underline{\hat{x}}$ is given by:

$$\hat{x}_r = \frac{1}{\lambda_r} < \underline{H}^{inc}, \underline{\psi}_r >_s \tag{5.11}$$

and, finally, $\underline{\mathbb{J}}_m(z,\varphi)$:

$$\underline{\mathbb{J}}_m(z,\varphi) = \sum_n \frac{1}{\lambda_n} < \underline{H}^{inc}, \underline{\psi}_n >_s \; \underline{\psi}_n(z,\varphi) \tag{5.12}$$

The eigencurrents that match better the incident field $\underline{H}^{inc}$ give rise to the largest scalar products. Since we consider thin slots and the incident field is the TEM mode, which is $\hat{\varphi}$-independent, it is apparent that the greatest contribution is given by the less oscillating eigencurrents $\underline{\psi}_n(z,\varphi)$. Since the eigenvalues of these are the smallest ones, the first terms of the summation are dominant.

In principle, the eigenfunctions $\{\underline{\psi}_n(z,\varphi)\}$ could be computed from the eigenvectors of the matrix $\underline{\underline{A}}$. However, there is a more efficient method, which provides a good approximation of the eigenfunctions and eigenvalues of the admittance operator, starting from a relatively small moment matrix.

Let us consider an array composed by N_{sub} identical subarrays. The antenna, then, can be described by the position of these subarrays and the geometry of a single subarray. We can say that the array is generated by a single subarray, which will be called “generating subarray”.
Assume that the generating subarray has eigencurrents $\underline{\psi}^{sub}_n(z,\varphi)$ with eigenvalues λ^{sub}_n with $n = 1, \ldots, N^{sub}_{eig}$ where N^{sub}_{eig} is the number of basis functions on the subarray. If the mutual coupling between the subarrays is ignored, the eigenvalues of the complete array are λ^{sub}_n each with multiplicity N_{sub}. In the same conditions, the eigencurrents corresponding to the eigenvalue

---

[1] In the case of degenerate eigenvalues we may conclude on physical grounds (conservation of energy) that the geometric and algebraic multiplicity of the eigenvalue are equal

λ_n^{sub} belong to the linear span of the N_{sub} independent currents, each of which is zero on all subarrays but one, where it is equal to $\underline{\psi}_n^{sub}(z,\varphi)$. We define E_n the set of these independent currents which correspond to the eigenvalue λ_n^{sub}. Figure 5.1 shows a symbolic representation of E_n for a linear array of four subarrays. If the mutual coupling is not ignored, the eigencurrents $\{\underline{\psi}_r(z,\varphi)\}$ are given by a linear combination of all the elements of the set $E = \bigcup_{n=1}^{N_{eig}^{sub}} E_n$. It is convenient to group these eigencurrents into N_{eig}^{sub} families according to which set E_n the dominant component of $\underline{\psi}_r(z,\varphi)$ belongs; the eigenvalues are grouped accordingly. Hence we use the notation $\{\underline{\psi}_{nq}(z,\varphi)\}$ and $\{\lambda_{nq}\}$, where the subscript q, ($q = 1,\dots,N_{sub}$) denotes the elements of the family n, ($q = 1,\dots,N_{sub}$). It will be shown in 5.7.2 that the elements of all the eigenvectors with a specific q have the same structure.

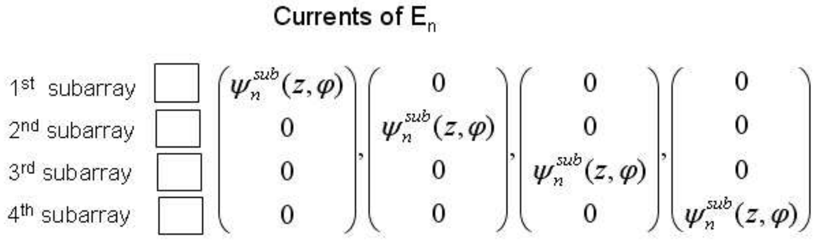

Figure 5.1: Schematic representation of the elements of E_n. The subarrays are symbolically denoted by rectangles

From another point of view, the generic eigencurrent $\underline{\psi}_{nq}(z,\varphi)$ can be seen as the sum of a "dominant part", which is a linear combination of the elements of E_n, and a "perturbation term", which is, instead, a linear combination of the elements of the other sets $E_{n'}$, with $n' \neq n$. Both terms are related to the coupling between the subarrays. In particular, we define "intra-mode" coupling the one between the elements of E_n, which is responsible of the "dominant part". The "inter-mode coupling" is the one taking place between the elements of different sets.

It is useful to introduce a complex valued perturbation ϵ_{nq} for each eigenvalue,

$$\epsilon_{nq} = \frac{\lambda_{nq} - \lambda_n^{sub}}{\lambda_n^{sub}}$$

The absolute value of ϵ_{nq} yields the relative deviation of the q-th eigenvalue of the family $\{\lambda_{nq}\}$ from the "reference" eigenvalue λ_n^{sub}. The range of this parameter depends clearly on the strength of the mutual coupling.

In order to fix the preceding concepts and to describe the main idea of the Eigencurrent Approach, it is useful to consider a simple example in detail. For this purpose we consider an array composed by two generating subarrays and four basis functions on each subarray. The generating subarray may consist of a single slot, as well as of a group of (not necessarily identical) slots. Assume that the eigenvalues λ_n^{sub}, with $n = 1, \ldots, 4$, and the eigencurrents $\underline{\psi}_n^{sub}(z, \varphi)$ of the generating subarray are known, as well as the inner product $< \cdot, \cdot >_{sub}$ with respect to which these eigencurrents are orthonormal. By definition, if the eigencurrents are chosen as expansion functions, the moment matrix of the generating subarray with respect to $< \cdot, \cdot >_{sub}$ is diagonal, with the eigenvalues λ_n^{sub} as elements (see Figure 5.2). Since the eigencurrents $\underline{\psi}_n^{sub}(z, \varphi)$ are

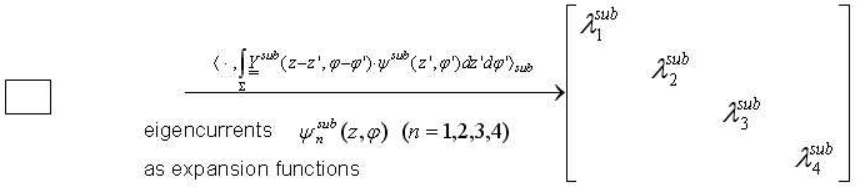

Figure 5.2: Moment matrix of the subarray: the basis functions are the eigencurrents and the inner product is $< \cdot, \cdot >_{sub}$

orthonormal with respect to $< \cdot, \cdot >_{sub}$, the currents of E are orthonormal with respect to the composite inner product, defined as:

$$< \cdot, \cdot >_{comp} = \sum_{q=1}^{N_{sub}} < (\cdot)_q, (\cdot)_q >_{sub} \tag{5.13}$$

The dots in $< \cdot, \cdot >_{comp}$ indicate the currents on the complete array, while $(\cdot)_q$ is a symbolic notation for the component of the corresponding currents on the $q-$th subarray. Note that (5.13) represents the natural generalization of $< \cdot, \cdot >_{sub}$ for the entire array. Indeed, if the mutual coupling is ignored the moment matrix is diagonalized by the currents of E with the eigenvalues λ_n^{sub} on the diagonal each with multiplicity N_{sub} (in the case under consideration N_{sub} is equal to two, see Figure 5.3). On the other hand, if the mutual coupling is not ignored, the moment matrix has a block structure: the blocks on the main diagonal are diagonal with $\{\lambda_n^{sub}\}$ as elements, while the off-diagonal blocks are non zero full matrices (see Figure 5.4). Let us see the meaning of the elements of the off-diagonal blocks in terms of inter- and intra-mode coupling. The element $(1, N_{eig}^{sub}+1)$ represents the intra-mode coupling between the elements of E_1, while the elements $(1, N_{eig}^{sub}+2), (1, N_{eig}^{sub}+3), \ldots, (1, 2N_{eig}^{sub})$ represents the inter-mode coupling between E_1 and

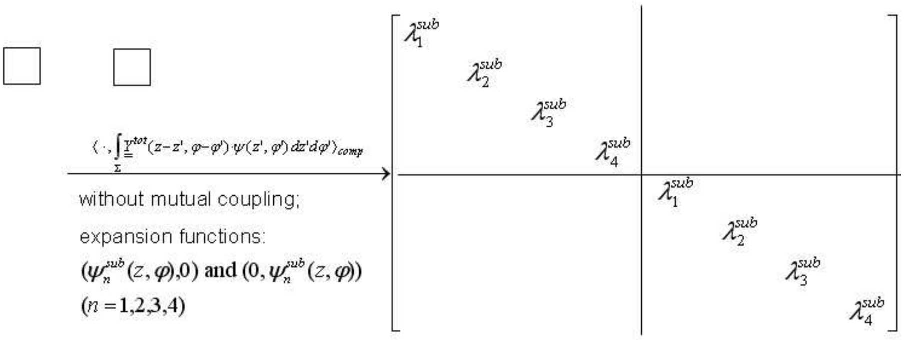

Figure 5.3: Moment matrix of the complete array using the subarray eigencurrents as basis functions and $< \cdot, \cdot >_{comp}$ as scalar product. In this case the mutual coupling is neglected

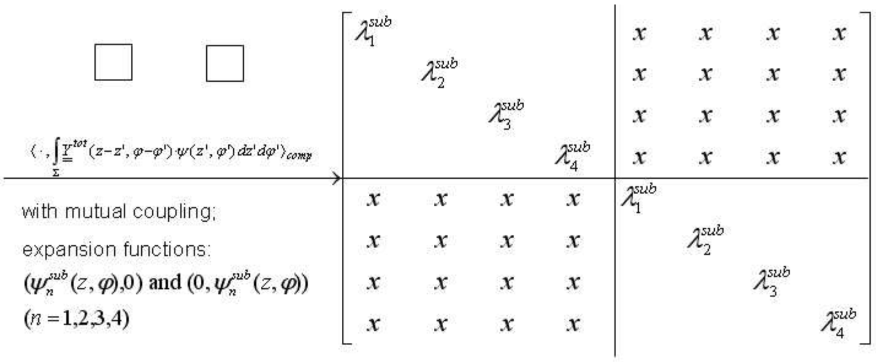

Figure 5.4: Moment matrix of the complete array using the subarray eigencurrents as basis functions and $< \cdot, \cdot >_{comp}$ as scalar product. In this case the mutual coupling between subarrays is not neglected

the other sets $E_{n'}$, with $n' = 2, \ldots, N_{eig}^{sub}$. Clearly, the presence of the off-diagonal block terms produces the perturbations $\{\varepsilon_{nq}\}$.

The elements of the eigenvectors $\underline{u}_{nq}$ of this matrix are the expansion coefficients of the eigencurrents $\underline{\psi}_{nq}(z,\varphi)$ in the basis of the the functions in the set E, *i.e.* the eigencurrents of the array in which the mutual coupling between subarrays is ignored. In general, these eigenvalues and eigencurrents can be computed only numerically from the complete moment matrix. However, if the spread of a group of eigenvalues, say the $n-$th group, is negligibly small, its elements can be set equal to λ_n^{sub} and the corresponding eigencurrents can be safely replaced by the currents of E_n. Indeed, in this case, the currents of E_n are coupled neither with each other nor with the other sets $E_{n'}$, *i.e.* the inter- and intra-mode couplings are negligible. This fact means that the

corresponding entries in the moment matrix are negligible and can be set equal to zero, *i.e.* the size of the moment matrix can be reduced.
An example is shown in Figure 5.5 where the spread of the 4^{th} group is assumed to be negligible, so that the eigenvalues and eigencurrents related to the other groups can be computed from the reduced moment matrix (see Figure 5.6) with a reduced computational effort.
Once the eigencurrents $\underline{\psi}_{nq}(z, \varphi)$ have been computed, one can construct a suitable scalar product $< \cdot, \cdot >_A$ such that the corresponding moment matrix is diagonal with the eigenvalues λ_{nq} along the diagonal. Following the example that we are discussing, we would finally obtain the matrix shown in Figure 5.7 where λ_{4q} has been set equal to λ_4^{sub} since the spread was considered negligible.

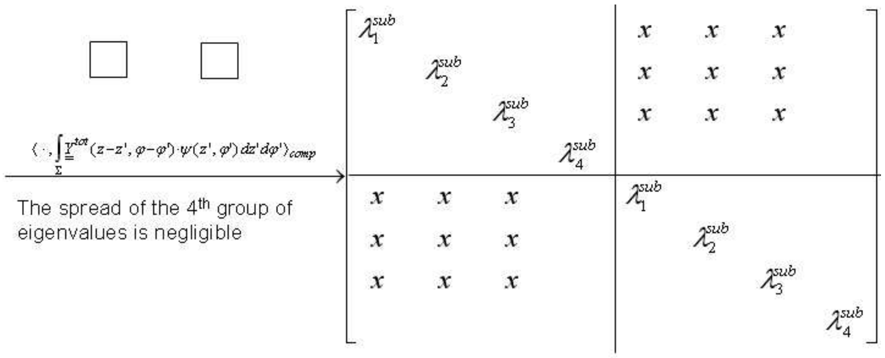

Figure 5.5: Moment matrix of the complete array using the subarray eigencurrents as basis functions and $< \cdot, \cdot >_{comp}$ as scalar product. The spread of the 4^{th}-group of eigenvalues is assumed to be negligible

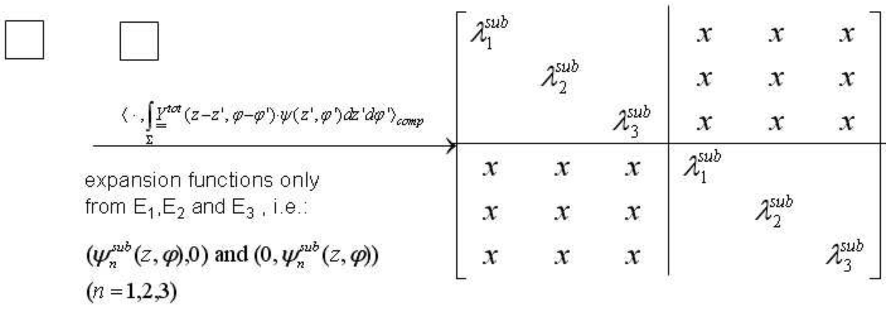

Figure 5.6: Reduced moment matrix of the complete array using the subarray eigencurrents as basis functions and $< \cdot, \cdot >_{comp}$ as scalar product

In principle, the described procedure can be iterated: the array made of two subarrays can be

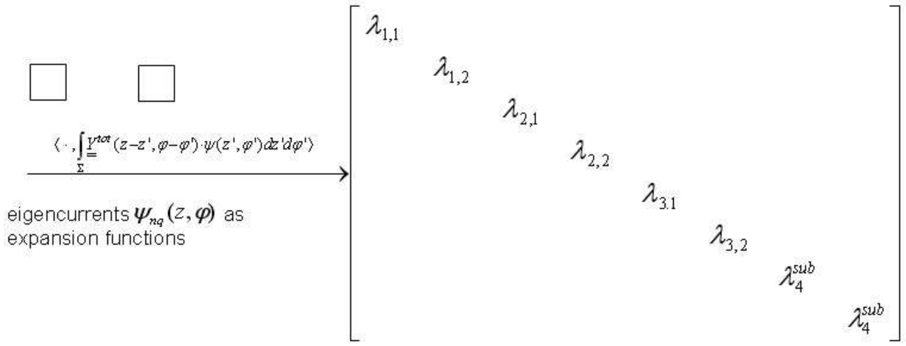

Figure 5.7: Moment matrix of the complete array using the eigencurrents $\{\underline{\psi}_{nq}\}$ as basis functions

viewed as the generating subarray of a larger structure.

In general, we need to construct the moment matrix only from sets E_n that contribute significantly to the mutual coupling between the subarrays.

These sets are not known a priori, but, as discussed in [31], we expect that they correspond to the lowest order eigenvalues. In 5.8 we carry out a direct analysis of the MoM matrix elements, which confirms this guess.

5.3 Eigencurrent Approach

We are now ready to describe the Eigencurrent Approach based on the preceding ideas. Here we list the steps of the method as reported in [31], the calculation details are described in the next sections of this chapter.

The method can be used in an iterative way, so here we describe the structure of the cycle. Assume that the eigenvalues λ_n^{sub} and eigencurrents $\underline{\psi}_n^{sub}(z,\varphi)$, with $n = 1, \ldots, N_{eig}^{sub}$, of the generating subarray are known as well as the scalar product $< \cdot, \cdot >_{sub}$ such that $\underline{\psi}_n^{sub}(z,\varphi)$ are orthonormal.

The approximate eigencurrents and eigenvalues of the complete array can be computed as follows:

1) Choose a new (higher level) generating sub-array of the complete array, consisting of N_{sub}

elements; it can even coincide with the complete array.

2) Define the sets E_n ($n = 1, \dots N_{eig}^{sub}$) such that each set E_n consists of N_{sub} independent currents, each of which is zero on all the sub-arrays but one, where it is equal to $\underline{\psi}_n^{sub}(z, \varphi)$. Let E be the union of these sets.

3) Let E^{cpl} be the union of the sets E_n that are expected to contribute to the mutual coupling. We construct a reduced moment matrix of the array using the scalar product $< \cdot, \cdot >_{comp}$ defined in (5.13) and the elements of E^{cpl} as basis functions.

4) Determine the eigenvalues λ_{nq} and the matrix of the eigenvectors $\underline{\underline{U}}_{nq}$ of the reduced moment matrix. Note that λ_{nq} are the approximate eigenvalues of the complete moment matrix; the eigenvectors represent the expansion coefficients of the eigencurrents $\underline{\psi}_{nq}(z, \varphi)$ in the basis of the elements of E^{cpl}. Let E^{eig} be the set of these eigencurrents.

5) Investigate the spreads of the families of eigenvalues $\{\lambda_{nq}\}_{q=1}^{N_{sub}}$ whether more sets E_n are required to describe the mutual coupling. If more sets are required, return to step 3).

6) Let E^{unc} be the union of the sets E_n that are not taken into account in the reduced moment matrix in step 3). By assumption the complete moment matrix is diagonalized by the elements of $E^{eig} \bigcup E^{unc}$, using a suitable scalar product $< \cdot, \cdot >_a$ which consists of a combination of $< \cdot, \cdot >_{sub}$ and $< \cdot, \cdot >_{comp}$;

7) Stop if the considered array is equal to the complete one. Otherwise return to step 1) where the new generating subarray becomes the array just considered. The scalar product $< \cdot, \cdot >_{sub}$ is replaced by $< \cdot, \cdot >_a$ and $\{\lambda_n^{sub}\}$ and $\{\underline{\psi}_n^{sub}(z, \varphi)\}$ are replaced by the new set of eigenvalues and by the elements of $E^{eig} \bigcup E^{unc}$, respectively.

The following initialization procedure can be employed in order to start the cycle above:

a) Choose a subarray;

b) Choose a set of basis functions. The expansion functions can be, for example, rooftops or entire domain basis functions;

c) Construct the moment-matrix $\underline{\underline{A}}_{sub}$ using the standard L^2 inner product;

d) Determine the eigenvalues and eigenvectors of $\underline{\underline{A}}_{sub}$;

e) Construct the new scalar product with respect to which the eigencurrents are orthonormal;

f) Start the Eigencurrent-Approach;

5.4 Initialization: Computation of the eigencurrents of a single slot

We analyze in detail the application of the Eigencurrent approach in the simple case of thin slots. Moreover, in the following, we will consider a single slot as generating subarray.
Let $\{u_n^{sub}(z,\varphi)\}$, with $n = 1, \ldots, N_{eig}^{sub}$, be the set of basis functions defined on the slot. Applying the MoM in the Galerkin form (see Chapter 3) we obtain the following linear system:

$$\underline{\underline{A}}_{sub} \cdot \underline{x}_{sub} = \underline{b}_{sub} \tag{5.14}$$

The matrix $\underline{\underline{A}}_{sub}$ is a $N_{eig}^{sub} \times N_{eig}^{sub}$ square matrix while $\underline{b}_{sub}$ is a $N_{eig}^{sub} \times 1$ column vector. Let $\underline{\underline{U}}_{sub}$ and $\{\lambda_n^{sub}\}$ be the matrices which contain the eigenvectors and eigenvalues of $\underline{\underline{A}}_{sub}$, respectively; in particular the r-th column of $\underline{\underline{U}}_{sub}$ is the r-th eigenvector of $\underline{\underline{A}}_{sub}$ with eigenvalue λ_r^{sub}. These eigenvectors contain the expansion coefficients, in the basis $\{u_n^{sub}(z,\varphi)\}$ of the slot eigencurrents $\{\underline{\psi}_r^{sub}(z,\varphi)\}$; the explicit expression for the r-th eigencurrent is:

$$\underline{\psi}_r^{sub}(z,\varphi) = \sum_{n=1}^{N_{eig}^{sub}} U_{sub}\big|_{n,r}\, \underline{u}_n^{sub}(z,\varphi) \tag{5.15}$$

To construct the new scalar product mentioned in step e) of the initialization procedure, we notice that the eigencurrents $\{\underline{\psi}_r^{sub}(z,\varphi)\}$ are linearly independent since $\underline{\underline{A}}_{sub}$ is a full rank matrix. It is well known that it is possible to define a set of functions $\{\underline{\phi}_p^{sub}(z,\varphi)\}$ bi-orthogonal to $\{\underline{\psi}_r^{sub}(z,\varphi)\}$. For this purpose we need first to compute the Gram Matrix $\underline{\underline{G}}_U$ of $\{\underline{\psi}_r^{sub}(z,\varphi)\}$ with respect the L^2- inner product $< \cdot, \cdot >$. It can be shown that the matrix $\underline{\underline{G}}_U$ is given by:

$$\underline{\underline{G}}_U = \underline{\underline{U}}_{sub}^H \cdot \underline{\underline{G}} \cdot \underline{\underline{U}}_{sub}$$

where the matrix $\underline{\underline{G}}$ is the Gram-matrix, obtained using the L^2-scalar product, of the basis functions defined on the slot. The functions $\{\underline{\phi}_p^{sub}(z,\varphi)\}$ are given by:

$$\underline{\phi}_p^{sub}(z,\varphi) = \sum_{r=1}^{N_{eig}^{sub}} G_U^{-1}|_{rp}\, \underline{\psi}_r^{sub}(z,\varphi) \tag{5.16}$$

and the new inner product $< \cdot, \cdot >_{sub}$ is defined as

$$< \underline{w}, \underline{\psi}_r >_{sub} = < \underline{w}, \underline{\phi}_r > = \int_\Sigma \underline{w}(z,\varphi) \cdot \underline{\phi}_r^*(z,\varphi) dz\, d\varphi \tag{5.17}$$

where $\underline{w} = \underline{w}(z,\varphi)$ is a generic function of (z,φ) and Σ represents the support of the slot. Hence, the procedure can be described in two alternative ways:

- the same set of functions $\{\underline{\psi}_r^{sub}(z,\varphi)\}$ is used both for expansion and testing, but the inner product used is $< \cdot, \cdot >_{sub}$
- $\{\underline{\psi}_r^{sub}(z,\varphi)\}$ are used for expansion and $\{\underline{\phi}_p^{sub}(z,\varphi)\}$ for testing but the standard L^2 inner product is adopted (non-Galerkin procedure)

It is useful to derive a compact form of the preceding results. Let $\underline{\underline{\Phi}}_{sub}$ be the matrix whose columns contain the expansion coefficients of $\{\underline{\phi}_p^{sub}(z,\varphi)\}$ in the basis $\{\underline{u}_n^{sub}(z,\varphi)\}$. Let us consider again the linear system (5.14), repeated here for the reader's convenience:

$$\underline{\underline{A}}_{sub} \cdot \underline{x}_{sub} = \underline{b}_{sub} \tag{5.18}$$

We change basis from $\{\underline{u}_n^{sub}(z,\varphi)\}$ to $\{\underline{\psi}_r^{sub}(z,\varphi)\}$ via $\underline{x}_{sub} = \underline{\underline{U}}_{sub} \cdot \underline{\hat{x}}_{sub}$ and multiply both sides of (5.14) by the matrix $\underline{\underline{\Phi}}_{sub}^H$:

$$\underline{\underline{\Phi}}_{sub}^H \cdot \underline{\underline{A}}_{sub} \cdot \underline{\underline{U}}_{sub} \cdot \underline{\hat{x}}_{sub} = \underline{\underline{\Phi}}_{sub}^H \cdot \underline{b}_{sub} \tag{5.19}$$

The product $\underline{\underline{\Phi}}_{sub}^H \cdot \underline{\underline{A}}_{sub} \cdot \underline{\underline{U}}_{sub}$ coincides with the diagonal matrix $diag\{\lambda_n^{sub}\}$, hence the vector $\underline{\hat{x}}_{sub}$, which contains the unknown expansion coefficients of the equivalent magnetic current distribution $\underline{\mathbb{J}}_m$ in the basis of the eigencurrents of the sub-array, is given by:

$$\underline{\hat{x}}_{sub} = diag\{\frac{1}{\lambda_n^{sub}}\} \cdot \underline{\underline{\Phi}}_{sub}^H \cdot \underline{b}_{sub} \tag{5.20}$$

and finally:

$$\underline{x}_{sub} = \underline{\underline{U}}_{sub} \cdot\ diag\{\frac{1}{\lambda_n^{sub}}\} \cdot \underline{\underline{\Phi}}_{sub}^H \cdot \underline{b}_{sub} \tag{5.21}$$

Table 5.1: First four slot eigenvalues $[\Omega^{-1}]$, computed using 20 triangular functions

λ_1^{sub}	$4.6 \cdot 10^{-5} - 1.5 \cdot 10^{-4}\jmath$
λ_2^{sub}	$6.8 \cdot 10^{-6} - 8.1 \cdot 10^{-4}\jmath$
λ_3^{sub}	$3.8 \cdot 10^{-6} - 1.7 \cdot 10^{-3}\jmath$
λ_4^{sub}	$8.3 \cdot 10^{-7} - 2.9 \cdot 10^{-3}\jmath$

5.5 Single slot Eigencurrents

In this section we analyze the eigencurrents of a single slot. We want first to illustrate the obvious fact that these eigencurrents can be computed with different choices of basis functions. Clearly, there are particular sets that are more representative of the eigencurrents and therefore they guarantee a more rapid convergence than other ones.

Since we use basis functions that are not orthonormal with respect to the scalar product L^2, the eigenfunctions and eigenvalues of the admittance operator have been determined solving the generalized eigenvalue problem:

$$\underline{\underline{A}}_{sub} \cdot \underline{x} = \lambda\, \underline{\underline{G}} \cdot \underline{x} \tag{5.22}$$

where $\underline{\underline{G}}$ is the Gram matrix of the expansion functions.

Let us consider a cable with the following parameters: inner and outer conductor radii $a = 12$ mm, $b = 30$ mm, width $s = 3$ mm, angular aperture $\alpha = 180°$, frequency $f = 1$ GHz, and relative permittivity $\varepsilon_{r1} = 1.26$. Since the slots are thin, we employ one weighted Chebyshev polynomial of the first kind for the z dependence. As for the $\varphi-$dependence, we use two different sets, piecewise triangular functions and weighted Chebyshev polynomials of the second kind (see section 3.4 for more details). The first four eigencurrents, computed with twenty triangular functions, are shown in Figure 5.8. They are sorted so that the corresponding eigenvalues, listed in Table 5.1, satisfy $|\lambda_n| < |\lambda_{n+1}|$. This ordering will always be used. Let us repeat the computation by using a basis of eight weighted Chebyshev polynomials of the second kind. The first four eigencurrents are shown in Figure 5.9, the corresponding eigenvalues are listed in Table 5.2.

Figures 5.10 and 5.11 show a comparison between the first eight eigencurrents in the basis of these two sets. We can note that there is a good agreement for the first four eigenfunctions, while the others do not match so well. A better agreement can be reached by increasing the number of basis functions. As a rule of thumb, N_{eig}^{sub} basis functions yield $N_{eig}^{sub}/2$ eigencurrents, so it is in

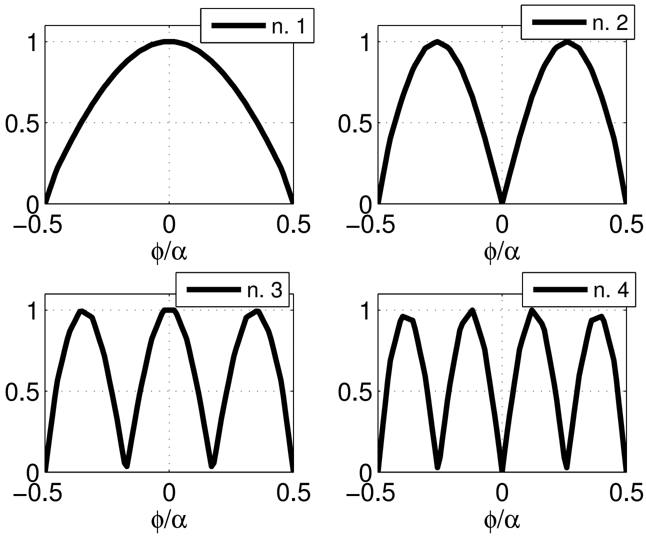

Figure 5.8: First four eigencurrents of a single slot $\underline{\psi}_r^{sub}(0,\varphi)$, computed using 20 triangular functions. Eigenfunctions normalization: maximum value

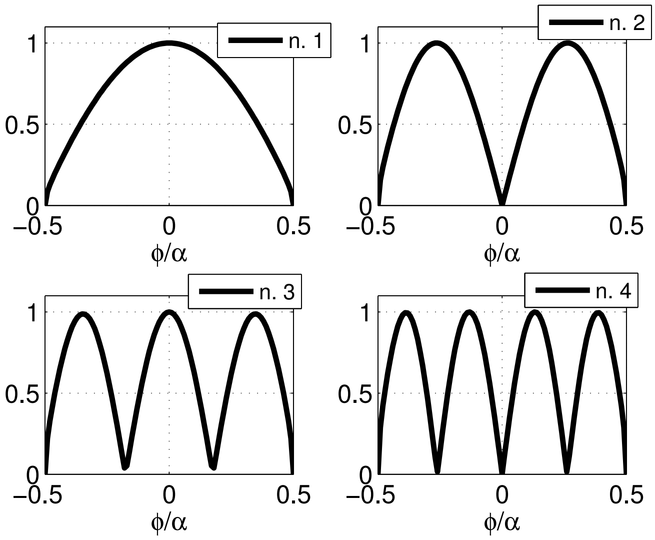

Figure 5.9: First four eigencurrents of a single slot $\underline{\psi}_r^{sub}(0,\varphi)$, computed using 8 weighted Chebyshev polynomials of the second kind. Eigenfunctions normalization: maximum value

Table 5.2: First four slot eigenvalues $[\Omega^{-1}]$ computed using 8 Chebyshev polynomials

λ_1^{sub}	$4.6 \cdot 10^{-5} - 1.4 \cdot 10^{-4} \jmath$
λ_2^{sub}	$7.0 \cdot 10^{-6} - 7.9 \cdot 10^{-4} \jmath$
λ_3^{sub}	$3.9 \cdot 10^{-6} - 1.7 \cdot 10^{-3} \jmath$
λ_4^{sub}	$8.6 \cdot 10^{-7} - 2.8 \cdot 10^{-3} \jmath$

particular the number of Chebyshev functions that must be increased.

Figure 5.12 shows the absolute values of the elements of the matrix of the eigenvectors $\underline{\underline{U}}_{sub}$ in

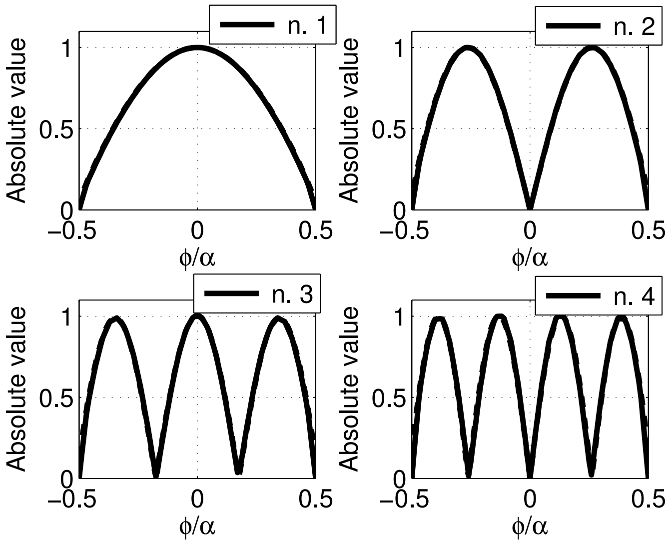

Figure 5.10: Comparison between the first four slot eigencurrents in the basis of the Chebyshev polynomials (solid line) and of the piecewise triangular functions (dashed line).

the case of eight weighted Chebyshev polynomials. It can be noticed that each weighted Chebyshev polynomial is a very good approximation of the slot eigencurrents, since the diagonal terms of the matrix are dominant. Moreover, the corresponding Gram Matrix is quasi-diagonal (see Figure 5.13), which means that the eigencurrents are almost orthogonal. Because of the slot symmetry, the eigencurrents are alternatively even and odd, obviously uncoupled. Since in our application the excitation term is φ-independent, in the following we will consider only the set of the even basis functions.

Since these eigenfunctions are sorted so that $|\lambda_n| < |\lambda_{n+1}|$, these results give a numerical confir-

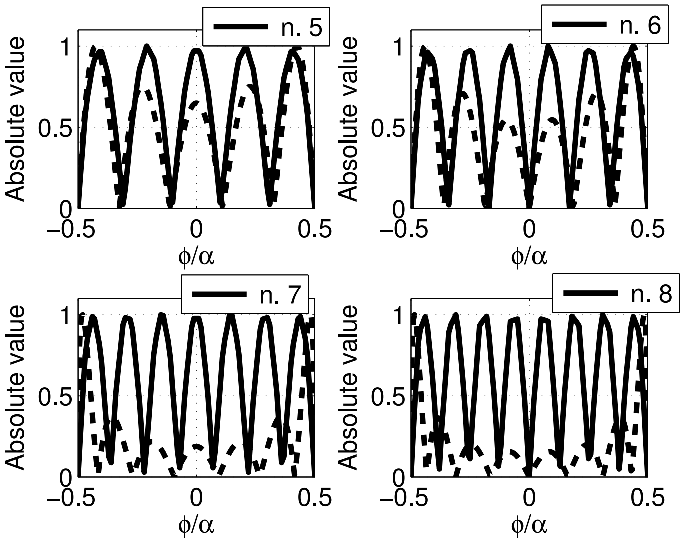

Figure 5.11: Comparison between the following four slot eigencurrents in the basis of the Chebyshev polynomials (solid line) and of the piecewise triangular functions (dashed line).

mation of the statement that larger eigenvalues belong to more oscillating eigenfunctions. Moreover, Figure 5.14 shows a plot of the inverse of the first slot eigenvalues. Note that the curve goes rapidly to zero, so that only few eigencurrents give a significant contribution to $\underline{\mathbb{J}}_m(z, \varphi)$, according to (5.12).

5.6 Parameter dependence of the Eigencurrents of a single slot

In the preceding section we have analyzed the eigencurrents of the admittance operator as a function of the number and kind of basis functions employed in the MoM scheme when the geometrical and electrical characteristics of the cable were fixed.

We want now to investigate the dependence of these eigencurrents on the angular aperture α and the frequency. For this purpose we fix the remaining geometrical and electrical parameters as follows: inner and outer conductor radii $\rho_1 = 12$ mm, $\rho_2 = 30$ mm, width $s = 3$ mm and relative permittivity $\varepsilon_{r1} = 1.26$. In the simulation we use four even weighted Chebyshev polynomials for the φ-dependence. In Figures 5.15 and 5.16 the amplitude and the phase of the

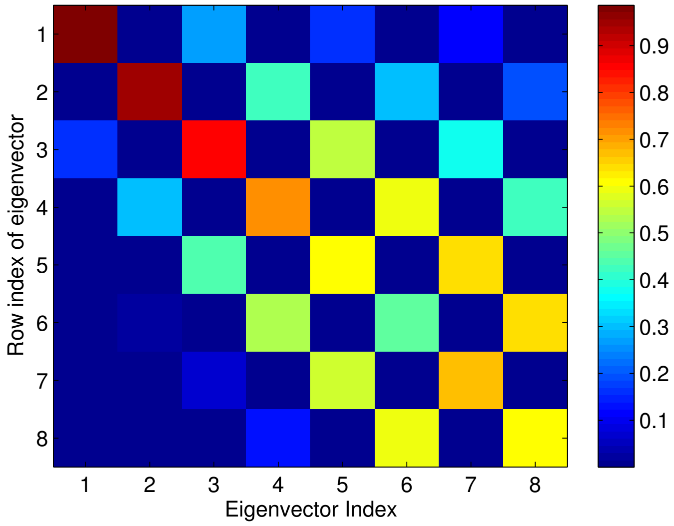

Figure 5.12: Color pattern representation of the eigenvector matrix $\underline{\underline{U}}_{sub}$ for a slot. 8 weighted Chebyshev polynomials were used. Eigenvector normalization: maximum component

first eigencurrent is shown for frequency $f = 1$ GHz and $\alpha = 45°,\ 90°,\ 135°,\ 180°$, respectively. The corresponding eigenvalues are reported in Table 5.3. On the other hand, in Figures 5.17 and 5.18 the amplitude and the phase of the first eigencurrents are shown for $\alpha = 90°$ and frequency $f = 0.25$ GHz, 0.5 GHz, 1 GHz, 2 GHz, while the corresponding eigenvalues are listed in Table 5.4. From Fig. 5.17 it is evident that the eigencurrents are practically independent of frequency and slot size, while the eigenvalues exhibit a consistent variation.

Table 5.3: Slot first eigenvalue $[\Omega^{-1}]$ for various angular apertures

α	λ_1^{sub}
$45°$	$1.3{\cdot}10^{-5} - 2.3{\cdot}10^{-3}j$
$90°$	$2.6{\cdot}10^{-5} - 7.0{\cdot}10^{-4}j$
$135°$	$369{\cdot}10^{-5} - 3.0{\cdot}10^{-4}j$
$180°$	$4.6{\cdot}10^{-5} - 1.4{\cdot}10^{-4}j$

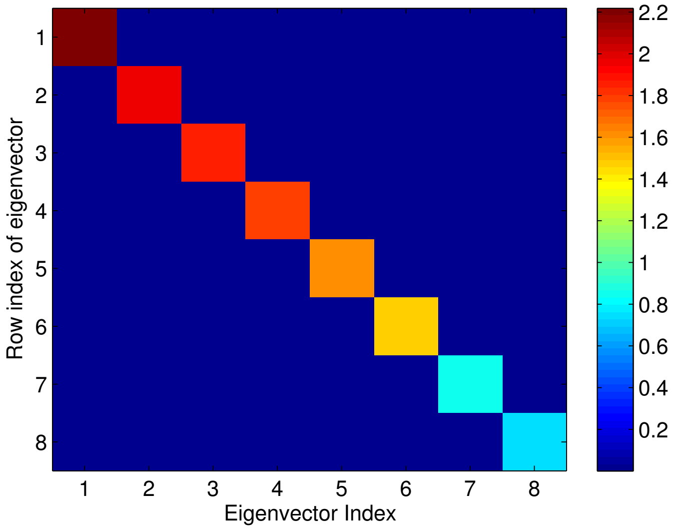

Figure 5.13: Color pattern representation of the Gram matrix of the eigencurrents of a slot (L^2 inner product).

Table 5.4: Slot first eigenvalue $[\Omega^{-1}]$ for various frequencies

f	λ_1^{sub}
0.25 GHz	$2.9{\cdot}10^{-5} - 1.0{\cdot}10^{-3}j$
0.5 GHz	$3.4{\cdot}10^{-5} - 4.6{\cdot}10^{-4}j$
1 GHz	$4.6{\cdot}10^{-5} - 1.4{\cdot}10^{-4}j$
2 GHz	$7.3{\cdot}10^{-5} - 8.7{\cdot}10^{-4}j$

This invariance of the eigencurrents gives a significant computational advantage in the use of the Eigencurrent Approach as analysis tool. Indeed, the eigencurrents need to be computed only for an initial set of geometrical parameters and frequency. The eigenvalues can be derived by the Rayleigh-Ritz quotients:

$$\lambda_n = \frac{< \underline{\psi}_n, \int \underline{\underline{Y}}^{sub} \cdot \underline{\psi}_n >}{< \underline{\psi}_n, \underline{\psi}_n >} \tag{5.23}$$

As an example, Figure 5.19 shows the relative error of the eigenvalues at 2 GHz computed by (5.23) with the eigencurrents evaluated at 0.2 GHz. The agreement is quite good, indeed the maximum relative error is less than 2.6%.

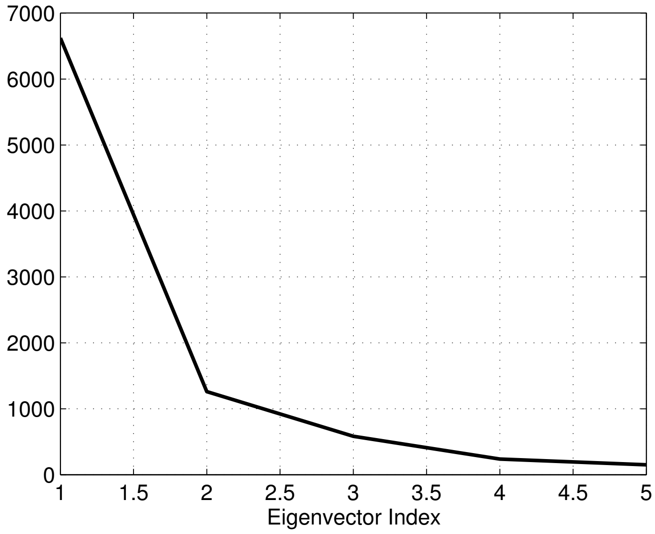

Figure 5.14: Absolute value of the inverse of the eigenvalues of a single slot

5.7 Eigencurrent Approach: Cycle

5.7.1 Calculation Details

In this section we discuss the computation details of the cycle as described in Section 5.3. Once the generating subarray in step 1 has been chosen and the corresponding eigenvalues and eigencurrents have been computed, we construct the sets E_n, as explained in Section 5.2. If all the sets E_n contribute to the mutual coupling between the subarrays, the complete moment matrix has to be computed and no numerical advantage is obtained by the application of the Eigencurrent Approach. If this is not the case, a reduced moment matrix is constructed from a selection of the sets E_n. Assume that the sets $E_1, \ldots, E_{N^{sub}_{cpl}}$, (whose union is denoted E^{cpl}), contribute to the mutual coupling and that, instead, the contribution of the remaining sets $E_{N^{sub}_{cpl}+1}, \ldots, E_{N^{sub}_{eig}}$, whose union is E^{unc}, to the mutual coupling is negligible. Then the complete moment matrix is block diagonal:

$$\underline{\underline{A}} = \begin{pmatrix} \underline{\underline{A}}^{cpl} & 0 \\ & \\ 0 & \underline{\underline{A}}^{unc} \end{pmatrix} \tag{5.24}$$

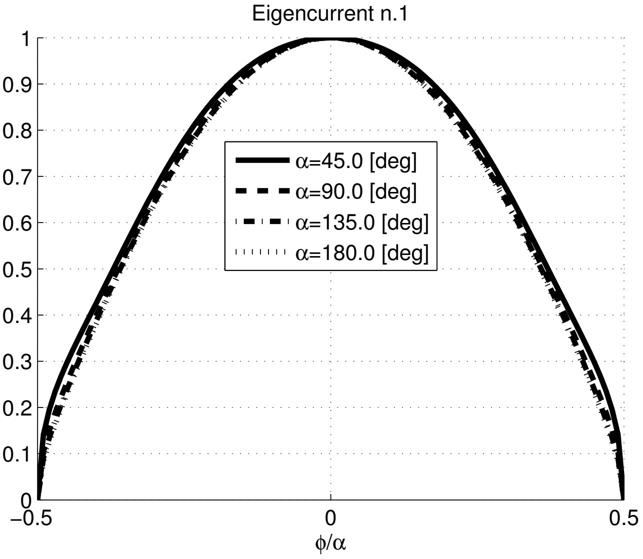

Figure 5.15: Amplitude of the first eigenfunction for various angular slot sizes; Eigencurrent normalization: maximum value

where $\underline{\underline{A}}^{unc}$ is diagonal with the eigenvalues λ_n^{sub} ($n = N_{cpl}^{sub} + 1, \ldots, N_{eig}^{sub}$), each with multiplicity N_{sub}, as elements. The upper block $\underline{\underline{A}}^{cpl}$ is a dense matrix. Let E^{eig} be the set of the eigencurrents related to the eigenvectors of $\underline{\underline{A}}^{cpl}$. We can define a scalar product $< \cdot, \cdot >_{eig}$ such that these eigencurrents are orthonormal. Since the moment matrix has the form shown in (5.24), the set of the eigencurrents of the array is given by the union of the elements of E^{eig} and E^{unc}. We can, then, finally define a new scalar product $< \cdot, \cdot >_A$:

$$< \underline{v}, \underline{w} >_A = < \underline{v}_1, \underline{w}_1 >_{eig} + < \underline{v}_2, \underline{w}_2 >_{comp} \tag{5.25}$$

with $\underline{v} = \underline{v}_1 + \underline{v}_2$ and $\underline{w} = \underline{w}_1 + \underline{w}_2$ where $\underline{v}_1$ and $\underline{w}_1$ belong to E^{eig}, while $\underline{v}_2$ and $\underline{w}_2$ belong to E^{unc}.

Finally, the unknown magnetic current distribution $\underline{\mathbb{J}}_m$ can be computed by:

$$\underline{\mathbb{J}}_m(z,\varphi) = \sum_{n=1}^{N_{cpl}} \sum_{q=1}^{N_{sub}} \frac{< \underline{H}^{inc}, \underline{\psi}_{nq} >_{eig}}{\lambda_{nq}} \underline{\psi}_{nq}(z,\varphi) + \sum_{n=N_{cpl}+1}^{N_f} \frac{\sum_{q=1}^{N_{sub}} < \underline{H}^{inc}, \underline{\psi}_{nq} >_{comp} \underline{\psi}_{nq}(z,\varphi)}{\lambda_n^{sub}} \tag{5.26}$$

where the scalar product $<, >_{comp}$ has been defined in (5.13).

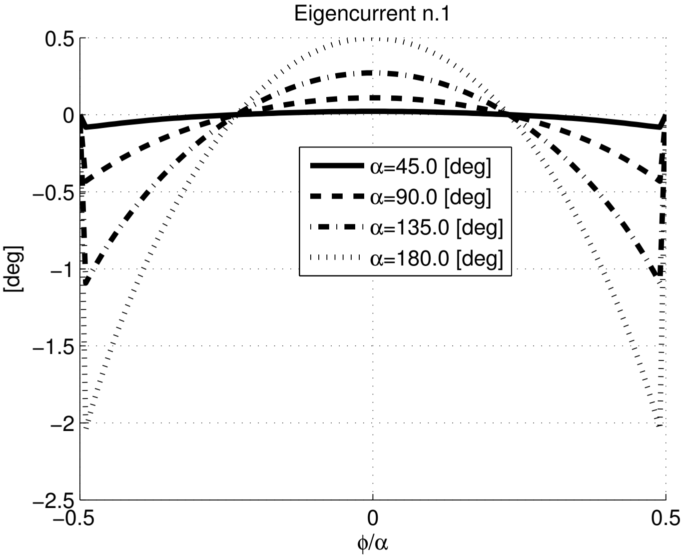

Figure 5.16: Phase of the first eigenfunction for various angular slot sizes.

5.7.2 Analysis of the spread of eigenvalues as Measure of Mutual Coupling

The efficiency of the Eigencurrent Approach is strictly related to the number of sets E_n that have to be taken into account in the cycle.

Here we first illustrate the validity of some conjectures, discussed in the first section of this chapter, on the behavior of the eigenvalues of the admittance operator of the array, then we will analyze the relation between the perturbation ϵ_{nq} and the error introduced by the application of the eigencurrent procedure. This preliminary analysis permits to prove the correctness of the Eigencurrent Approach.

In the following simulations, we will employ one basis function for the z-dependence and three even weighted Chebyshev polynomials of the second kind for the φ-dependence. The geometrical and electrical characteristics of the slotted cable are: inner/outer conductor radii 3.4/8.8 mm, slot angular width $\alpha = 180°$, dielectric permittivity $\epsilon_{r1} = 1.26$ and frequency $f = 1$ GHz.

In order to start our investigation, let us consider a uniform LCX composed by ten apertures with a slot separation $L = 15$ cm. Figure 5.20 shows a sketch in the complex plane of the array and subarray (slot) eigenvalues.

It is interesting to observe that the array eigenvalues (represented by circles) lie in three different areas the complex plane, this fact gives a preliminary justification of our subdivision into groups. Moreover it can be noted that while the first ten array eigenvalues are clearly distinguishable

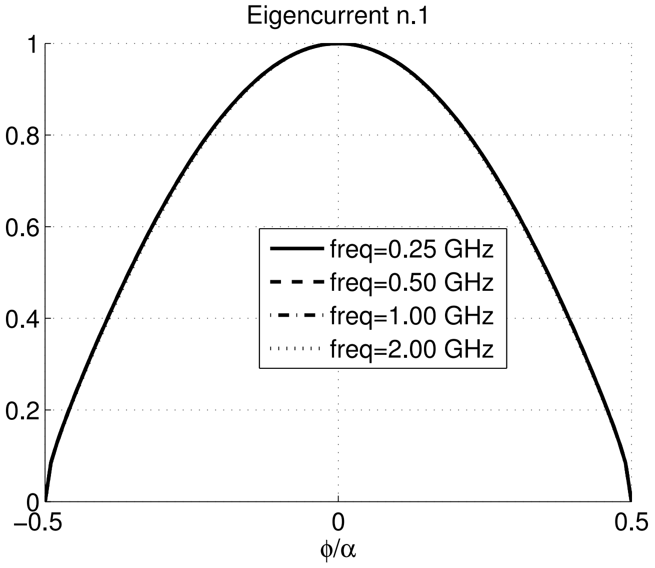

Figure 5.17: Amplitude of the first eigenfunction for various frequencies

from λ_1^{sub} (represented in figure by a triangle near the real axis), the others are so close to the corresponding sub-array eigenvalues to be indistinguishable. From a quantitative point of view this fact can be illustrated by analyzing the absolute value of the perturbations ϵ_{nq} as a function of the index q, that scans the eigenvalues in a specific group, for n=1, 2 and 3 (see Fig. 5.21). From the plot it is evident that only the eigenvalues related to λ_1^{sub} present a significant perturbation (of the order even of 50% in the case under consideration). This observation permits to conclude that the eigenvalues $\{\lambda_{nq}\}$ can be approximated with λ_n^{sub} for $n > 1$,

It is interesting to analyze the behavior of the maximum and minimum values of ϵ_{nq} as a function of the number of slots considered. The results are shown in Figure 5.22 where it can be noticed that while the maxima tend to increase as a function of the number of subarrays, the minima decrease to a constant value that is close to zero. It can be shown that the maxima related to the second and third sets E_n tend, slowly, to a constant maximum value that is, anyway, less than 0.1%. This observation permits to assert that the preceding consideration is valid independently on the number of apertures in the LCX. Until now we have numerically shown that, for what concerns the eigenvalues, the coupling is appreciable only on the elements related to E_1; we still need to verify that the eigenvalues and eigencurrents of admittance operator of the array computed from the reduced moment matrix, *i.e.* the moment matrix built using only the elements of E_1 as basis functions, represent a suitable approximation of the corresponding "exact" eigenvalues and eigencurrents computed from the complete moment matrix built using all the set E_n. For this purpose, in Figures 5.23 and 5.24 the relative errors for all the eigenfunctions (in

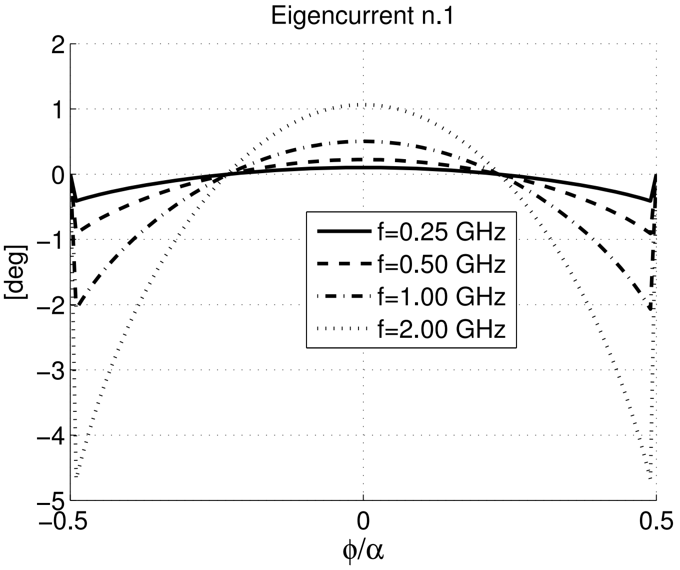

Figure 5.18: Phase of the first eigenfunction for various frequencies

L^2 norm) and eigenvalues are reported. From the plot the accuracy of the eigencurrent approach approximation is evident.

In order to conclude our investigation, it is interesting to analyze the relation between the spread of the perturbation ϵ_{nq} and the relative error on the electromagnetic solution that one produces neglecting some sets E_n in the cycle procedure of the Eigencurrent Approach. For this purpose, as suggested in [31] section 6.3, it is useful to introduce the maximum relative perturbation of the $n-$th group, with respect to the first subarray eigenvalue:

$$MRP_n^{[N_{sub}]} = max\{|\varepsilon_{nq}|\}_{q=1}^{N_{sub}} \cdot |\lambda_1^{sub}|/|\lambda_n^{sub}| \tag{5.27}$$

and the maximum relative L^2 difference:

$$MRD_{L^2} = max_{q=1,\dots,N_{sub}} \frac{||\tilde{\underline{J}}_m^{(q)} - \underline{\mathbb{J}}_m^{(q)}||_{L^2}}{||\underline{\mathbb{J}}_m^{(q)}||_{L^2}} \tag{5.28}$$

Here $\underline{\mathbb{J}}_m^{(q)}$ and $\tilde{\underline{J}}_m^{(q)}$ are the equivalent magnetic currents on the $q-$th slot obtained by the MoM and eigencurrent approach, respectively. We expect a strict relation between these two parameters. To verify this statement we consider a LCX composed by 40 slots and we compare the preceding quantities as a function of the slot spacing L normalized to the equivalent wavelength $\overline{\lambda}$. Figure 5.25 (left) shows that $MRP_n^{[40]}$ of the three groups of eigenvalues: it can be observed that all the curves show the same behavior as a function of the spacing. In particular, the perturbation of

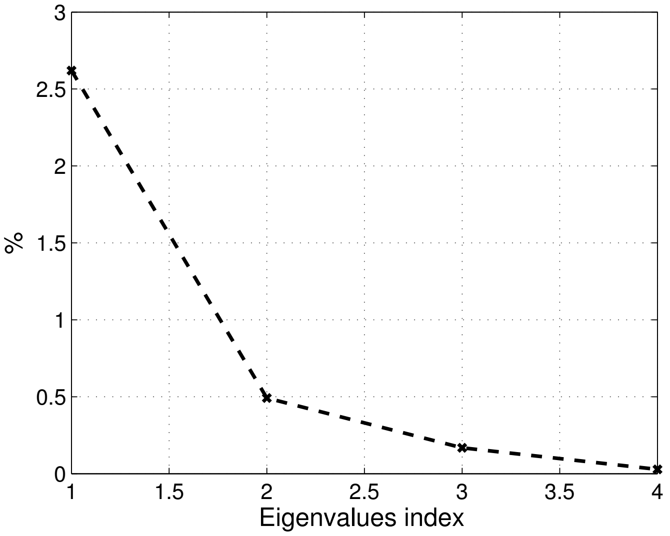

Figure 5.19: Percent relative error of the eigenvalues at $f = 2$ GHz, estimated via (5.23) with the eigencurrents computed at 0.2 GHz

the second and third groups are 24dB-32dB and 32dB-42dB lower than the perturbations of the first group, respectively. Figure 5.25 (right) shows that MRD_{L^2} exhibits a behavior qualitatively similar to that of the maximum absolute perturbations.

5.7.3 Description of the Eigenvalues and Eigencurrents of the array

In this section we want to investigate some interesting properties of the eigenvalues and eigencurrents of the admittance operator of the array of slots, using the basis of the elements of E.
Let us analyze the position of the eigenvalues $\{\lambda_{nq}\}$ in the complex plane as a function of the number of subarrays. For this purpose we consider two LCXs composed by 15 and 29 identical slots, respectively, whose geometrical and electrical characteristics are: inner/outer conductor radii 3.4/8.8 mm, slot angular width $\alpha = 180°$, slot separation $L = \lambda_0/2$, dielectric permittivity $\epsilon_{r1} = 1.26$ and frequency $f = 1$ GHz. In the simulation we employ one basis function for the z-dependence and three even weighted Chebyshev polynomials of the second kind for the $\varphi-$dependence.
Figures 5.26 and 5.27 show the plots of the eigenvalues of the first two groups normalized to the absolute value of the corresponding single slot eigenvalue. From a direct comparison we can

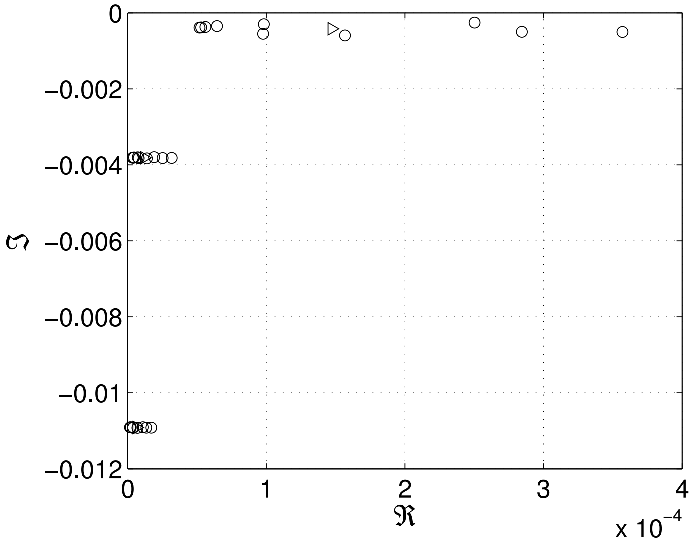

Figure 5.20: Array (o) and subarray ($\triangleright$) eigenvalues in the complex plane. Note that the subarray eigenvalues λ_2^{sub} and λ_3^{sub} cannot be distinguished from the corresponding groups of the array and are located very close to the imaginary axis.

conclude that each group tends to line up on a curve in the complex plane independently on the number of slots. This statement is not only valid for the first two groups, but it is completely general.

Moreover, we can note that the eigenvalues tend to accumulate, as the number of slots is increased, to a specific eigenvalue (in the plots it is labelled by the number 1). As found in [31] pag 156, this eigenvalue belongs to an eigencurrent without phase jumps in the coefficients of the dominant single slot eigencurrent. In this and in the following section the eigenvectors of each family E_n are sorted in ascending order according to the number of phase jumps.

Let us now analyze how the eigencurrents of a LCX are described in the basis $E_1 \bigcup E_2$. For this purpose we consider the eigenvector components of the moment matrix related to the LCX of 15 slots just considered. In Figure 5.28 the pattern of the absolute values of the components of the matrix of the eigenvectors of the Moment Matrix in the basis E are shown. From the plot it can be noted, as one can expect after the investigation done in the preceding section, that the eigencurrents $\{\underline{\psi}_{nq}(z, \varphi)\}$ are a linear combination of the currents of the corresponding set E_n plus a perturbation (represented by the off-diagonal blocks) that is practically negligible (see, for example, the zoom in Figure 5.29).

It is interesting to consider the distribution of the dominant coefficients of the eigencurrent of the array in the basis E. For this purpose in Fig. 5.30 (top), the coefficients of $\underline{\psi}_{1,k}(z, \varphi)$, for

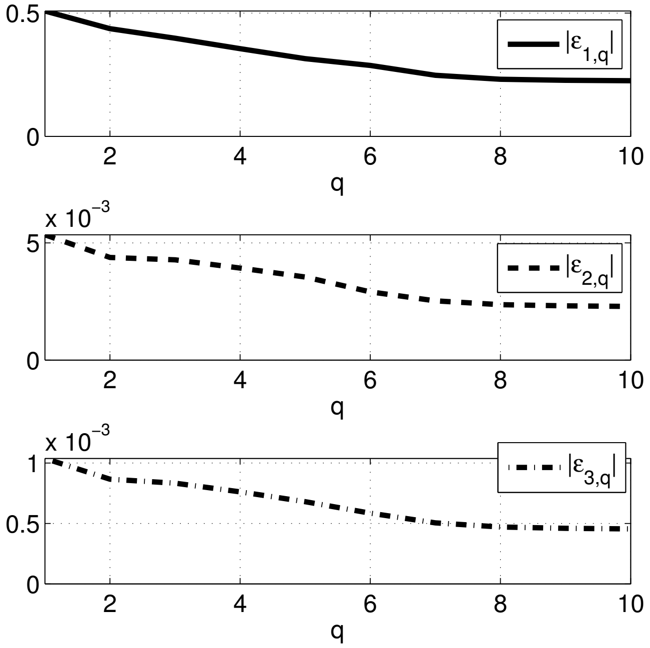

Figure 5.21: Absolute value of ϵ_{nq} for each family n as a function of the index q

k=1,2 and 3, in the basis $\underline{\psi}_1^{sub}(z,\varphi)$ are shown for an array of 15 slots. The curves in the bottom part of the figure represent the relevant plot for $\underline{\psi}_{2,k}(z,\varphi)$ in the basis $\underline{\psi}_2^{sub}(z,\varphi)$. Hence, these are the plots of the first three columns of each sub-block of the matrix in Figure 5.28. Finally in Fig. 5.31 the same plots are reported for the case of 30 slots. By inspection of the figures, one can conclude that not only the "shape" is practically independent on the number of slots, but also is the same for the eigencurrents related to E_1 and E_2. This behavior of the eigenvector coefficients is a consequence of the Toeplitz form of the moment matrix. In particular this result would be exact if the moment matrix were tridiagonal [33]

5.7.4 Parameter Dependence of the Eigencurrents

In this section we investigate the dependence of the dominant coefficients of the array eigencurrents on the geometrical and electrical parameters of a LCX. This kind of analysis can be considered the extension of what has been done in section 5.6 where we have analyzed the de-

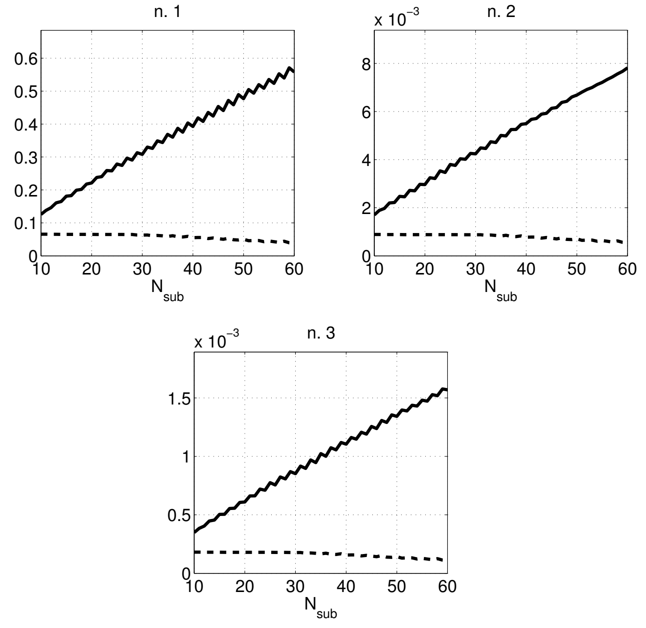

Figure 5.22: Maxima and minima of the absolute value of the perturbations $\{|\epsilon_{nq}|\}_{q=1}^{N_{sub}}$ of the first three groups of eigenvalues as a function of N_{sub}, *i.e.* the number of slots in the array

pendence of the single slot eigencurrents on the frequency and on the angular aperture α.
In particular, here we focus our attention on the dependence on the slot distance L, the angular aperture α, the frequency and the number of apertures.
Let us consider the behavior of the eigencurrents $\psi_{1q}(z, \varphi)$ for a LCX composed by 30 equal slots as a function of the slot separation L. The fixed geometrical and electrical parameters are: inner/outer conductor radii 3.4/8.8 mm, slot angular width $\alpha = 180°$, dielectric permittivity $\epsilon_{r1} = 1.26$ and frequency $f = 1$ GHz. In Figures 5.32 and 5.33 the absolute value and the phase of the dominant coefficients of the first four eigencurrents $\psi_{1q}(z, \varphi)$ are shown for $L = 10$ cm and $L = 18$ cm. From the plots it can be noted that the eigenvector coefficients are practically independent of the slot separation (maximum difference less than $1e - 3$ in amplitude and less than $5°$ in phase).
Let us turn now our investigation to the frequency dependence of the dominant coefficients. For this purpose we consider the same LCX as before, with a slot distance $L = 18$ cm. In Figures 5.34 and 5.35 the dominant coefficients, of the first four eigencurrents $\psi_{1q}(z, \varphi)$ are shown for two values of frequency $f = 0.5$ GHz(+) and $f = 2$ GHz(o). In this case the curves show a larger change than before.
Finally, let us analyze the dependence of the dominant eigencurrent coefficients on the geomet-

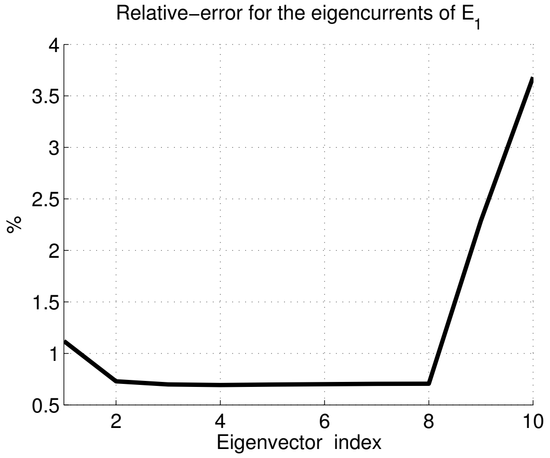

Figure 5.23: Percentage error for the eigenvectors related to E_1

rical apertures of the slots. For this purpose we consider the same LCX as before and we fix the frequency equal to 1GHz. Since it has been discussed in Section 8.3 that a way to control the radiation power of a LCX consists in tapering, by groups, the slot angular dimensions, if we want to employ the eigencurrent approach to such structure this kind of investigation becomes clearly quite important. In Figures 5.36 and 5.37 the absolute value and the phase of the coefficients of the dominant single-slot eigencurrents for the first four eigencurrents $\underline{\psi}_{1q}(z, \varphi)$ are shown for various angular apertures $\alpha = [90°, 135°, 180°]$. It is clear that these eigencurrents do not depend appreciably on the slot angular apertures.

To summarize, the preceding results have shown the almost complete independence of the dominant eigencurrent coefficients on the geometrical parameters of the LCX. This observation can be usefully employed, since once the eigencurrents have been computed for a specific set of parameters, the same coefficients can be employed for another geometrical set and the corresponding eigenvalues can be computed using the Rayleigh-Ritz quotient.

5.8 Numerical justification of the behavior of the eigenvalues of the admittance operator

In the preceding sections we have commented some peculiarities of the eigencurrents and eigenvalues of the array and thanks to these properties the EigenCurrent Approach can be efficiently

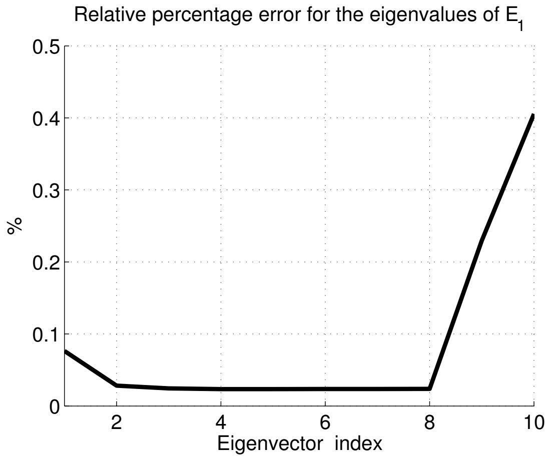

Figure 5.24: Percentage error for the eigenvalues related to E_1

applied to the analysis of LCX. The main points are:

- The eigenvalues related to the family E_1 have a significant spread with respect to the slot eigenvalue λ_1^{sub}, while the eigenvalues related to $E_{n'}$, with $n' > 1$, have a negligible spread

- The off-diagonal blocks of the matrix of the coefficients of the array eigencurrent, described in the basis E assume negligible values.

Both aspects are related to the inter and intra mode coupling effects between the eigencurrents of different slots. In section 5.2 it has been discussed how these two types of coupling are related to some specific entries of the moment matrix. In this section we want to give a qualitative justification of both observations starting from the behavior of the elements of the array moment matrix in the basis E. For this purpose let us consider the following three types of matrix elements:

- a) $\sum_n \int_{\Re} |\tilde{\psi}_1^{sub}(\chi, n)|^2 Y^{tot}(\chi, n) e^{-\jmath \chi L} d\chi$, that is the intra-mode coupling term between the elements of E_1

- b) $\sum_n \int_{\Re} \tilde{\psi}_1^{sub}(\chi, n) \tilde{\psi}_3^{*sub}(\chi, n) Y^{tot}(\chi, n) e^{-\jmath \chi L} d\chi$, that is the inter-mode coupling term between the elements of E_1 and E_2

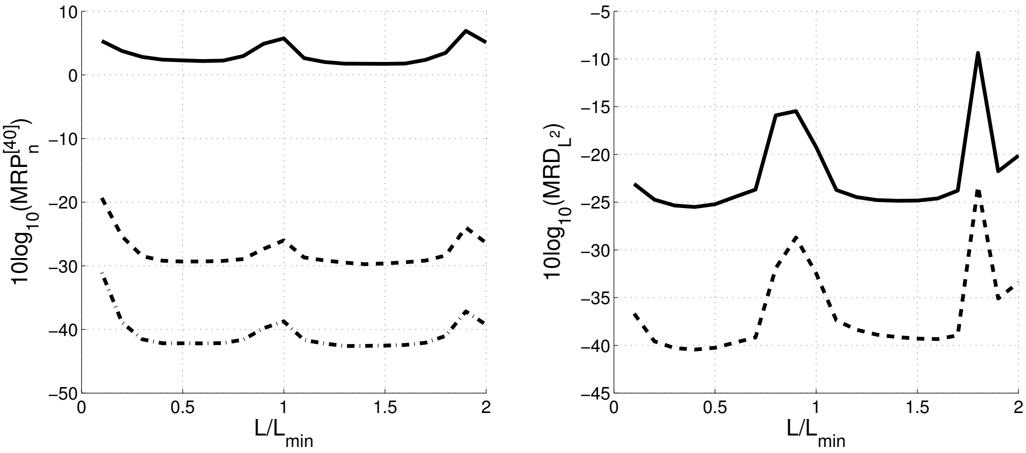

Figure 5.25: Left: $MRP_n^{[40]}$ (in dB) of the 1^{st}(solid curve), 2^{nd} (dashed curve) and 3^{rd} (dashed-dotted curve) group of eigenvalues as a function of the spacing for a LCX with 40 slots. Right: MRD_{L^2} with 1 group of coupling eigencurrents (solid curve) , 2 group of coupling eigencurrent (dashed curve)

- c) $\sum_n \int_{\Re} |\tilde{\psi}_2^{sub}(\chi, n)|^2 Y^{tot}(\chi, n) e^{-\jmath\chi L} d\chi$, that is the intra-mode coupling term between the elements of E_2

where L is the distance between two slots and the superscript $\tilde{}$ indicates the double Fourier transform of the eigenfunctions. The numerical results shown in this section refers to a specific LCX whose geometrical and electrical characteristics are: inner/outer conductor radii 3.4/8.8 mm, slot angular width $\alpha = 180°$, dielectric permittivity $\epsilon_{r1} = 1.26$, frequency $f = 1$ GHz and spacing $L = 11$ cm.

In our qualitative analysis we now assume the slot eigencurrents ψ_n^{sub} coincides, for what concern the φ-dependence, with the weighted Chebyshev polynomials of the second order, i.e.:

$$\psi_q^{sub}(z,\varphi) = \frac{1}{\sqrt{1-(2z/s)^2}} U_{2q-1}(2\varphi/\alpha)\sqrt{1-(2\varphi/\alpha)^2} = f(z)\, g_q(\varphi) \qquad (5.29)$$

$$\text{for } q = 1, \ldots, N_{eig}^{sub}$$

This statement is valid since in section 5.5 it has been observed that the set of weighted Chebyshev polynomials of the second order is a very good approximation of the slot eigencurrents. Under this assumption the preceding terms become:

- a) $\sum_n |\tilde{g}_1(n)|^2 \int_{\Re} |\tilde{f}(\chi)|^2 Y^{tot}(\chi, n) e^{-\jmath\chi L} d\chi = \sum_n |\tilde{g}_1(n)|^2 I(n)$

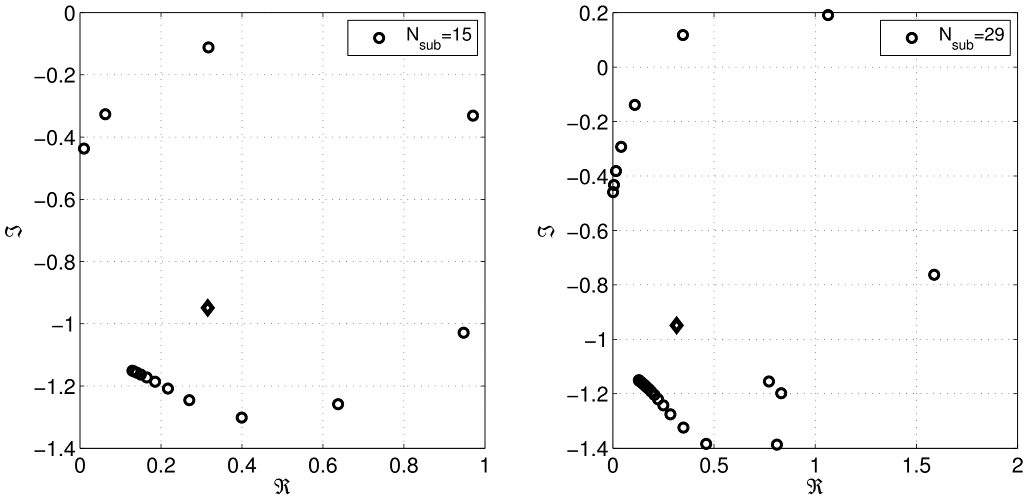

Figure 5.26: Normalized (with respect to $|\lambda_1^{sub}|$) eigenvalues ($\circ$) of the 1^{st} group for a LCX of 15 (left) and 29 (right) slots and the corresponding normalized eigenvalue ($\diamondsuit$) of a single slot, *i.e.* λ_1^{sub}

- b) $\sum_n \tilde{g}_1(n)\tilde{g}_2^*(n) \int_{\Re} |\tilde{f}(\chi)|^2 Y^{tot}(\chi,n)e^{-\jmath\chi L}d\chi = \sum_n \tilde{g}_1(n)\tilde{g}_2^*(n)I(n)$

- c) $\sum_n |\tilde{g}_2(n)|^2 \int_{\Re} |\tilde{f}(\chi)|^2 Y^{tot}(\chi,n)e^{-\jmath\chi L}d\chi = \sum_n |\tilde{g}_2(n)|^2 I(n)$

where $I(n) = \int_{\Re} |\tilde{f}(\chi)|^2 Y^{tot}(\chi,n)e^{-\jmath\chi L}d\chi$.
Since the factor $I(n)$ is common to all the terms, let us start analyzing its behavior as a function of n. As discussed in detail in chapter 10, it is useful to subdivide the preceding integral into the sum of internal and external contributions: $I(n) = I_{int}(n) + I_{ext}(n)$. As shown in section 10.3, the computation of $I_{int}(n)$ can be done by means of the Cauchy Theorem. In this way we obtain:

$$I_{int}(n) = \sum_q e^{-\jmath k_{zn}^{(q)} L} Res_q(n) \tag{5.30}$$

where $k_{zn}^{(q)}$ is the propagation constant of the $q-th$ mode of the coaxial cable with azimuthal index n and $Res_q(n)$ is the corresponding residue term, which is a combination of Bessel functions of the first and second kind. Since in the standard application of LCX only the TEM mode is above cut-off, due to the exponential term, only the component with $n = 0$ is non negligible.

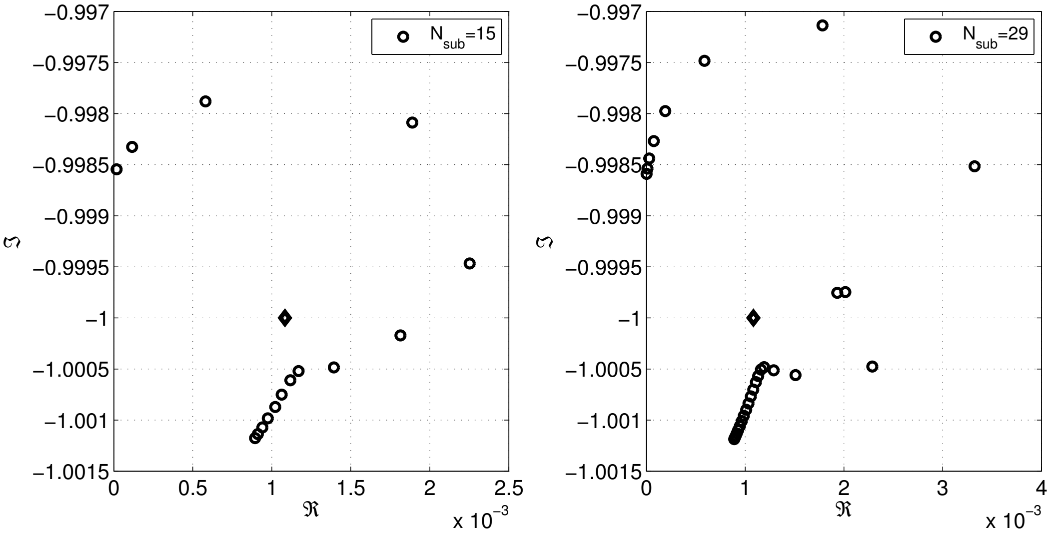

Figure 5.27: Normalized (with respect to $|\lambda_2^{sub}|$) eigenvalues (○) of the 2^{nd} group for a LCX of 15 (left) and 29 (right) slots and the corresponding normalized eigenvalue (◇) of a single slot, *i.e.* λ_2^{sub}

Let us now consider the term $I_{ext}(n)$. In section 10.3 it has been shown that its computation can be reported to the computation of the following integral:

$$I_{ext}(n) = \int_0^{\infty} e^{-t\,(k_0 L)}\, h(t;n)\, dt \tag{5.31}$$

where the function $h(t;n)$ is a combination of Hankel functions of the first and second kind. A numerical investigation has shown that the term with $n = 0$ is the dominant one (see figure 5.38). Then, let us consider the products $\tilde{g}_i(n)\tilde{g}_j^*(n)$ for the three cases of interest, *i.e.* $i, j = 1, 2$. In Figure 5.39 it can be observed that only in the case $i = 1, j = 1$ (case a)), the product is different from zero in $n = 0$.

Combining the results of Figures 5.38 and 5.39 we can conclude that intra-mode coupling between the elements of E_1 is not negligible. On the other hand, this fact does not happen in the cases b) and c) and, qualitatively speaking, it is responsible of the low (almost insignificant) intra-mode coupling between the elements of E_2 and of the inter-mode coupling between the elements of E_1 and E_2.

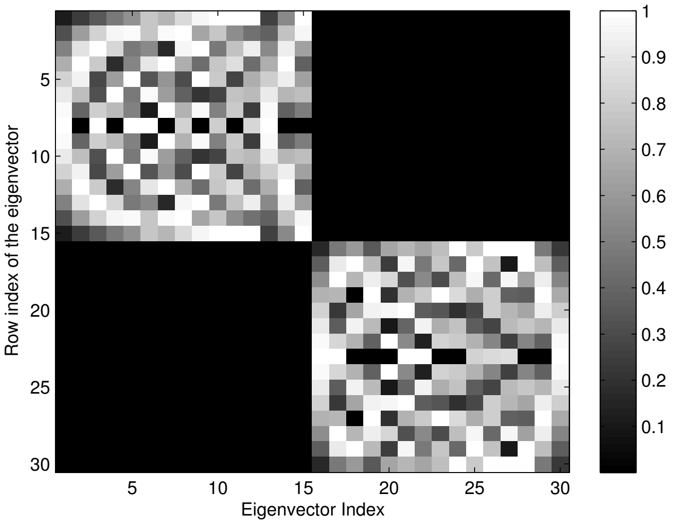

Figure 5.28: Pattern of the absolute values of the components of the eigencurrents $\{\underline{\psi}_{nq}(z,\varphi)\}$, with $n = 1, 2$, in the basis E, for a LCX of 15 slots. Eigenvector normalization: maximum coefficient

5.9 Numerical validation of the Eigencurrent Approach

In this section we validate the Eigencurrent Approach and its implementation in terms of accuracy and CPU time reduction. The comparison refers to the computation of the unknown magnetic current distribution once the series of integrals have been evaluated.

In particular we make the following comparison. We fix the slot geometry and separation and analyze LCXs with different number of apertures: 40, 100, 200, 500 and 1000 slots. The geometrical and electrical characteristic of the structure are: inner/outer conductor radii 3.4/8.8 mm, slot angular width $\alpha = 180°$, slot separation $L = 11$ cm, dielectric permittivity $\epsilon_{r1} = 1.26$. The slot magnetic current has been represented by three basis functions (Chebyshev polynomials of the first kind for the z-dependence and of the second kind for the φ-dependence). In the eigencurrent approach, only the elements of the first group E_1 in the cycle have been employed.

Figures 5.40 and 5.41 show the frequency response of the reflection and transmission coefficient of a 200 slot cable, computed by the two techniques. The results are in extremely good agreement.

Table 5.5 shows a summary of the percentage CPU time reduction on the solution obtained between the two methods. The L^2-norm error (in terms of MRD_{L^2}, see (5.28)) remains lower then

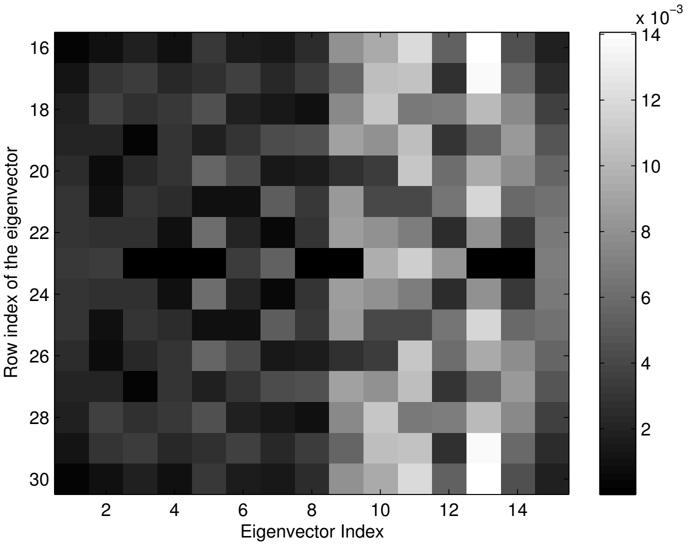

Figure 5.29: Zoom of figure 5.28 which shows the components of $\{\underline{\psi}_{2q}(z,\varphi)\}$ in the basis E_1. Same pattern for the components of $\{\underline{\psi}_{1q}(z,\varphi)\}$ in the basis E_2. Eigenvector normalization: maximum coefficient

1%. As reported in the table, the advantage in terms of computation times using the eigencurrent approach becomes remarkable as the number of slots is increased. Moreover the application of the Eigencurrent Approach becomes really important when the number of slots is very large (more than 1000 slots). Indeed, in this case the standard method of moment code cannot be applied, while the Eigencurrent Approach can be still efficiently used.

It is important to remark that in the case under examination we employ a small set of entire domain basis functions for the representation of the slot magnetic current. In the preceding section it has been shown that only the elements belonging to E_1 have to be taken into account in the cycle scheme, therefore the size of the moment matrix is reduced only by a factor of 9. If roof-top or RWG subdomain basis functions were used, as it would be necessary in the case of complex shape slots, the reduction factor would be much higher, as in [31].

This method can be successfully applied to LCX consisting of groups of slots with slightly different size, as proposed in section 8.3. In this case the Eigencurrent Approach can be applied twice, first for the computation of the eigencurrents and eigenvalues of each subarray which coincides with the blocks of equal slots, then to the entire antenna.

Finally, it is important to remark that, since the computation time of the projection integrals is considerable, the global time saving is of the order of 50%.

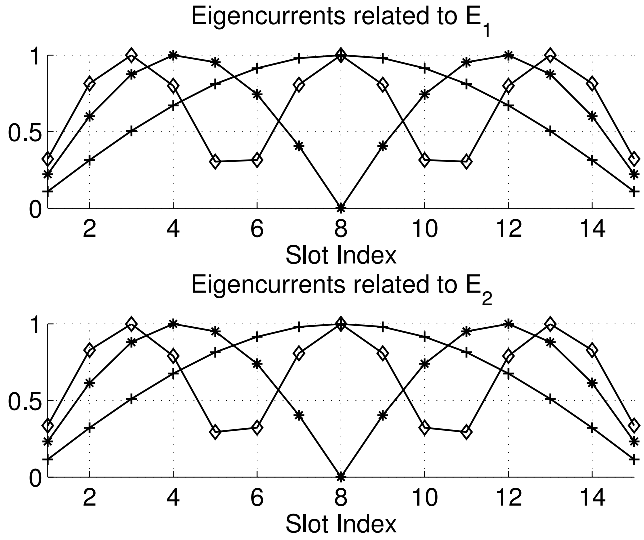

Figure 5.30: LCX of 15 slots. Amplitude of the coefficients of the first three eigencurrents $\psi_{1,q}$ (top) and $\psi_{2,q}$ (bottom), ($q = 1(+)$, $q = 2(*)$ and $q = 3(\diamondsuit)$), in the basis ψ_1^{sub} and ψ_2^{sub}, respectively.

5.10 Conclusion

In this chapter we have described the application to the analysis of LCX of the Eigencurrent Approach, a method originally developed for linear array of patches.

We have shown the importance of employing eigencurrents as expansion functions in order to avoid the storage and inversion of the Moment Matrix. It has been shown that these eigencurrents present a negligible dependence on the geometrical parameters of the slot.

Then the eigencurrents of the entire array in the basis of the ones of a slot have been analyzed. In particular the behavior of the shape of the dominant coefficient of each eigenvector has been considered. It has been numerically proved the approximate invariance of this shape with respect to changes in the geometrical and electrical characteristics of the slots. According to this analysis the eigencurrents and eigenvalues of the array have been organized in groups and the spread of these eigenvalues has been used as a quantitative measure of the coupling between the slots.

By this analysis it has been shown how to compute these eigencurrents as a linear concatenation of the subarray ones. Finally the effective accuracy of the method and its computational advantages have been shown in the simulation of very large LCX.

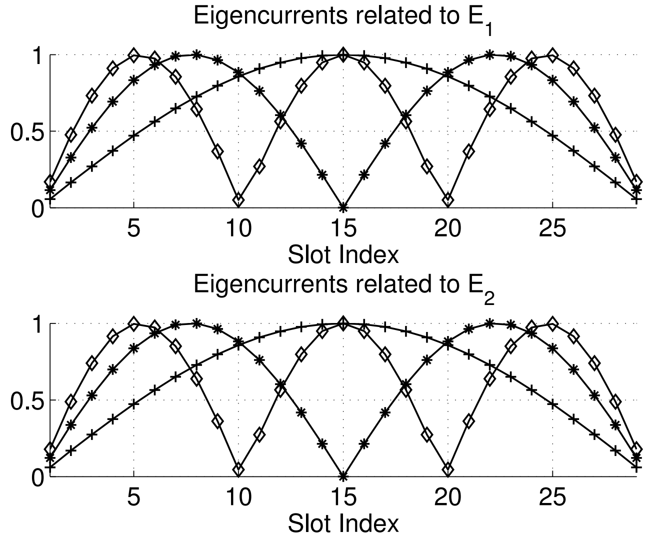

Figure 5.31: As Figure 5.30 but in the case of LCX with 29 slots

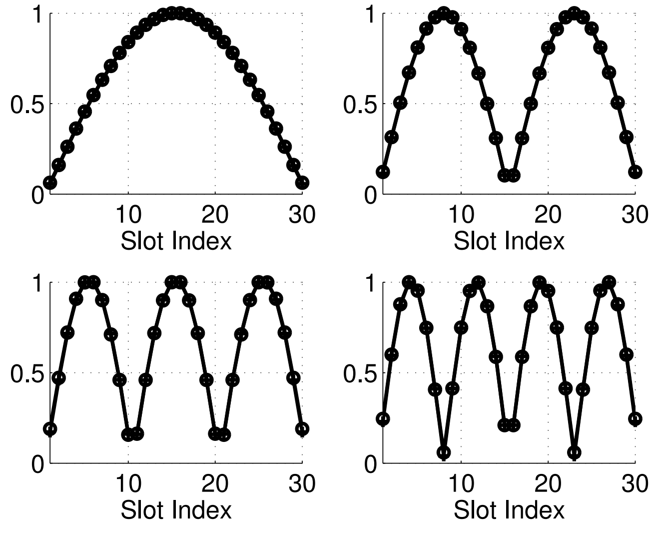

Figure 5.32: Absolute value of the expansion coefficients of $\psi_{1q}(z,\varphi)$ in the basis E_1 for $L = 10$ cm(+) and $L = 18$ cm(o). The curves are superimposed.

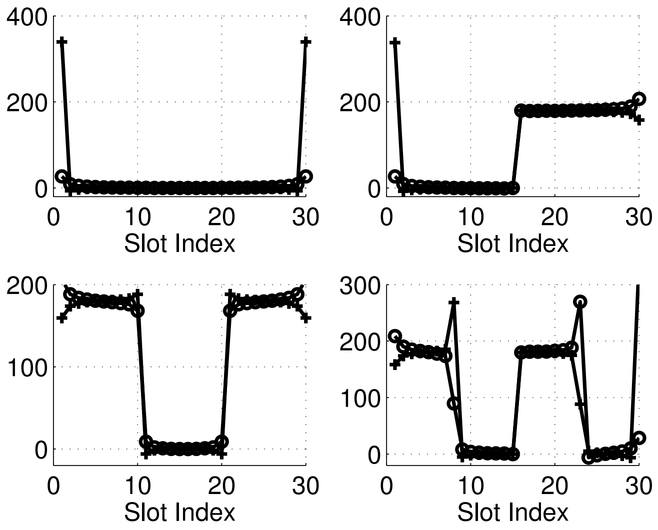

Figure 5.33: Phase (deg) of the expansion coefficients of $\psi_{1q}(z, \varphi)$ in the basis E_1 for $L = 10$ cm(+) and $L = 18$ cm(o). The curves are almost superimposed.

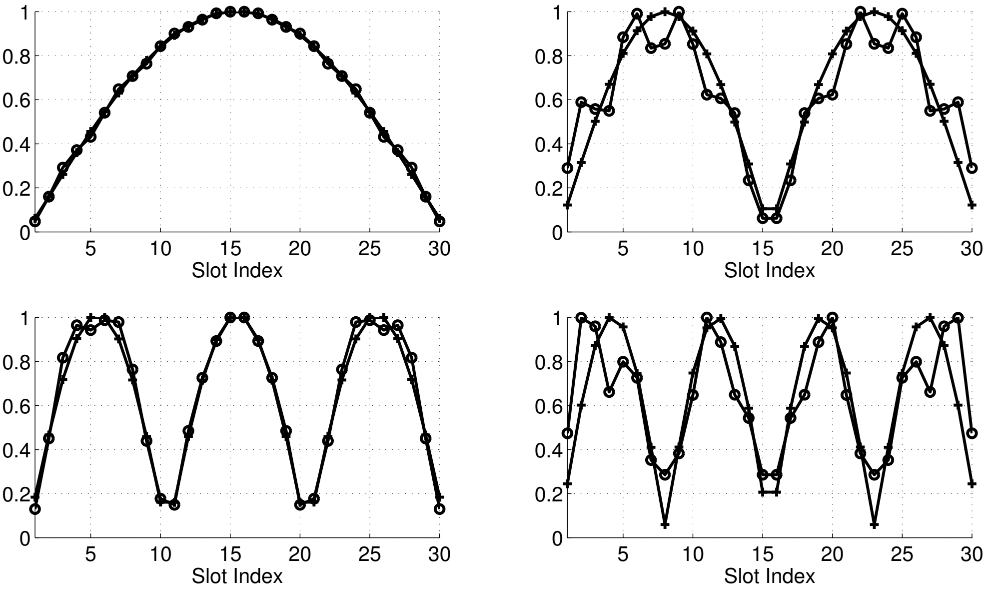

Figure 5.34: Absolute value of the expansion coefficients of $\psi_{1q}(z, \varphi)$ in the basis E_1 for $f = 0.5$ GHz(+) and $f = 2$ GHz(o). Eigencurrent normalization: maximum component

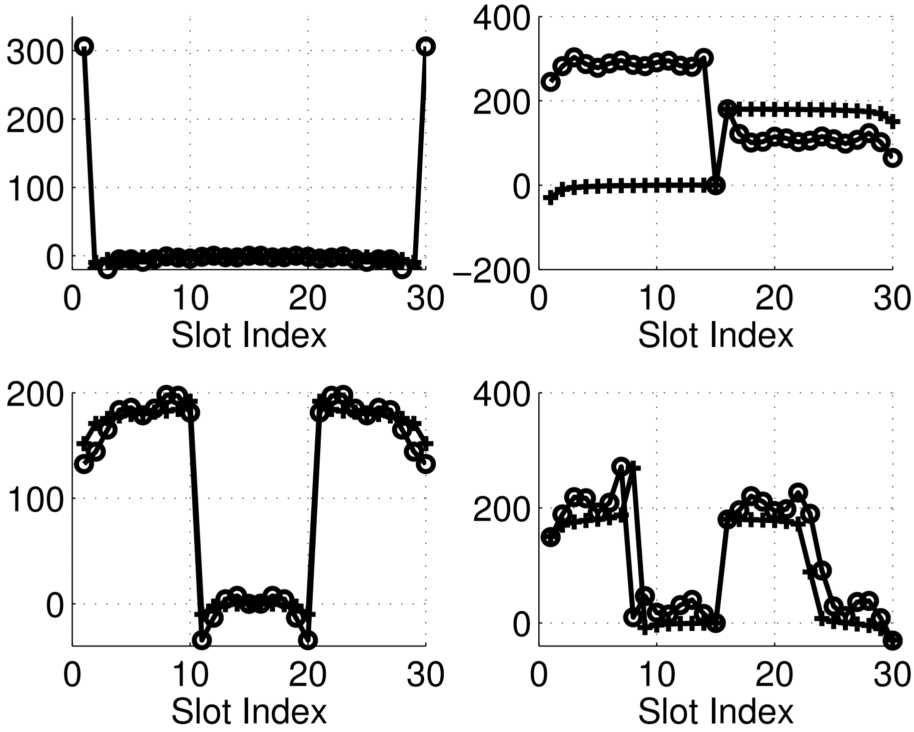

Figure 5.35: Phase of the expansion coefficients of $\psi_{1q}(z,\varphi)$ in the basis E_1 for $f = 0.5$ GHz(+) and $f = 2$ GHz(o).

Table 5.5: Percentage CPU time reduction of the Eigencurrent Approach versus the standard Method of Moment Code for different number of slots

Number of slots	Percentage CPU time Reduction
40	10%
100	100%
200	500%
500	1400%
1000	1500%

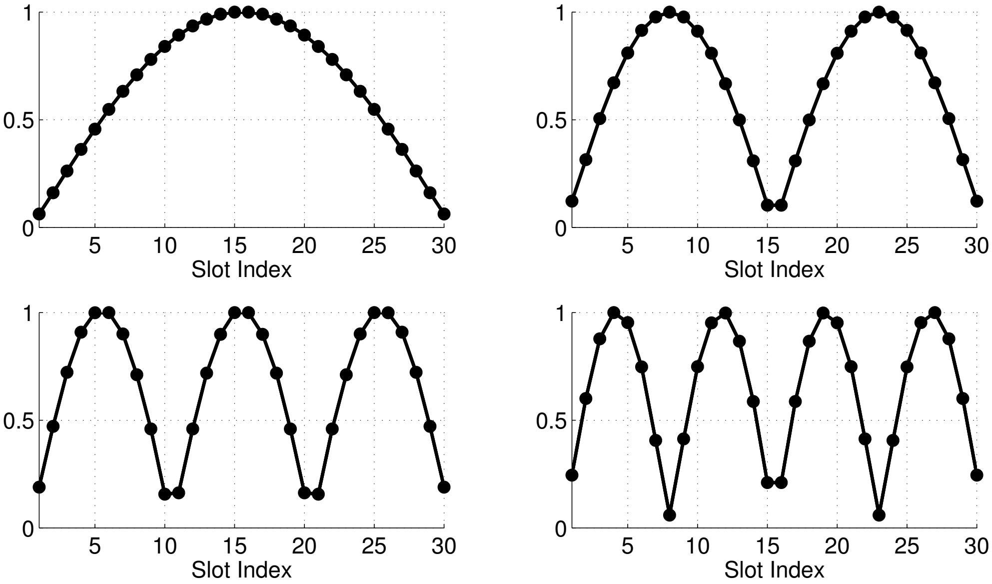

Figure 5.36: Absolute value of the expansion coefficients of $\psi_{1q}(z,\varphi)$ in the basis E_1 for various values of the angular aperture α. In particular $\alpha = \{90°(+), 135°(o), 180°(*)\}$. The curves are indistinguishable. Eigencurrent normalization: maximum component

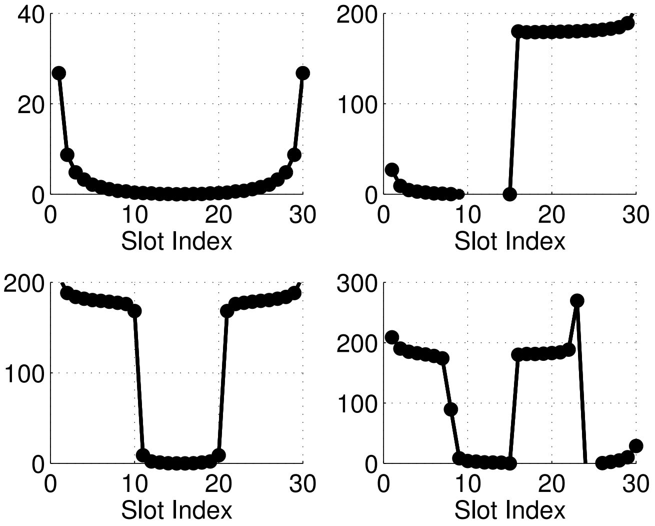

Figure 5.37: Phase (deg) of the expansion coefficients of $\psi_{1q}(z,\varphi)$ in the basis E_1 for various values of the angular aperture α. In particular $\alpha = \{90°(+), 135°(o), 180°(*)\}$. The curves are indistinguishable.

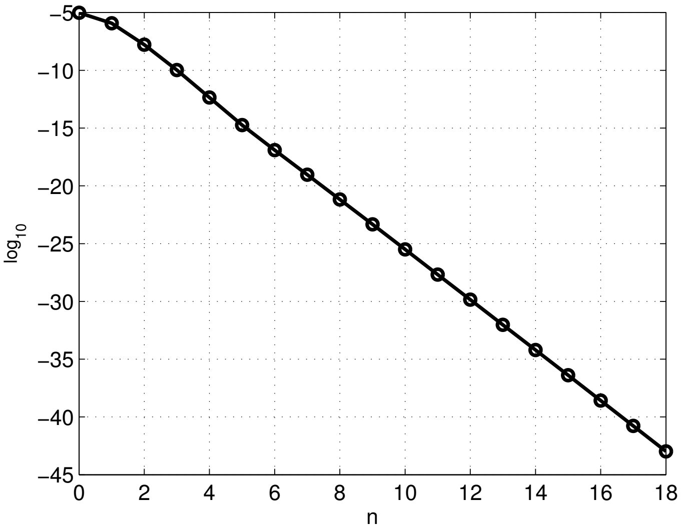

Figure 5.38: Absolute value (dB) of the integrals $I_{ext}(n)$ as a function of n

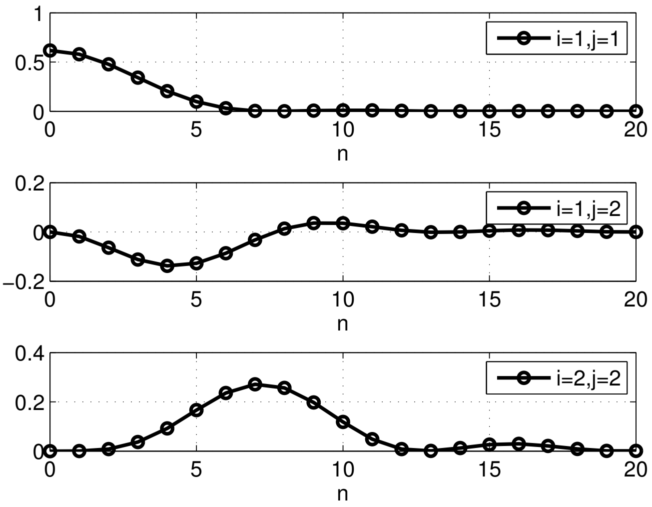

Figure 5.39: Products $\tilde{g}_i(n)\tilde{g}_j^*(n)$ as a function of n for $i, j = 1, 2$

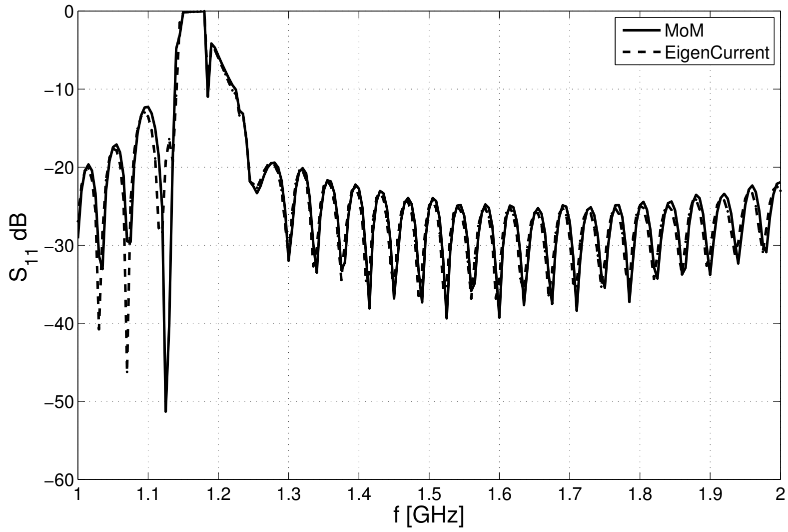

Figure 5.40: Comparison between the reflection coefficient (in dB) computed by the Method of Moment code and the Eigencurrent Approach for a LCX composed by 200 slots.

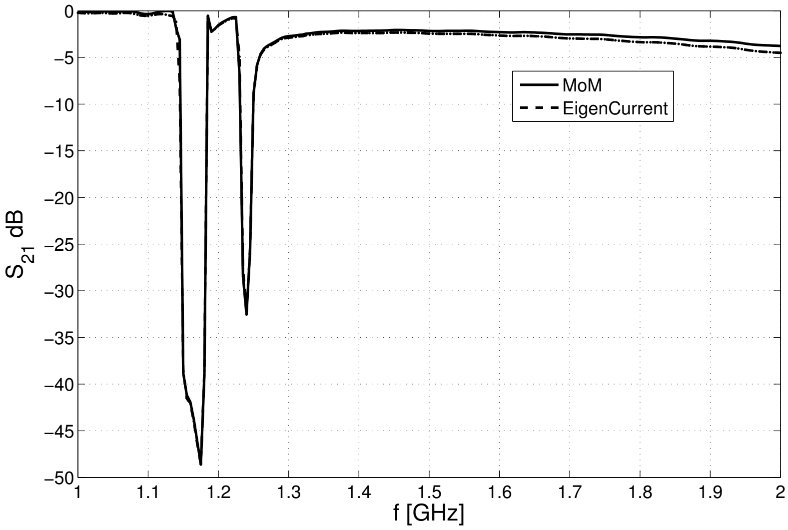

Figure 5.41: Comparison between the transmission coefficient (in dB) computed by the Method of Moment code and the Eigencurrent Approach for a LCX composed by 200 slots.

Chapter 6

Slotted Coaxial Cables: numerical results

6.1 Introduction

In this chapter we present some numerical results obtained with the methods described in Chapters 3 and 4.
First a cable with a single slot is considered. We derive a simple equivalent circuit for the TEM mode, in the form of a parallel resonator connected in series to the main line. We define the slot radiation efficiency, a parameter that plays an important role in Chapter 8, and obtain a plot in terms of the electrical slot length. Also the slot reflection coefficient is parameterized in the same way.

In Section 6.3 the properties of Bloch waves in a periodically slotted cable are discussed in depth. It is shown that practically only one Bloch wave is excited by the discontinuity between unslotted and slotted cable. This property holds in general, also in the case of a finite number of slots. On this basis, a simple model is derived, to describe the magnetic currents on the various slots.

Finally, a comparison is presented between the radial and longitudinal analysis of the same LCX. The agreement is remarkable, while the Bloch wave analysis is considerably faster when the cable has more than a few tens of slots.

6.2 TEM equivalent circuit of a single slot

A slot in the outer conductor of a coaxial cable represents a discontinuity for the incident TEM mode and it can be useful to derive its equivalent circuit.

Let us consider the longitudinal equivalent circuit of Figure 3.4, particularized here in the case of the TEM mode. The circuit of Figure 6.1 shows that the currents in $z = z_1$ and $z = z_2$ are equal, whereas the voltages $V(z_1)$ and $V(z_2)$ are different due to the distributed voltage generators $\overline{v}(z)$. The discontinuity, then, can be described by a series impedance Z_{slot} as shown in Figure 6.2.

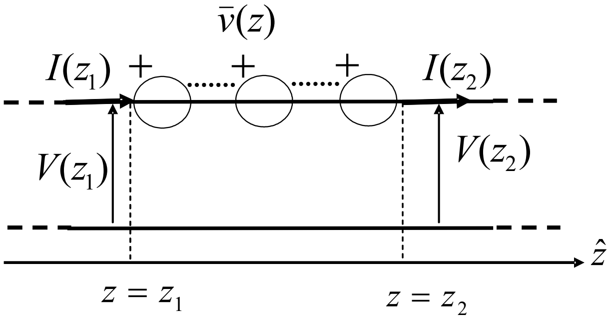

Figure 6.1: TEM mode equivalent circuit of a single slot

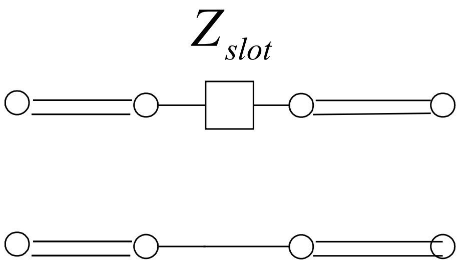

Figure 6.2: Definition of the slot impedance Z_{slot}

The normalized impedance z_{slot} can be related to the reflection coefficient S_{11} by the following equation:

$$z_{slot} = \frac{Z_{slot}}{Z_\infty} = \frac{S_{11}}{2(1 - S_{11})} \tag{6.1}$$

As an example, Figure 6.3 shows a frequency plot of the slot normalized impedance z_{slot}, in the case of a $\alpha = 270°$, width $s = 3$ mm slot in a coaxial cable with inner conductor radius $a = 12$ mm, outer conductor radius $b = 30$ mm, relative permittivity $\varepsilon_{r1} = 1.26$. The response is similar

to that of a parallel RLC resonator, hence we plot in Figure 6.4 the normalized slot admittance $y_{slot} = 1/z_{slot}$, which exhibits a nearly frequency independent conductance and a hyperbolic susceptance curve. The equivalent circuit of the slot can be conveniently drawn in the form of Figure 6.5. The elements R, L and C have been determined numerically by local best fit and are plotted in Figures 6.6, 6.7 and 6.8. We see that their frequency variation is very weak, which confirms the validity of the equivalent circuit.
Observe that the resonance $\Im\{y_{slot}\} = 0$ occurs when the frequency is $f = 1.015$ GHz. If we define an average wavelength $\overline{\lambda} = \lambda_0/\sqrt{(1+\varepsilon_{r1})/2}$ to take approximately into account the presence of two different dielectrics, we see that resonance occurs for $b\alpha/\overline{\lambda} = 0.508$, *i.e.* for a slot length very close to half wavelength, as one could expect.

If we use a single expansion function for the magnetic current, we can obtain an explicit

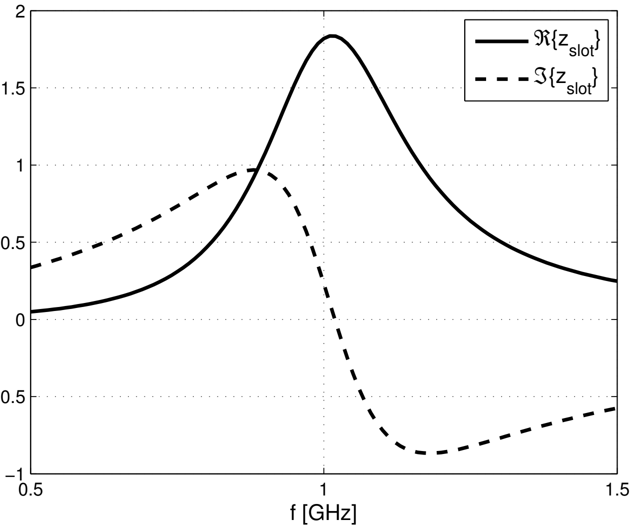

Figure 6.3: Real and imaginary part of the normalized slot impedance z_{slot}

expression of the real and imaginary parts of the normalized slot admittance $y_{slot} = g_{slot} + j\, b_{slot}$. In fact, combining (6.1) and the explicit expression of S_{11} (3.39), after some simplifications, we

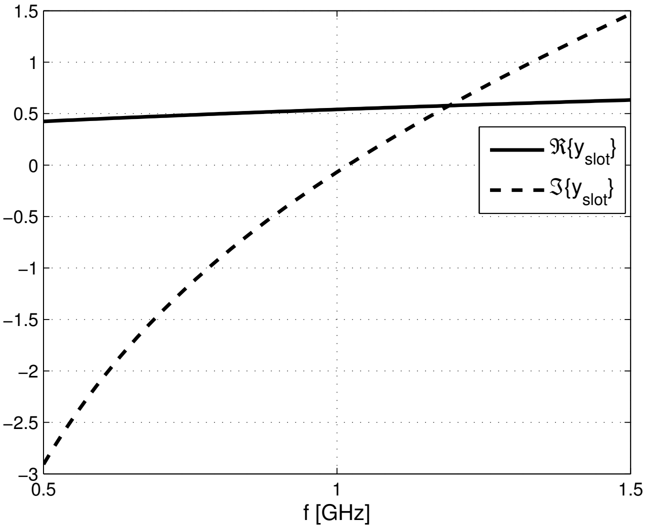

Figure 6.4: Real and imaginary part of the normalized slot admittance y_{slot}

obtain:

$$g_{slot} = \frac{\sum_n \int_{-k_0}^{k_0} \Re\{Y^{ext}(\chi,n)\}\,|\tilde{u}(\chi,n)|^2 d\chi}{4\pi^2 Y_\infty |h_\varphi(b)|^2 |\tilde{u}(k_1,0)|^2} \tag{6.2}$$

$$b_{slot} = \frac{\sum_n \int_{-\infty}^{\infty} \Im\{Y^{tot}(\chi,n)\}\,|\tilde{u}(\chi,n)|^2 d\chi}{4\pi^2 Y_\infty |h_\varphi(b)|^2 |\tilde{u}(k_1,0)|^2} \tag{6.3}$$

where Y_∞ and $h_\varphi(b)$ are the TEM admittance and magnetic field evaluated on the outer conductor. The slot conductance is essentially a radiation conductance and correctly depends only on the external part of the total admittance $Y^{tot}(\chi,n)$. On the other hand the slot susceptance b_{slot} is linked to the reactive field excited inside and outside the cable and is related to $Y^{tot}(\chi,n)$.

In the standard application of an LCX, each slot should radiate, as much as possible, a constant power level in order to maintain a uniform electromagnetic coverage along the tunnel where the LCX is placed. For this to be possible, it is necessary that each slot radiates only a small amount of the incident power and hence it must be electrically small.

From this point of view, it is convenient to define a slot radiation efficiency $\eta_{slot} = P_{rad}/P_{inc}$, which clearly is related to the circuit parameters previously introduced. In general, both the slot radiation efficiency and reflection coefficient depend on frequency and cable and slot size.

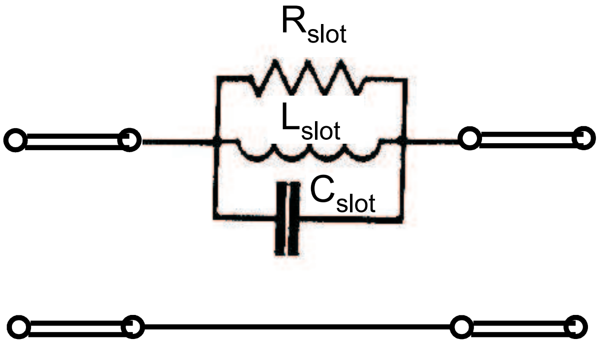

Figure 6.5: TEM mode slot equivalent circuit in the form of a parallel RLC resonator

However, extensive numerical experiments have shown that an important global parameter is the slot electrical length $\rho_2\alpha/\overline{\lambda}$. Figures 6.9 and 6.10 show plots of the slot efficiency and of the corresponding reflection coefficient versus the slot electrical length, for different values of the slot width s. These plots have been generated by keeping the cable characteristic impedance constant, $Z_\infty = 50\Omega$. The dependence of these parameters on the slot width s is very weak, in the range of interest.

Moreover, a single slot arrives at radiating 50% of the incident power at resonance, *i.e.* when its geometrical length $\rho_2\alpha$ is close to $\overline{\lambda}/2$. The corresponding reflection coefficient in this condition is about -6 dB. Obviously, these curves are valid only in a certain parameter range. In particular, the higher order cable modes must be well below cut-off and the slot angular width must lie in the range $10° \lesssim \alpha \lesssim 350°$

As indicated above, the slots of a LCX should radiate very little, hence we are mainly interested in the highlighted part of Figure 6.10 and 6.9, where the slot presents a very low value of S_{11} (less than -30dB) and the radiated power is only a few percent of the incident one.

In these conditions, the mutual interactions among the slots can be attributed to the TEM mode only and the theory of small reflections, (see Figure 6.11) [12], can be used to predict the qualitative properties of the frequency behavior of the slotted cable.

Assuming that the slots are identical and have equal spacing L, the input reflection coefficient for a LCX with N_{slot} slots can be written as:

$$\Gamma_{in} \approx \Gamma_{slot} \sum_{n=0}^{N_{slot}-1} (\mathrm{e}^{-2jk_1L})^n = \Gamma_{slot} \exp\{j(N_{slot}-1)k_1L\} \frac{\sin(N_{slot}k_1L)}{\sin(k_1L)} \tag{6.4}$$

This response, shown in Figure 6.12 in the case $N_{slot} = 40$, is characterized by reflection peaks and reflection nulls. Their frequencies are given by:

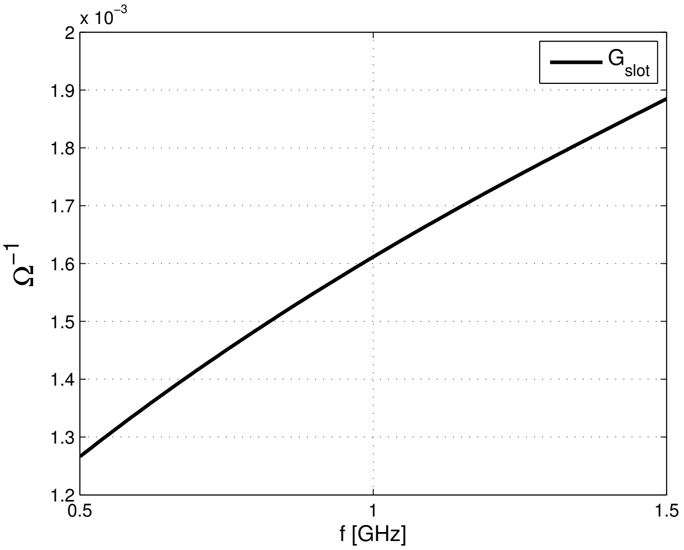

Figure 6.6: Frequency plot of the slot conductance G_{slot}

nulls: $f_z = m\,\dfrac{c_{light}}{2\sqrt{\varepsilon_1}N_{slot}L}$ with integer m

peaks: $f_p = m\dfrac{c_{light}}{2\sqrt{\varepsilon_1}L}$ with integer m

The frequency separation of two adjacent peaks is, hence:

$$\Delta f = \frac{c_{light}}{2\sqrt{\varepsilon_{r1}}L}$$

and there are N_{slot} nulls between two peaks. These results have been confirmed by a full-wave simulation. The cable data are $a = 3.4$ mm, $b = 8.8$ mm, $s = 3$ mm, $\varepsilon_r = 1.26$ and $\alpha = \pi$. Figure 6.13, where the two curves are superimposed, shows that the agreement is quite good, apart form the reflection peaks that clearly cannot be described by small reflection theory.

6.3 Properties of the Bloch waves in a slotted cable

A slotted cable, examined from the longitudinal point of view, is an open periodic waveguide, with period L. Hence we may expect that it has a continuous spectrum of Bloch waves (radiated

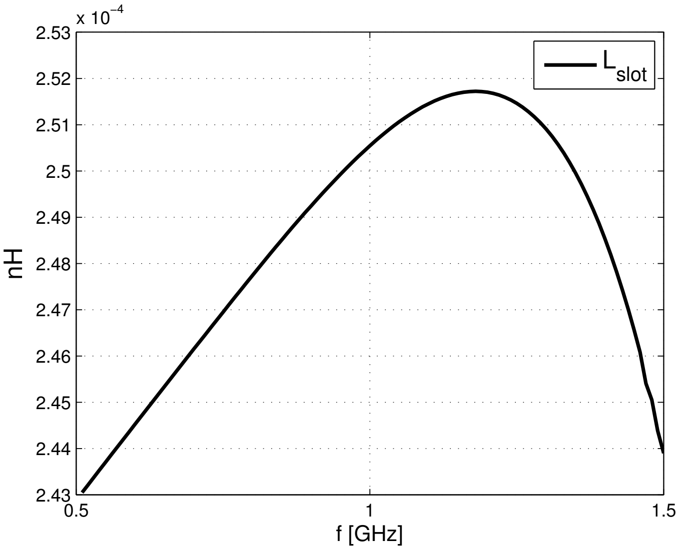

Figure 6.7: Frequency plot of the slot inductance L_{slot}

Bloch waves) and a finite number (possibly zero) of surface Bloch waves (guided Bloch waves). Depending on the frequency, each of these waves may have a real propagation constant k_B (passband) or a complex one $k_B = p\pi/L - j\alpha$, with integer p (stopband). As recalled in Section 4.5, each Bloch wave can also be seen as a collection of spatial harmonics [30]. If the period L is smaller than L_{min}, where $L_{min} = \lambda_0/(1+\sqrt{\varepsilon_{r1}})$, then all the spatial harmonics lie outside of the "visible range" $[-k_0, k_0]$ and a Bloch (slow) wave exists, with propagation constant larger than k_0, *i.e.* a surface Bloch wave.

In order to verify the preceding considerations, we have analyzed a lossless LCX with inner conductor radius $a = 8$ mm, outer conductor radius $b = 20.65$ mm, $\varepsilon_{r1} = 1.26$, and complete apertures ($\alpha = 2\pi$) of width $s = 3.24$ mm. Of the cable modes, only the TEM has been considered accessible. The continuous spectrum has been discretized by using 101 Chebyshev weighted polynomials and one Laguerre polynomial: such a large number is absolutely not necessary for the accurate computation of the slot aperture field, but is useful to appreciate the Bloch wave spectrum.

Three slot spacings have been considered: in case a) $L = 0.43L_{min}$ so that a surface wave is expected, while in cases b) and c) $L = 1.5L_{min}$ and $L = 1.891L_{min}$, respectively, and only continuous spectrum should be present. The Bloch propagation constants k_{Bj} at $f = 2$ GHz are

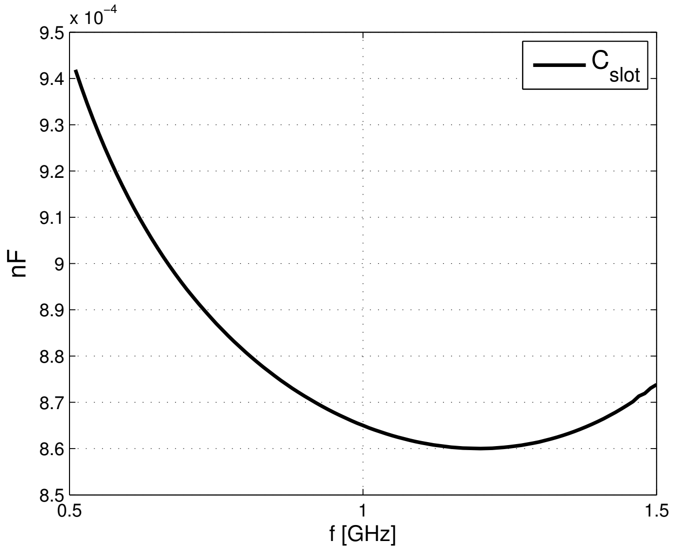

Figure 6.8: Frequency plot of the slot capacitance C_{slot}

shown in Figures 6.14 , 6.15 and 6.16 for the cases a), b) and c), respectively. In all cases, one recognizes a number of points in the interval $-k_0 \leq k_{Bj} \leq k_0$ that increases with the number of basis functions $\{l_n(\tau)\}$ used to discretize the continuous spectrum. These are fast Bloch waves and can be considered as a numerical approximation of the continuous spectrum of Bloch waves of the slotted cable.

Moreover, in case a) there is also an isolated point with k_B slightly larger than k_0, whose position is quite stable when the number of expansion functions is changed: this is a surface Bloch wave. The composition of the relevant eigenvector is shown in Figures 6.17 and 6.18 for the progressive wave and the regressive one. The cell transmission matrix has size 204×204, hence the eigenvectors have 204 components, the first 102 referring to progressive waveguide modes, the other 102 to regressive ones. The dominant coefficients refer to the progressive (position 1) and regressive (position 103) TEM mode. The first is larger than the second, or viceversa according to the progressive or regressive character of the Bloch wave.

Figure 6.19 shows the excitation coefficients of all the 102 progressive Bloch waves when a TEM mode impinges on the junction between an unslotted cable and a semi-infinite slotted one with the spacing of case a). These are the elements of the first column of the matrix S_{21}^{us} defined by (4.85). We can see that the surface Bloch wave, whose index is 1, is the most heavily excited.

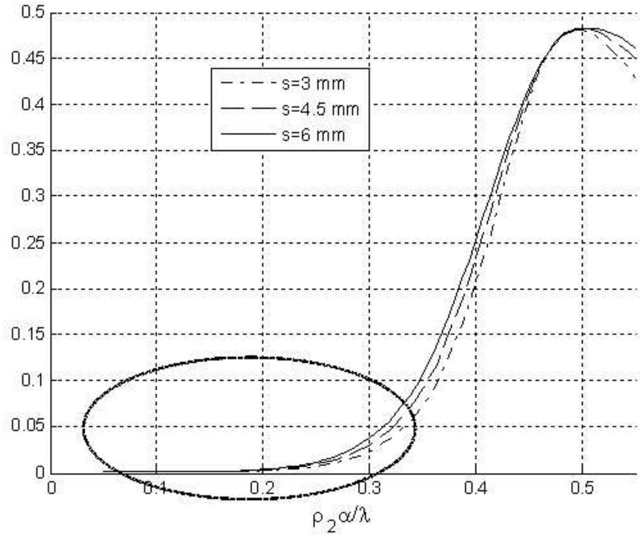

Figure 6.9: Radiation efficiency η_{slot} of an isolated slot versus $\rho_2\alpha/\overline{\lambda}$

In cases b) and c), no surface Bloch wave is possible on the slotted cable, since at least one spatial harmonic lies in the visible range. However, also in this case, when a TEM mode impinges on the junction unslotted-slotted cable, mainly a single Bloch wave is excited, as shown in Figures 6.20 and 6.21, although with quite different absolute levels. It turns out that this Bloch wave is evanescent in case c) (stop band), since its propagation constant is purely imaginary. Moreover, if we analyze its modal composition, shown in Figure 6.22, we note that the coefficients of the progressive and regressive waveguides modes are equal, so that no active power is carried by this wave. On the other hand, in case b) the propagation constant of the most excited Bloch wave is real ($k_B = -0.29k_0$). Its modal composition is shown in Figure 6.23: we see that this wave is mainly composed by the progressive and regressive TEM modes (components in position 1-103) but has also quite strong components related to the regressive composite modes (components in positions 104-204).

It is interesting to analyze how the propagation constant of the most excited (progressive) Bloch wave, changes as a function of the normalized period L/L_{min} (see Figure 6.24). The study has been carried out on a LCX with semicircular apertures and the following geometrical characteristics: inner conductor radius $a = 6$ mm, outer conductor radius $b = 15$ mm, $\varepsilon_{r1} = 1.26$, slot width and angular aperture $s = 3$ mm, $\alpha = 180°$, and frequency $f = 1$ GHz. As already discussed in the preceding example, when $L/L_{min} < 1$, the propagation constant of the mostly excited Bloch wave is $k_B > k_0$ since the wave is of surface type (slow). On the other hand,

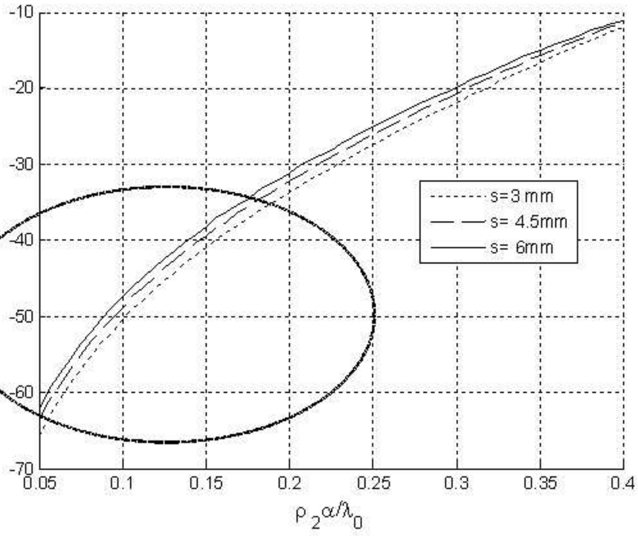

Figure 6.10: Reflection coefficient of an isolated slot versus $\rho_2\alpha/\overline{\lambda}$

when the period $L/L_{min} < 1$, the mostly excited Bloch wave is fast, with propagation constant $k_B < k_0$. Note that the discontinuity in the plot is artificial and arises because the phase shift per cell $k_B d$ has been taken always in the fundamental range $(-\pi, \pi]$.

We see that the transition between slow and fast behavior occurs at $L = L_{min}$, in which case $k_B = -k_0$ corresponding to backfire radiation. When the spacing L is increased, k_B becomes progressively less negative until it vanishes for $L = 1.8L_{min}$, corresponding to broadside radiation. The statements about the radiation directions are supported by the examination of the eigenvector content. As an example, consider the case $L = 1.25\,L_{min}$, in which the mostly excited Bloch wave has a propagation constant $k_B = -0.56\,k_0$. We must not be surprised by the fact that a progressive Bloch wave has a negative propagation constant. This wave is progressive because it carries active power in the positive z direction. If we attribute this propagation constant to the -1 harmonic (recall (4.78)), the fundamental has the value $k_B + 2\pi/L = 1.139k_0$.

To analyze the eigenvector, we distinguish the TEM mode from the continuous spectrum. The latter is reconstructed as a sum of expansion functions weighted by the eigenvector coefficients. The result is shown in Figures 6.25, 6.26 for the progressive and regressive power waves of the external modes for the azimuthal harmonics $m = 0, \pm 1$. As for the TEM mode, the coefficients are 0.98 and -0.04 for the progressive and regressive waves, respectively. Hence, this Bloch wave consists mainly of a progressive TEM mode, inside the cable, accompanied by a weak trail of progressive TM and TE continuous spectrum modes in the outside region. Figure 6.26 exhibits a clear peak at $\tau = 0.84k_0$, which means that the Bloch wave produces a consistent radiation at

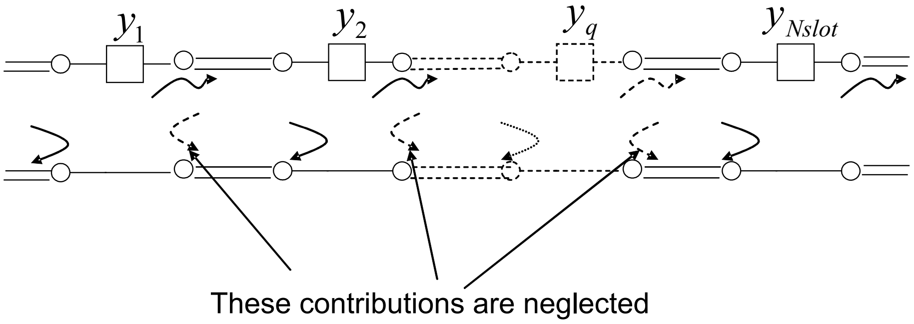

Figure 6.11: Small reflection theory concept

the angle $\theta = 180° - \arcsin(\tau/k_0) = 122°$.

Let us consider now the actual case of a cable with a large but finite number of slots. The result of a careful numerical analysis is that the mostly excited Bloch wave is the same as in the case of the semi-infinite slotted cable. When this wave (call it Forward wave) reaches the junction between the slotted and unslotted cable, it gives rise to several reflected Bloch waves that, on the further reflection on the first junction, couple only with the Forward wave. Moreover, it can be observed that all the regressive Bloch waves have globally a negligible effect on the magnetic currents on the slots. Hence, the results obtained above, in the idealized case of a semi-infinite slotted cable, maintain their validity. In particular, the field propagating in the region of the slotted cable is essentially a progressive wave. The magnetic currents in the various slots are almost identical apart from a complex amplitude coefficient x_q:

$$x_q = x_0 \, \mathrm{e}^{-j\, k_z q\, L} \tag{6.5}$$

The real part of k_z is essentially the propagation constant of the mostly excited progressive Bloch wave and then it is close to the TEM value $k_0\sqrt{\varepsilon_{r1}}$. Although Bloch waves have real propagation constants in their pass-bands, they form a continuum and their combined effect can be conveniently described by an imaginary part of k_z, which depends on the slot characteristics and describes the effect of the power leakage. The value of this imaginary part will be determined in Section 8.2 as a function of slot size and spacing.

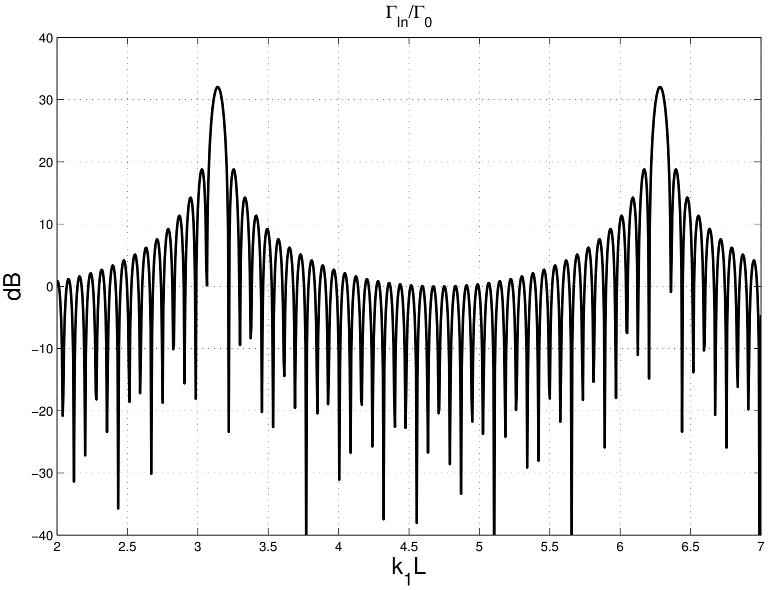

Figure 6.12: Small reflection theory approximation: response of a 40 slot array

6.4 TEM mode behavior in a slotted cable

It is useful to see the validity of the simple exponential model of the slot coefficients, presented in the last section, in a specific example, where in particular the attention is focused on the behavior of the TEM mode in the cable.
Let us consider an LCX with 200 slots, whose geometrical and electrical characteristics are: inner and outer conductor radii $a = 6$ mm and $b = 15$ mm, permittivity $\varepsilon_{r1} = 1.26$, slot width, angular length and spacing $s = 3$ mm, $\alpha = 180°$ and $L = 20$ cm and frequency $f = 1$ GHz. Since $L_{min} = 14.1$cm, the cable is in mono-radiation condition. The unknown magnetic current on each slot has been approximated with three basis functions, but the first one is by far the mostly excited one and we will focus our attention on its coefficient. Also, sixty azimuthal harmonics have been used in the construction of the Green's function.

The first check is on the phase of the main coefficient, which results to be essentially that of the mostly excited Bloch wave field at each slot location. Figure 6.27 shows, for each slot, the difference between the phase of the main coefficient and $k_B L_q$, where L_q denotes the distance of the q-th slot from the array input. We can notice that the structure of the phase difference

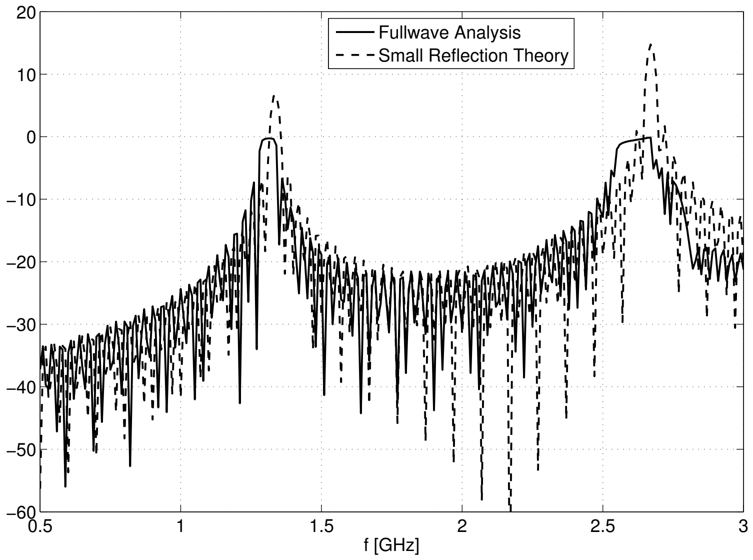

Figure 6.13: Input reflection coefficient of an array of 40 slots versus frequency. Comparison between small reflection theory and full wave approach.

is complicated, but small over the array length. Figures 6.28, 6.29 show the amplitudes of the TEM progressive and regressive voltages at the midpoints z_q between the q-th and $(q+1)$-th slot, computed according to the following equations:

$$V^+(z_q) = V^{inc}\,\mathrm{e}^{-j\,k_1\,(L/2+z_q+s/2)} - \frac{1}{2}\sum_{r=1}^{q} \tilde{\mathring{v}}_q(k_1)\mathrm{e}^{-j\,k_1\,(L/2+z_q-z_r)} \tag{6.6}$$

$$V^-(z_q) = +\frac{1}{2}\sum_{r=1}^{q} \tilde{\mathring{v}}_q(-k_1)\mathrm{e}^{-j\,k_1\,(L/2+z_q-z_r)} \tag{6.7}$$

where $\mathring{v}_q(z)$, with $q = 1, \ldots, N_{slot}$, is the equivalent voltage generator at the q-th slot location. The values are normalized to the incident voltage at the beginning of the array and the end of the cable is assumed to be matched. The plots show clearly that the regressive voltage is much smaller than the progressive one; this fact confirms that the electromagnetic phenomenon is purely progressive. The progressive voltage has an exponential decay amounting to about 20% over the array length, with a slight ripple. It is to be remarked that the slots are coupled both through the TEM mode and through the space wave propagating just outside of the cable. The simplified model of an electric current along the external conductor of the cable, employed in Section 7.3, can be used here in order to explain the ripple in Figure 6.28. In fact, as it has been verified through a Fourier analysis, this ripple is caused by the interference of an electromagnetic

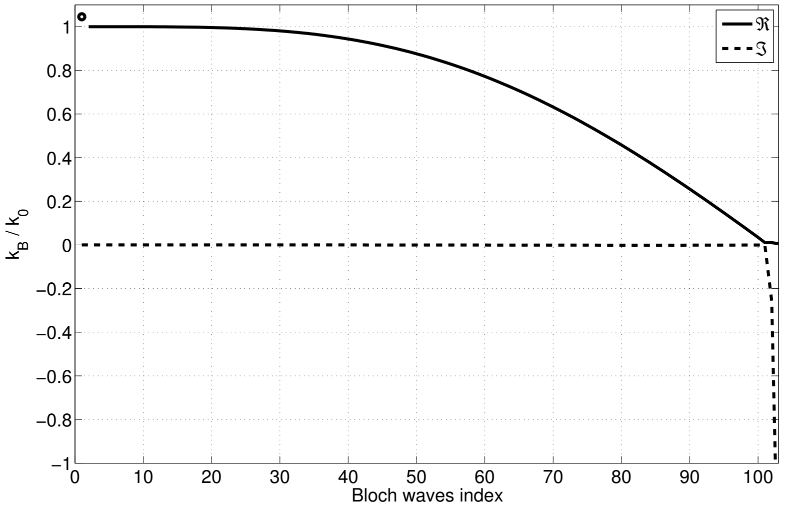

Figure 6.14: Real and imaginary part of the Bloch wave propagation constants k_{Bj} for case a): slot spacing $L = 0.43 L_{min}$. Note the isolated point that corresponds to the surface Bloch wave

field presenting a dominant progressive phase shift of the form $\mathrm{e}^{-j\,k_0 z}$ with the TEM mode.

Finally, Figure 6.30 shows a plot of the TEM power flow along the cable, which practically coincides with that of Figure 6.28, owing to the very small regressive voltage. The same exponential decay characterizes also the amplitude distribution of the main basis function coefficient and this fact finally justifies completely the model (6.5).

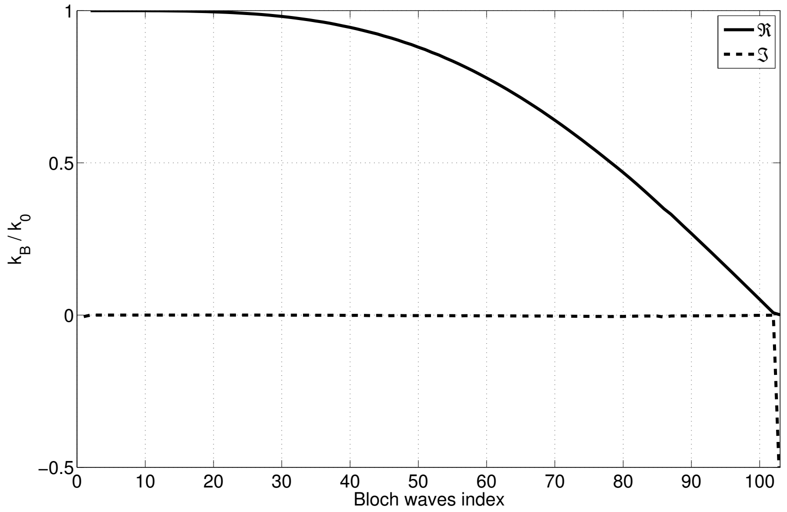

Figure 6.15: Real and imaginary part of the Bloch wave propagation constants for case b): slot spacing $L = 1.5L_{min}$. There is no surface Bloch wave

6.5 Comparison between transverse and longitudinal approach

In the two preceding chapters, two completely different methods have been described for the analysis of LCX. The first views the slotted cable in the transverse direction and computes the electric field in the slots by solving a magnetic field integral equation. The second carries out the study in the longitudinal direction on the basis of Bloch wave theory. Since the free space region surrounding the cable is an open waveguide, we face the problem of discretizing its continuous spectrum.

It is interesting to compare the two approaches in the specific case of a cable with 200 slots. The apertures have an angular extent $\alpha = \pi/2$, the width is $s = 3$ mm, the inner and outer conductor radii are $a = 5.8$ mm and $b = 15$ mm and $\varepsilon_{r1} = 1.26$.

For the transverse approach, three basis functions have been used to represent the magnetic current and the azimuthal series in the computation of the moment matrix elements has been truncated according to the criterion of Section 3.6. In the longitudinal approach, ten Chebyshev weighted polynomials and one Laguerre polynomial have been used for the continuous spectrum discretization, as well as three angular harmonics; only the TEM mode has been considered in the cable. Hence the slot GSM has a size $2 \cdot [3 \cdot (10 + 1) + 1]$.

Figure 6.31 shows a comparison between the TEM mode reflection responses computed by the

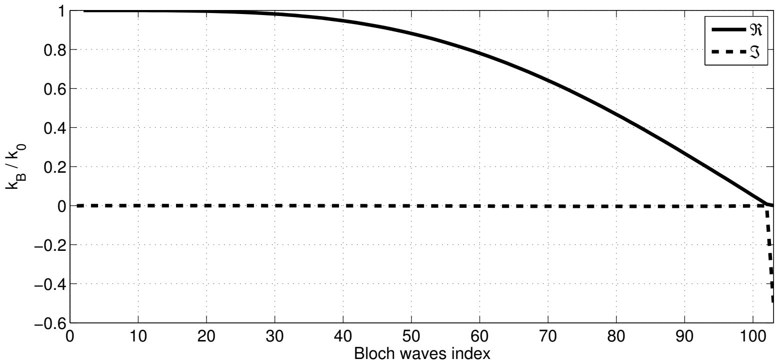

Figure 6.16: Real and imaginary part of the Bloch wave propagation constants for case c): slot spacing $L = 1.89L_{min}$. There is no surface Bloch wave

two approaches. The agreement is practically perfect, with a slight difference showing up only in the upper frequency band, but the CPU time is widely different. In general, with these parameters, the Bloch wave method is more convenient when the cable contains more that twenty slots.

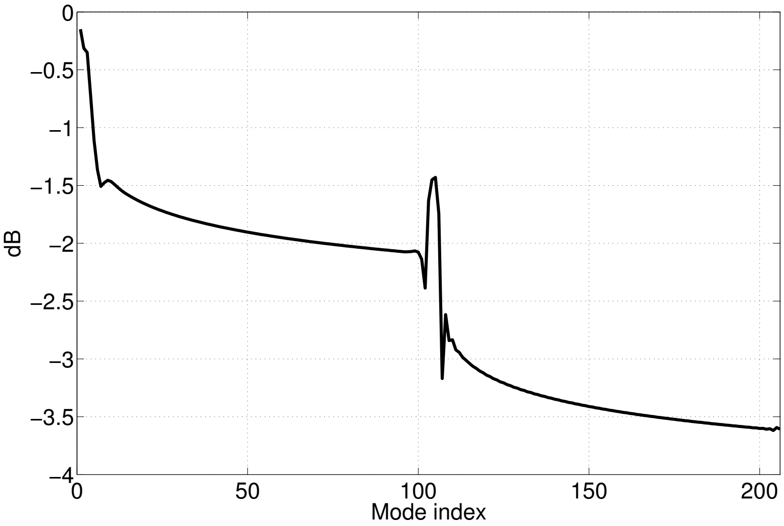

Figure 6.17: Modal composition of the progressive Surface Bloch Wave (in dB), the peaks correspond to the TEM progressive mode (position 1) and to the regressive one (position 103)

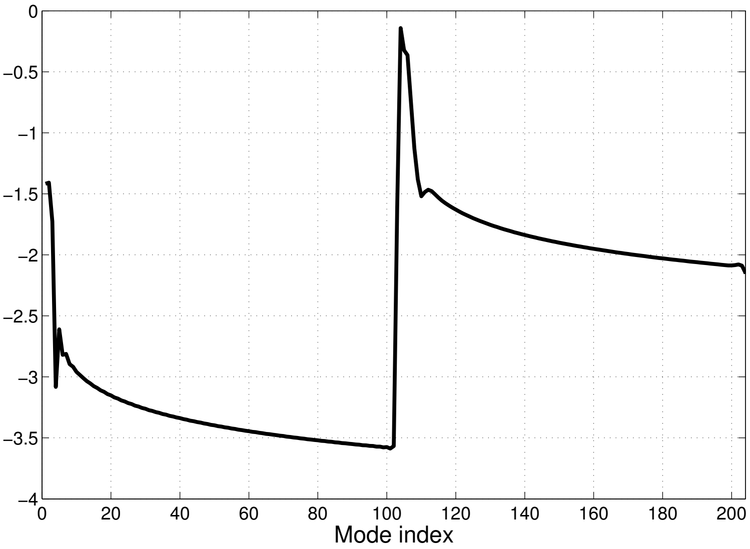

Figure 6.18: Modal composition of the regressive Surface Bloch Wave (in dB), the peaks correspond to the TEM progressive mode (position 1) and to the regressive one (position 103)

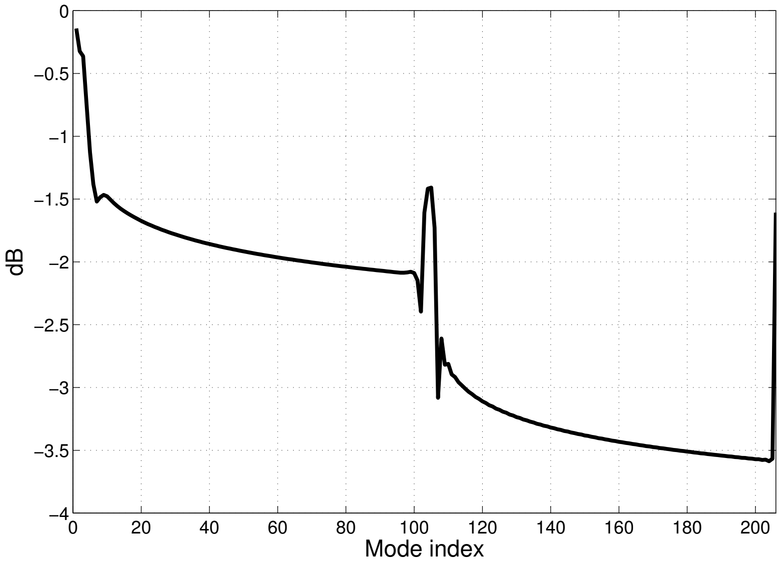

Figure 6.19: Bloch wave excitation coefficients at the junction unslotted-slotted cable for case a) ($L = 0.43L_{min}$), in which a surface Bloch wave exists. Its index is 1

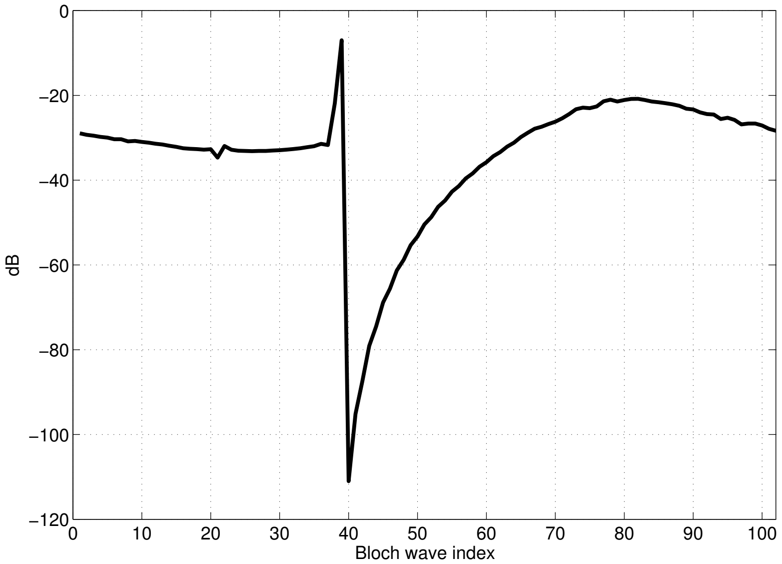

Figure 6.20: Bloch wave excitation coefficients at the junction unslotted-slotted cable for case b) ($L = 1.5L_{min}$), in which no surface Bloch wave exists.

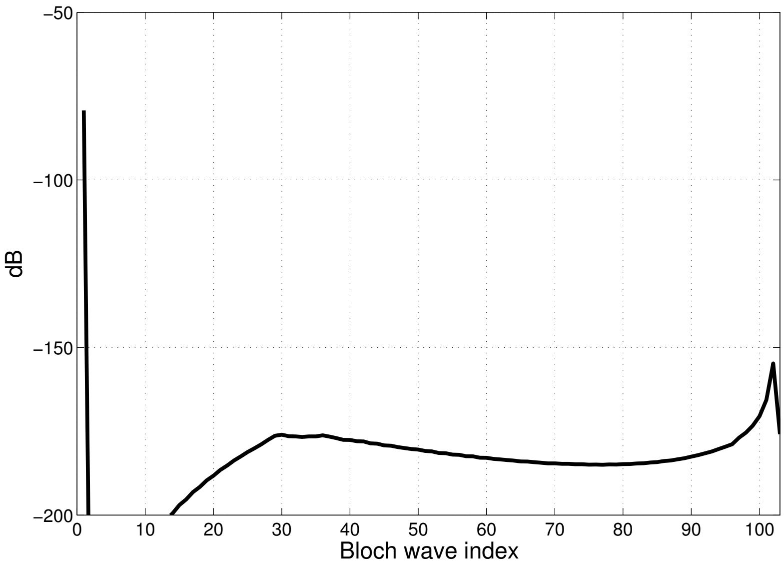

Figure 6.21: Bloch wave excitation coefficients at the junction unslotted-slotted cable for case c) ($L = 1.89L_{min}$), in which no surface Bloch wave exists

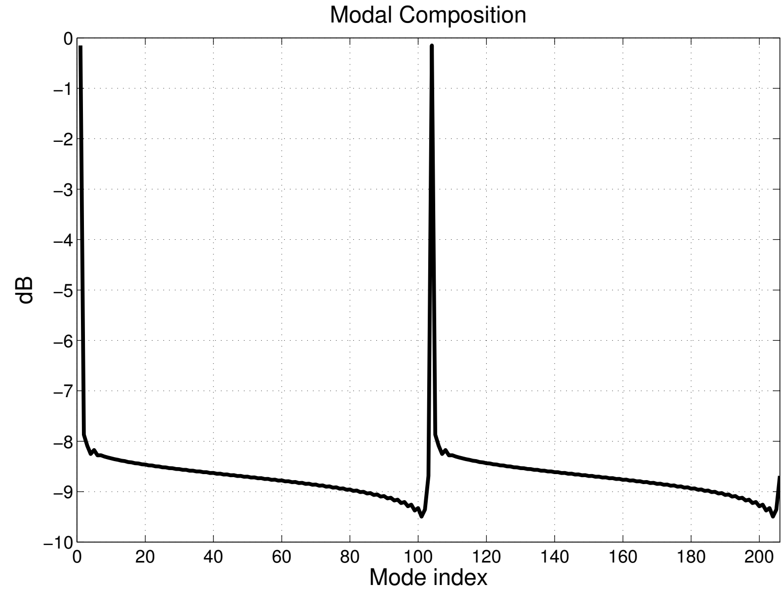

Figure 6.22: Modal composition of the most excited Bloch wave in case c) (in dB), the peaks correspond to the TEM progressive mode (position 1) and to the regressive one (position 103). This Bloch wave is in stop band.

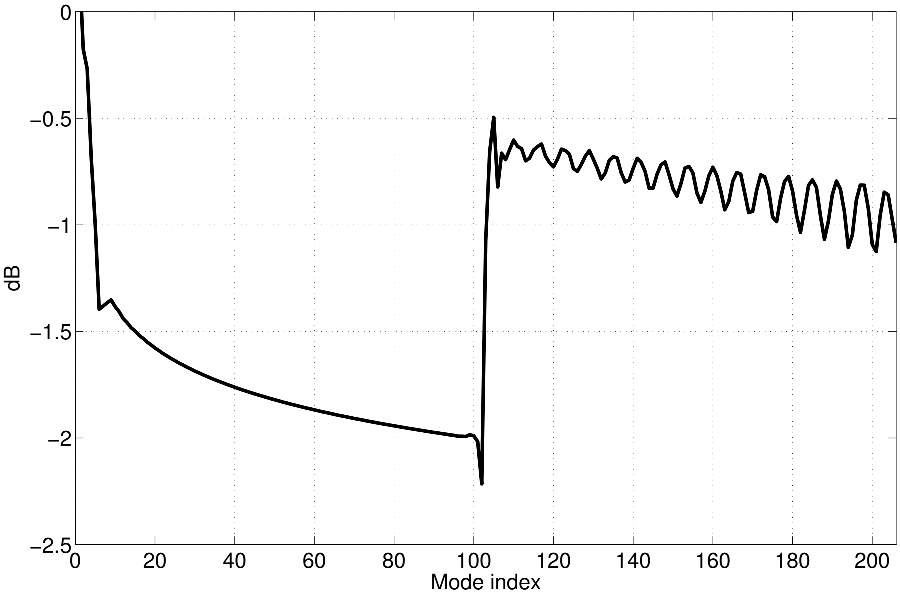

Figure 6.23: Modal composition of the most excited Bloch wave in case b) (in dB), the peak correspond to the TEM progressive mode (position 1)

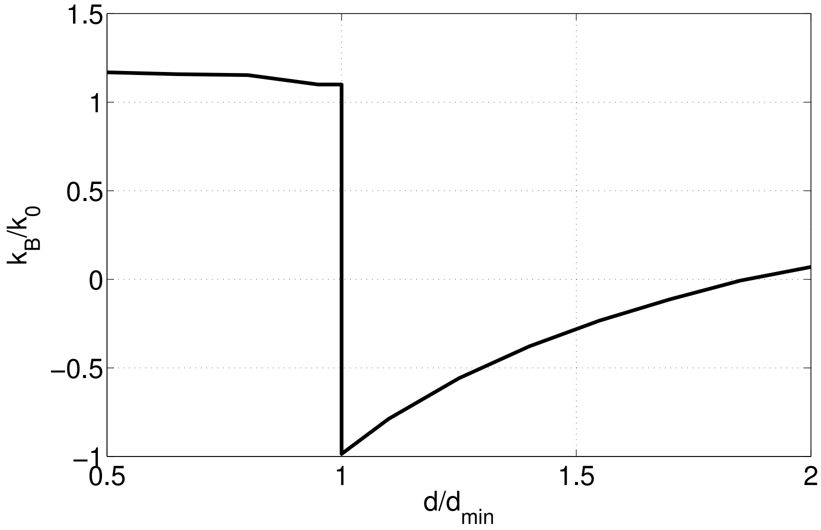

Figure 6.24: Propagation constant of the most excited progressive Bloch wave versus the normalized period L/L_{min}

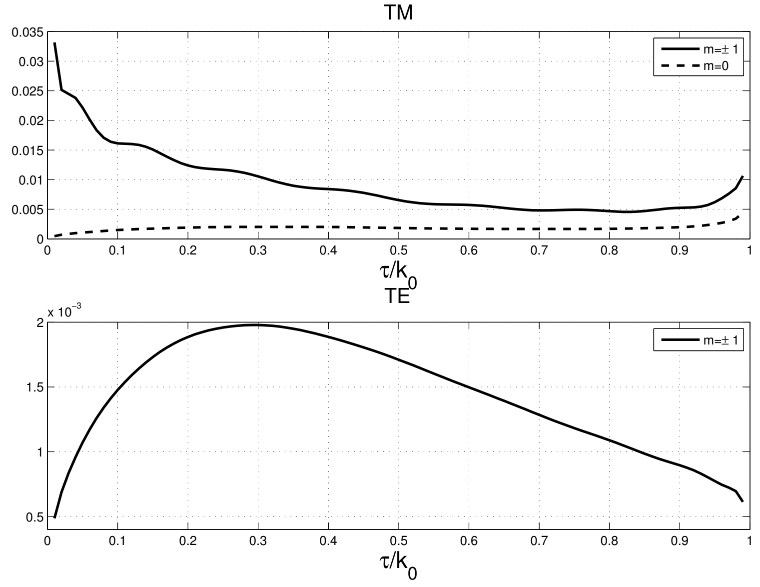

Figure 6.25: Continuous spectrum composition of the Bloch wave: TM and TE progressive power waves

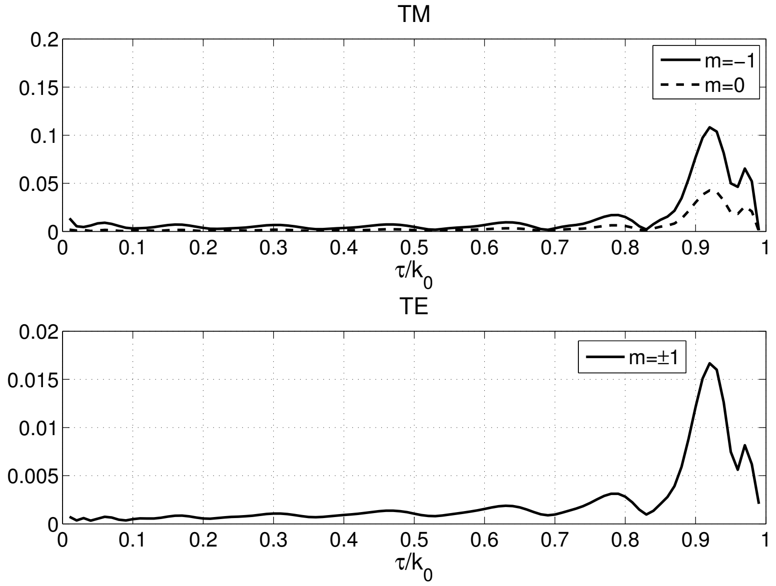

Figure 6.26: Continuous spectrum composition of the Bloch wave: TM and TE regressive power waves

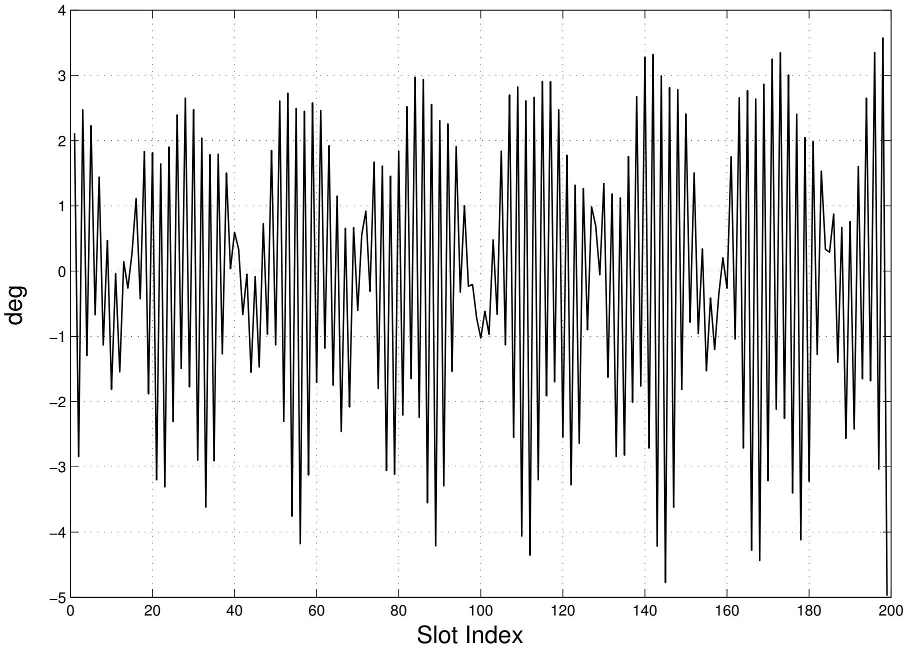

Figure 6.27: Difference between the phases of the main coefficient on each slot and that of the mostly excited Bloch wave

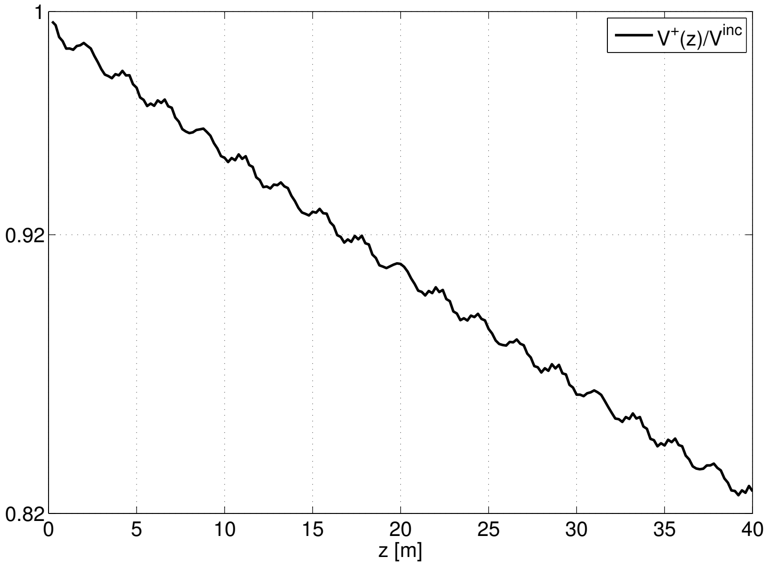

Figure 6.28: TEM mode progressive voltage, normalized to the incident voltage at the array input

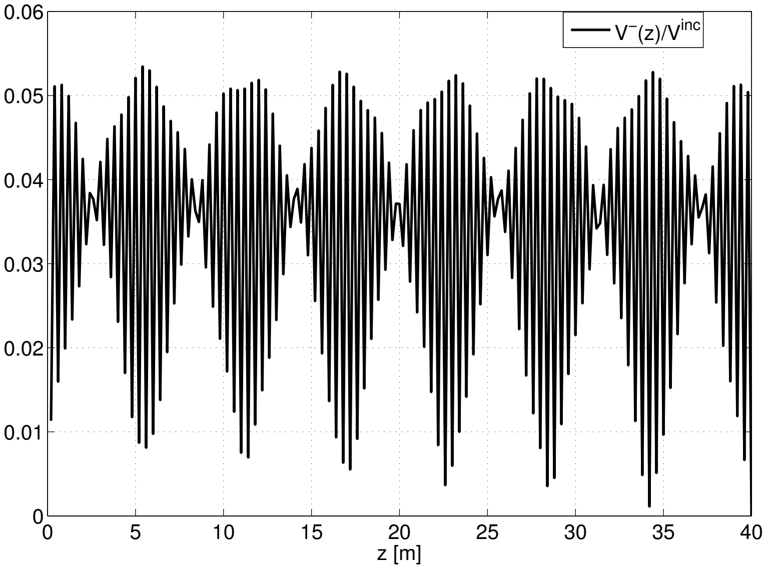

Figure 6.29: TEM mode regressive voltage, normalized to the incident voltage at the array input

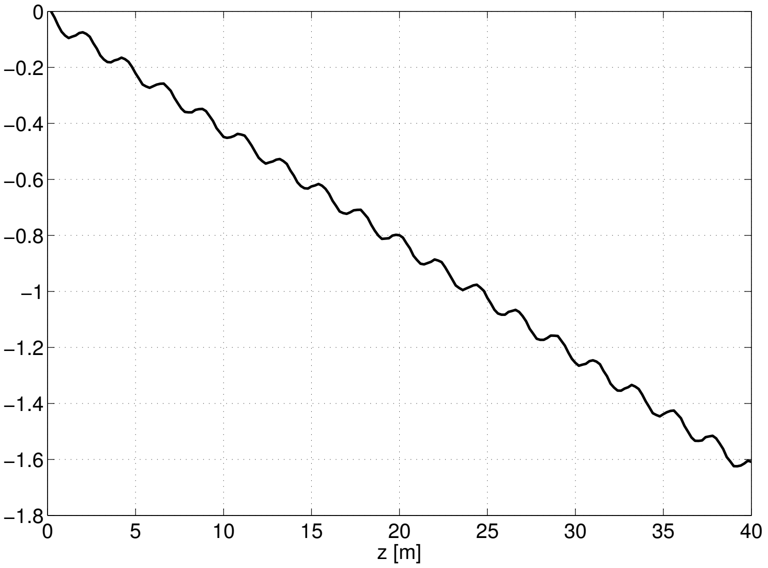

Figure 6.30: TEM mode power flow along the line, normalized to the incident power at the array input

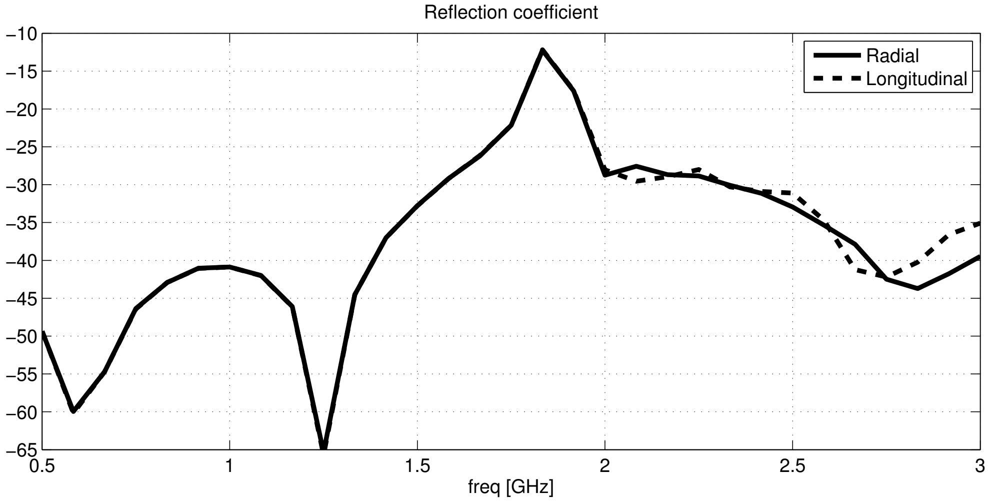

Figure 6.31: TEM reflection coefficient [dB], computed according to the transverse approach (solid line) and to the longitudinal approach (dashed line)

Chapter 7

Radiation Properties of Slotted Coaxial Cables

7.1 Introduction

In the preceding chapters we have focused our attention on the scattering characteristics of a slot array, in this chapter we will determine its radiation properties.

The first step is the computation of the radiation pattern of a single slot on the outer conductor of an infinite coaxial cable. The radial transmission line theory enables us to compute the spectral representation of the radiated field. The inverse transform cannot be performed in closed form and we exploit the classical saddle point method to obtain an asymptotic estimate valid in the far field region of the slot. The accuracy of the result is confirmed by a direct numerical evaluation of the radiation integral along the steepest descent path (SDP).

The slot radiation pattern seems strange at first sight, since it is characterized by a minimum in the broadside direction and a steady increase as endfire is approached. The reason for this can be attributed to the presence of the infinitely long cylinder on which the aperture lies. Actually, the observer can be in the far field region of the slot, but never of the cylinder. To verify this point we studied in an approximate way the problem of a slot on a finite length cylinder. In particular, we computed both the magnetic current associated to the slot and the electric current induced on the metal, in the assumption the cylinder is infinite. Applying the Equivalence theorem, the

cylinder is removed and the two current distributions radiate in free space. The finite length of the cylinder is taken into account by simple truncation, hence using a kind of Physical Optics approximation.
The patterns obtained in this way have always a null in the endfire direction, as intuitively expected, but have also main lobes approaching endfire if the cable length is increased, thus confirming the original results of Section 7.2.
It is interesting to note that the pattern of a slot on a finite length cylinder can be explained also by the elementary model of a filamentary electric current with progressive phase shift from the center to the ends.

After studying the radiation properties of a single slot, we turn to the array of N_{slot} slots. It is to be remarked that in the practical exploitation of LCX, the receiver is always in the near field region of the array, but in the far field region of every slot. This enables us to compute the array radiated field by superposition of the slot pattern obtained in Section 7.2. On the basis of the conclusions of Section 6.3, the slot aperture field are assumed all equal apart from a progressive (complex) phase shift, associated to the mostly excited Bloch wave.

The application of the Poisson sum formula to the expression of the array radiated field converts it into a summation of spatial harmonics, thus enabling a connection with the Bloch wave point of view, developed in Chapter 6. Examples of computation of radiation fields of cables with different slot spacings are perfectly explained in terms of the various operation modes introduced in Section 4.5 : surface wave, mono radiation and multiradiation operation.

7.2 Radiation properties of a single slot

Let us start by computing the field radiated by a single slot. Using the model developed in Chapter 2, we must determine the field generated by a magnetic current distribution $\underline{\mathbb{J}}_m$, directed along $\hat{\varphi}$, placed on a metallic cylinder of radius ρ_2.
The radial equivalent circuit of the structure is shown in Figure 7.1, where a voltage generator, whose value is proportional to the Fourier transform of $\underline{\mathbb{J}}_m$, is connected to a semi-infinite transmission line, starting at $\rho = \rho_2$. Recalling (2.71) and (2.72), we find that voltage and current at

a generic section ρ are given by

$$\begin{aligned}\overset{\leadsto}{\underline{V}}(\rho) &= \overset{\leadsto}{\underline{\underline{P}}}_v(\rho,\,\rho_2)\cdot\overset{\leadsto}{\underline{V}}(\rho_2)=\overset{\leadsto}{\underline{\underline{P}}}_V(\rho,\,\rho_2)\cdot\mathring{\underline{v}} && (7.1)\\ \overset{\leadsto}{\underline{I}}(\rho) &= \overset{\leadsto}{\underline{\underline{P}}}_i(\rho,\,\rho_2)\cdot\overset{\leadsto}{\underline{I}}(\rho_2)=\overset{\leadsto}{\underline{\underline{P}}}_I(\rho,\,\rho_2)\cdot\overset{\leadsto}{\underline{\underline{Y}}}(\rho_2)\cdot\mathring{\underline{v}} && (7.2)\end{aligned}$$

Inserting the explicit expressions of propagators and line admittance, we obtain the following expressions for the radiated fields:

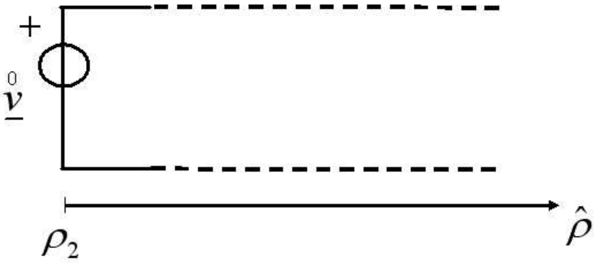

Figure 7.1: Equivalent radial circuit for the computation of the radiated field

$$\begin{aligned}E_\rho(\rho,\varphi,z) &= \frac{1}{4\pi^2\omega\epsilon}\sum_n \mathrm{e}^{-jn\varphi}\int_{-\infty}^{+\infty}\left(\frac{j\omega\epsilon_2}{\tau}\frac{H_n^{'(2)}(\tau\rho)}{H_n^{(2)}(\tau\rho_2)}-\frac{j\,n^2\chi^2}{\omega\mu\rho_2^2\tau^3}\frac{H_n^{(2)}(\tau\rho)}{(H_n^{'(2)}(\tau\rho_2))^2}\right)\tilde{\mathbb{J}}_m(\chi,n)\,\mathrm{e}^{-j\chi\,z}d\chi\\ E_\varphi(\rho,\varphi,z) &= \frac{1}{4\pi^2}\sum_n n\mathrm{e}^{-jn\varphi}\int_{-\infty}^{+\infty}\frac{\chi}{\tau^2}\left(\frac{H_n^{'(2)}(\tau\rho)}{\rho_2\,H_n^{'(2)}(\tau\,\rho_2)}-\frac{H_n^{(2)}(\tau\rho)}{\rho\,H_n^{(2)}(\tau\,\rho_2)}\right)\tilde{\mathbb{J}}_m(\chi,n)\,\mathrm{e}^{-j\chi\,z}d\chi \qquad (7.3)\\ E_z(\rho,\varphi,z) &= \frac{1}{4\pi^2}\sum_n \mathrm{e}^{-jn\varphi}\int_{-\infty}^{+\infty}\frac{H_n^{(2)}(\tau\rho)}{H_n^{(2)}(\tau\rho_2)}\tilde{\mathbb{J}}_m(\chi,n)\,\mathrm{e}^{-j\chi z}d\chi\end{aligned}$$

$$\begin{aligned}H_\rho(\rho,\varphi,z) &= -\frac{1}{4\pi^2\omega\mu\rho}\sum_n n\,\mathrm{e}^{-jn\varphi}\int_{-\infty}^{+\infty}\frac{H_n^{(2)}(\tau\rho)}{H_n^{(2)}(\tau\rho_2)}\tilde{\mathbb{J}}_m(\chi,n)\,\mathrm{e}^{-j\chi z}d\chi\\ H_\varphi(\rho,\varphi,z) &= \frac{1}{4\pi^2}\sum_n \mathrm{e}^{-jn\varphi}\int_{-\infty}^{+\infty}\left(\frac{j\omega\epsilon_2}{\tau}\frac{H_n^{'(2)}(\tau\rho)}{H_n^{(2)}(\tau\rho_2)}-\frac{j\,n^2\beta^2}{\omega\mu\rho_2^2\tau^3}\frac{H_n^{(2)}(\tau\rho)}{H_n^{'(2)}(\tau\rho_2)^2}\right)\tilde{\mathbb{J}}_m(\chi,n)\,\mathrm{e}^{-j\chi z}d\chi \qquad (7.4)\\ H_z(\rho,\varphi,z) &= -\frac{1}{4\pi^2}\sum_n n\mathrm{e}^{-jn\varphi}\int_{-\infty}^{+\infty}\frac{\chi}{\tau^2}\frac{j\,\chi}{\omega\mu\rho\tau}\frac{H_n^{(2)}(\tau\rho)}{H_n^{'(2)}(\tau\,\rho_2)}\tilde{\mathbb{J}}_m(\chi,n)\,\mathrm{e}^{-j\chi\,z}d\chi\end{aligned}$$

where $\tilde{\mathbb{J}}_m(\chi, n)$ is the double Fourier Transform of $\mathbb{J}_m(z, \varphi)$.
These expressions are valid for every point around the cable. In the applications, the observation points lie always in the near field region of the complete array but in the far field region of the single slots. Hence we will proceed to the asymptotic evaluation of these integrals, for $k_0 R \to \infty$.

Let us consider in detail the case of E_z. First, it is convenient to rewrite (7.4) using spherical coordinates, see Figure 7.2:

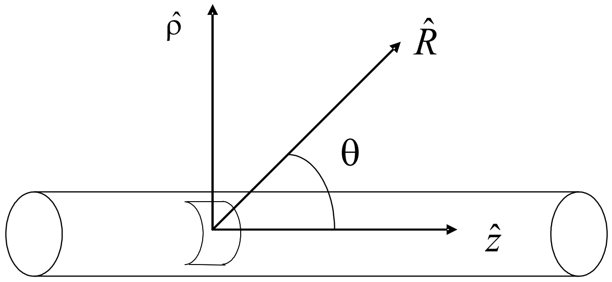

Figure 7.2: Spherical reference system for a single slot

$$E_z(R, \varphi, \theta) = \frac{1}{4\pi^2} \sum_n \mathrm{e}^{-jn\varphi} \int_{-\infty}^{+\infty} \frac{H_n^{(2)}(\tau\, R \sin\theta)}{H_n^{(2)}(\tau \rho_2)} \tilde{\mathbb{J}}_m(\chi, n)\, \mathrm{e}^{-j\chi\, R\cos\theta} d\chi \tag{7.5}$$

In order to apply the Saddle Point Method, we must reduce this expression to the form

$$E_z(R, \varphi, \theta) = \sum_n \mathrm{e}^{-jn\varphi} \int_{-\infty}^{+\infty} f(\chi, \theta) \mathrm{e}^{-jk_0 R q(\chi)} d\chi \tag{7.6}$$

to be evaluated for $k_0 R \to \infty$. To eliminate the branch point singularity related to $\tau = \sqrt{k_0^2 - \chi^2}$, we apply the change of variable (see [8]) $\chi = k_0 \cos w$, so that $\tau = k_0 \sin w$. In the new variable (7.5) becomes:

$$E_z(R, \varphi, \theta) = -\frac{k_0}{4\pi^2} \sum_n \mathrm{e}^{-jn\varphi} \int_\Gamma \sin w \frac{H_n^{(2)}(k_0 R \sin w \sin\theta)}{H_n^{(2)}(k_0\, \rho_2 \sin w)} \tilde{\mathbb{J}}_m(k_0 \cos w, n)\, \mathrm{e}^{-jk_0\, R\cos\theta\cos w} dw \tag{7.7}$$

where Γ is the path, in the complex w plane, shown in Figure 7.3. Recalling the large argument expansion of the Hankel function, we see that it is convenient to multiply and divide by the factor $\exp(-j\, k_0 R \sin w \sin\theta)$:

$$E_z(R, \varphi, \theta) = -\frac{k_0}{4\pi^2} \sum_n \mathrm{e}^{-jn\varphi} \int_\Gamma \sin w \frac{H_n^{(2)}(k_0 R \sin w \sin\theta) \mathrm{e}^{+j\, k_0 R \sin w \sin\theta}}{H_n^{(2)}(k_0\, \rho_2 \sin w)} \cdot$$

$$\cdot \tilde{\mathbb{J}}_m(k_0 \cos w, n)\, \mathrm{e}^{-jk_0\, R\cos(\theta - w)} dw \tag{7.8}$$

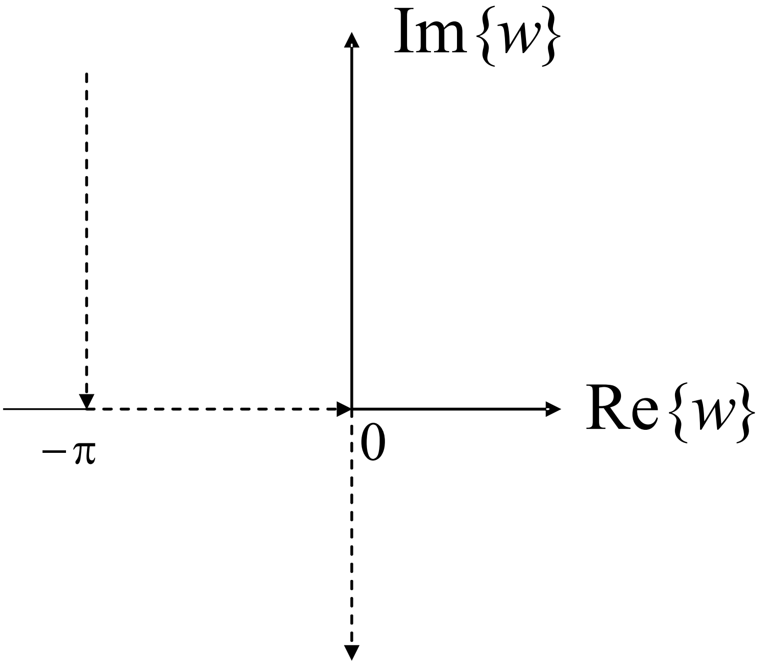

Figure 7.3: Path Γ in the complex w plane

The function $q(\chi)$ of (7.6) is readily identified as $q(w) = \cos(\theta - w)$. The saddle point, defined by the condition

$$\frac{dq}{dw}|_{w=w_s} = 0$$

is $w_s = \theta$. The Steepest Descent Path (SDP) is the curve in the w plane passing through w_s, along which $\mathfrak{Im}\{q(w)\}$ is constant. This means that along the SDP the last exponential in the above equation is not oscillating but has the fastest (exponential) decay when moving away from the saddle point w_s. The explicit parameterization of the SDP curve, shown in Figure 7.4 is:

$$w(x) = x + j \log\left(\frac{1 + \sin(x - \theta)}{\cos(x - \theta)}\right) \tag{7.9}$$

where $x \in [\theta - \pi/2, \theta + \pi/2]$. The integrand has a branch point in $w = 0$, but no singularities between the original path Γ and the SDP, so that the contour deformation can be carried out without changing the value of the integral. Figure 7.5 shows plots of the integrand evaluated on the SDP, for various values of θ. The radius of the cable outer conductor is $\rho_2 = 3$ cm, the slot has a width $s = 3$ mm and an angular aperture $\alpha = 360°$, the frequency is $f = 1$ GHz. The observation points lie in the plane $\varphi = 0°$ on a circle of radius $R = 1$ m. We see that the plots are very regular, except when θ is small. In these cases, the $w = 0$ singularity shows up with a peak. Note that up to this point there is no approximation and the integral can be

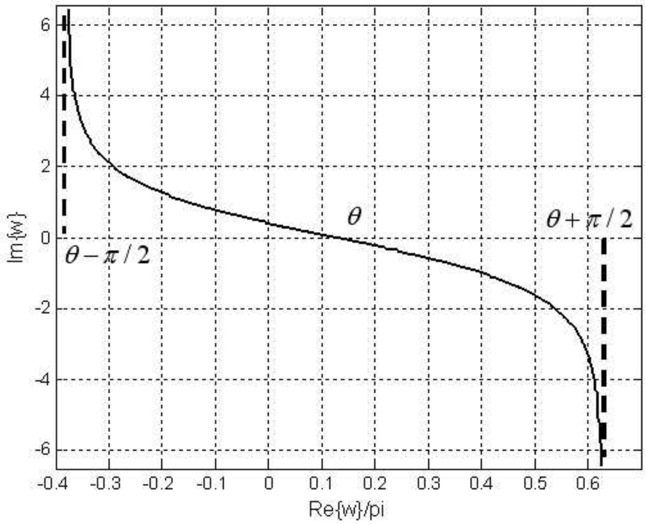

Figure 7.4: Γ and the SDP path

simply evaluated by numerical quadrature. If $k_0 R \gg 1$ and θ is not too close to 0 or π, it is possible to derive an analytical expression according to the saddle point method. Indeed, the Hankel function $H_n^{(2)}(k_0 R \sin(w) \sin\theta)$ can be approximated by its asymptotic expression for large argument, i.e.:

$$H_n^{(2)}(x) \sim \sqrt{\frac{2}{\pi\, x}} \mathrm{e}^{-j(x - n\pi/2 - \pi/4)} \qquad \text{for } x \gg n \tag{7.10}$$

Substituting (7.10) in (7.7) we obtain:

$$E_z(R,\varphi,\theta) = -\frac{1}{4\pi^2}\sqrt{\frac{2\,k_0}{\pi \sin\theta R}} \sum_n j^n \mathrm{e}^{-jn\varphi} \int_{SDP} \frac{\tilde{\mathbb{J}}_m(k_0 \cos w, n)\sqrt{\sin w}}{H_n^{(2)}(k_0\,\rho_2 \sin w)}\, \mathrm{e}^{-jk_0 R \cos(\theta - w)} dw \tag{7.11}$$

Applying the Saddle Point Method (see [8]), the far field expression of E_z is given by:

$$E_z(R,\varphi,\theta) \approx -\frac{\mathrm{e}^{-jk_0 R}}{4\pi\, R} \left(\frac{2j}{\pi} \sum_n j^n \mathrm{e}^{-jn\varphi} \frac{\tilde{\mathbb{J}}_m(k_0 \cos\theta, n)}{H_n^{(2)}(k_0\,\rho_2 \sin\theta)} \right) \tag{7.12}$$

The accuracy of (7.12) is proved by a comparison, shown in Figure 7.6, with the results of the numerical evaluation of the integral along the SDP. The figure shows a very good agreement between the two curves except for values of θ close to 0 or π, where the presence of further peaks is not accounted for by the saddle point formula.

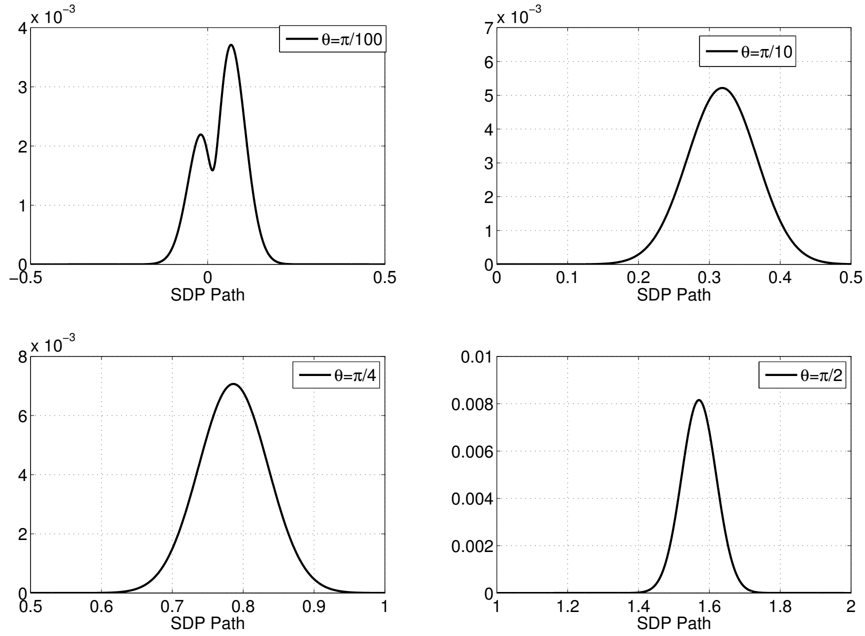

Figure 7.5: Integrand function evaluated along the SDP for different values of θ

Using the same procedure as before, we obtain the far field expressions of the other components of the radiated field:

$$
\begin{aligned}
&E_\rho(R,\varphi,\theta) \approx \psi(R)\sum_n \tilde{\mathbb{J}}_m(k_0\cos\theta,n)\left(\frac{2j\cos\theta}{\sin\theta}\frac{j^n e^{-jn\varphi}}{H_n^{(2)}(k_0\rho_2\sin\theta)} + \frac{-2j\cos^3(\theta)}{\pi\, k_0^2\rho_2^2\sin\theta}\frac{j^n n^2 e^{-jn\varphi} H_n^{(2)}(k_0\rho_2\sin\theta)}{[H_n^{'(2)}(k_0\rho_2\sin\theta)]^2}\right)\\
&E_\varphi(R,\varphi,\theta) \approx \psi(R)\cdot\sum_n -\tilde{\mathbb{J}}_m(k_0\cos\theta,n)\frac{n\,e^{-jn\varphi}}{\pi\,k_0\sin\theta}\left[\frac{j}{R\,\rho_2\,H_n^{'(2)}(k_0\rho_2\sin(\theta))} - \frac{(-1)^n}{R^2\sin(\theta)\,H_n^{(2)}(k_0\rho_2\sin(\theta))}\right]\\
&H_\rho(R,\varphi,\theta) \approx \frac{\psi(R)}{R}\sum_n -\frac{2jn\,j^n e^{-jn\varphi}}{\omega\mu\pi}H_n^{(2)}(k_0\,\rho_2\sin\theta)\tilde{\mathbb{J}}_m(k_0\cos\theta,n)\\
&H_\varphi(R,\varphi,\theta) \approx \psi(R)\sum_n \tilde{\mathbb{J}}_m(k_0\cos\theta,n)\left(-\frac{2j\omega\varepsilon}{k_0\sin\theta}\frac{j^n e^{-jn\varphi}}{\pi\,H_n^{(2)}(k_0\rho_2\sin\theta)} + \frac{2j\cos^2(\theta)}{\pi\omega\mu\,k_0\rho_2^2\sin^3\theta}\frac{j^n n^2 e^{-jn\varphi}H_n^{(2)}(k_0\rho_2\sin\theta)}{[H_n^{'(2)}(k_0\rho_2\sin\theta)]^2}\right)\\
&H_z(R,\varphi,\theta) \approx \psi(R)\sum_n \tilde{\mathbb{J}}_m(k_0\cos\theta,n)\left(-\frac{j}{\omega\mu\,R\sin\theta}\frac{j^n\,n\,e^{-jn\varphi}}{\pi\,H_n^{'(2)}(k_0\rho_2\sin\theta)}\right)
\end{aligned}
\tag{7.13}
$$

where

$$\psi(R) = \frac{\mathrm{e}^{-jk_0R}}{4\pi\,R}$$

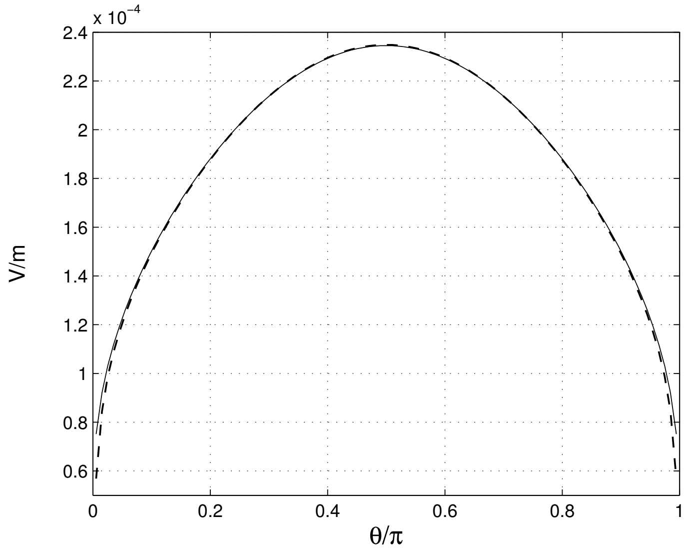

Figure 7.6: $E_z(\theta)$ for $R = 3$ m. Comparison between the numerical integration along the SDP (solid line) and the analytical approximation (Dashed line)

is the Helmholtz function. It is important to remark that the components E_z, E_ρ and H_φ decay as $1/R$, while E_φ, H_z and H_ρ as $1/R^2$. This fact means that in the far field region the main field components are E_z, E_ρ and H_φ.

Figures 7.7 and 7.8 show that the analytical approximations are very close to the results of the numerical integration. Let us now consider in detail the expressions (7.13). The component E_z correctly approaches zero for θ close to $0, \pi$, so that boundary conditions are satisfied. On the contrary, the components H_φ and E_ρ are apparently unbounded in the same conditions. This behavior is related to the assumption that the cylinder is infinite. At any rate, the singularities are unreachable, because the observation points must always lie outside the cylinder. In the next paragraph, it will be shown that if the cylinder is finite, these singularities disappear but still the radiation pattern presents two maxima which tend to the end-fire direction when the length of the cable is increased.

Let us specialize the above formulas for the case where the magnetic current distribution J_m

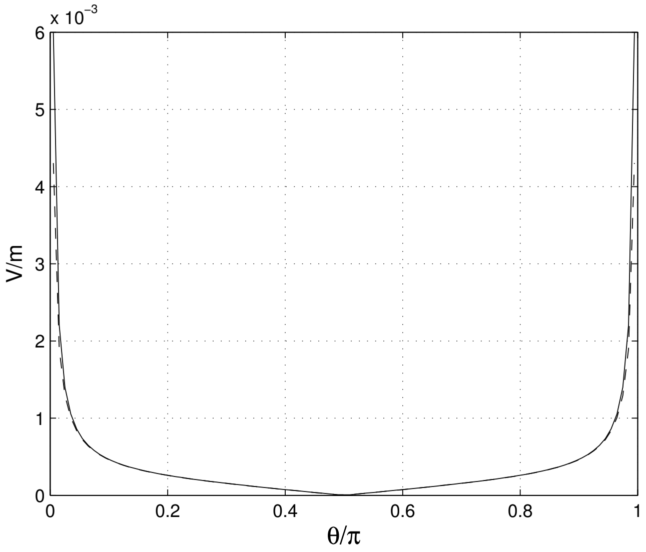

Figure 7.7: $E_\rho(\theta)$ for $R = 3$ m. Comparison between the numerical integration along the SDP (solid line) and the analytical approximation (Dashed line)

does not depend on φ. Eqs. 7.12 and 7.13 reduce to:

$$
\begin{aligned}
E_z(R,\varphi,\theta) &\approx \psi(R)\frac{2j\tilde{\mathbb{J}}_m(k_0\cos\theta)}{\pi\, H_0^{(2)}(k_0\,\rho_2\sin\theta)} \\
E_\rho(R,\varphi,\theta) &\approx \psi(R)\frac{2j\cos\theta\tilde{\mathbb{J}}_m(k_0\cos\theta)}{\pi\sin\theta\, H_0^{(2)}(k_0\rho_2\sin\theta)} \\
H_\varphi(R,\varphi,\theta) &\approx -\psi(R)\frac{2j\omega\varepsilon\,\tilde{\mathbb{J}}_m(k_0\cos\theta)}{k_0\pi\sin\theta H_0^{(2)}(k_0\rho_2\sin\theta)}
\end{aligned}
\tag{7.14}
$$

The total electric field

$$\underline{E} = E_z\hat{z} + E_\rho\hat{\rho}$$

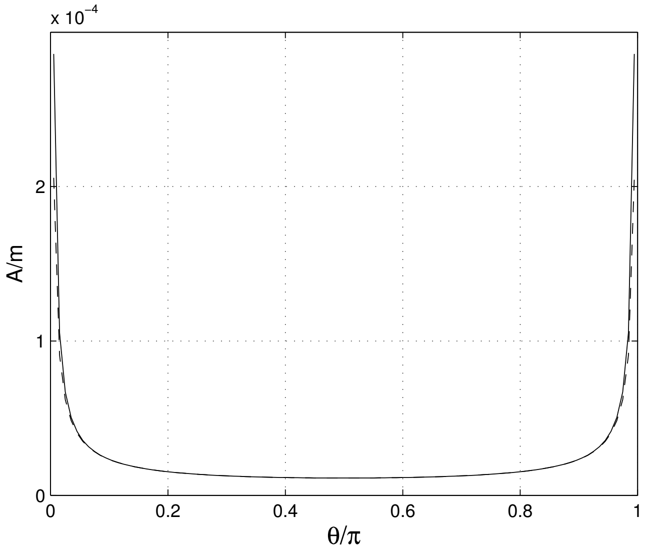

Figure 7.8: $H_\varphi(\theta)$ for $R = 3$ m. Comparison between the numerical integration along the SDP (solid line) and the analytical approximation (Dashed line)

becomes in the spherical reference system:

$$\begin{aligned}
\underline{E} &= \psi(R)\left\{(\hat{R}\cos\theta - \hat{\theta}\sin\theta)\left(2j\frac{\tilde{\mathbb{J}}_m(k_0\cos\theta)}{\pi\, H_0^{(2)}(k_0\,\rho_2\sin\theta)}\right)+\right.\\
&+ \left.(\hat{R}\sin\theta + \hat{\theta}\cos\theta)\left(\frac{2j\cos\theta\tilde{\mathbb{J}}_m(k_0\cos\theta)}{\pi\sin\theta\, H_0^{(2)}(k_0\rho_2\sin\theta)}\right)\right\} =\\
&= \frac{\mathrm{e}^{-jk_0R}}{4\pi\, R}\frac{2j\,\tilde{\mathbb{J}}_m(k_0\cos\theta)}{\pi\sin\theta H_0^{(2)}(k_0\rho_2\sin\theta)}\hat{\theta}
\end{aligned}$$

i.e. the electric field is directed along $\hat{\theta}$ and is orthogonal to the magnetic field and to the observation direction. Moreover, the ratio of the absolute values of the electric and magnetic field gives:

$$\frac{|\underline{E}(R,\varphi,\theta)|}{|\underline{H}(R,\varphi,\theta)|} = \frac{k_0}{\omega\varepsilon} = Z_0$$

i.e. the electric and magnetic fields satisfy the spherical wave impedance relation.
The same results hold for the general case, but the computational details are more involved.
Since the azimuthal dimension of the slots is small in comparison with the wavelength, the radiated field can be expected to depend weakly on φ. As an example, Figure 7.9 shows the radiation pattern of H_φ versus φ for $\theta = \pi/2$. The cylinder has a radius $\rho_2 = 8.8$ mm and the slot is such that $\rho_2\alpha/\lambda_0 = 1/10$.

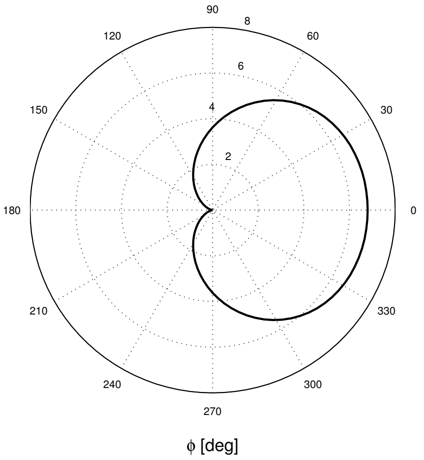

Figure 7.9: Normalized radiation pattern of H_φ (in dB) for $\theta = \pi/2$. The slot is centered at $\varphi = 0$ and $\rho_2\alpha/\lambda_0 = 0.1$

7.3 Radiation from a slot on a finite length cylinder

In the preceding section the expressions of the field radiated by a magnetic current distribution located on a infinite metallic cylinder have been obtained. It has been pointed out that those formulas predict a radiated field that increases when the observation direction approaches the end-fire direction. At first this result is surprising, but we have to realize that, in this configuration, the metal cylinder plays the major role and not the slot. In order to show this point in greater detail let us repeat the computation of the radiated field, but assuming that the length L_{cyl} of the cylinder is large but finite. We introduce a surface Σ, flush with the metallic cylinder and apply the Equivalence Theorem (see figure 7.10) to remove the conductor, introducing in its place an equivalent electric current $\underline{\mathbb{J}}_e$

$$\underline{\mathbb{J}}_e(\varphi, z) = \hat{\rho} \times \underline{H}(\rho = \rho_2^+, \varphi, z)$$

where $\underline{H}(\rho = \rho_2^+, \varphi, z)$ is the magnetic field along the conductor, which can be computed by the radial transmission line formalism:

$$\underline{H}(\rho = \rho_2^+, \varphi, z) = -\frac{\hat{\varphi}}{4\pi^2}\left\{\sum_n \mathrm{e}^{-j\,n\varphi}\int_{\Re} Y_{ext}(\chi, n)\tilde{J}_m(\chi, n)\,\mathrm{e}^{-j\chi\,z}d\chi\right\}$$

Since we want to explain the case of an infinite cylinder, we compute $\underline{H}(\rho = \rho_2^+, \varphi, z)$ in the

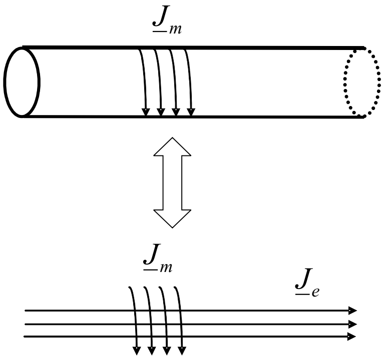

Figure 7.10: Application of the Equivalence Theorem

assumption that the cylinder is infinite and then we truncate the resulting current:

$$\underline{\mathbb{J}}_{et} = -\hat{z}\frac{1}{4\pi^2}\left\{\sum_n e^{-jn\varphi}\int_{\Re} Y_{ext}(\chi,n)\tilde{J}_m(\chi,n)\,e^{-j\chi z}d\chi\right\}\text{rect}\left(\frac{z}{L_{cyl}}\right) \tag{7.15}$$

Moreover, the effects of the cylinder bases will be neglected.
The field radiated by the electric and magnetic currents is computed by the radial line equivalent circuit shown in figure 7.11. where $\overline{\underline{\underline{Y}}}(\chi,n)$ and $\underline{\underline{Y}}^{ext}(\chi,n)$ are the regular and centrifugal wave

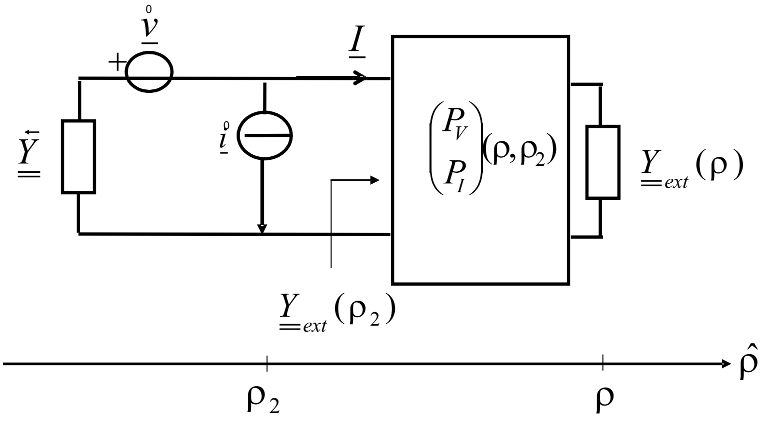

Figure 7.11: Equivalent radial circuit

admittance computed in section 2.3, the generators $\overset{\circ}{v}$ and $\overset{\circ}{i}$, in accordance with (2.12), have the form:

$$\underline{\overset{\circ}{v}}(\chi, n) = \begin{pmatrix} -\tilde{J}_m(\chi, n) \\ 0 \end{pmatrix} \tag{7.16}$$

$$\underline{\overset{\circ}{i}}(\chi, n) = \begin{pmatrix} \tilde{J}_{et}(\chi, n) \\ 0 \end{pmatrix} \tag{7.17}$$

where $\tilde{J}_m$ and $\tilde{J}_{et}$ are the double Fourier transforms of J_m and J_{et}.
From inspection of the circuit we obtain:

$$\underline{I}(\rho) = -\underline{\underline{P}}_I(\rho, \rho_2)\left(\underline{\underline{\overline{Z}}} + \underline{\underline{Z}}^{ext}\right)^{-1} \cdot \left(\underline{\overset{\circ}{v}} + \underline{\underline{\overline{Z}}} \cdot \underline{\overset{\circ}{i}}\right) \tag{7.18}$$

The φ component of the radiated magnetic field is obtained by inverse Fourier transform:

$$H_\varphi(\rho, \phi, z) = \frac{1}{4\pi^2} \sum_n \mathrm{e}^{-j\,n\varphi} \int_{\Re} \mathrm{e}^{-j\chi\,z} \underline{\underline{P}}_I(\rho, \rho_2)\left(\underline{\underline{\overline{Z}}} + \underline{\underline{Z}}^{ext}\right)^{-1} \cdot \left(\overset{\circ}{v} + \underline{\underline{\overline{Z}}}\overset{\circ}{i}\right) d\chi \tag{7.19}$$

and similar expressions for the other field components. In view of (7.15) and (7.17), the explicit expression of $\underline{\overset{\circ}{i}}(\chi, n)$ is:

$$\overset{\circ}{i}(\chi, n) = -\hat{u} \sum_n \mathrm{e}^{-j\,n\varphi} \int_{\Re} Y_{uu}^{ext}(\overline{\chi}, n)\tilde{J}_m(\overline{\chi}, n) \frac{2\sin\frac{L_{cyl}}{2}(\chi - \overline{\chi})}{(\chi - \overline{\chi})} d\overline{\chi} \tag{7.20}$$

where the convolution of the transforms can be recognized. Substituting in (7.19)we get:

$$\begin{aligned} H_\varphi(\rho, \phi, z) = -\frac{1}{4\pi^2} \sum_n \mathrm{e}^{-j\,n\varphi} \int_{\Re} \frac{H_n^{\prime(2)}(\tau\rho)}{H_n^{\prime(2)}(\tau\,\rho_2)}\, \mathrm{e}^{-j\chi\,z}\left(\overline{Z}_{uu} + Z_{uu}^{ext}\right)^{-1} \cdot \\ \left\{\tilde{J}(\chi, n) + \overline{Z}_{uu}(\chi, n) \int_{\Re} Y_{ext}(\overline{\chi}, n)\tilde{J}(\overline{\chi}, n) \frac{2\sin\frac{L_{cyl}}{2}(\chi - \overline{\chi})}{(\chi - \overline{\chi})} d\overline{\chi}\right\} d\chi \end{aligned} \tag{7.21}$$

The external integral can be approximated by the Saddle Point Method as shown in the preceding section. The final expression is:

$$\begin{aligned} H_\varphi(\rho, \phi, z) = -\psi(R) \cdot \sum_n \mathrm{e}^{-j\,n\varphi} \frac{2j}{\pi} \frac{\left(\overline{Z}_{uu} + Z_{uu}^{ext}\right)^{-1}(k_0\cos\theta, n)}{H_n^{\prime(2)}(k_0\,b\sin\theta)} \cdot \\ \left[\tilde{J}_m(k_0\cos\theta, n) + \overline{Z}_{uu}(k_0\cos\theta, n) \int_{\Re} Y_{uu}^{ext}(\overline{\chi}, n)\tilde{J}_m(\overline{\chi}, n) \frac{2\sin\frac{L_{cyl}}{2}(k_0\cos\theta - \overline{\chi})}{k_0\cos\theta - \overline{\chi}} d\overline{\chi}\right] \end{aligned} \tag{7.22}$$

where $\psi(R)$ is the Helmholtz function. The remaining integral is computed by extracting the singular part in Y_{uu}^{ext} and, subsequently, applying the Double Exponential transformation (more details can be found in paragraph 10.2).

Figure 7.12 shows a plot of H_φ versus θ. The cable geometrical characteristics are: outer conductor radius $b = 8.8$ mm, slot width $s = 3$ mm, $\alpha = 2\pi$ (complete slot), frequency $f = 1$ GHz and cylinder length $L_{cyl} = 10\lambda_0$. The pattern presents two maxima for $\theta = 22°$ and $\theta = 158°$, but goes to zero when the observation point approaches the endfire direction. Figures 7.13, 7.14 and 7.15 show the radiation patterns for cylinders of length L_{cyl} equal to $20\lambda_0$, $40\lambda_0$, $100\lambda_0$, respectively. The maxima move to the end fire direction and the field presents an oscillatory behavior, with a decreasing ripple when the length of the cable is increased.

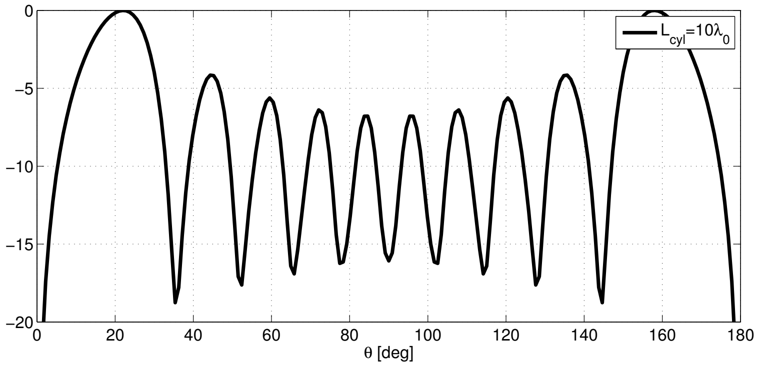

Figure 7.12: Normalized radiation pattern of H_φ, in dB, for $L_{cyl} = 10\lambda_0$

It is interesting that this type of pattern can be qualitatively explained also in terms of a very simple model. The magnetic current ring, owing to $k_0 b \ll 1$ is equivalent to an electric

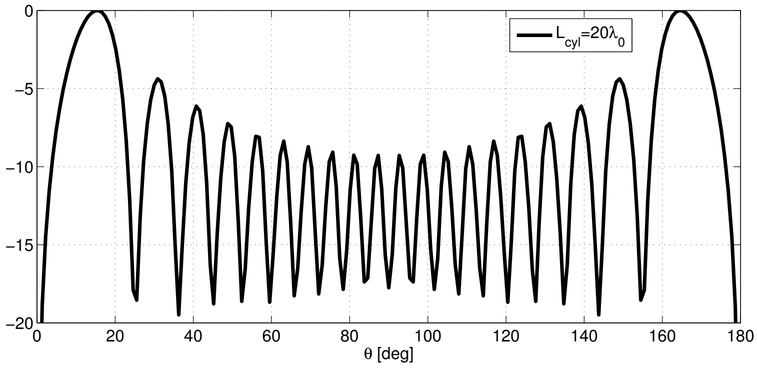

Figure 7.13: Normalized radiation pattern of H_φ, in dB, for $L_{cyl} = 20\lambda_0$

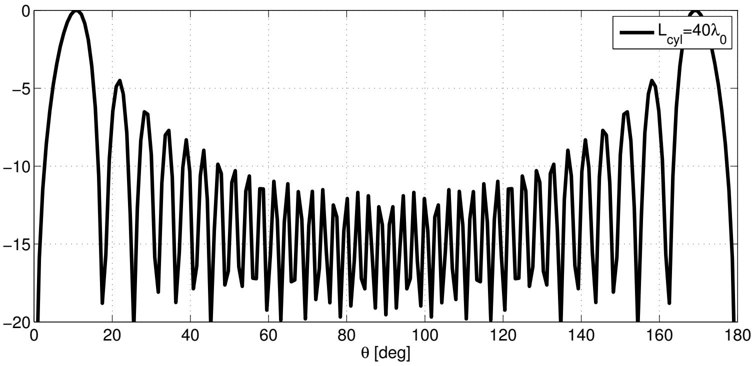

Figure 7.14: Normalized radiation pattern of H_φ, in dB, for $L_{cyl} = 40\lambda_0$

dipole parallel to the z axis. The electric current density $\underline{\mathbb{J}}_{et}$ can be roughly approximated with a filamentary current on the axis $I(z) = I_0 \exp(-jk_0|z|)$ (the slot width s is neglected). The H_φ pattern produced by this current is

$$\begin{aligned} H_\varphi(R,\theta,\varphi) &= -j\psi(R)I_0\frac{k_0L_{cyl}}{2}\left\{\mathrm{e}^{-j\frac{k_0L_{cyl}}{2}\sin^2\frac{\theta}{2}}\mathrm{sinc}\left(\frac{k_0L_{cyl}}{2\pi}\sin^2\frac{\theta}{2}\right)+\right.\\ &\left.\mathrm{e}^{-j\frac{k_0L_{cyl}}{2}\cos^2\frac{\theta}{2}}\mathrm{sinc}\left(\frac{k_0L_{cyl}}{2\pi}\cos^2\frac{\theta}{2}\right)\right\}\sin\theta \qquad (7.23)\end{aligned}$$

This pattern is shown in Fig. 7.16 for $L_{cyl} = 10\lambda_0$. To this pattern, we should add that of the equivalent electric dipole, corresponding to the slot. Since it is not easy to relate its moment to I_0 and its effect is negligible at endfire, where we want to focus our attention, we neglect it.

The pattern (7.23) consists of two sinc functions, one centered at $\theta = 0°$, the other at $\theta = 180°$.The effect of the latter is negligible in the neighborhood of $\theta = 0°$, provided $k_0L_{cyl} \gg 1$. The first zero, closest to endfire is given by

$$\theta_z = 2\arcsin\sqrt{\frac{\lambda}{L_{cyl}}}$$

and the fist maximum can be estimated by

$$\theta_{max} \simeq \sqrt{\frac{4\lambda}{3L_{cyl}}}$$

This shows clearly that the maximum shifts to endfire for increasing L_{cyl}.

To conclude, Figure 7.17 shows a comparison between H_φ computed in the hypothesis of infinite cylinder (*i.e.* by (7.13)) and using (7.23) for the case of $L_{cyl} = 100\lambda_0$. Note that, apart from the

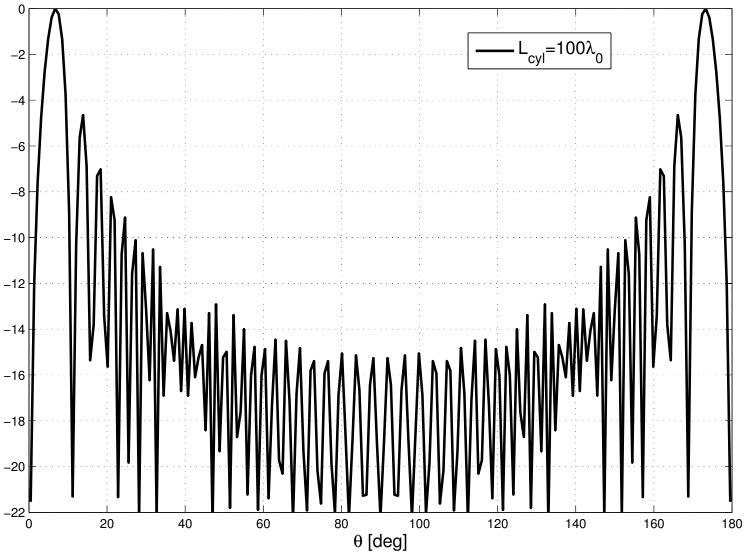

Figure 7.15: Normalized radiation pattern of H_φ, in dB, for $L_{cyl} = 100\lambda_0$

oscillatory behavior, there is a very good agreement between the two curves, which confirms the correctness of the (7.13).

7.4 The near field of a linear array

After discussing the radiation properties of a single slot, we are ready to find the field radiated by the complete array. The observation point lies usually in the near field region of the array and the radiated field will be found by superposition of the far field expressions (7.12 and 7.13) once the magnetic current distribution on each slot is known.

Let us fix the origin of the global reference in that point of the axis that is in correspondence of the center of the first slot. Analogously, the origin of the local reference of the q-th slot is in the corresponding point on the axis. Then the values of R_q and θ_q for any point $P = (\rho, \varphi, z)$ of interest, needed in (7.13), are given by (see Figure 7.18):

$$R_q = \sqrt{\rho^2 + (z - L_q)^2}$$
$$\theta_q = \arctan\left(\frac{\rho}{z - L_q}\right)$$

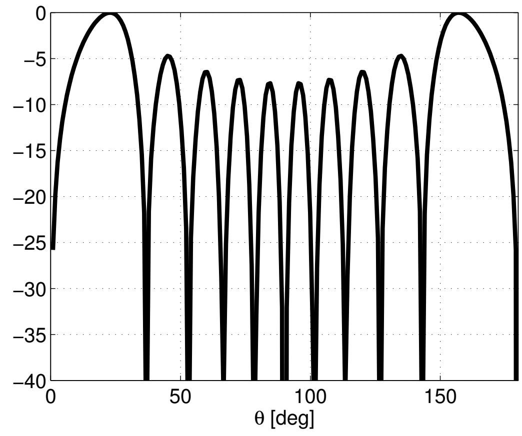

Figure 7.16: Pattern of (7.23), in dB, for $L_{cyl} = 10\lambda_0$

If we carry out this method, we obtain plots with characteristics that can vary widely when the cable parameters are changed. In order to understand the underlying phenomena, we examine the structure from the point of view of array theory.

Let us consider a LCX with N_{slot} slots, all equal and L-spaced. On the basis of the conclusions reached in Chapter 6, it will be assumed that the magnetic current distribution is the same on all the slots, apart for an amplitude coefficient x_q that changes from slot to slot according to the law:

$$x_q = x_0 \, \mathrm{e}^{-j\,k_z q\,L} \tag{7.24}$$

where k_z is a complex propagation constant whose real part is essentially that of the mostly excited Bloch wave of the periodic structure, which is close to the TEM propagation constant in the cable $k_0\sqrt{\varepsilon_{r1}}$, and the imaginary part takes into account the possible dielectric and metallic losses, as well as the radiation phenomenon. The equivalent magnetic current distribution $\underline{\mathbb{J}}_m$, then, has the form:

$$\underline{\mathbb{J}}_m = \sum_{q=1}^{N_{slot}} x_q u(z - q\,L, \varphi)\,\hat{\varphi}$$

and the z component of the radiated electric field, for instance, is:

$$\begin{aligned} E_z(\rho, \varphi, z) &= \sum_q x_q \left\{ \sum_n \mathrm{e}^{-j\,n\varphi} \right. \\ &\left. \int_{\Re} \mathrm{e}^{-j\chi\,q\,L} P_V(\rho, \rho_2; \chi, n) \tilde{u}(\chi, n) \mathrm{e}^{-j\chi\,z} d\chi \right\} \end{aligned} \tag{7.25}$$

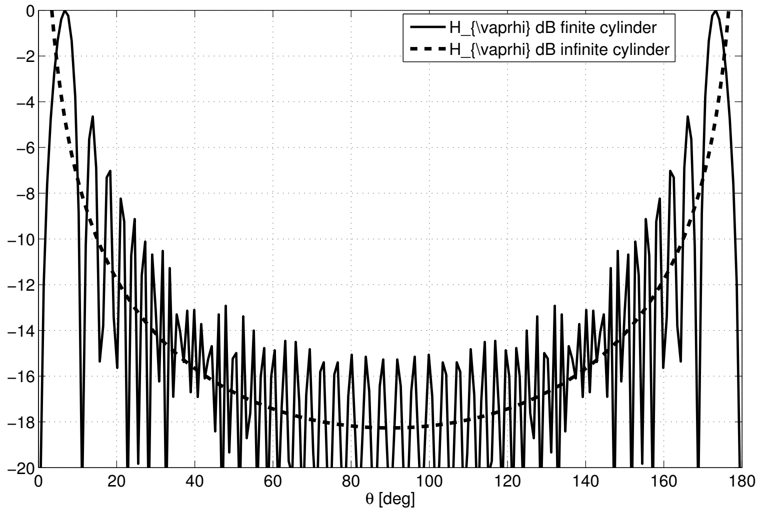

Figure 7.17: Radiation patterns of a slot in an infinite cylinder and in a $100\lambda_0$ long cylinder

where P_v is the uu component of the voltage propagator, computed in paragraph 2.4 and $u(z,\varphi)$ is the shape function of the current on the slot, with transform $\tilde{u}(\chi,n)$. Combining (7.24) and (7.25), we obtain:

$$\begin{aligned} E_z(\rho,\varphi,z) &= x_0 \sum_q \mathrm{e}^{-j\,k_z q\,L} \left\{ \sum_n \mathrm{e}^{-j\,n\varphi} \cdot \right. \\ & \left. \int_{\Re} \mathrm{e}^{-j\chi\,q\,L} P_V(\rho,\rho_2;\chi,n) \mathrm{e}^{-j\chi\,z} \tilde{u}(\chi,n) d\chi \right\} \end{aligned} \tag{7.26}$$

Multiplying by the factor $\mathrm{e}^{-j\,k_z z}\mathrm{e}^{+j\,k_z z}\mathrm{e}^{-j\,k_z qL}\mathrm{e}^{+j\,k_z qL}$, after some mathematical manipulations we get:

$$\begin{aligned} E_z(\rho,\varphi,z) &= x_0 \mathrm{e}^{-j\,k_z z} \sum_q \left\{ \sum_n \mathrm{e}^{-j\,n\varphi} \cdot \right. \\ & \left. \int_{\Re} \mathrm{e}^{-j(\chi-k_z)(z-\,q\,L)} P_v(\rho,\rho_2;\chi,n) \tilde{u}(\chi,n) d\chi \right\} \end{aligned} \tag{7.27}$$

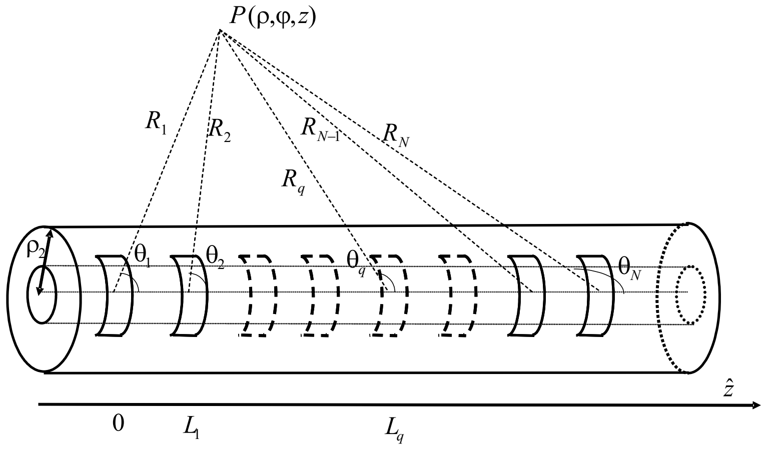

Figure 7.18: Computation of the field radiated by an array of slots

We let $\chi - k_z = t$:

$$\begin{aligned} E_z(\rho,\varphi,z) &= x_0 \mathrm{e}^{-j\,k_z z} \sum_q \left\{ \sum_n \mathrm{e}^{-j\,n\varphi} \cdot \right. \\ & \left. \int_{\Re} \mathrm{e}^{-j\,t\,(z-\,q\,L)} P_v(\rho,\rho_2; t+k_z, n) \tilde{u}(t+k_z,n) dt \right\} = \\ &= x_0 \mathrm{e}^{-j\,k_z z} \sum_n \mathrm{e}^{-j\,n\varphi} \sum_q h(z-qL;\rho,n) \end{aligned} \tag{7.28}$$

where we have defined

$$h(z;\rho,n) = \int_{\Re} \mathrm{e}^{-j\,t\,z} P_v(\rho,\rho_2 t + k_z, n) \tilde{u}(t+k_z,n) dt$$

Eq. 7.28 could be transformed by the use of the Poisson sum formula [34] if the array were infinite. Since N_{slot} is generally very large, we neglect the end point effects and write:

$$\sum_q h(z-qL;\rho,n) = \frac{1}{L} \sum_q \mathrm{e}^{-jq\frac{2\pi}{L}} \tilde{h}(-q\frac{2\pi}{L};\rho,n) \tag{7.29}$$

where $\tilde{h}(\chi)$ is the Fourier Transform of $h(z)$. Finally, we obtain:

$$\begin{aligned} E_z(\rho,\varphi,z) &= \frac{x_0}{L} \mathrm{e}^{-j\,k_z z} \sum_q \mathrm{e}^{-2j\pi\,z\,q/L} \\ & \left\{ \sum_n \mathrm{e}^{-j\,n\varphi} P_v(\rho,\rho_2; k_z - q\frac{2\pi}{L}, n) \tilde{u}(k_z - q\frac{2\pi}{L}, n) \right\} \end{aligned} \tag{7.30}$$

If we compare this expression with (4.77), we recognize the quantity within braces above as the spatial harmonics representation of a Bloch wave. We can immediately apply the results of the discussion made in Section 4.5. Assuming $\varepsilon_{r1} < 9$:

1. when
$$L < \frac{\lambda_0}{1+\sqrt{\varepsilon r1}}$$
no harmonic is in the visible range. The radiated field is expected to be low, since it is of the surface wave type, with an exponential field decay along ρ;

2. when
$$\frac{\lambda_0}{1+\sqrt{\varepsilon r1}} \leq L < \frac{2\lambda_0}{1+\sqrt{\varepsilon r1}}$$
the “-1” harmonic alone is in the visible range. We expect a larger radiated field with almost constant amplitude over the length of the array, apart from the exponential decay related to the imaginary part of k_z in (7.24); the decay along ρ is algebraic $(1/\sqrt{\rho})$;

3. when
$$L > \frac{2\lambda_0}{1+\sqrt{\varepsilon r1}}$$
More than one harmonic is in the visible range. The field decay is again $1/\sqrt{\rho}$, so we expect a relatively strong radiation with high ripple due to the interference of the radiating harmonics

Of course these remarks apply to all field components.

To see in practice the validity of the preceding considerations, let us consider a one kilometer long LCX with L-spaced identical slots. The inner and outer conductor radii are $\rho_1 = 10$ mm and $\rho_2 = 30$ mm, the slot width and angular length are $s = 3$ mm and $\alpha = 180°$, the dielectric permittivity is $\varepsilon_{r1} = 1.26$, the frequency is $f = 1$ GHz. Moreover, we assume that the value of k_z in (7.24) is $k_z = k_0\sqrt{\varepsilon_{r1}} - 0.0001j$. The radiated field, computed by direct summation of the contributions of the various slots, having the excitation coefficients x_q of (7.24), is explored moving the observation point on a line parallel to the cable, at a distance $\rho = 3$ m, in front of the semicircular slots.
First we assume that the spacing between the slots is $L = 7.5$ cm, *i.e.* less than $\lambda_0/(1+\sqrt{\varepsilon_{r1}}) = 14.7$ cm, so that no space harmonic is radiating. Figure 7.19 shows a plot of the ratio between

the amplitude of the Poynting vector of the radiated field and the incident power in the cable (normalized to the cable cross section). Radiation is very weak as expected, apart from the array ends. Obviously, this end point contribution could not be described by the model (7.30), because, for the application of Poisson formula, the array was assumed of infinite extent. This behavior, however, is typical of all surface wave antennas [30], pag. 302. Figure 7.20 shows that the Poynting vector is parallel to the cable axis. In conclusion, the field is practically confined in the neighborhood of the cable and the radiated power flows parallel to the cable, coherently with the existence of a surface wave.

Next we assume that the slot spacing is $L = 20$ cm, *i.e.* such that the LCX is in the "Mono-Radiation Condition" (see Figures 7.21 and 7.22). In this case there is a very strong radiation phenomenon, with a low ripple level, along the length of the slotted cable where the field decays linearly, in dB scale, due to the imaginary part of k_z. Along the unslotted region, instead, the field has an extremely fast decay.

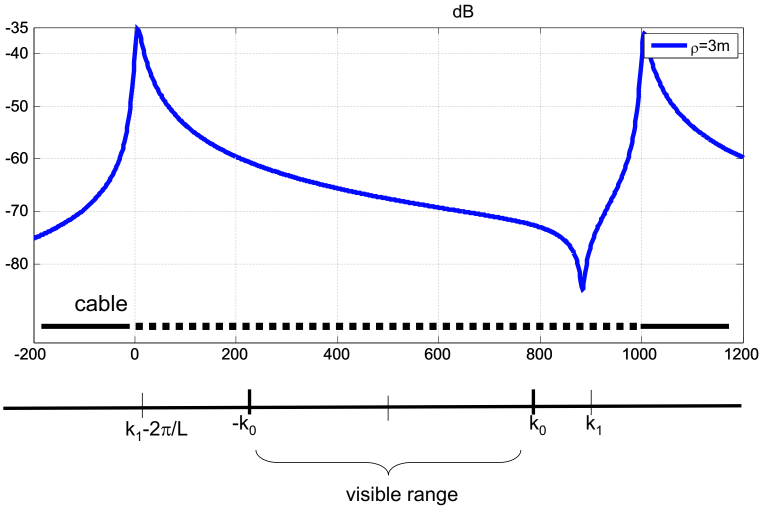

Figure 7.19: Normalized Poynting vector amplitude (in dB) in the "Surface Wave" operation

Moreover, the Poynting vector forms an angle of $116°$ with the cable axis that is in perfect agreement with the analytical formula deduced at the end of Section 4.5.

Finally, we assume that the slot spacing is increased up to $L = 37$ cm, so as to be in the "Multi Radiation operation". The radiated field is as strong as before, as shown in Figure 7.23, but with a high level ripple due to the interference between the two radiating harmonics. From the preceding results it is clear that the "Mono-Radiation operation" represents the best choice from

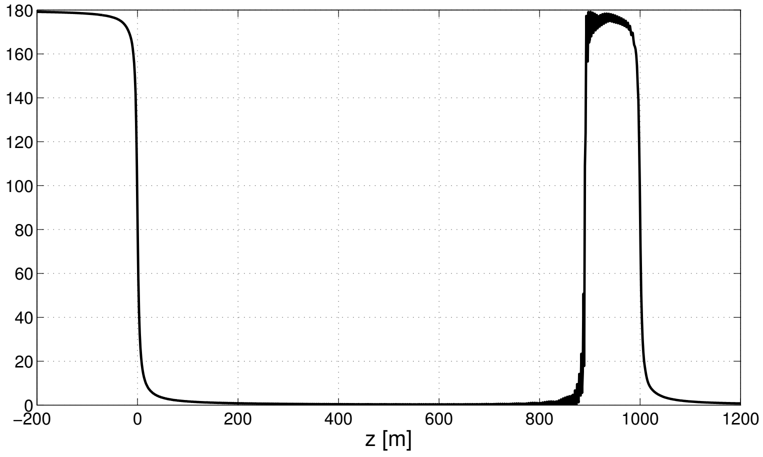

Figure 7.20: Poynting vector direction in the “Surface Wave” operation. The angle is measured with respect to the z axis.

the application point of view because the region around the cable is illuminated with a practically uniform, relatively strong field. The problem in this structure is the efficiency: the slots are all equal and are designed so that their radiated power is very small. In this way, the last slots radiate a power with almost the same level as the first, but globally, the total radiated power is a small fraction of the available one. In Chapter 8 where the design problems will be addressed, a high efficiency solution will be proposed.

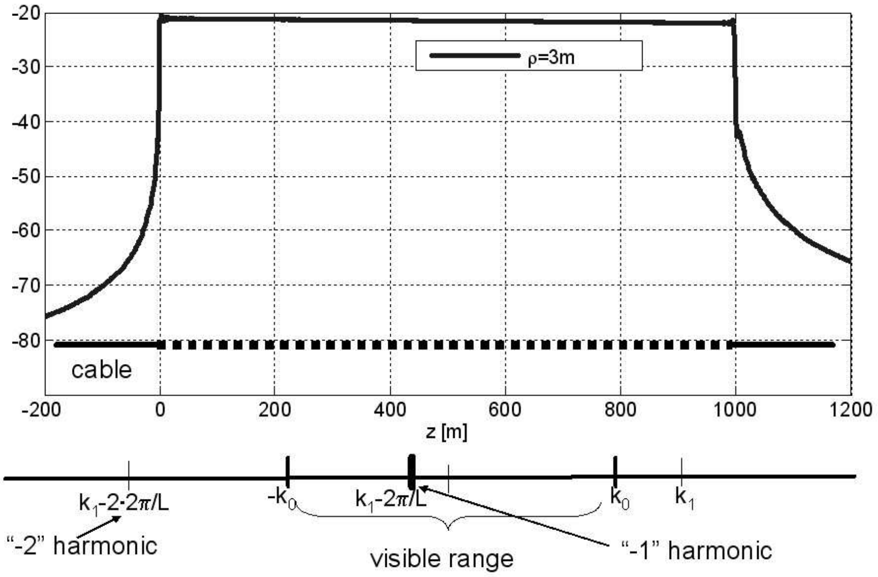

Figure 7.21: Normalized Poynting vector amplitude (in dB) in the "Mono Radiation" operation

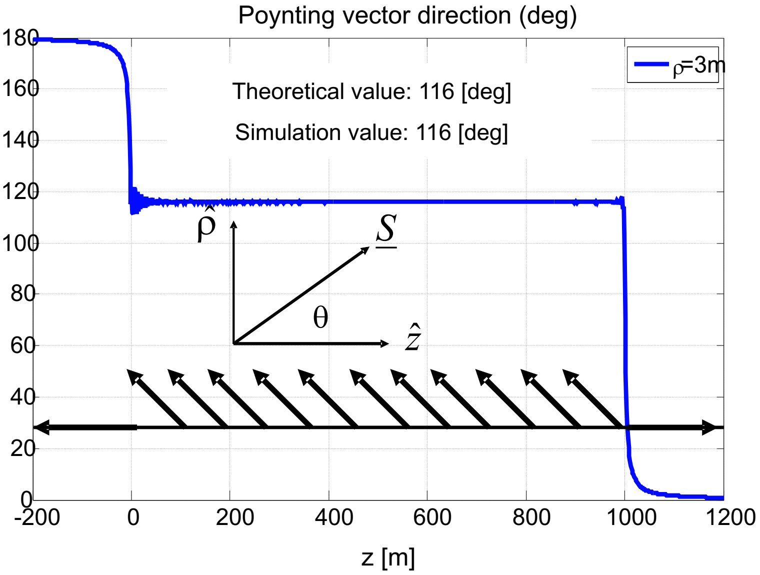

Figure 7.22: Poynting vector direction in the "Mono Radiation" operation.

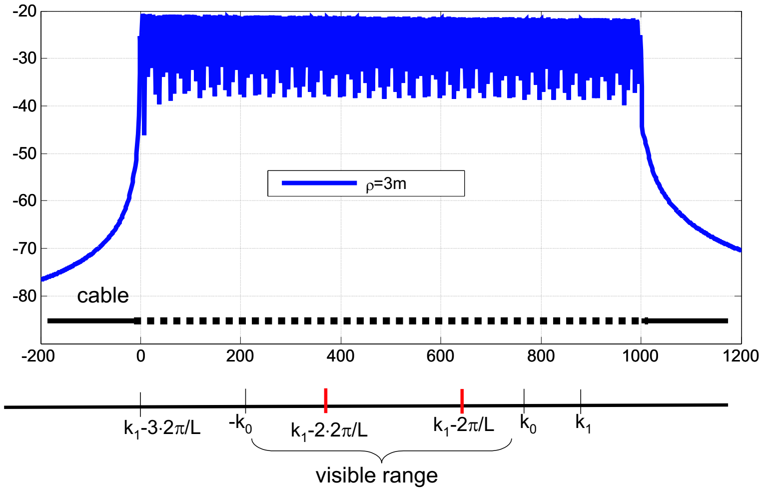

Figure 7.23: Normalized Poynting vector amplitude (in dB) in the “Bi-Radiation” condition

Chapter 8

Design of Slotted Coaxial Cables

8.1 Introduction

In the preceding chapters, the analysis of LCX has been thoroughly discussed, in the present chapter we will develop some design guidelines.

In Chapter 6 it has been shown that the properties of LCX can be described quite accurately by the simple model of an array of slots where the excitation coefficients follow an exponential law, see (6.5). It is necessary, at this point, to clarify the relationship between the decay constant along the cable and the slot characteristics.

The preceding numerical and theoretical analysis has shown that the "Mono-Radiation condition" represents the best choice in order to control the radiation properties of a LCX, since it allows the generation of a quite uniform pattern, free from ripple. However, it has also been shown that, if the slots are identical, the radiated field, measured on a line at fixed distance from the cable, decreases exponentially as a function of z, with the same decay law as the slot excitation coefficients. Two design options are open at this point.

The first one is based on the use of slots that radiate a very small fraction of the incident power. In this way the radiated power level is almost constant over the cable length, but the antenna efficiency is very low and most of the power is dissipated in the matched load at the end of the cable.

Alternatively, more efficient slots are used, so that almost all the power incident on the array is radiated. In this case the radiated power level is strongly non uniform and the contribution of the

last slots is almost negligible.
Clearly, both options are unsatisfactory. In the present chapter, we will derive a suitable design procedure in order to overcome the outlined problems. This goal is reached by an extensive use of the tools developed in the preceding sections.

8.2 Determination of the decay constant

In Section 6.3 it was shown that a simple LCX model is that of an array of slots with complex amplitude coefficients x_q:

$$x_q = x_0 \, \mathrm{e}^{-j\,(k_{Re} - jk_{Im})q\,L} \tag{8.1}$$

The real parameter k_{Re} is essentially the propagation constant of the mostly excited progressive Bloch wave and then it is close to the TEM value $k_0\sqrt{\varepsilon_{r1}}$. The imaginary parameter $-jk_{Im}$ depends on the slot characteristics and describes the effect of the power leakage.
For the design of LCX, it would be useful to know the relationship between the decay constant k_{Im} and the geometrical and electrical parameters of the cable. The relationship

$$k_{Im} = k_{Im}\left(\frac{L}{L_{min}}, \frac{\rho_2\alpha}{\overline{\lambda}}\right)$$

has been obtained numerically by best fitting on the data generated in a simulation exercise and is displayed in the contour plots of Figures 8.1, 8.2 and 8.3, which refer to cables with different numbers of slots. These data assume that the first higher order cable mode (TM$_{10}$) is well below cut-off. The horizontal axis shows the values of the slot spacing L/L_{min}, normalized to the minimum spacing that allows mono radiation operation

$$L_{min} = \frac{\lambda_0}{1+\sqrt{\varepsilon_{r1}}}$$

The electrical slot length $b\alpha/\overline{\lambda}$ is shown on the vertical axis. These figures indicate that the value of k_{Im} is substantially independent of the number of apertures, at least if their number is sufficiently large. It turns out to be also practically independent of the slots width s provided it is much smaller than the wavelength.

The other parameter of interest for LCX is the array input reflection coefficient. This quantity has been determined for the same cases as before and the results are shown in the contour plots

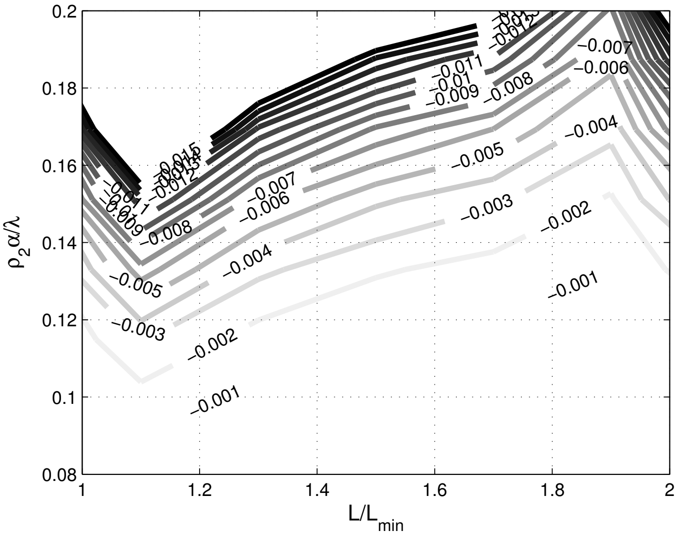

Figure 8.1: The decay constant k_{Im} for cables with 100 slots

of Figures 8.4, 8.5 and 8.6. Again, the figures show that the reflection coefficient is practically independent of the number of slots, provided $\rho_2\alpha/\overline{\lambda} < 0.2$.

Note that in the band of mono-radiation operation there is a region where the LCX presents a low reflection coefficient (< -30dB). Moreover, it is interesting to note that close to $L/L_{min} = 1$ and $L/L_{min} = 2$ the curves of both k_{Im} and S_{11} change abruptly. This fact is related to the first and second harmonics of the series (7.30) that are at the cut-off exactly in those points. In the literature on periodic structures, these are known as Wood's anomalies [35].

8.3 Design of uniformly radiating LCX

To identify a design strategy that can lead to LCX that radiate uniformly over their length the highest possible fraction of the incident power, it is useful to introduce a simplified model, based on the full wave results discussed in the preceding sections.
For this purpose, we neglect the TEM power reflected from the slots and recall from Section 6.2 the definition of slot radiation efficiency η_q^s, with $q = 1, \ldots, N_{slot}$ as the ratio between the power

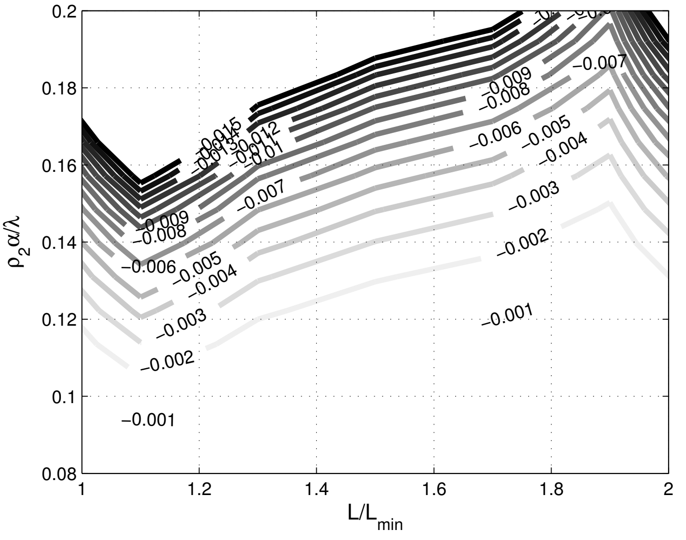

Figure 8.2: The decay constant k_{Im} for cables with 150 slots

P_q^{rad} radiated by the q-th slot and the power P_q^{inc} incident on it. For simplicity, we assume first that the cable is lossless.

The equations of the model, illustrated in Figure 8.7, are

$$\begin{aligned} P_q^{rad} &= \eta_q^s P_q^{inc} && (8.2)\\ P_q^T &= P_q^{inc}(1-\eta_q^s) && (8.3)\\ P_{(q+1)}^{inc} &= P_q^T && (8.4)\\ &\text{for } q = 1, \dots, N_{slot} \end{aligned}$$

Assuming that all the slot efficiencies are given, the total radiated power is

$$P^{rad} = \sum_{q=1}^{N_{slot}} P_q^{rad} = \sum_{q=1}^{N_{slot}} \eta_q^s P_q^{inc} \tag{8.5}$$

The incident power on the q-th slot, if the reflected power is neglected, is given by

$$P_q^{inc} = (1-\eta_{(q-1)}^s)P_{(q-1)}^{inc} = P_1^{inc}\prod_{r=1}^{q-1}(1-\eta_r^s) \tag{8.6}$$

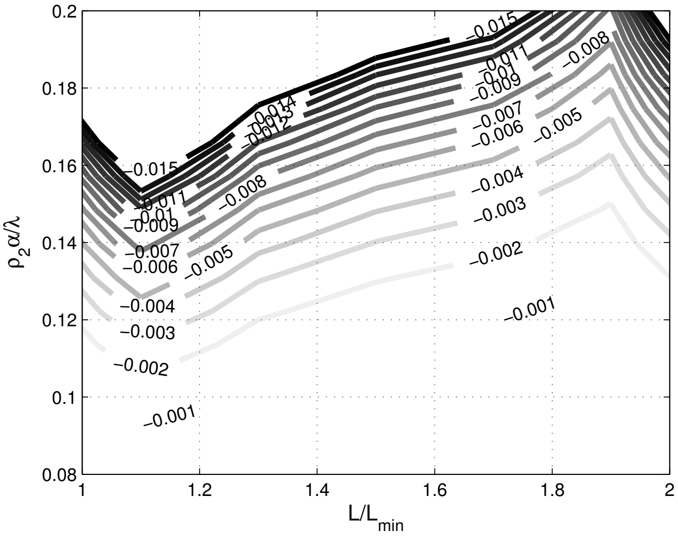

Figure 8.3: The decay constant k_{Im} for cables with 200 slots

where P_1^{inc} is the power incident on the array. Substituting

$$P^{rad} = P_1^{inc} \sum_{q=1}^{N_{slot}} \eta_q^s \prod_{r=1}^{q-1} (1 - \eta_r^s) \tag{8.7}$$

If all the slots are equal, *i.e.* $\eta_q^s = \eta^s$, for $q = 1, \ldots, N_{slot}$, the preceding formula can be evaluated in closed form:

$$\begin{aligned} P^{rad} &= P_1^{inc} \eta^s \sum_{q=1}^{N_{slot}} (1 - \eta^s)^{q-1} = P_1^{inc} \eta^s \frac{(1 - \eta^s)^{N_{slot}} - 1}{(1 - \eta^s) - 1} \\ &= P_1^{inc} \left(1 - (1 - \eta^s)^{N_{slot}}\right) \end{aligned} \tag{8.8}$$

and the power dissipated on the matched load, placed after the N_{slot}-th slot, is

$$P^{load} = P_1^{inc} (1 - \eta^s)^{N_{slot}} \tag{8.9}$$

We can define an array efficiency η^a as:

$$\eta^a = \frac{P^{rad}}{P_1^{inc}} \tag{8.10}$$

Hence, array efficiency and slot efficiency are related by

$$\eta^a \ = \ \left(1 - (1 - \eta^s)^{N_{slot}}\right) \tag{8.11}$$

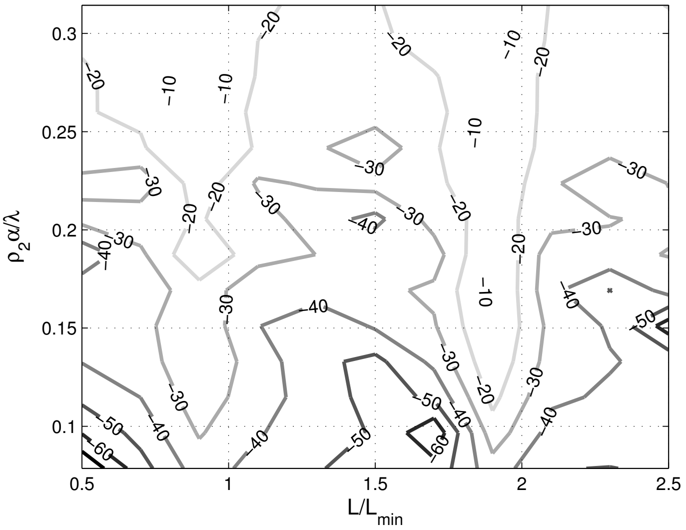

Figure 8.4: Array input reflection coefficient S_{11}dB for for cables with 100 slots

Moreover, the power radiated by the q-th slot is

$$P_q^{rad} = P_1^{inc}\eta^s(1-\eta^s)^{q-1} \qquad q = 1, 2, \ldots, N_{slot} \tag{8.12}$$

Hence, the array radiation is obviously non uniform and we can define a taper T:

$$T = \frac{P_1^{rad}}{P_{N_{slot}}^{rad}} = (1-\eta^s)^{(1-N_{slot})} \tag{8.13}$$

Both the total radiated power and the taper depend on the slot efficiency η^s, which can be eliminated between the two,

$$P^{rad} = P_1^{inc}\left[1 - \frac{(1-\eta^s)}{T}\right] \simeq P_1^{inc}\left(1 - \frac{1}{T}\right) \tag{8.14}$$

where we have taken into account the usual smallness of the slot efficiency η^s. This equation shows clearly that radiation uniformity and antenna efficiency are contrasting requirements.
A pictorial view of two opposite designs is shown in Figures 8.8 and 8.9, which refers to a cable with $N_{slot} = 1000$ slots. In the former case the slots are small and $\eta^s = 1/1000$ and the taper is 4.34dB but only 63% of the available power is radiated. In the latter $\eta^s = 4.64/1000$, which guarantees a high array efficiency (99%), but the taper increases to 20 dB.

If a high array efficiency is desired, together with a low taper, the slots must be different one from the other, with sizes increasing from the input toward the output in order to compensate for the

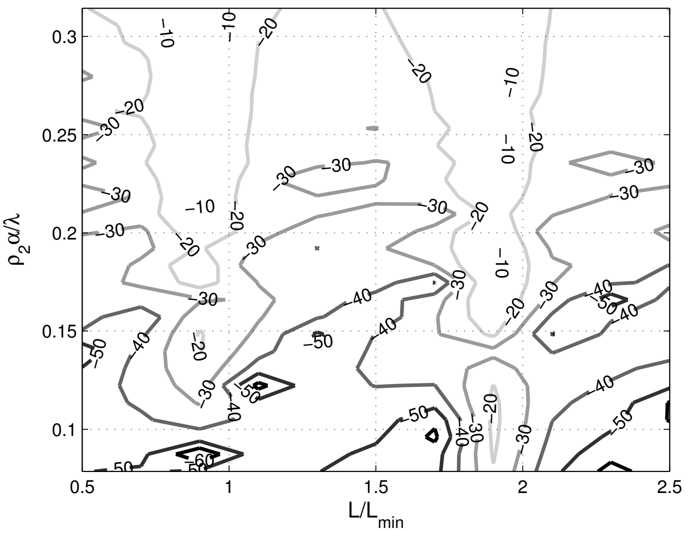

Figure 8.5: Array input reflection coefficient S_{11}dB for for cables with 150 slots

power already radiated by the preceding slots. This idea can be formalized as follows. Assume the goal of a certain array efficiency η^a, for generality not necessarily equal to one. The total radiated power is then $P^{rad} = P_1^{inc}\eta^a$ and if this is to be uniformly radiated, $P_q^{rad} = P^{rad}/N_{slot}$. The radiation efficiency of the q-th slot η_q^s is then given by

$$\eta_q^s = \frac{P_q^{rad}}{P_q^{inc}} = \frac{\frac{P^{rad}}{N_{slot}}}{P_1^{inc} - P^{rad}\frac{q-1}{N_{slot}}} = \frac{\eta^a}{N_{slot} - \eta^a(q-1)} \qquad q = 1, 2, \ldots, N_{slot} \tag{8.15}$$

The efficiency of the last slot (the largest one) is then

$$\eta_{N_{slot}}^s = \frac{\eta^a}{N_{slot}(1-\eta^a) + \eta^a} = \frac{1}{1 + N_{slot}\frac{1-\eta^a}{\eta^a}} = \frac{1}{1 + N_{slot}\frac{P^{load}}{P^{rad}}} \tag{8.16}$$

Clearly, $\eta_{N_{slot}}^s = 1$ if no power has to be dissipated in the matched load ($\eta^a = 1$). This requirement is impossible to satisfy, since it was shown in Section 6.2 that the maximum slot efficiency is about 0.5. For various reasons, there could be in general an upper bound η_{max}^s on the slot efficiencies. In this case, the preceding equation gives the minimum power on the load:

$$\frac{P_{min}^{load}}{P^{rad}} = \frac{1}{N_{slot}}\left(\frac{1}{\eta_{max}^s} - 1\right) \tag{8.17}$$

In (8.16) we used the fact that

$$\frac{P^{load}}{P^{rad}} = \frac{1-\eta^a}{\eta^a} \tag{8.18}$$

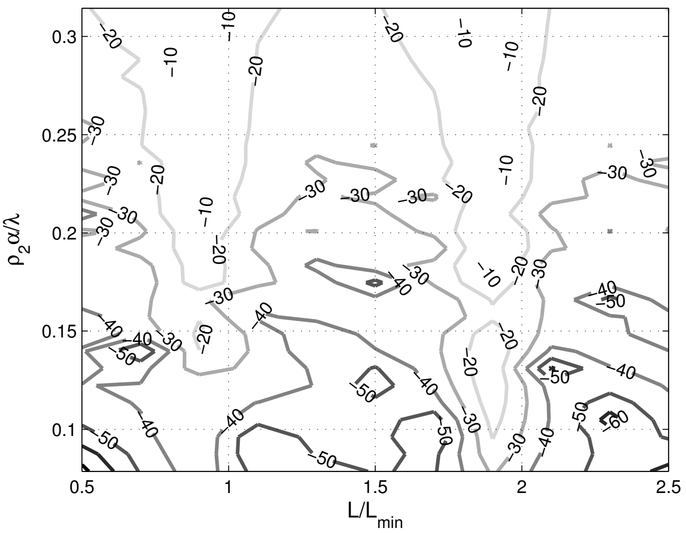

Figure 8.6: Array input reflection coefficient S_{11}dB for for cables with 200 slots

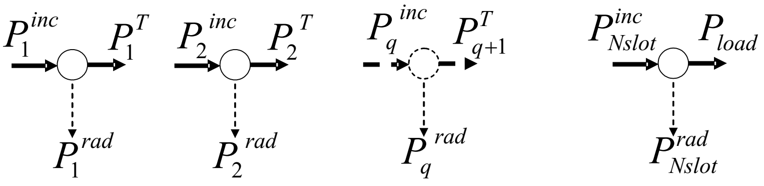

Figure 8.7: Simplified model of slotted coaxial cable

From the preceding two equations we get the maximum array efficiency η^a_{max} compatible with the bound on the slot efficiency:

$$\eta^a_{max} = \frac{1}{1 + \frac{P^{load}_{min}}{P^{rad}}} = \frac{1}{1 + \frac{1}{N_{slot}}\left(\frac{1}{\eta^s_{max}} - 1\right)} \tag{8.19}$$

The various slot efficiencies are then obtained by (8.15).

In practice the ohmic losses in a long cable cannot be neglected. We want now to see what changes in the above discussion arise because of this. Assume first that all the slot efficiencies are given.

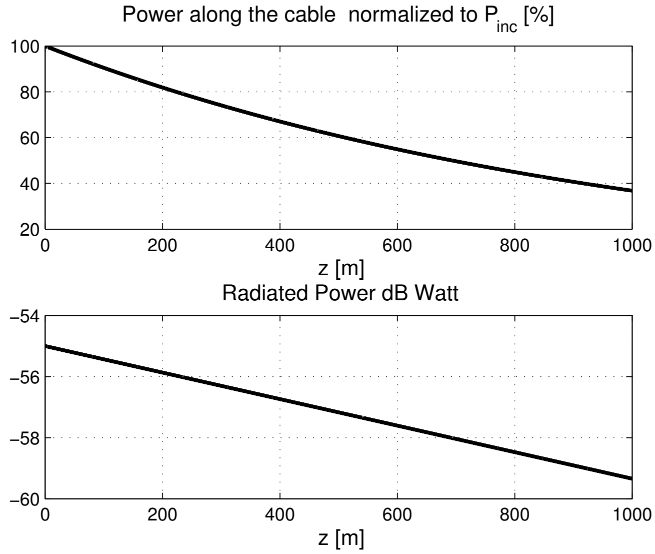

Figure 8.8: Case 1: LCX with 1000 small slots: slot efficiency $\eta^s = 1.0 \cdot 10^{-3}$, array efficiency $\eta^a = 0.63$, taper $T = 4.34$dB

The equations of the model (8.5) become:

$$\begin{aligned} P_q^{rad} &= \eta_q^s P_q^{inc} && (8.20)\\ P_q^T &= P_q^{inc}(1-\eta_q^s) && (8.21)\\ P_{(q+1)}^{inc} &= P_q^T \exp(-2\alpha L) = P_q^T E && (8.22)\\ & \text{for } q = 1, \dots, N_{slot} \end{aligned}$$

where all ohmic losses are accounted for by the exponential (denoted by E, for brevity) through an equivalent attenuation constant. This expression is justified by the smallness of the regressive wave, discussed in Section 6.4.

Combining (8.5) with (8.23) we obtain the total power radiated by the array:

$$P^{rad} = P_1^{inc} \sum_{q=1}^{N_{slot}} \eta_q^s E^{q-1} \prod_{r=1}^{q-1} (1-\eta_r^s) \tag{8.23}$$

The power dissipated in the matched load is

$$P^{load} = P_{N_{slot}}^{inc}(1-\eta_{N_{slot}}^s) = P_1^{inc} E^{N_{slot}-1} \prod_{r=1}^{N_{slot}-1} (1-\eta_r^s) \tag{8.24}$$

If all the slots are equal, i.e. $\eta_q^s = \eta^s$, for $q = 1, \dots, N_{slot}$, (8.23) can be computed in closed

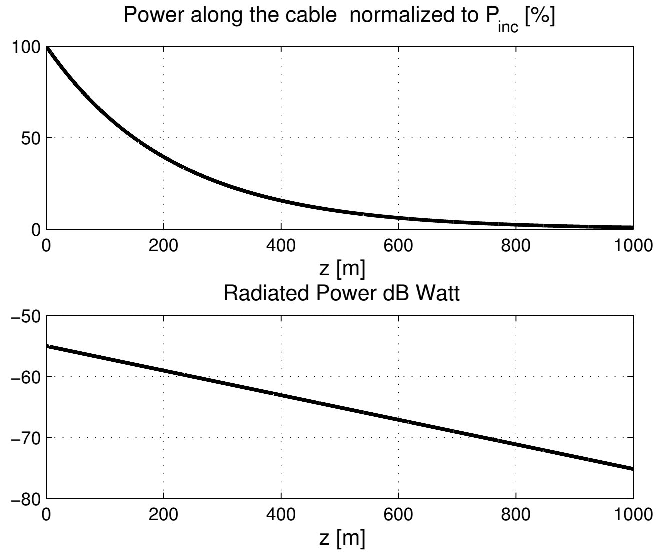

Figure 8.9: Case 2: LCX with 1000 large slots: slot efficiency $\eta^s = 4.64 \cdot 10^{-3}$, array efficiency $\eta^a = 0.99$, taper $T = 20$dB

form:

$$P^{rad} = P_1^{inc} \left[1 - (1-\eta^s)^{N_{slot}} E^{N_{slot}}\right] \frac{1}{E + \frac{1-E}{\eta^s}} \tag{8.25}$$

while the power radiated from the q-th slot is:

$$P_q^{rad} = P_1^{inc} \eta^s E^{q-1} (1-\eta^s)^{q-1} \qquad q = 1\,, 2, \ldots, N_{slot} \tag{8.26}$$

As in the lossless case, the array radiation is obviously non uniform and the taper T is given by:

$$T = \frac{P_1^{rad}}{P_{N_{slot}}^{rad}} = \frac{(1-\eta^s)^{(1-N_{slot})}}{E^{N_{slot}-1}} \tag{8.27}$$

The total radiated power is related to the taper T by an equation more complicated than (8.14):

$$P^{rad} = P_1^{inc} \left[1 - \frac{E(1-\eta^s)}{T}\right] \frac{1}{E + (1-E)/\eta^s} \tag{8.28}$$

However, since in general $1 - E \simeq 2\alpha L \ll \eta^s$, it is still true that

$$\eta^a \simeq \left(1 - \frac{1}{T}\right) \tag{8.29}$$

Let us now turn to the design problem, where again the goal is that of obtaining a uniform radiation from each slot of the array, *i.e.* $P_q^{rad} = P^{rad}/N_{slot}$ for $q = 1, ..., N_{slot}$ where P^{rad} is the total radiated power.

Let η^a the desired array efficiency; in this case its maximum value is strictly less than 1, because of the power dissipation. The total radiated power is then $P^{rad} = P_1^{inc}\eta^a$ and that radiated by each slot $P_q^{rad} = P^{rad}/N_{slot}$. The radiation efficiency of the q-th slot η_q^s is as usual defined by

$$\eta^s = \frac{P_q^{rad}}{P_q^{inc}}$$

To use this equation, we need the incident power on the q-th slot. This is given recursively by

$$P_q^{inc} = (P_{q-1}^{inc} - P_q^{rad})E \qquad \text{for } q = 2, \ldots, N_{slot}$$

from which

$$P_q^{inc} = P_1^{inc}E^{q-1} - P^{rad}E\frac{E^{q-1}-1}{E-1} \tag{8.30}$$

Hence the efficiencies of the various slots turn out to be given by

$$\eta_q^s = \frac{P^{rad}/N_{slot}}{P_1^{inc}E^{q-1} - \frac{P^{rad}}{N_{slot}}\frac{E^{q-1}-1}{E-1}E} \tag{8.31}$$

Let us compute the power dissipated in the matched load, after the last slot:

$$P^{load} = P_{N_{slot}}^{inc} - P_{N_{slot}}^{rad} \tag{8.32}$$

Using (8.30),

$$\frac{P^{load}}{P_1^{inc}} = E^{N_{slot}-1} - \frac{\eta^a}{N_{slot}}\frac{E^{N_{slot}}-1}{E-1} \tag{8.33}$$

If we enforce $P^{load} = 0$, we find the maximum array efficiency η^{opt}, compatible with the given cable loss:

$$\eta^{opt} = N_{slot}\frac{E^{N_{slot}-1}(E-1)}{E^{N_{slot}}-1} \tag{8.34}$$

Owing to the generally very small loss, this expression can be simplified:

$$\eta^{opt} \simeq 1 - \frac{N_{slot}-1}{2}(1-E) + \frac{(N_{slot}-1)(N_{slot}-5)}{12}(1-E)^2 \tag{8.35}$$

In general, the efficiency of the last slot is, from (8.31):

$$\eta_{N_{slot}}^s = \frac{\eta^a}{N_{slot}E^{N_{slot}-1} - \eta^a E\frac{E^{N_{slot}-1}-1}{E-1}} \tag{8.36}$$

If we set $\eta^a = \eta^{opt}$, trying to exploit to the maximum degree the available power, we obtain obviously the impossible result $\eta^s_{N_{slot}} = 1$.

In practice the slot efficiency is bounded by η^s_{max} and the last equation yields the corresponding maximum array efficiency

$$\eta^a_{max} = \frac{N_{slot}\,\eta^s_{max}\,E^{N_{slot}-1}}{1 + E\,\eta^s_{max}\,\frac{E^{N_{slot}-1}-1}{E-1}} \tag{8.37}$$

With this value of array efficiency, recalling (8.33), we can compute the power dissipated in this case in the matched load:

$$\frac{P^{load}}{P^{inc}_1} = \frac{E^{N_{slot}}(1-\eta^s_{max})}{1 + E\,\eta^s_{max}\,\frac{E^{N_{slot}-1}}{E-1}} \tag{8.38}$$

The power dissipated in the cable, because of ohmic losses, is obtained by difference:

$$\begin{aligned}\frac{P^{diss}}{P^{inc}_1} &= 1 - \frac{P^{rad}}{P^{inc}_1} - \frac{P^{load}}{P^{inc}_1} = && (8.39)\\ &= 1 - E^{N_{slot}-1} - \eta^a\left[1 - \frac{1}{N_{slot}}\frac{E^{N_{slot}}-1}{E-1}\right] && (8.40)\end{aligned}$$

where (8.33) has been used. An approximate expression of this equation is clearer:

$$\frac{P^{diss}}{P^{inc}_1} \simeq 1 - E^{N_{slot}-1} - \eta^a\frac{N_{slot}-1}{2}(1-E) \tag{8.41}$$

This equation shows clearly that the dissipated power in the cable decreases monotonically when the array efficiency is increased. The power dissipated in the matched load has the same behavior. In conclusion, the design starts from the value of the maximum slot efficiency η^s_{max} that we decide to use. With this value we compute the array efficiency η^a with (8.37) and finally the various slot efficiencies by the following equation, derived from (8.31):

$$\eta^s_q = \frac{\eta^a}{N_{slot}E^{q-1} - \eta^a_{max}E\frac{E^{q-1}-1}{E-1}} \tag{8.42}$$

In this way the slot efficiencies increase progressively from the first, $\eta^s_1 = \eta^a/N_{slot}$, to the last one $\eta^s_{N_{slot}} = \eta^s_{max}$ in order to compensate for both the radiated and the dissipated power.

To complete the design, the slot size should be determined. The function

$$\eta^s_q = f\left(\frac{\rho_2\,\alpha}{\lambda}\right) \tag{8.43}$$

was derived numerically in section 6.2 in the case of an isolated slot. For this application, to take approximately the multiple interactions into account, we have characterized the slot in its operating environment, *i.e.* in a periodic array, in order to determine the relation

$$\eta_q^s = f\left(\frac{b\rho_2\,\alpha}{\bar{\lambda}}, \frac{L}{L_{min}}\right) \tag{8.44}$$

In particular, a 100 slot LCX has been simulated and the function f has then been computed by averaging the properties of the central 20 slots. Due to the fact that the slots radiate a small amount of power, it is not surprising that the result is not too different from that of Figure 6.9.

In conclusion, the design is carried out in two steps. First, the slot spacing L is selected, so that the array is in the mono-radiation condition and the S_{11} value is sufficiently low. Then the maximum slot efficiency η_{max}^s is selected and the various radiation efficiencies η_q^s are computed according to (8.42). The slot sizes are finally obtained by numerical inversion of the function f. Note that the simple model, used in this section, is progressively less valid as the η_q^s value increases, since the slot reflection coefficient can no longer be neglected, as Figure 6.10 shows. This consideration is to be taken into account in the selection of the maximum slot efficiency η_{max}^s.

As an example, let us consider the design of a LCX with a length of 100 meters, which should produce a uniform field in the frequency range which corresponds to the first GSM band (*i.e.* 890 MHz-960 MHz). The cable characteristics are: inner and outer conductor radii $\rho_1 = 12$ mm, $\rho_2 = 30$ mm, dielectric permittivity $\varepsilon_{r1} = 1.26$, equivalent loss tangent $\tan\delta = 10^{-4}$, slot width and spacing $s = 3$ mm and $L = 20$ cm. The maximum slot radiation efficiency has been fixed at $\eta_{max}^s = 0.45$.

The slot size distribution is shown in Figure 8.10. The array of 500 slots has been simulated by the HFIE technique: the reflection and transmission coefficients in the band and the radiated field as a function of z at $\rho = 3$ m for the lower, higher and center frequency are shown in Figures 8.11 and 8.12. It can be noted that the usual decay of the radiated power has been even overbalanced, so that radiation is stronger at the array end than at the input. The reason is that the simple model used in this section is no longer applicable near the array end, where slots are too large. The dissipated is about 13% of the input incident power, while the TEM power at the end of the array is less than 4%.

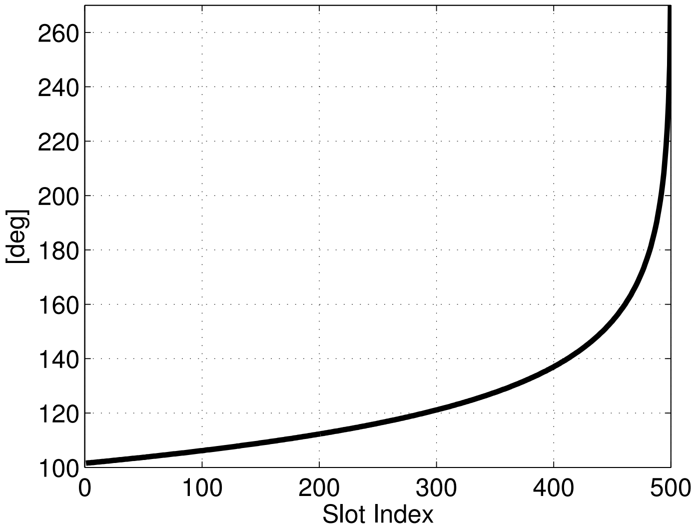

Figure 8.10: Angular slot size distribution. The radiation slot efficiencies range from 0.0018 to 0.45

It is evident that, from a manufacturing point of view, a cable with continuously varying slot size may be very expensive. A possible solution is to use a staircase approximation of the angular slot size distribution, as shown in Figure 8.13 where groups of 50 identical slots have been used. The electromagnetic response, in terms of reflection and transmission coefficients and the radiated field, of this last structure is shown in Figures 8.14 and 8.15, the power loss is still about 13% of the input incident power while the TEM power at the end of the array is now about 18% in the frequency band. The main effect of this kind approximation is represented by an increase of the power dissipated in the matched load at the end of the array. Moreover, the radiation pattern shows peaks near the array end that were not present in Figure 8.12. These peaks appear at the junctions between different cable sections. It has to be remarked that in both cases, however, not all the power is radiated by the array. This fact is due also to the higher order effects that could not be taken into account in the simplified model. In general, if necessary, an optimization procedure could be adopted on the final structure in order to minimize the power dissipated in the matched load at the end of the cable.

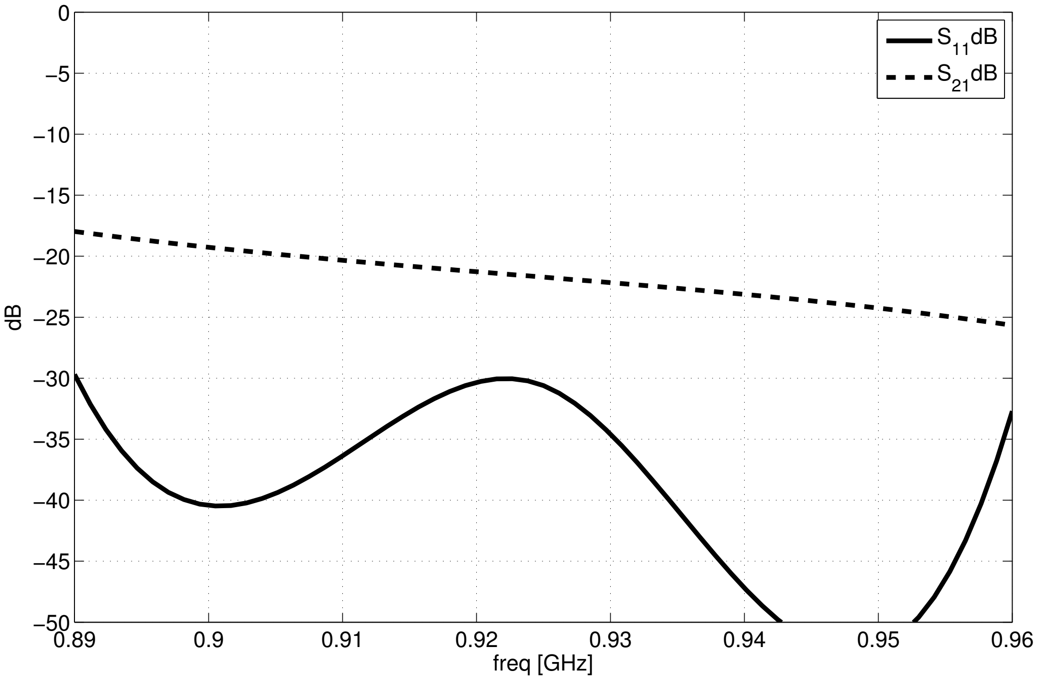

Figure 8.11: Array reflection and transmission coefficients (dB)

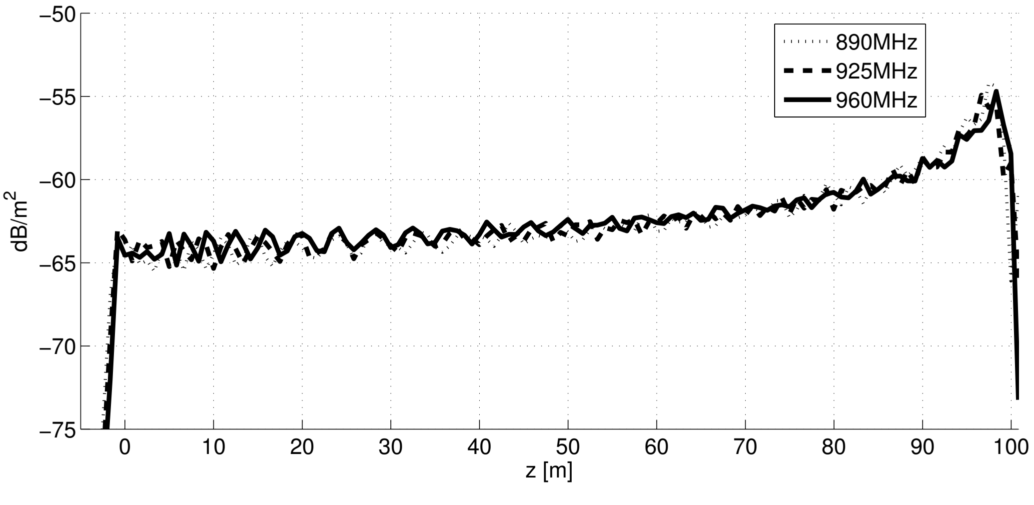

Figure 8.12: Poynting vector amplitude at $\rho = 3m$ in dBW/m^2 for f=890, 925 and 960 MHz. The direction is $\theta = 120^\circ$

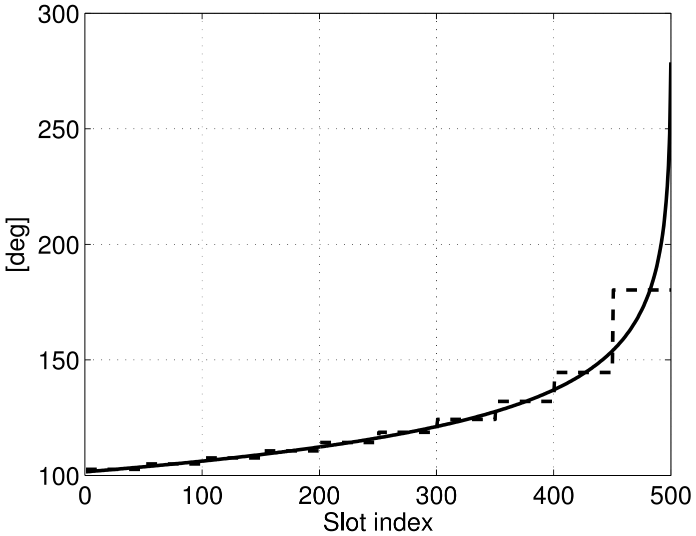

Figure 8.13: Angular slot size distributions, continuous curve and its staircase approximation

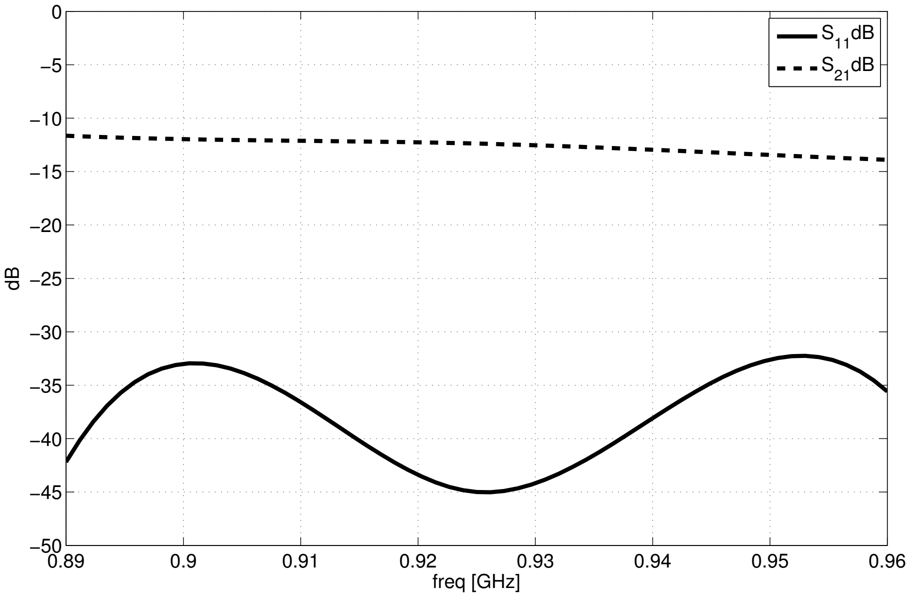

Figure 8.14: Reflection and Transmission coefficients (in dB) of the array where the slot dimensions are constant in sub-groups of 50 elements

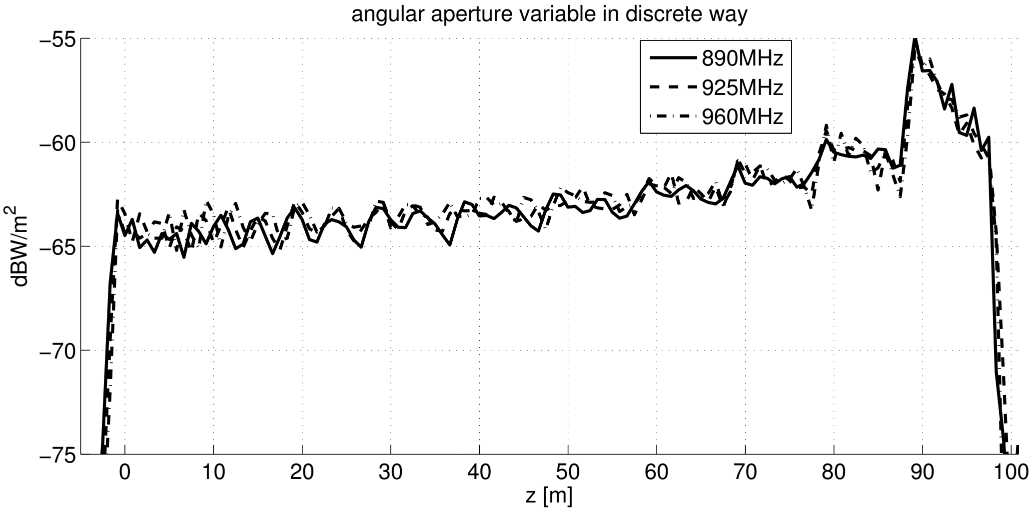

Figure 8.15: Poynting vector amplitude at $\rho = 3$ m in dBW/m^2 for f=890, 925 and 960 MHz of the array where the slot dimensions are constant in sub-groups of 50 elements

Chapter 9

Ring Cavity Filters

9.1 Introduction

Stop band filters are commonly used in antenna systems to isolate receivers from the signals produced by transmitters, internal or external to the system, operating in adjacent frequency bands. Generally, in high power or low noise applications, such filters are built by means of rectangular waveguides, loaded by stubs or resonant irises [36]. These structures are very effective both from the electrical and the manufacturing point of view, but do not allow double polarization operation. If this is required, square or circular waveguides can be used instead of rectangular ones.

A circular waveguide configuration, which may be preferable for reasons of connection compatibility with a round horn antenna, may be realized with radial stubs. Figure 9.1 shows the longitudinal section of a cylindrical waveguide with a single radial stub. The typical frequency response of a stub loaded guide, shown in Figure 9.2, is characterized by the presence of a couple of zeros, one in S_{11}, the other in S_{21}. This behavior is not difficult to explain. The fundamental mode equivalent circuit of the stub, seen as a double step discontinuity, is depicted in Figure 9.3, where $\underline{\underline{S}}_A$ and $\underline{\underline{S}}_B$ are the scattering matrices of the two steps. This is also the equivalent circuit of a Fabry-Perot interferometer and it is well known that its reflection coefficient is zero whenever the Round-Trip-Phase-Shift (RTPS) is an integer multiple of 2π:

$$RTPS = \angle S_{11}^{A} + \angle S_{11}^{B} - 2\,k_z\,s = 2\pi n$$

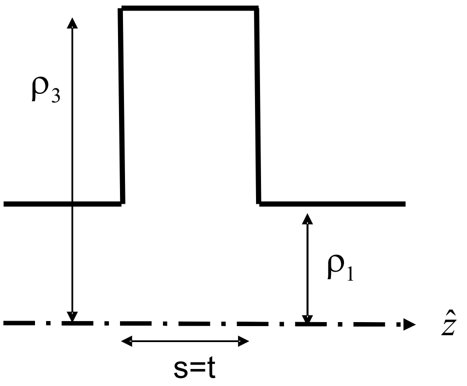

Figure 9.1: Standard stub in circular waveguide

with k_z denoting the TE_{11} propagation constant.

On the other hand, from a transverse point of view, the stub is seen as a shorted line, which transforms a short into a virtual open circuit when its length is about $\lambda/4$, owing to the not complete equivalence between radial and uniform waveguides. The open circuit blocks the TE_{11} longitudinal currents, giving rise to the transmission zero.

The same effect can be obtained if the stub height is increased by multiples of $\lambda/2$, with a consequent narrowing of the transmission stop-band, sometimes a desirable effect. However, in this case, the transverse size of the device can become excessive and a possible solution to reduce it, is shown in Figure 9.4). It has been proved numerically that in this way the transverse size of the device can be reduced by 30%.

A drawback of both the standard stub and of the "mushroom" stub is that it is not possible to control independently the position of the two zeros. This flexibility requires a further degree of freedom, which can be offered by the asymmetric structure of Figure 9.5. By changing the offset L between the cap and the stem of the "mushroom", the desired result is obtained.

In the next section we compute the Generalized scattering matrix of this asymmetric cavity.

9.2 Analysis of the asymmetric ring cavity

In this section, the integral equation technique, discussed in Chapter 3, will be applied to construct a S-matrix model of the asymmetric mushroom stub of Figure 9.5. The cap (region "3") is coupled to the circular waveguide (region "1") by means of a radial waveguide (stem, region "2"), whose width is s. The radii of the circular waveguide and of the cylindrical cavity are de-

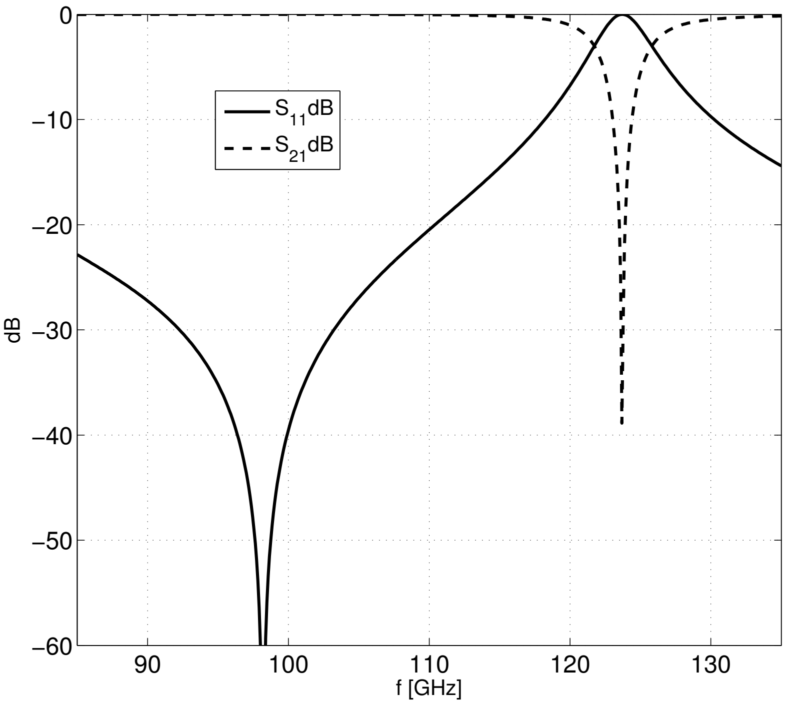

Figure 9.2: Frequency response of a stub loaded waveguide

noted by ρ_1, ρ_2 and ρ_3, respectively. Let t be the length of the cavity and L the offset between the symmetry planes of the cap and of the stem. The incident magnetic field is $\underline{H}_1^{inc}$, propagating in the main waveguide. This scattering problem is solved by the domain decomposition method in way similar to that used in the analysis of leaky coaxial cables. Here we will employ the superscripts "1", "2" and "3" to refer to the three different regions.

Applying the Equivalence Theorem, the two apertures are closed by perfect electric conductors and two couples of current distributions $(\pm\underline{\mathbb{J}}_{m,\rho_1})$ and $(\pm\underline{\mathbb{J}}_{m,\rho_2})$, are placed in $\rho = \rho_1^{\pm}$ and $\rho = \rho_2^{\pm}$, as shown in Figure 9.6. If we denote by $\underline{E}_{\rho_1}$ and $\underline{E}_{\rho_2}$ the electric fields in the apertures in $\rho = \rho_1$ and $\rho = \rho_2$, they are given by:

$$\begin{aligned} \underline{\mathbb{J}}_{m,\rho_1}(\rho,\varphi,z) &= \left(\underline{E}_{\rho_1}(\rho,\varphi,z) \times (-\hat{\rho})\right) \frac{\delta(\rho-\rho_1)}{\rho} && (9.1) \\ \underline{\mathbb{J}}_{m,\rho_2}(\rho,\varphi,z) &= \left(\underline{E}_{\rho_2}(\rho,\varphi,z) \times (-\hat{\rho})\right) \frac{\delta(\rho-\rho_2)}{\rho} && (9.2) \end{aligned}$$

By enforcing the tangential magnetic field continuity in the slots, we obtain the HFIE of the

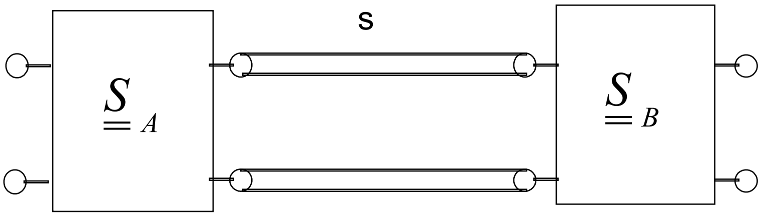

Figure 9.3: Fundamental mode equivalent circuit of the stub

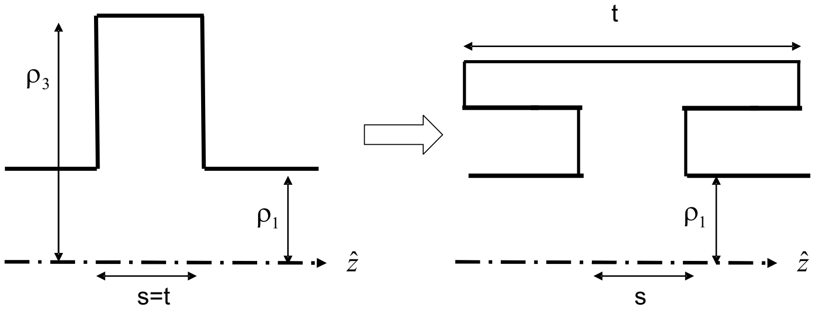

Figure 9.4: From a standard stub to a symmetrical “mushroom” stub

problem, in the form of a system of coupled integral equations:

$$\left\{\begin{array}{l} \underline{H}_1^{inc}(\rho_1,\varphi,z)+\underline{H}_1^{scat}\{\underline{\mathbb{J}}_{m,\rho_1}\}(\rho_1,\varphi,z)=\underline{H}_2^{scat}\{-\underline{\mathbb{J}}_{m,\rho_1},\underline{\mathbb{J}}_{m,\rho_2}\}(a,\varphi,z) \\ \\ \text{for } \rho=\rho_1,\ \varphi\in[0,2\pi] \text{ and } z\in[-s/2,s/2] \end{array}\right. \tag{9.3}$$

$$\left\{\begin{array}{l} \underline{H}_2^{scat}\{-\underline{\mathbb{J}}_{m,\rho_1},\underline{\mathbb{J}}_{m,\rho_1}\}(\rho_2,\varphi,z)=\underline{H}_3^{scat}\{-\underline{\mathbb{J}}_{m,\rho_2}\}(\rho_2,\varphi,z) \\ \\ \text{for } \rho=\rho_2,\ \varphi\in[0,2\pi] \text{ and } z\in[-s/2,s/2] \end{array}\right. \tag{9.4}$$

To make (9.3) and (9.4) explicit, we need to determine the relations between the magnetic current distributions and the scattered fields. The radial transmission line theory can be very helpful for this purpose. By adopting this radial point of view, the structure can be viewed as a thick iris, which couples two radial guides, one of which starts at $\rho = 0$ (the main waveguide) and the other (the cavity) is shorted. In practice, we have two step discontinuities between three different radial waveguides. The radial guides differ in their size: one has infinite cross section (1) the other two are finite. The equivalent radial circuit is shown in Figure 9.7. Here $\mathring{\underline{v}}_{1\,\rho_1}(\chi,n)$, $\mathring{\underline{v}}_{2\,\rho_1}(m,n)$, $\mathring{\underline{v}}_{2\,\rho_2}(m,n)$ and $\mathring{\underline{v}}_{3\,\rho_2}(m,n)$ are the voltage generators representing the magnetic currents. The

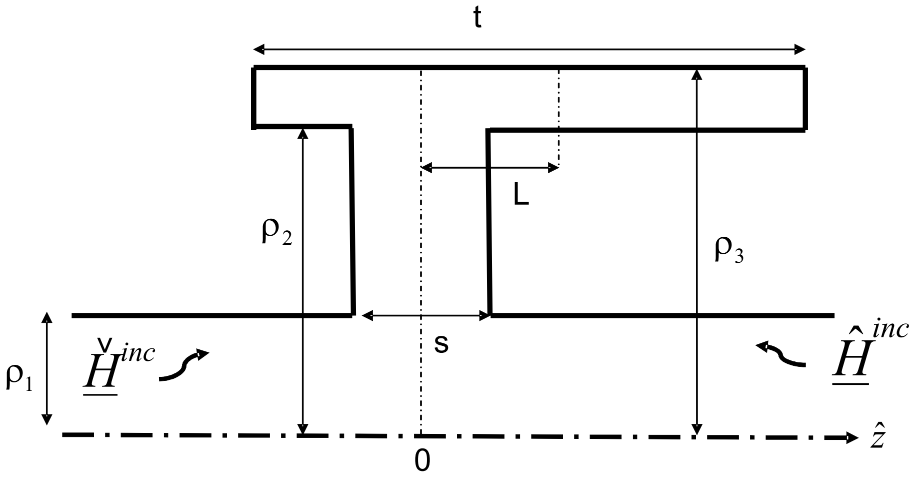

Figure 9.5: Longitudinal section of the circular waveguide loaded by an asymmetrical "mushroom" stub

first argument refers the longitudinal direction and is continuous for the guide "1" but discrete for the guides "2" and "3"; the second refers to the $\hat{\varphi}$ direction and is the same that characterizes the incident field, since the aperture is complete. The matrix $\underline{\underline{Y}}_1$ is the input admittance at $\rho = \rho_1$ (for the regular wave) of a line starting at $\rho = 0$, $\underline{\underline{Y}}_3$ is the input admittance of the shorted radial line representing the cylindrical cavity. $\underline{\underline{Y}}_{cc}$ is the short circuit admittance matrix of the line between $\rho = a$ and $\rho = \rho_2$, representing the thick iris. Its elements are 2×2 matrices in the usual u, v basis. The current generator $\overset{\circ inc}{\underline{I}}$ is the Fourier transform of the incident magnetic field in $\rho = \rho_1^-$. Finally the vector currents represent the scattered magnetic field in the radial domain. By inspection of the circuit we deduce :

$$\begin{aligned}
\underline{I}_{1\,\rho_1} &= \overset{\circ inc}{\underline{I}}_1 - \underline{\underline{Y}}_1 \cdot \underline{\mathring{v}}_{1\,\rho_1} && (9.5)\\
\underline{I}_{2\,\rho_1} &= \underline{\underline{Y}}_{cc}|_{1,1} \cdot \underline{\mathring{v}}_{2\,\rho_1} + \underline{\underline{Y}}_{cc}|_{1,2} \cdot \underline{\mathring{v}}_{2\,\rho_2} && (9.6)\\
\underline{I}_{2\,\rho_2} &= \underline{\underline{Y}}_{cc}|_{2,1} \cdot \underline{\mathring{v}}_{2\,\rho_1} + \underline{\underline{Y}}_{cc}|_{2,2} \cdot \underline{\mathring{v}}_{2\,\rho_2} && (9.7)\\
\underline{I}_{3\,\rho_2} &= -\underline{\underline{Y}}_3 \cdot \underline{\mathring{v}}_{3\,\rho_2} && (9.8)
\end{aligned}$$

Using the formalism developed in Chapter 2, we take the suitable inverse Fourier transforms of the preceding relations in order to make explicit the scattered terms in (9.3)and (9.4). In vector form one obtains:

$$\begin{aligned}
&\underline{H}^{inc}(\rho_1, \varphi, z) \times \hat{\rho} + \sum_n \int_{\Re} \underline{\underline{B}}^T \cdot \underline{\underline{K}}_\infty(z, \varphi) \cdot \underline{Y}_1(\rho_1, \chi, n) \cdot \underline{\mathring{v}}_{1\,\rho_1}(\chi, n)\, d\chi = \\
&\qquad = \sum_{n,m} \underline{\underline{B}}^T \cdot \underline{\underline{K}}_s(z, \varphi) \cdot [\underline{\underline{Y}}_{cc}|_{1,1} \cdot \underline{\mathring{v}}_{2\,\rho_1} + \underline{\underline{Y}}_{cc}|_{1,2} \cdot \underline{\mathring{v}}_{2\,\rho_2}](m, n) \qquad (9.9)
\end{aligned}$$

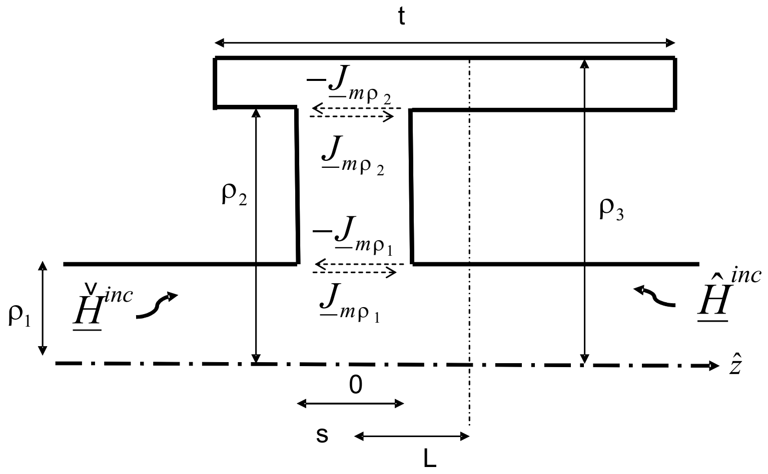

Figure 9.6: Application of the equivalence theorem to derive the system of coupled integral equations

$$\sum_{n,m} \underline{\underline{B}}^T \cdot \underline{\underline{K}}_s(z,\varphi) \cdot [\underline{\underline{Y}}_{cc}|_{2,1} \cdot \underline{\mathring{v}}_{2\,\rho_1} + \underline{\underline{Y}}_{cc}|_{2,2} \cdot \underline{\mathring{v}}_{2\,\rho_2}] = \sum_{n,m} \underline{\underline{B}}^T \cdot \underline{\underline{K}}_t(z-L,\varphi) \cdot \underline{\underline{Y}}_3 \cdot \underline{\mathring{v}}_{3\,\rho_2} \quad (9.10)$$

where $\underline{\underline{B}} = \hat{u}\hat{z} + \hat{v}\hat{\varphi}$ and $\underline{\underline{K}}_\infty$, $\underline{\underline{K}}_s$ and $\underline{\underline{K}}_t$ are the kernels introduced in Section 2.8 :

$$\underline{\underline{K}}_\infty(z,\varphi;\chi,n) = \frac{\mathrm{e}^{j\,n\varphi}\mathrm{e}^{j\,\chi\,z}}{4\pi^2} \cdot (\hat{\varphi}\hat{\varphi} + \hat{z}\hat{z}) \quad (9.11)$$

$$\underline{\underline{K}}_s(z,\varphi;\,m,n) = \frac{\mathrm{e}^{j\,n\,\varphi}}{\pi\,s\,\epsilon_m} \cdot \left[\sin\left(\frac{m\pi\,z}{s} + \frac{m\pi}{2}\right)\hat{\varphi}\hat{\varphi} + \cos\left(\frac{m\pi\,z}{s} + \frac{m\pi}{2}\right)\hat{z}\hat{z}\right] \quad (9.12)$$

$$\underline{\underline{K}}_t(z,\varphi;\,m,n) = \frac{\mathrm{e}^{j\,n\,\varphi}}{\pi\,t\,\epsilon_m} \cdot \left[\sin\left(\frac{m\pi\,z}{t} + \frac{m\pi}{2}\right)\hat{\varphi}\hat{\varphi} + \cos\left(\frac{m\pi\,z}{t} + \frac{m\pi}{2}\right)\hat{z}\hat{z}\right] \quad (9.13)$$

The subscripts s and t denote the kernels referring to the second and third radial waveguides, respectively.

Let us consider a general multimode field in the circular waveguide incident on the slot from the left and from the right. Using the same formalism as in Chapter 3, the tangential magnetic field on the wall can be expressed as:

$$\underline{H}_{tg}^{inc}(\rho_1,z,\varphi) = \underline{\check{H}}_{tg}^{inc}(\rho_1,z,\varphi) + \underline{\hat{H}}_{tg}^{inc}(\rho_1,z,\varphi) \quad (9.14)$$

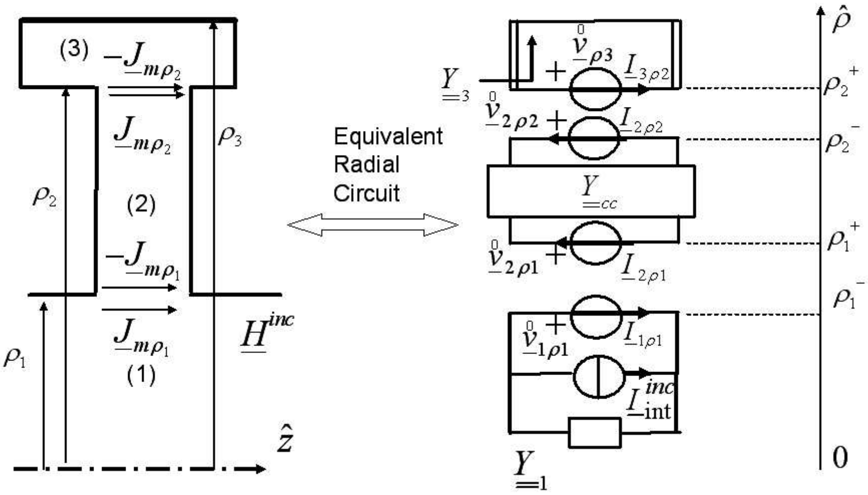

Figure 9.7: Equivalent radial circuit of the circular waveguide loaded by an asymmetrical "mushroom" stub

with

$$\check{\underline{H}}_{tg}^{inc}(\rho_1, z, \varphi) = \sum_i Y_{\infty i}\check{V}_i^{inc}(z_1)\mathrm{e}^{-j\,k_{z\,i}(z-z_1)}\check{\underline{h}}_i^{tg}(a)\mathrm{e}^{j\,m(i)\varphi} \tag{9.15}$$

$$\hat{\underline{H}}_{tg}^{inc}(a, z, \varphi) = -\sum_i Y_{\infty i}\hat{V}_i^{inc}(z_2)\mathrm{e}^{j\,k_{z\,i}(z-z_2)}\hat{\underline{h}}_i^{tg}(a)\mathrm{e}^{j\,m(i)\varphi} \tag{9.16}$$

and

$$\check{\underline{h}}_i^{tg}(\rho_1) = h_{\varphi i}(\rho_1)\hat{\varphi} + h_{zi}(\rho_1)\hat{z} \tag{9.17}$$

$$\hat{\underline{h}}_i^{tg}(\rho_1) = h_{\varphi i}(\rho_1)\hat{\varphi} - h_{zi}(\rho_1)\hat{z} \tag{9.18}$$

where $k_{z\,i}$, $Y_{\infty\,i}$, are the propagation constant and modal admittance of the i-th mode of the circular waveguide. $\check{V}_i^{inc}(z_1)$ and $\hat{V}_i^{inc}(z_2)$ are incident voltages on the left ($z = z_1$) and on the right ($z = z_2$) reference planes of the structure. The relation between the magnetic currents and voltage generators can be written as:

$$\underline{\mathring{v}}_{1\,\rho_1}(\chi, n) \;=\; \int_{\Re}\int_0^{2\pi} \underline{\underline{B}} \cdot \underline{\underline{K}}_{\infty}(\varphi, z;\, \chi,\, n) \cdot \underline{\mathbb{J}}_{m,\rho_1}(\varphi, z) \times \hat{\rho}\, d\varphi\, d\, z \tag{9.19}$$

$$\underline{\mathring{v}}_{2\,\rho_1}(m, n) \;=\; \int_{\Re}\int_0^{2\pi} \underline{\underline{B}} \cdot \underline{\underline{K}}_{\,s}(\varphi, z;\, m,\, n) \cdot \underline{\mathbb{J}}_{m,\rho_1}(\varphi, z) \times \hat{\rho}\, d\varphi\, d\, z \tag{9.20}$$

$$\underline{\mathring{v}}_{2\,\rho_2}(m, n) \;=\; \int_{\Re}\int_0^{2\pi} \underline{\underline{B}} \cdot \underline{\underline{K}}_{\,s}(\varphi, z;\, m,\, n) \cdot \underline{\mathbb{J}}_{m,\rho_2}(\varphi, z) \times \hat{\rho}\, d\varphi\, d\, z \tag{9.21}$$

$$\underline{\mathring{v}}_{3\,\rho_2}(m, n) \;=\; \int_{\Re}\int_0^{2\pi} \underline{\underline{B}} \cdot \underline{\underline{K}}_{\,t}(\varphi, z + L;\, m,\, n) \cdot \underline{\mathbb{J}}_{m,\rho_2}(\varphi, z) \times \hat{\rho}\, d\varphi\, d\, z \tag{9.22}$$

The various admittances can be computed relatively easily employing the radial line transmission theory, see Section 2.6.

As it has been done in the analysis of LCX, it is convenient to solve the HFIE directly in the spectral domain. We introduce a set $\{\underline{u}_c(z, \varphi)\}$ of vector basis functions in order to expand the unknown magnetic current distributions, i.e.:

$$\underline{\mathbb{J}}_{m\,\rho_1}(z, \varphi) \;=\; \sum_{c=1}^{N_f} x_c \underline{u}_c(z, \varphi) \tag{9.23}$$

$$\underline{\mathbb{J}}_{m\,\rho_2}(z, \varphi) \;=\; \sum_{c=1}^{N_f} y_c \underline{u}_c(z, \varphi) \tag{9.24}$$

and the equivalent voltage generators get the form:

$$\underline{\mathring{v}}_{1\,\rho_1}(\chi, n) = \underline{\underline{B}} \cdot \sum_{c=1}^{N_f} x_c \underline{\tilde{u}}_c(\chi, n) \tag{9.25}$$

$$\begin{aligned}
\underline{\mathring{v}}_{2\,\rho_1}(m, n) &= \underline{\underline{B}} \cdot \sum_{c} x_c\, \underline{\acute{u}}_c(m, n) \\
\underline{\mathring{v}}_{2\,\rho_2}(m, n) &= \underline{\underline{B}} \cdot \sum_{c} y_c\, \underline{\acute{u}}_c(m, n) \\
\underline{\mathring{v}}_{3\,\rho_2}(m, n) &= \underline{\underline{B}} \cdot \sum_{c} y_c\, \underline{\grave{u}}_c(m, n)
\end{aligned} \tag{9.26}$$

where:

$$\begin{aligned}
\tilde{\underline{u}}_c(\chi,n) &= \int_{\Re}\int_0^{2\pi} \underline{\underline{K}}_{\infty}(\varphi,z;\,\chi,\,n)\cdot\underline{u}_c(z,\varphi)d\varphi\,d\,z && (9.27)\\
\acute{\underline{u}}_c(m,n) &= \int_{\Re}\int_0^{2\pi} \underline{\underline{K}}_{s}(\varphi,z;\,m,\,n)\cdot\underline{u}_c(z,\varphi)d\varphi\,d\,z && (9.28)\\
\grave{\underline{u}}_c(m,n) &= \int_{\Re}\int_0^{2\pi} \underline{\underline{K}}_{t}(\varphi,z-L;\,m,\,n)\cdot\underline{u}_c(z,\varphi)d\varphi\,d\,z && (9.29)
\end{aligned}$$

Note that $\acute{\underline{u}}_c$ and $\grave{\underline{u}}_c$ can be obtained as suitable combinations of the even and odd parts of the Fourier transform of $\underline{u}_c$.

Applying the Galerkin version of the Method of Moments, we project (9.9) and (9.10) on $\underline{u}_r(z,\varphi)$, $r=1,\ldots,N_f$, obtaining:

$$\begin{aligned}
<\underline{H}^{inc}\times\hat{\rho},\underline{u}_r> &= \sum_c x_c \sum_n \int_{-\infty}^{+\infty} \tilde{\underline{u}}^*_r(\chi,n)\cdot\underline{\underline{B}}^T\cdot\underline{\underline{Y}}^{tot}(\chi,n)\cdot\underline{\underline{B}}\cdot\tilde{\underline{u}}_c(\chi,n)d\chi +\\
&+ \sum_c x_c \sum_{n,m} \acute{\underline{u}}^*_r(m,n)\cdot\underline{\underline{B}}^T\cdot\underline{\underline{Y}}_{cc}|_{11}(m,n)\cdot\underline{\underline{B}}\cdot\acute{\underline{u}}_c(m,n) +\\
&+ \sum_c y_c \sum_{n,m} \acute{\underline{u}}^*_r(m,n)\cdot\underline{\underline{B}}^T\cdot\underline{\underline{Y}}_{cc}|_{12}(m,n)\cdot\underline{\underline{B}}\cdot\acute{\underline{u}}_c(m,n) && (9.30)
\end{aligned}$$

$$\begin{aligned}
0 &= \sum_c x_c \sum_{n,m} \acute{\underline{u}}^*_r(m,n)\cdot\underline{\underline{B}}^T\cdot\underline{\underline{Y}}_{cc}|_{21}(m,n)\cdot\underline{\underline{B}}\cdot\acute{\underline{u}}_c(m,n) +\\
&+ \sum_c y_c \sum_{n,m} \acute{\underline{u}}^*_r(m,n)\cdot\underline{\underline{B}}^T\cdot\underline{\underline{Y}}_{cc}|_{22}(m,n)\cdot\underline{\underline{B}}\cdot\acute{\underline{u}}_c(m,n) +\\
&+ \sum_c y_c \sum_{n,m} \grave{\underline{u}}^*_r(m,n)\cdot\underline{\underline{B}}^T\cdot\underline{\underline{Y}}_3(m,n)\cdot\underline{\underline{B}}\cdot\grave{\underline{u}}_c(m,n) && (9.31)
\end{aligned}$$

It is convenient to write this linear system in matrix form:

$$\begin{aligned}
\underline{\underline{A}}\cdot\begin{pmatrix}\underline{x}\\ \underline{y}\end{pmatrix} &= \left[\begin{pmatrix}\check{\underline{B}}\\ \underline{0}\end{pmatrix}+\begin{pmatrix}\hat{\underline{B}}\\ \underline{0}\end{pmatrix}\right]\\
\Rightarrow\begin{pmatrix}\underline{x}\\ \\ \underline{y}\end{pmatrix} &= \underline{\underline{A}}^{-1}\left[\begin{pmatrix}\check{\underline{B}}\\ \\ \underline{0}\end{pmatrix}+\begin{pmatrix}\hat{\underline{B}}\\ \\ \underline{0}\end{pmatrix}\right]=\begin{pmatrix}\check{\underline{\underline{C}}}_x & \hat{\underline{\underline{C}}}_x\\ \\ \check{\underline{\underline{C}}}_y & \hat{\underline{\underline{C}}}_y\end{pmatrix}\cdot\begin{pmatrix}\check{\underline{V}}^{inc}\\ \\ \hat{\underline{V}}^{inc}\end{pmatrix} && (9.32)
\end{aligned}$$

The matrices $\underline{\underline{C}}$ have size $N_f\times N_i$.

The right hand side shows explicitly the contributions of the field incident from the left and from the right. Due to the fact that the three regions are completely separated by perfect conductor walls, the admittance moment matrix can be decomposed into the sum of a diagonal matrix relative to the terminal cavities (in the transverse view, the cylindrical waveguide is a cavity) and a full matrix relative to the connecting guide:

$$\underline{\underline{A}} = \begin{pmatrix} \underline{\underline{A}}^{wg} & 0 \\ & \\ 0 & \underline{\underline{A}}^{cav} \end{pmatrix} + \begin{pmatrix} \underline{\underline{A}}^{conn}_{11} & \underline{\underline{A}}^{conn}_{12} \\ & \\ \underline{\underline{A}}^{conn}_{21} & \underline{\underline{A}}^{conn}_{22} \end{pmatrix} \tag{9.33}$$

where:

$$\underline{\underline{A}}^{wg}|_{r,c} = \sum_n \int_{-\infty}^{+\infty} \tilde{\underline{u}}^*_r(\chi,n) \cdot \underline{\underline{B}}^T \cdot \underline{\underline{Y}}_1(\chi,n) \cdot \underline{\underline{B}} \cdot \tilde{\underline{u}}_c(\chi,n) d\chi \tag{9.34}$$

$$\underline{\underline{A}}^{conn}_{11}|_{r,c} = \sum_{n,m} \acute{\underline{u}}^*_r(m,n) \cdot \underline{\underline{B}}^T \cdot \underline{\underline{Y}}_{cc}|_{11}(m,n) \cdot \underline{\underline{B}} \cdot \acute{\underline{u}}_c(m,n) \tag{9.35}$$

$$\underline{\underline{A}}^{conn}_{12}|_{r,c} = \sum_{n,m} \acute{\underline{u}}^*_r(m,n) \cdot \underline{\underline{B}}^T \cdot \underline{\underline{Y}}_{cc}|_{12}(m,n) \cdot \underline{\underline{B}} \cdot \acute{\underline{u}}_c(m,n) \tag{9.36}$$

$$\underline{\underline{A}}^{conn}_{21}|_{r,c} = \sum_{n,m} \acute{\underline{u}}^*_r(m,n) \cdot \underline{\underline{B}}^T \cdot \underline{\underline{Y}}_{cc}|_{21}(m,n) \cdot \underline{\underline{B}} \cdot \acute{\underline{u}}_c(m,n) \tag{9.37}$$

$$\underline{\underline{A}}^{conn}_{22}|_{r,c} = \sum_{n,m} \acute{\underline{u}}^*_r(m,n) \cdot \underline{\underline{B}}^T \cdot \underline{\underline{Y}}_{cc}|_{22}(m,n) \cdot \underline{\underline{B}} \cdot \acute{\underline{u}}_c(m,n) \tag{9.38}$$

$$\underline{\underline{A}}^{cav}|_{r,c} = \sum_{n,m} \grave{\underline{u}}^*_r(m,n) \cdot \underline{\underline{B}}^T \cdot \underline{\underline{Y}}_3(m,n) \cdot \underline{\underline{B}} \cdot \grave{\underline{u}}_c(m,n) \tag{9.39}$$

Adopting the same formalism as in the Chapter 2, the two terms on the right hand side of (9.32) can be written as:

$$\check{\underline{B}} = \underline{\underline{U}}^{-+} \cdot \check{\underline{\underline{h}}} \cdot \underline{\underline{Y}}_{\infty} \cdot \underline{\underline{D}}_1 \cdot \check{\underline{V}}^{inc} \tag{9.40}$$

$$\hat{\underline{B}} = \underline{\underline{U}}^{-+} \cdot \hat{\underline{\underline{h}}} \cdot \underline{\underline{Y}}_{\infty} \cdot \underline{\underline{D}}_2^{-1} \cdot \hat{\underline{V}}^{inc} \tag{9.41}$$

The amplitudes of all the incident modes (TE and TM) have been grouped in the vectors $\check{\underline{V}}^{inc}$ and $\hat{\underline{V}}^{inc}$.

Once the linear system is solved, we can derive the scattering matrix of the device. The scattered voltages are computed as shown in Section 3.3 and the result is:

$$\underline{\check{V}}^{scat} = \frac{1}{2}\underline{\underline{D}}_1 \cdot \underline{\underline{\hat{h}}}^* \cdot \underline{\underline{W}} \cdot \underline{\underline{U}}^{--T} \cdot \underline{x} \tag{9.42}$$

$$\underline{\hat{V}}^{scat} = -\frac{1}{2}\underline{\underline{D}}_2^{-1} \cdot \underline{\underline{\check{h}}}^* \cdot \underline{\underline{W}} \cdot \underline{\underline{U}}^{--T} \cdot \underline{x} \tag{9.43}$$

where the dyadic $\underline{\underline{W}}$ is defined by

$$\underline{\underline{W}} = \hat{\varphi}\hat{\varphi} + \left(\frac{k_z^*}{k_z}\right)\hat{z}\hat{z}$$

Hence, on introducing power waves as usual, the scattering matrix of the cavity has the following submatrices:

$$\underline{\underline{S}}_{11} = \underline{\underline{Y}}_\infty^{1/2}\underline{\underline{\check{M}}} \cdot \underline{\underline{\check{C}}}_x \cdot \underline{\underline{Y}}_\infty^{-1/2}$$

$$\underline{\underline{S}}_{12} = \underline{\underline{Y}}_\infty^{1/2}\underline{\underline{\check{M}}} \cdot \underline{\underline{\hat{C}}}_x \cdot \underline{\underline{Y}}_\infty^{-1/2} + \underline{\underline{D}}$$

$$\underline{\underline{S}}_{21} = \underline{\underline{Y}}_\infty^{1/2}\underline{\underline{\hat{M}}} \cdot \underline{\underline{\check{C}}}_x \cdot \underline{\underline{Y}}_\infty^{-1/2} + \underline{\underline{D}}$$

$$\underline{\underline{S}}_{22} = \underline{\underline{Y}}_\infty^{1/2}\underline{\underline{\hat{M}}} \cdot \underline{\underline{\hat{C}}}_x \cdot \underline{\underline{Y}}_\infty^{-1/2}$$

where the $N_i \times N_i$ matrix $\underline{\underline{D}}$ represents the direct contribution of the incident voltages:

$$\underline{\underline{D}} = \underline{\underline{D}}_2^{-1} \cdot \underline{\underline{D}}_1$$

with $\underline{\underline{D}}_1$, $\underline{\underline{D}}_2$ defined in Eqs. (3.19) and (3.20) and the $N_i \times N_f$ matrices $\underline{\underline{\check{M}}}$, $\underline{\underline{\hat{M}}}$ are the matrix operators that relate the coefficients of the magnetic current $\underline{\mathbb{J}}_{m,a}$ to the scattered waves. Their expressions are:

$$\underline{\underline{\check{M}}} = \frac{1}{2}\underline{\underline{D}}_1 \cdot \underline{\underline{\check{h}}}^* \cdot \underline{\underline{W}} \cdot \underline{\underline{U}}^{--T}$$

$$\underline{\underline{\hat{M}}} = -\frac{1}{2}\underline{\underline{D}}_2^{-1} \cdot \underline{\underline{\hat{h}}}^* \cdot \underline{\underline{W}} \cdot \underline{\underline{U}}^{--T}$$

It is to be noted that the scattered waves in the circular waveguide depend explicitly on $\underline{\mathbb{J}}_{m,\rho_1}$ only, because the opening between regions “1” and “2” is closed with a perfect conductor. However, the value of $\underline{\mathbb{J}}_{m,\rho_1}$ depends on $\underline{\mathbb{J}}_{m,\rho_2}$, so that the presence of region “3” is indirectly taken into account.

It can be proved that, if the metallic and dielectric losses are neglected, the scattering matrix, relative to the above cut off modes in the the cylindrical waveguide is unitary. This is an algebraic property, independent of the number of expansion functions and of number of terms in the series defining the moment matrix. Moreover, the scattering matrix is symmetric, because the structure is reciprocal and the mode functions are real.

The filter consists generally of N_{slot} cavities. Its response can be easily computed as usual, by defining the accessible modes in the cylindrical waveguide and using the cascading algorithm.

The elements of the moment matrix have been computed using special numerical techniques, the computation details are reported in paragraphs 10.6 and 10.7.

9.3 Expansion functions

Due to the rectangular shape of the apertures, on which the equivalent magnetic currents are defined, it is convenient to employ entire domain basis functions. Moreover, the slot is angularly complete, so that the discontinuity couples only the modes of the circular waveguide which have the same azimuthal index of the incident field. In the frequency range under consideration, the only mode above cut off is the fundamental one, *i.e.* the TE_{11}, hence only the TE and TM mode with second index equal to one are excited. In order to construct an efficient code, we decided to use basis functions that satisfy the Meixner edge conditions [24]:

$$\underline{u}_n(z,\varphi) = \phi_n(z)\cos\varphi\,\hat{\varphi} + \zeta_n(z)\sin\varphi\,\hat{z} \tag{9.44}$$

with

$$\phi_n(z) = C_n^{1/6}\left(\frac{2z}{s}\right)\left[1-\left(\frac{2z}{s}\right)^2\right]^{-1/3}$$

$$\zeta_n(z) = C_n^{7/6}\left(\frac{2z}{s}\right)\left[1-\left(\frac{2z}{s}\right)^2\right]^{2/3}$$

where $C_n^{\alpha}(z)$ are the Gegenbauer polynomials of degree n, [10]. Some of these functions are plotted in Figures 9.8 and 9.9. The functions $\phi_n(z)$ diverge at the domain limits as $|z \pm s/2|^{-1/3}$ and are useful to expand a current component parallel to the 90° edge. On the contrary, $\zeta_n(z)$

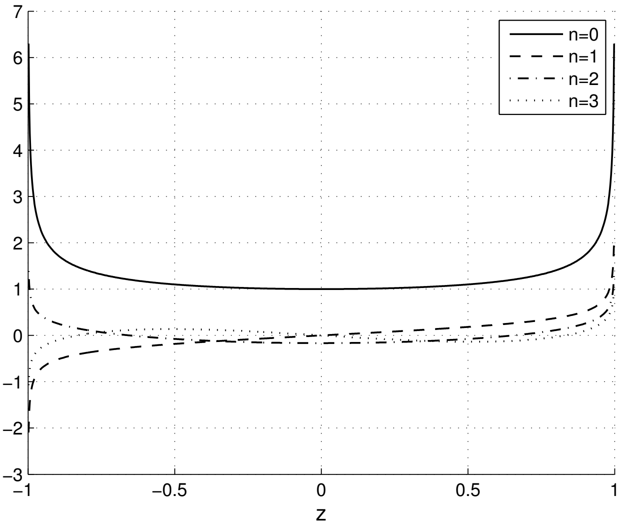

Figure 9.8: Plot of $\phi_n(z)$ for $n = 0, 1, 2, 3$ with $s = 2$

vanish as $|z \pm s/2|^{2/3}$ and are appropriate to represent the current component normal to the edge. The Fourier transform of these functions can be evaluated in closed form as [37]:

$$\begin{aligned}\tilde{\phi}_n(\chi) &= \left(\frac{\pi\, s}{2}\right)\left(\frac{\chi\, s}{2}\right)^{-\frac{1}{6}} J_{n+\frac{1}{6}}\left(\frac{\chi\, s}{2}\right)\\ \tilde{\zeta}_n(\chi) &= \left(\frac{\pi\, s}{2}\right)\left(\frac{\chi\, s}{2}\right)^{-\frac{7}{6}} J_{n+\frac{7}{6}}\left(\frac{\chi\, s}{2}\right)\end{aligned}$$

Since $\phi_n(z)$ and $\zeta_n(z)$ are even (odd) real functions for even (odd) n, their Fourier transforms are real even (imaginary odd) functions, respectively.
Some of these transforms are plotted in Figures 9.10 and 9.11.

9.4 Convergence study

In order to study the convergence of the numerical scheme that has been developed, let us consider a single cavity. The geometrical and electric characteristics of the structure are: cylindrical waveguide radius $\rho_1 = 7.7$ cm, cavity inner wall radius $\rho_2 = 10$ cm, cavity outer wall radius $\rho_3 = 12$ cm, aperture width $s = 2$ cm, cavity length $t = 3$ cm, asymmetry length $L = 0$ and frequency $f = 1.4$ GHz. In Figure 9.12 and 9.13 the fundamental mode reflection and transmis-

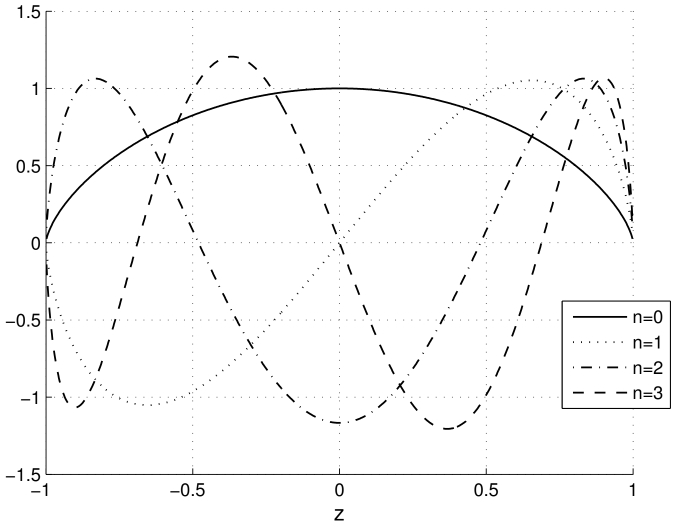

Figure 9.9: Plot of $\zeta_n(z)$ for $n = 0, 1, 2, 3$ with $s = 2$

sion coefficients (in dB) versus the number of expansion functions N_f are shown. From the plots we note that three basis functions are sufficient to guarantee a good accuracy. Finally, Figures 9.14 and 9.15 show a comparison between the frequency response of the structure computed by the integral equation technique presented here and CST Microwave Studio. The two curves are practically indistinguishable, but the computation times are widely different.

9.5 Design of ring cavity filters

The method described in the preceding sections will be used now to analyze both symmetric and asymmetric stubs.

Let us define $h = \rho_3 - \rho_1$, $d = \rho_2 - \rho_1$ and λ_{0RX} and λ_{0TX} the wavelengths corresponding to the zeros of the reflection and transmission coefficients, respectively. Figure 9.16 shows a contour line representation of the parameters $\rho_1/\lambda_{0RX} = f(h/\rho_1, t/\rho_1)$ and $\rho_1/\lambda_{0RX} = g(h/\rho_1, t/\rho_1)$ of the stub for the case $s = \rho_1/3$ and $d = \rho_1/3$. The maps are very general, because they depend only slightly on s/ρ_1 and d/ρ_1. These plots, as well as that of Figure 9.17 show clearly the strict relation existing between the frequencies of the these two zeros.

An asymmetrical configuration (*i.e.* $L \neq 0$) allows instead the independent control of the position of these zeros. As an example, the frequency behavior of a single stub for different values of

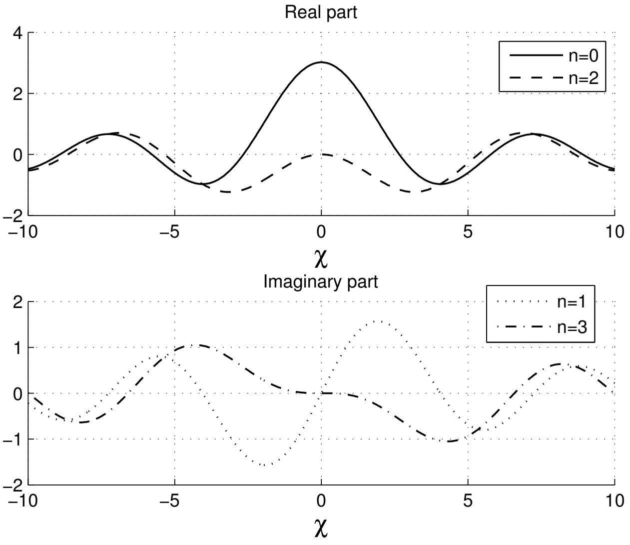

Figure 9.10: Plot of $\tilde{\phi}_n(\chi)$. The functions are real for $n = 0, 2, \ldots$ and pure imaginary for $n = 1, 3, \ldots$

the offset L is shown in Figure 9.18. The geometrical characteristics are $\rho_1 = 5.2$ mm, $s = 0.4\rho_1$, $t = 1.8\rho_1$, $d = 0.2\rho_1$ and $h = 0.43\rho_1$. We see that a variation of the offset L induces a small change in the position of the reflection zero and a large change in that of the transmission zero. Hence, by a proper choice of h/ρ_1, t/ρ_1, and L/ρ_1, we obtained the flexibility required by the design.

By cascading a number of stubs, higher order filters can be realized. Moreover, this type of cavity allows some interesting configurations, as that shown in Figure 9.19, where different kinds of stubs are used: in this way a three cavity filter has the same total length as a two cavity one.

As a first design example, let us consider a dual polarization filter with the following specifications: X-Ku operating band, pass band centered at 9.7 GHz $\pm\ 8\%$ with a return loss greater than 35dB and stop band centered at 15.45 GHz $\pm\ 1.8\%$ with attenuation greater than 30dB.

A 5-stub configuration has been chosen and the geometry is shown in Figure 9.20, whereas the corresponding frequency response is in Figure 9.21. The design is carried out by choosing the frequencies of the reflection and transmission zeros of the various stubs. Since the stubs are very weakly coupled, the designer has a good control on the electromagnetic characteristics of the device. Then, the various dimensions have been obtained using the design maps. The frequency behavior of each stub is shown in Figure 9.22: the filter is symmetric, thus there are only three different stubs. Note that the transverse occupation has been reduced by 25% with respect to the use of straight stubs.

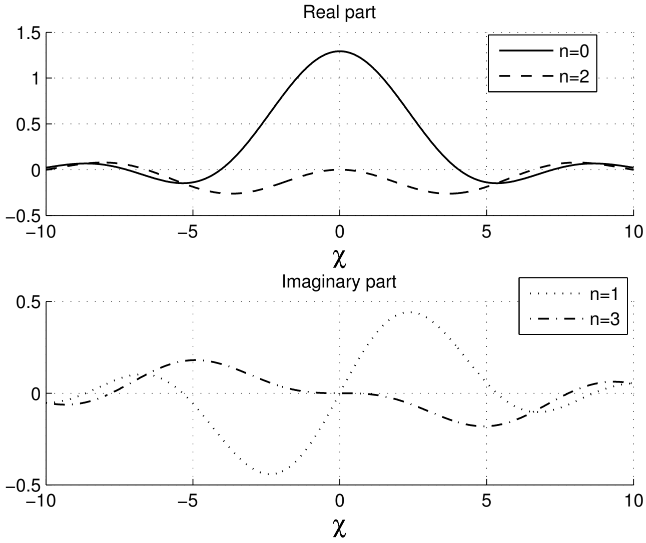

Figure 9.11: Plot of $\tilde{\zeta}_n(\chi)$. The functions are real for $n = 0, 2, \ldots$ and pure imaginary for $n = 1, 3, \ldots$

As another design example of a dual polarization filter, let us assume the following specifications: return loss greater than 25 dB at 1.55 GHz$\pm 10\%$ and isolation greater than 40 dB at 2 GHz, with minimum longitudinal and radial dimensions. The geometry of the filter is shown in Figure 9.23 and the corresponding frequency response in Figure 9.24. Note that all the specifications have been satisfied using a four-asymmetric-stub configuration.

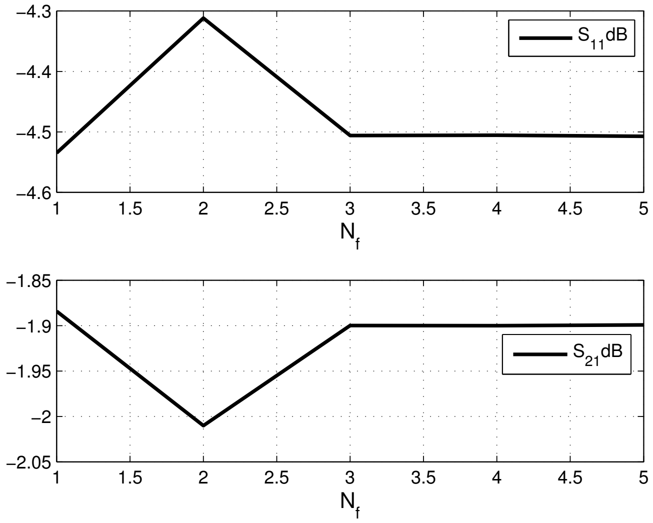

Figure 9.12: Cavity reflection and transmission coefficients versus the number of basis functions

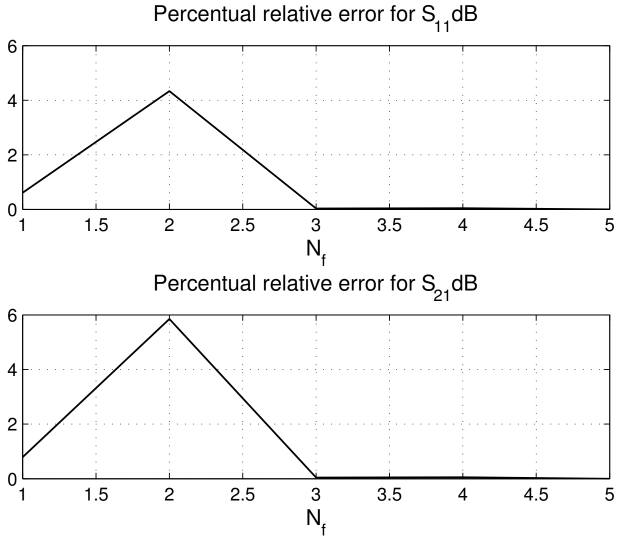

Figure 9.13: Relative error of the cavity reflection and transmission coefficients versus the number of basis functions

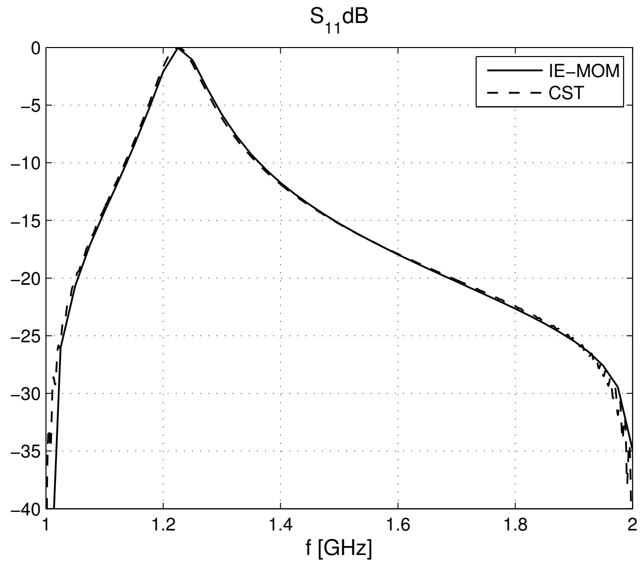

Figure 9.14: Reflection coefficient versus frequency. Comparison between integral equation technique (solid line) and CST Microwave studio (dashed line)

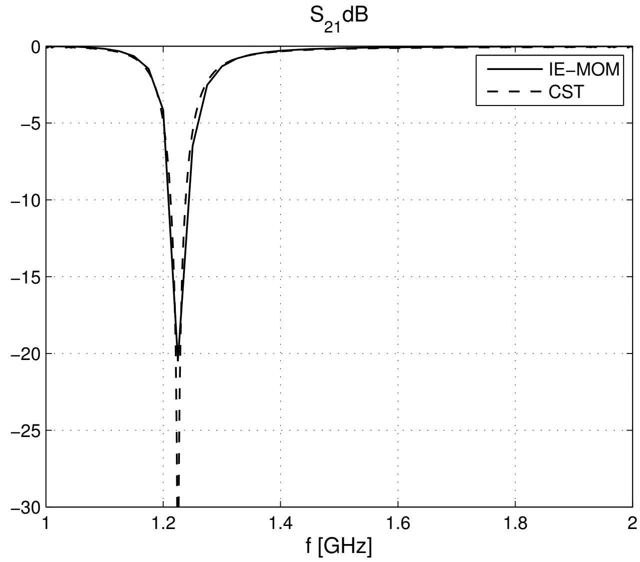

Figure 9.15: Transmission coefficient versus frequency. Comparison between integral equation technique (solid line) and CST Microwave studio (dashed line)

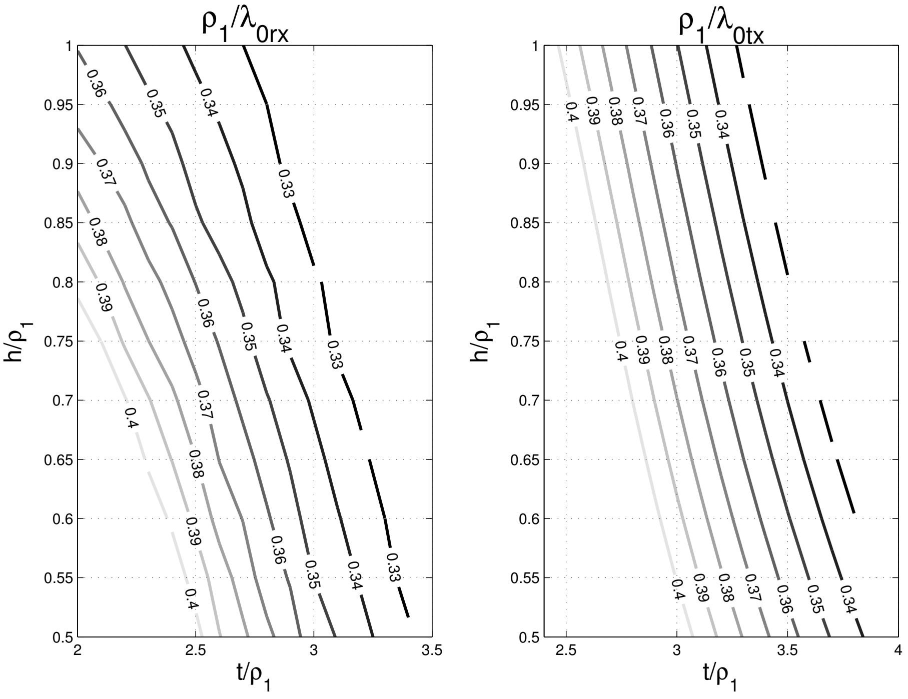

Figure 9.16: Contours of ρ_1/λ_{0RX} (left) and ρ_1/λ_{0TX} (right) in the plane of the parameters h/ρ_1 and t/ρ_1, for a symmetrical stub

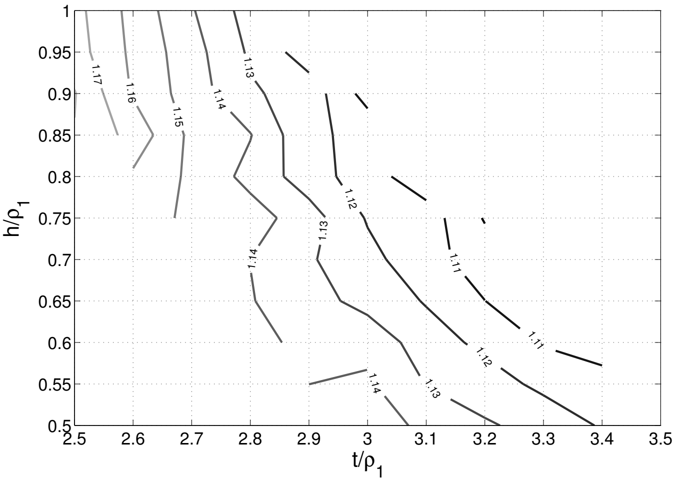

Figure 9.17: Contours of $\lambda_{0RX}/\lambda_{0TX}$ in the plane of the parameters h/ρ_1 and t/ρ_1, for a symmetrical stub

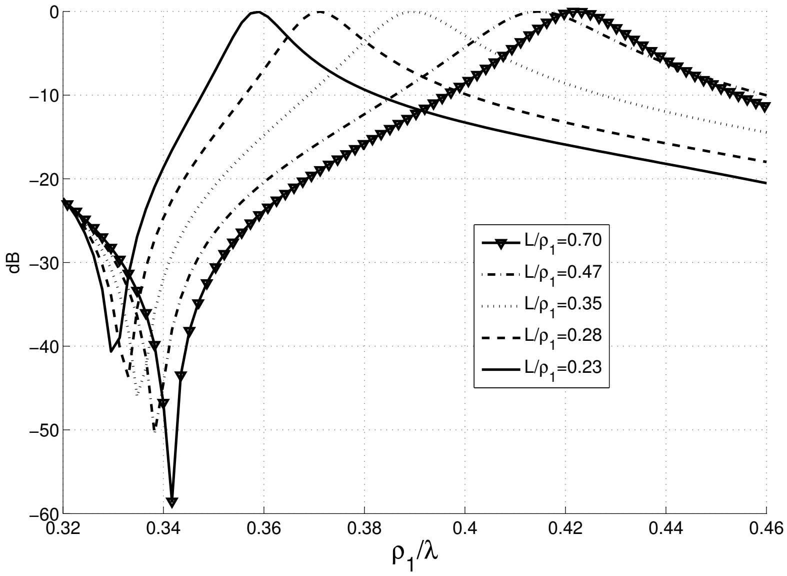

Figure 9.18: Frequency reflection response of an asymmetric stub for various values of the offset L

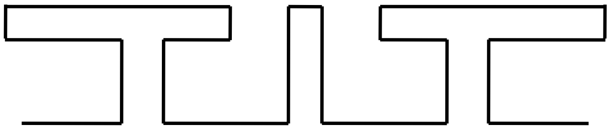

Figure 9.19: Compact filter configuration with various kinds of stubs

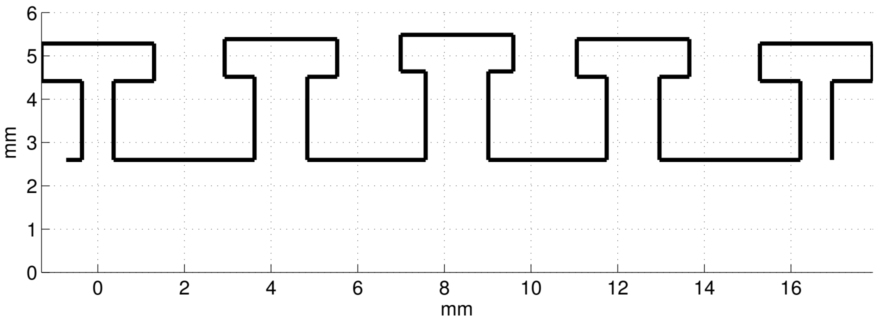

Figure 9.20: Stub geometry for the pass-band filter

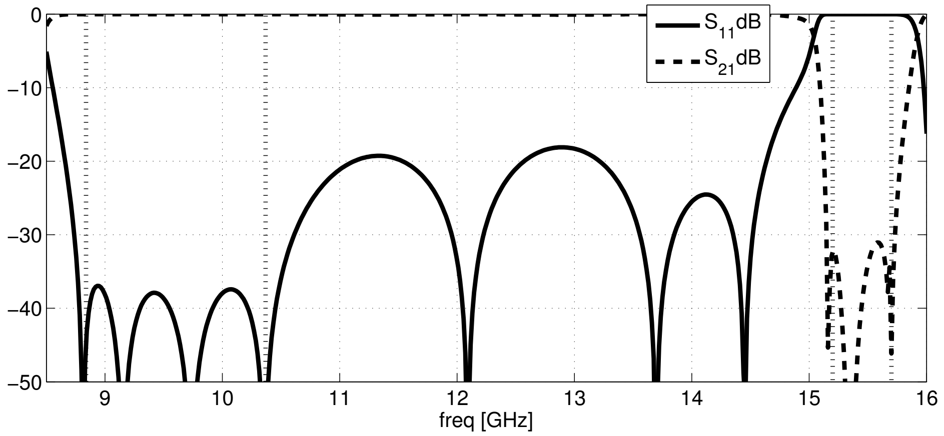

Figure 9.21: Frequency Response of the filter of Figure 9.20

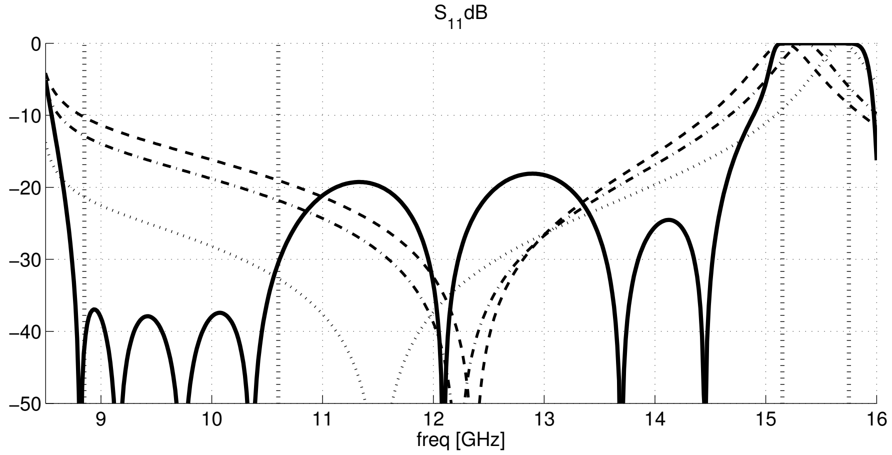

Figure 9.22: Reflection coefficient of the filter of Figure 9.20 and of the individual stubs

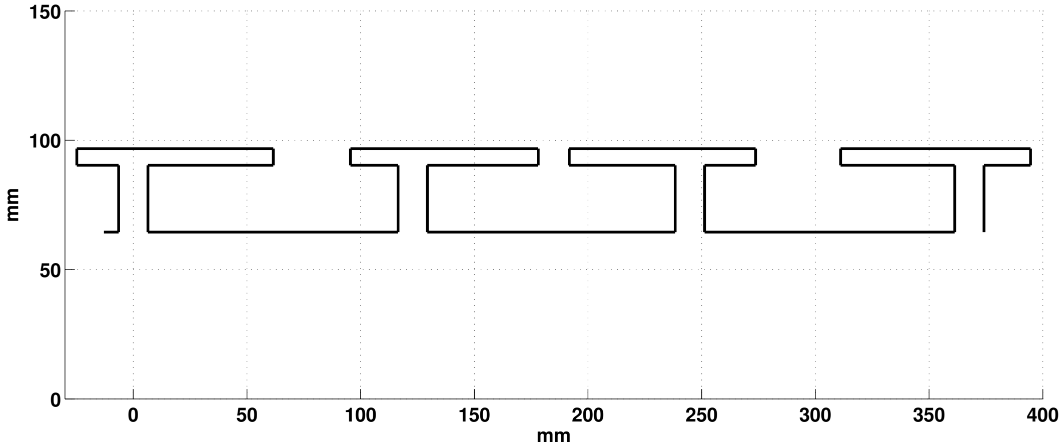

Figure 9.23: Geometry of the cells for the stop band filter

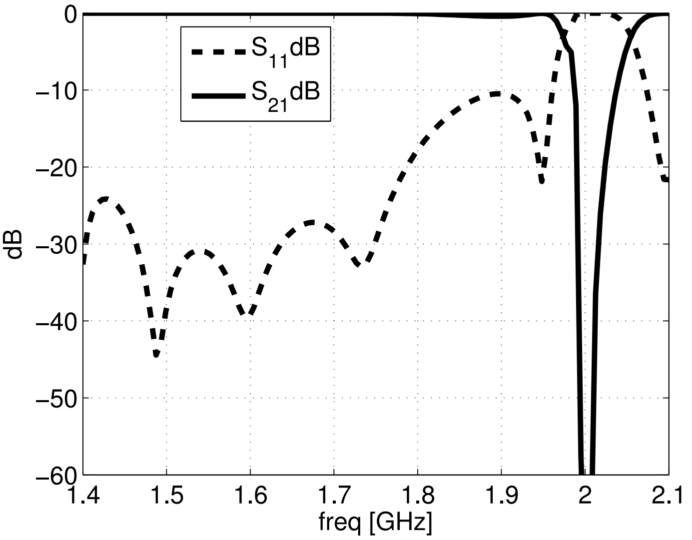

Figure 9.24: Frequency Response of the structure of Figure 9.23

Chapter 10

Numerical Issues

10.1 Introduction

The solution of the integral equations related to the analysis of LCX and ring cavity filters, and the discretization of the slot scattering operator require the computation of series of integrals where the integrand functions are combination of Bessel and Hankel functions. Owing to the presence of poles and ranch cuts, the application of standard integration routines is not possible or not efficient. For this reason we have developed special numerical schemes that are briefly described in the present chapter.

10.2 Double exponential transforms

In order to describe the method, we start with the general idea. Suppose that the following integral is to be evaluated:

$$I = \int_{-1}^{1} f(x)dx \tag{10.1}$$

Use the change of variable $x = \varphi(t)$, such that $\varphi(-1) = -\infty$ and $\varphi(1) = \infty$:

$$I = \int_{-\infty}^{\infty} f(\varphi(t))\varphi'(t)dt \tag{10.2}$$

Applying the trapezoidal formula to (10.2) we obtain:

$$I = h \sum_{k=-\infty}^{\infty} f(\varphi(kh))\varphi'(kh) + O\left(\exp(-\frac{2\pi\, d}{h})\right) \tag{10.3}$$

where d is the distance from the real t axis of the closest singularity of $\varphi(t)\varphi'(t)$. The formula (10.3) is quite efficient if one employs as $\varphi(t)$ that one proposed by H.Takahasi and M.Mori ([39]):

$$x = \varphi(t) = \tanh(\frac{\pi}{2}\sinh(t)) \tag{10.4}$$

In the actual computation the infinite summation (10.3) must be truncated in such a way that the order of the truncation error is equal to that of the discretization error $O\left(\exp(-2\pi\, d/h)\right)$. Operating in this way, the following quadrature formula results:

$$I = h \sum_{k=-N}^{N} f(\varphi(kh))\varphi'(kh) + O\left(\exp(-\frac{CN}{\log N})\right) \tag{10.5}$$

where $2N + 1$ function evaluations are required. Since the integrand in (10.2) has a double exponential decay, (10.5) is called double exponential (DE) formula. It is optimal in the sense that no quadrature formula can be obtained by variable transformation with a smaller error [39].

Let us now consider the application of the preceding idea in a particular case that occurs in the computation of the projection integrals.
Let us consider the following integral:

$$I = \int_0^{\infty} f(x)dx \tag{10.6}$$

where the integrand is such that

$$f(n\mu + \theta) = 0 \text{ for large integers } n \tag{10.7}$$

where μ and θ are some constants. This means that $f(x)$ has an infinite number of zeros with spacing μ for large x.
By the variable transformation:

$$\begin{cases} x = M\varphi(t) \\ \lim\limits_{t\to-\infty} \varphi(t) = 0 \\ \lim\limits_{t\to\infty} \varphi(t) = \infty \end{cases}$$

where M is some large positive constant to be defined later, (10.6) becomes:

$$I = \int_{-\infty}^{\infty} f(M\varphi(t))M\varphi'(t)dt \tag{10.8}$$

The application of the trapezoidal rule, with the constant shift θ/M of the nodes, leads to:

$$I = Mh \sum_{k=-\infty}^{\infty} f(M\varphi(nh+\theta/M))\varphi'(nh+\theta/M) \tag{10.9}$$

we choose $\varphi(t)$ such that:

$$\begin{cases} \lim\limits_{t\to\infty} \dfrac{\varphi(t)}{t} = 1 \\ \lim\limits_{t\to-\infty} \varphi'(t) = 0 \end{cases} \tag{10.10}$$

then the argument of $f(x)$ in 10.9 approaches $Mnh+\theta$ when $n \to \infty$. Applying on t a mesh size h such that $Mh = \mu$, for large n we obtain:

$$f(M\varphi(nh+\theta/M)) \simeq f(Mnh+\theta) = f(n\mu+\theta) = 0 \tag{10.11}$$

then we can truncate the summation I_h at some moderate positive n if $\varphi(t)$ approaches t rapidly enough. For large negative n we can truncate the summation because of the second of (10.10). A typical and useful transformation for this kind of integrals is given by:

$$\varphi(t) = \frac{t}{1-\exp(-K\sinh(t))} \tag{10.12}$$

where K is some positive constant. The derivative is given by:

$$\varphi'(t) = \frac{1-(1+Kt\cosh(t))\exp(-K\sinh t)}{(1-\exp(-K\sinh t))^2} \tag{10.13}$$

and the functions $\varphi(t)$ and $\varphi'(t)$ have the following behavior:

$$\varphi(t) = \begin{cases} |t|\exp(-1/2K\ \exp|t|) \simeq 0 & t \to -\infty \\ \\ \frac{1}{K} & t \to 0 \\ \\ t + t\ \exp(-1/2K\ \exp|t|) \simeq t & t \to +\infty \end{cases} \tag{10.14}$$

$$\varphi'(t) = \begin{cases} \frac{1}{2}K|t|\exp|t|\exp(-1/2K\ \exp|t|) \simeq 0 & t \to -\infty \\ \\ \frac{1}{2} & t \to 0 \\ \\ 1 & t \to +\infty \end{cases} \tag{10.15}$$

In other words, the derivative $\varphi'(t)$ approaches zero double exponentially as $t \to -\infty$, while the function $\varphi(t)$ itself approaches t double exponentially as $t \to +\infty$. Note that using this method it is really important to be careful in the numerical evaluation of $\varphi(t)$ and $\varphi'(t)$ in the neighborhood of $t = 0$ since the numerical accuracy can be compromised by the loss of significant digits.

Let us consider now the application of the Double Exponential formula to the computation of the projection integrals considered in this work, such as a generic element of the sub-matrix A_{rc}, see section 3.5. If weighted Chebyshev polynomials are employed as basis functions, the generic projection integral takes the following form:

$$\int_A^\infty Y_{uu}(\chi,n)\tilde{f}_r(\chi)\tilde{f}_c(\chi)d\chi = \left(\frac{s\pi}{2}\right)^2(-1)^r(j)^{r+c}\int_A^\infty Y_{uu}(\chi,n)J_r^*(s\chi/2)J_c(s\chi/2)d\chi \quad (10.16)$$

Since the Bessel functions $J_r(x)$ for $x \gg r$ present an oscillating behavior as a cosine, the D.E. can be employed. In Figures 10.1 and 10.2, the logarithm of the absolute value of $Y_{uu}(\chi, n = 0)|f_1(\chi, n = 0)|^2$ for $\chi \in [2k_0, 100k_0)$ and the integrand function after the DE transformation are shown using $K = 5$. The geometrical characteristics of the LCX are: inner conductor radius $a = 6$ mm, outer conductor radius $b = 15$ mm, slot width $s =$ 3mm and frequency $f = 1$ GHz. Note that the elements of (10.9) decay double exponentially to zero and the only the terms which belong to the interval $[-100, 0]$ give a significant contribution. With similar manipulations one can successfully employ the DE transformation to the computation of the elements uv,vu and vv.

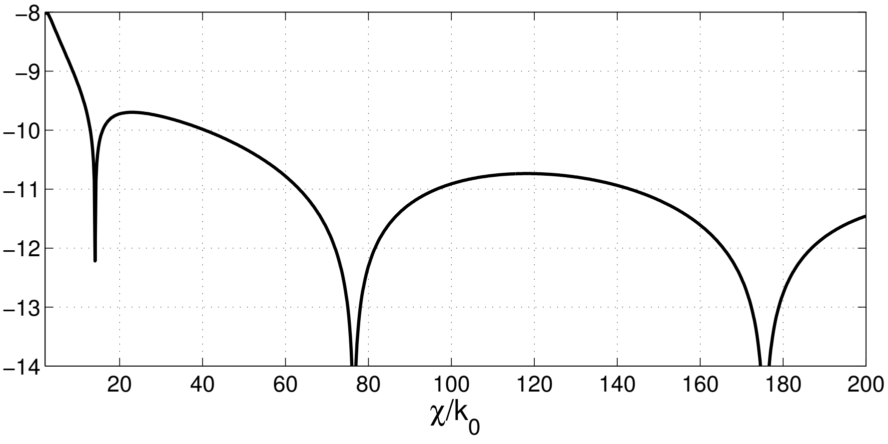

Figure 10.1: Integrand function in the χ variable before the DE transformation

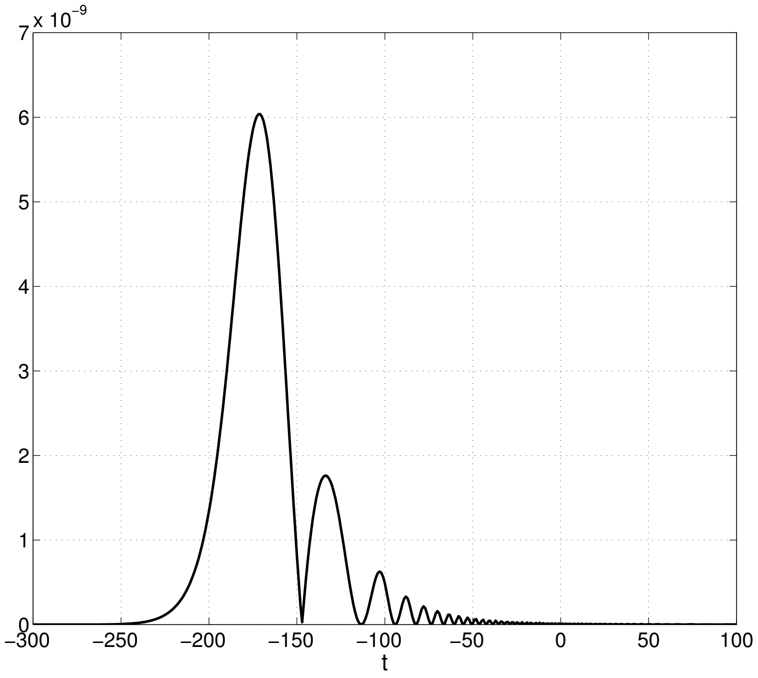

Figure 10.2: Integrand function in the t variable after the DE transformation

10.3 Computation of the projection integrals for the HFIE

The computation of the elements of the moment matrix represents the core of the integral equation technique and, at the same time, the main limitation to its practical application for the analysis of real LCX.

Let us start by considering the expression of a generic element of the moment matrix, as given in Section 3.5:

$$\begin{aligned} A_{\,r,c} &= \sum_n \int_{-\infty}^{+\infty} \tilde{u}^*_{t(r)}(\chi, n; s_{q(r)}, \alpha_{q(r)}) Y^{tot}_{uu}(\chi, n) \tilde{u}_{t(c)}(\chi, n; s_{q(c)}, \alpha_{q(c)})\, \mathrm{e}^{-j\,\chi(L_{q(c)}-L_{q(r)})}\, d\chi = \\ &= \sum_{n=-N_{max}}^{N_{max}} \int_{\Re} \tilde{G}(\chi, n)\, \mathrm{e}^{-j\,\chi\, L} d\chi \end{aligned} \tag{10.17}$$

where $\tilde{G}(\chi, n)$ is a generic function (which assumes different expressions, depending on the basis functions used and on the type of components uu, vu, uv or vv involved) and L is the distance between the centers of two slots. Since the slots in the standard LCX are thin in comparison with the wavelength and oriented along $\hat{\varphi}$, we will discuss in detail the case of the uu component of the admittance

$$Y_{uu}^{int}=-\frac{j\omega\varepsilon_1}{\tau_1}\frac{J_n(\tau_1\rho_1)Y_n'(\tau_1\rho_2)-J_n'(\tau_1\rho_2)Y_n(\tau_1\rho_1)}{J_n(\tau_1\rho_1)Y_n(\tau_1\rho_2)-J_n(\tau\rho_2)Y_n(\tau_1\rho_1)}+\frac{j\chi^2n^2}{\omega\mu_0\rho_2^2\tau_1^3}\frac{J_n'(\tau_1\rho_1)Y_n(\tau_1\rho_2)-J_n(\tau_1\rho_2)Y_n'(\tau_1\rho_1)}{J_n'(\tau\rho_1)Y_n'(\tau_1\rho_2)-J_n'(\tau_1\rho_2)Y_n'(\tau_1\rho_1)}$$

$$Y_{uu}^{ext}=\frac{j\omega\epsilon_0}{\tau}\frac{H_n'^{(2)}(\tau\rho_2)}{H_n^{(2)}(\tau\rho_2)}-\frac{j\chi^2n^2}{\omega\mu\tau^3\rho_2^2}\frac{H_n^{(2)}(\tau\rho_2)}{H_n'^{(2)}(\tau\rho_2)}$$

These expressions apply in the case the dielectric cover is absent. Since each element of the moment matrix is given by a series of integrals, it is convenient to analyze the behavior of the integrand as a function of the n variable. In section 2.7 it has been shown that $Y_{uu}^{tot}(\chi,n)$ is an even function of the two variables χ and n. Moreover, if all the slots are centered in $\varphi=0$ and a TEM incident field is considered, for symmetry reasons only the basis functions even in φ are excited, which gives rise to a function $G(\chi,n)$ even in n so that the series (10.17) can be reduced as:

$$\sum_{n=-N_{max}}^{N_{max}}\int_{\Re}\tilde{G}(\chi,n)\,\mathrm{e}^{-j\chi L}d\chi=\int_{\Re}\tilde{G}(\chi,0)\,\mathrm{e}^{-j\chi L}d\chi+2\sum_{n=1}^{N_{max}}\int_{\Re}\tilde{G}(\chi,n)\,\mathrm{e}^{-j\chi L}d\chi \quad (10.18)$$

In order to identify the best numerical strategy for an accurate and fast evaluation of the integrals, let us examine the properties of $G(\chi,n)$. The function $G(\chi,n)$ has poles and branch point singularities in the complex plane χ. Hence, its definition is complete when appropriate branch cuts are specified. From the general modal theory [8], we know that the poles are related to the guided modes of the structure, while the branch cuts are associated to the radiated modes. The global structure, *i.e.* coaxial cable and the region around it, supports two different sets of guided modes: the modes of the coaxial cable and those of the open waveguide consisting of the cable outer conductor, the dielectric cover and free space (see Figure 10.3). Let us consider where these singularities are in the complex χ plane under the assumption the dielectric media are lossless. In this case the poles which correspond to below cut-off (cable) modes are on the imaginary axis, while the poles related to the above cut off modes of the coaxial cable and of the open waveguide

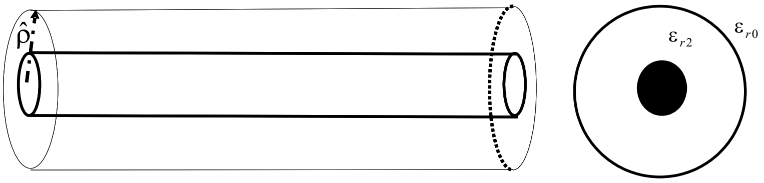

Figure 10.3: Coaxial cable with dielectric cover

belong to the intervals $[-k_0\sqrt{\varepsilon_{r1}}, k_0\sqrt{\varepsilon_{r1}}]$ and $[-k_0\sqrt{\varepsilon_{r2}}, k_0\sqrt{\varepsilon_{r2}}]$, respectively, where ε_{r2} is the relative dielectric permittivity of the cover. A pictorial view of the preceding considerations is shown in Figure 10.4 where the dashed lines represent the branch cuts, while the dot points represent the poles. Branch lines have been chosen that guarantee $\Im\tau_2 < 0$ on the entire top sheet of the Riemann surface, [8]. If the dielectric media are not ideal, then the situation is modified as plotted in Figure 10.5.

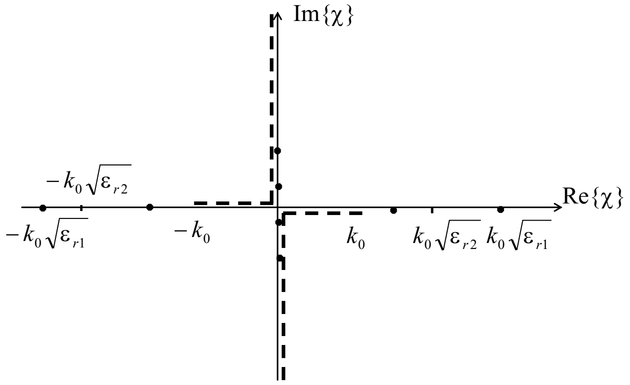

Figure 10.4: Complex plane χ with poles and branch cuts if the media are lossless

Apparently, $G(\chi, n)$ is not an analytical function due to the presence of the complex conjugate

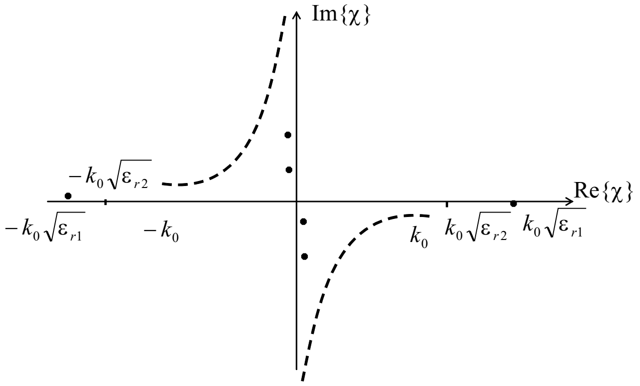

Figure 10.5: Complex plane χ with poles and branch cuts in the general case

operator applied to the test function. Actually, since the $u_r(z, \varphi)$ are real, the complex conjugate

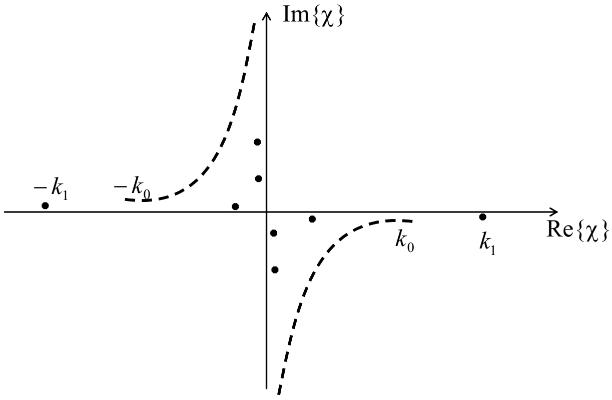

Figure 10.6: Complex plane χ with poles and branch cuts in the case the dielectric cover is neglected

of the Fourier transform, $\tilde{u}_r^*(\chi,n)$ can be manipulated as follows:

$$\tilde{u}_r^*(\chi,n) = \left(\int_{-\infty}^{+\infty}\int_0^{2\pi} u_r(z,n)\,\mathrm{e}^{+j\,z\chi}\,\mathrm{e}^{+j\,n\varphi} d\,z\,d\,\varphi\right)^* =$$

$$\int_{-\infty}^{+\infty}\int_0^{2\pi} u_r^*(z,n)\,\mathrm{e}^{-j\,z\chi}\,\mathrm{e}^{-j\,n\varphi} d\,z\,d\,\varphi = \tilde{u}_r(-\chi,-n) \tag{10.19}$$

If weighted Chebyshev polynomials are employed and the slots are centered in φ equal to zero, it is possible to prove that

$$\tilde{u}_r(-\chi,-n) = (-1)^r \tilde{u}_r(\chi,n) \tag{10.20}$$

Finally, the function $G(\chi,n)$ can be written as:

$$G(\chi,n) = (-1)^r\,\tilde{u}_c(\chi,n)\,Y^{tot}(\chi,n)\tilde{u}_r(\chi,n) \tag{10.21}$$

$$\tag{10.22}$$

and the integrand function is clearly analytical. This property will be employed for the computation of the mutual coupling projection integrals.

Since the function $G(\chi,n)$ consists of the sum of two terms ($Y^{tot} = Y^{int} + Y^{ext}$) it is convenient to consider them separately. Hence, we write:

$$\int_{-\infty}^{+\infty} G(\chi,n)\mathrm{e}^{-j\chi L} d\chi = \int_{-\infty}^{+\infty} G_{int}(\chi,n)\mathrm{e}^{-j\chi L} d\chi + \int_{-\infty}^{+\infty} G_{ext}(\chi,n)\mathrm{e}^{-j\chi L} d\chi$$

where:

$$G_{int}(\chi,n) = \tilde{u}_c(\chi,n)\,Y_{int}(\chi,n)\tilde{u}_r^*(\chi,n)$$
$$G_{ext}(\chi,n) = \tilde{u}_c(\chi,n)\,Y_{ext}(\chi,n)\tilde{u}_r^*(\chi,n)$$

10.3.1 case 1: Self-Coupling and internal contribution

As just discussed, the integrand function in this case presents only poles in the complex plane whose position corresponds to the propagation constants of the modes of the coaxial cable. Since the basis functions have finite support, their transform are entire functions and the Jordan's Lemma can not be applied. Note that the kernel $Y_{int}(\chi, n)$ is an even function in the variable χ, as it has been pointed out in the first chapter. The Fourier Transforms of the basis functions are, instead, even or odd; for symmetry, half of the integrals are zero. The non zero ones can be reduced as:

$$\int_{-\infty}^{\infty} \tilde{u}_r(\chi, n)\, Y_{int}(\chi, n)\, \tilde{u}_c(\chi, n)\, d\chi = 2 \int_{0}^{\infty} \tilde{u}_r(\chi, n)\, Y_{int}(\chi, n)\, \tilde{u}_c(\chi, n)\, d\chi \tag{10.23}$$

In the following, the dielectric losses are neglected, the extension to the general case is obtained by analytic continuation.

Using the small argument expansion of Bessel functions of the first and second kind for $\chi \to k_0\sqrt{\varepsilon_{e1}}$ (i.e. $\tau_1 \to 0$) the function Y^{int} has the following asymptotic behavior:

$$Y^{int}(\chi \simeq k_0\sqrt{\varepsilon_{r1}}, n) \propto \begin{cases} \dfrac{1}{k_0\sqrt{\varepsilon_{r1}} - \chi} & \text{if } n\text{=0} \\ \\ O(k_0\sqrt{\varepsilon_{r1}} - \chi) & \text{if } n > 0 \end{cases} \tag{10.24}$$

where $O()$ is the Landau symbol.

From the preceding formula it is clear that the singularity in $\chi = k_0\sqrt{\varepsilon_{r1}}$ is present only for $n = 0$. The computation of the integral requires an analytical extraction of this pole. The other poles, which lie on the imaginary axis, have an effect on the quadrature techniques if they are not too far from the integration path. For this purpose, it is convenient to subdivide the integration domain in the following way:

$$\int_{0}^{\infty} d\chi = \int_{0}^{2k_1} d\chi + \int_{2k_1}^{\infty} d\chi \tag{10.25}$$

The first element of (10.25) is computed by an analytical extraction, if $n = 0$, and the difference by the trapezoidal rule. For $n \neq 0$, a trapezoidal scheme is directly employed. On the other hand, the second term of (10.25) has been evaluated using the DE technique (see section 10.2 for more details).

10.3.2 case 2: Mutual Coupling and internal contribution

Since real LCX are composed by thousands of slots, the parameter L in (10.17) can be greater than hundreds of wavelengths, in absolute value. Due to the exponential term, the integrand function is highly oscillating and any standard numerical scheme is bound to fail. Even if a direct application of the double exponential transform is still possible, it is more convenient to deform the integration path as shown in Figure 10.7 and apply the Cauchy Theorem. Using the notation shown in figure, we have:

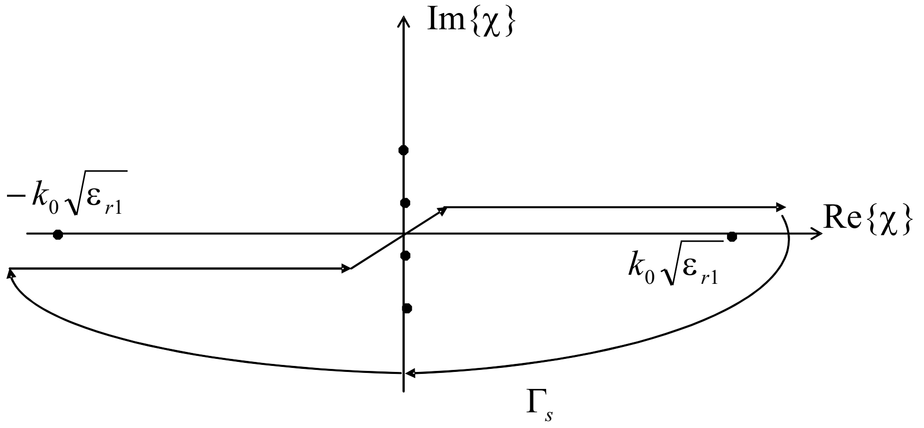

Figure 10.7: Deformation of the integration path for the application of Cauchy theorem

$$\int_{-\infty}^{\infty} d\chi + \int_{\Gamma_s} = \pm 2j\pi \sum_q \mathrm{Res}\{\chi_q\} \tag{10.26}$$

where Res represents the residue of the q-th pole and the sign on the second term of (10.26) depends on the sign of L.

The integral on the semicircular arc gives no contribution because $|L| > s$ (we are computing the mutual coupling term) and the exponential $\exp(-j\chi L)$ counterbalances the divergence of the expansion functions transforms. Then:

$$\int_{\infty}^{\infty} d\chi = \pm 2j\pi \sum_q \mathrm{Res}\{\chi_q\} \tag{10.27}$$

Clearly, these residues decrease exponentially because the corresponding poles (apart the TEM one) are on the imaginary axis; in the standard operating mode, only the first one or two poles, for the azimuthal index n less than three or four, give a significant contribution. This fact can be easily explained considering that only the subset, which is composed by the accessible modes,

gives a significant contribution.
The exact position of the poles can be found solving the following non linear equations:

$$J_n(\tau\, a)\, Y_n(\tau\, b) - J_n(\tau\, b)\, Y_n(\tau\, a) = 0 \text{ for the TM modes}$$
$$J_n'(\tau\, a)\, Y_n'(\tau\, b) - J_n'(\tau\, b)\, Y_n'(\tau\, a) = 0 \text{ for the TE modes}$$

whose solution are listed ([10]) for different couples of the radii (a, b).

10.3.3 case 3: Self Coupling and external contribution

In this case, the singularities of the integrand are branch points. The associated cuts, physically, correspond to the continuous spectrum of the radiated modes. The effect of the branch cuts on the quadrature scheme is present for any value of n, but requires a particular attention if n is equal to zero and one since the integrand function diverges for $\chi = k_0$. Indeed, the expansion of Y^{ext} for $\chi \simeq k_0$ (i.e. $\tau \simeq 0$) obtained substituting the series expansion of $H_n^{(2)}(x)$ and $H_n'^{(2)}(x)$ for $x \to 0$:

$$Y^{ext}(\chi, n) \propto \begin{cases} \dfrac{jY_0}{2\rho_2(k_0-\chi)} \dfrac{1}{\dfrac{j\pi}{2} + \gamma_e + \log\left(b/2\sqrt{2k_0(k_0-\chi)}\right)} & \text{for } n\text{=0} \\[2ex] \gamma_e - \log 2 + \log b\sqrt{2k_0(k_0-\chi)} & \text{for } n\text{=1} \\[2ex] O(k_0-\chi) & \text{for } n > 1 \end{cases} \tag{10.28}$$

where γ_e is the Euler constant. Figures 10.8, 10.9, 10.10, and 10.11, show plots of the external admittance $Y_{ext}(\chi, n)$ and the differences with respect to its approximate expressions for $n = 0, 1$.

Note that the asymptotic expression of $Y^{ext}(\chi, n)$ for $n = 0$ presents a spurious pole in $\chi_p = k_L$, with $k_L = k_0 + 2\mathrm{e}^{-2\gamma_e}/(k_0\rho_2^2)$, which sets a limit on the use of that formula.
For this reason the integration path has been divided in two parts:

$$\int_0^\infty d\chi = \int_0^{\chi_1} d\chi + \int_{\chi_1}^\infty d\chi \tag{10.29}$$

where the value of χ_1 depends on n.
If $n = 0$, χ_1 is chosen as the midpoint between k_0 and χ_p. Then the asymptotic behavior is

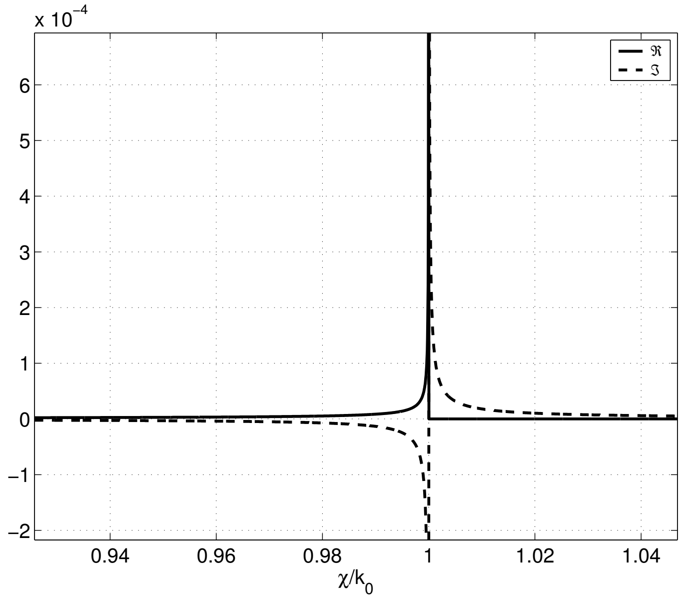

Figure 10.8: Real and imaginary part of $Y^{ext}(\chi, n)$ for $n = 0$

extracted and computed analytically, the remaining part is evaluated by the trapezoidal rule, while the second term of (10.29) is treated using the Double Exponential technique.

If $n = 1$, we choose $\chi_1 = 2k_0$ and the same scheme as before. Finally for $n > 2$ the entire integral is computed by the DE technique.

Note that the corresponding series converges with $50 - 60$ terms, approximatively.

If the dielectric cover is taken into account, some poles, corresponding to the guided modes of the external waveguide, can lie in the range $\chi \in [k_0, k_0\sqrt{\varepsilon_{r2}}]$. In this case, it is convenient to deform the integration path as shown in Figure 10.12. In this way the singularities can be avoided and the integrand function is smooth. This integral can be efficiently computed using the FFT algorithm.

10.3.4 case 4: Mutual Coupling and external contribution

In this case from a direct application of the Cauchy Theorem one obtains (see Figure 10.13):

$$\int_{-\infty}^{\infty} = \int_{\Gamma_1} + \int_{\Gamma_c} + \int_{\Gamma_2} + 2\pi j \sum_q Res\{\chi_q\} \tag{10.30}$$

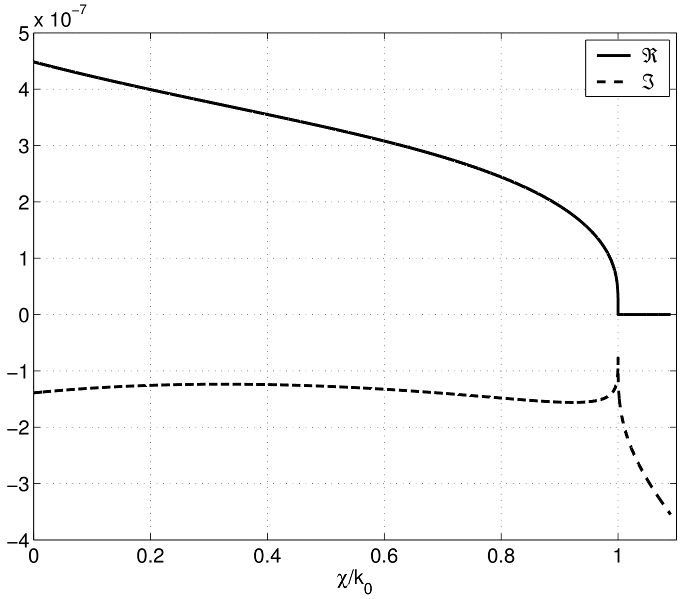

Figure 10.9: Real and imaginary part of the difference between $Y^{ext}(\chi, n)$ and its approximate expression in the case $n = 0$

since the terms $\int_{\Gamma_{v1}} d\chi$ and $\int_{\Gamma_{v2}} d\chi$ are equal to zero because of Jordan's Lemma. Γ_c is a semi circle of infinitesimal radius around $\chi = k_0$ and the integral on it is evaluated analytically. Then we should compute numerically the integrals along $\int_{\Gamma_1}$ and $\int_{\Gamma_2}$ where the integrand is oscillating. In order to avoid this problem, it is convenient to deform the branch cuts as shown in Figure 10.14. On this path, the function decays rapidly without oscillations. In this case, however, $\Im\tau_2 > 0$ in the subregion A, which then belongs to the so called "improper sheet" of the Riemann surface on which the integrand is defined. The poles in this region are known in literature as "leaky waves". A useful parameterization of Γ_1, Γ_c and Γ_2 is:

$$\begin{aligned} \Gamma_1 :&\quad \chi = k_0 - R - j\,u \text{ with } u \in (-\infty, 0] \\ \Gamma_c :&\quad \chi = k_0 - R\,\mathrm{e}^{-j\theta} \text{ with } \theta \in [0, \pi] \\ \Gamma_2 :&\quad \chi = k_0 + R - j\,u \text{ with } u \in [0, -\infty) \end{aligned}$$

It can be proved that the term $\int_{\Gamma_c} d\chi$ tends to zero for $R \to 0$ while the terms $\int_{\Gamma_1} d\chi$ and $\int_{\Gamma_2} d\chi$ can be combined in:

$$\int_{\Gamma_1} + \int_{\Gamma_2} = \int_0^\infty \frac{\mathrm{e}^{-u}}{u}\left(\frac{4\omega\epsilon_2}{\pi\,\rho_2}\frac{1}{\underline{\tau}^2 H_n^{(1)}(\rho_2\underline{\tau})H_n^{(2)}(b\underline{\tau})} + \right.$$

$$\left. + \frac{4n^2(k_2 - ju/L_s)^2}{\omega\mu\,\rho_2^3\pi\underline{\tau}^4}\frac{1}{H_n'^{(1)}(b\underline{\tau})H_n'^{(2)}(\rho_2\underline{\tau})}\right)\tilde{u}_c(k_0 - ju/L, n)\tilde{u}_r(k_0 - ju/L, n)du \tag{10.31}$$

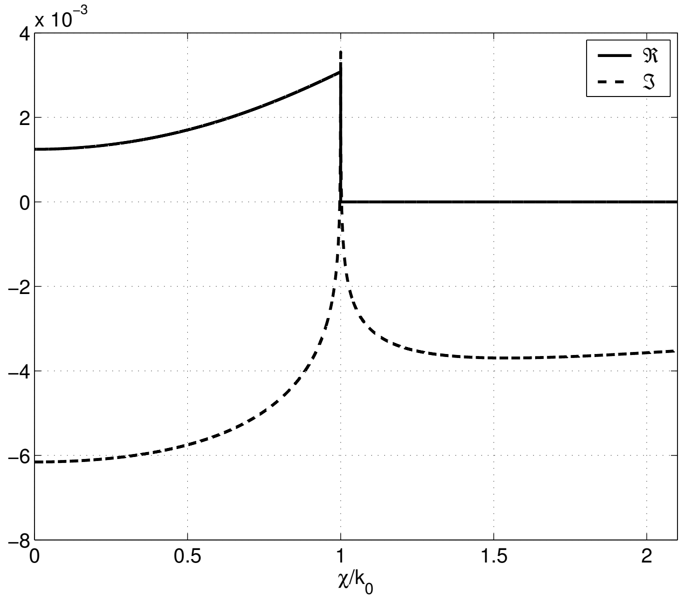

Figure 10.10: Real and imaginary part of $Y^{ext}(\chi, n)$ for $n = 1$

where $\underline{\tau} = \sqrt{k_0^2 - (k_0 - ju/L)^2}$ with the imaginary part that is positive or equal to zero and $u \in [0, \infty)$.

The preceding integrand is singular for $u = 0$ and requires an analytical extraction of the singularity. The remaining part can be computed using a gaussian-Laguerre quadrature scheme with few nodes since, along the new path, the integrand function is not oscillating.

The computation of the residue terms in (10.30) requires the computation of the complex poles related to the leaky waves. If the dielectric cover is neglected, the position of these zeros can easily found as complex zeros of the Hankel functions $H_n^{(2)}$ and $H_n'^{(2)}$ that are reported in [10], for example. In the other case a numerical routine becomes necessary and the problem can become quite cpu time consuming since the number of these poles for any value of n is not known a priori. On the other hand, this problem can be avoided, considering that the contribution of these leaky waves decays exponentially in relation to the imaginary part of the pole. Moreover, our final purpose is to compute the integral and not the position of the leaky waves: hence, we can define a suitable rectangle in the region A and compute the corresponding contour integral. This rectangle has to be chosen so that the leaky wave poles existing outside of it can be safely neglected because their contribution is negligible. Applying the Cauchy Theorem:

$$\oint_{\gamma} = -2j\pi\Sigma\text{Res} \tag{10.32}$$

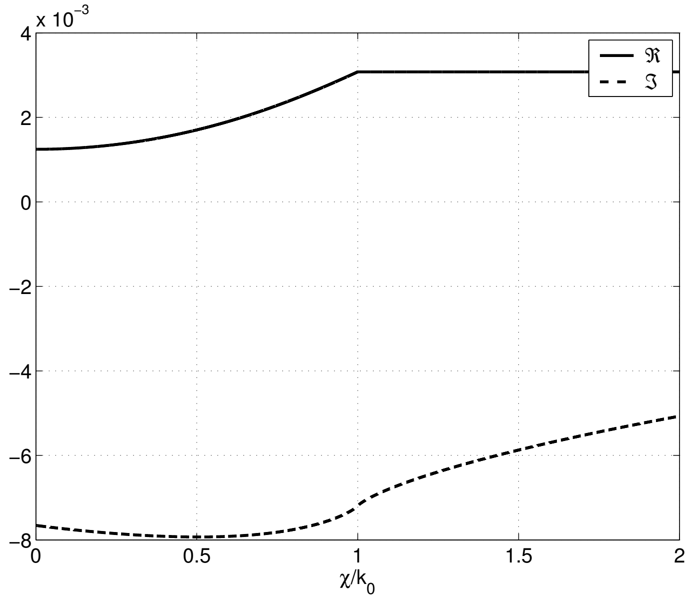

Figure 10.11: Real and imaginary part of the difference between $Y^{ext}(\chi, n)$ and its approximate expression in the case $n = 1$. Note that the singularity has been extracted

where $\gamma = \bigcup_{q=1}^{q=4} \gamma_q$ and has the following parameterization:

$$\begin{aligned}
&\gamma_1 : \chi = j\,x && \text{for } x \in [-k_I, 0]\\
&\gamma_2 : \chi = x && \text{for } x \in [0, k_0]\\
&\gamma_3 : \chi = k_0 + j\,x && \text{for } x \in [0, -k_I]\\
&\gamma_4 : \chi = x - j\,k_I && \text{for } x \in [k_0, 0]
\end{aligned}$$

The integrand function is not oscillatory along γ_3 and the integral can be computed by trapezoidal rules, while along γ_2, γ_3 and γ_4 it is convenient to employ the FFT algorithm.

10.4 Behavior of the Series of Integrals in HFIE solution

When the angular width α of the slots is small, the number of integrals to compute becomes really large. This fact is based on the observation made in section 3.6 that convergence is reached if the number of azimuthal harmonics taken into account is $N = 2N_{max} + 1 = 1 + 2\lceil 50/\alpha \rceil$. Even if a quite sophisticated scheme to speed up the computation of the projection integrals has been developed, numerical problems can be expected when Bessel functions of quite high order

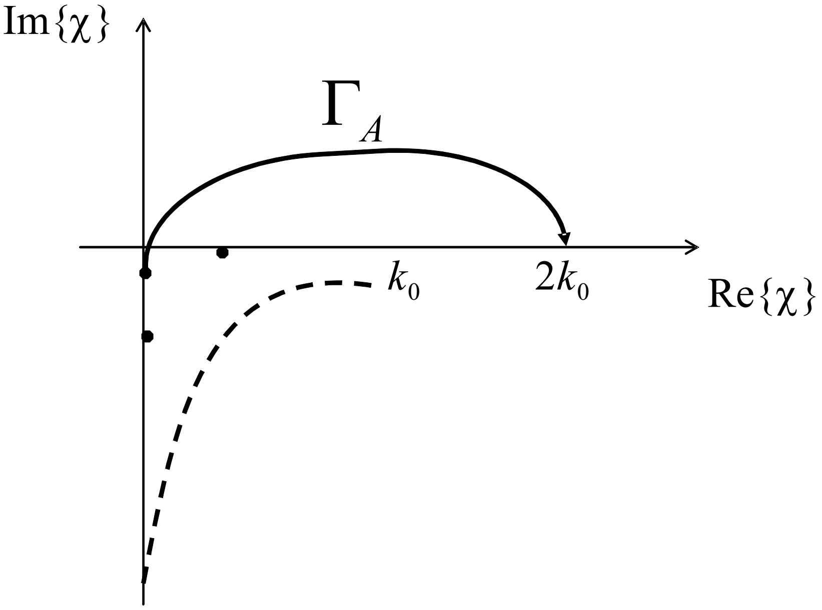

Figure 10.12: Deformed path in order to avoid the poles related to the guided waves in the external waveguide

have to be computed, in particular for the computation of Y_{int}, which is given as a ratio of two differences. On the other hand if we study the dependence of the series terms on the azimuthal order n, we see that the behavior is very regular. This facts suggests an analysis of the qualitative behavior n of the integrand functions. Let us start considering the generic element related to A_{uu}:

$$\int_{-\infty}^{+\infty} Y_{uu}^{tot}(\chi, n)\tilde{f}_c(\chi)\,\tilde{f}_r^*(\chi)d\chi \tag{10.33}$$

It can be shown that the asymptotic behavior of the integrand is (see paragraph 2.7):

$$Y_{uu}^{tot}(\chi, n) \approx \begin{cases} n\left(\dfrac{j\omega\varepsilon_0}{\tau_2} - \dfrac{j\omega\varepsilon_1}{\tau_1} + \dfrac{j\chi^2}{\omega\mu\,\rho_2^2\tau_1^3} - \dfrac{j\chi^2}{\omega\mu\,\rho_2^2\tau_2^3}\right) & \text{when } |\tau\,\rho_2| \ll n \\ \dfrac{j\omega(\varepsilon_1+\varepsilon_0)}{\chi} - n^2\,\dfrac{2j}{\chi\omega\mu\,\rho_2^2} & \text{when } |\tau\,b| \gg n \end{cases} \tag{10.34}$$

Then one can assume that the general behavior of (10.33) is:

$$\int_{-\infty}^{+\infty} d\chi \approx A + B\,n + C\,n^2 \tag{10.35}$$

where A, B and C are some constants to be computed using a least square method. In order to verify the preceding results, Figure 10.16)(left) shows a comparison between (10.33) and the

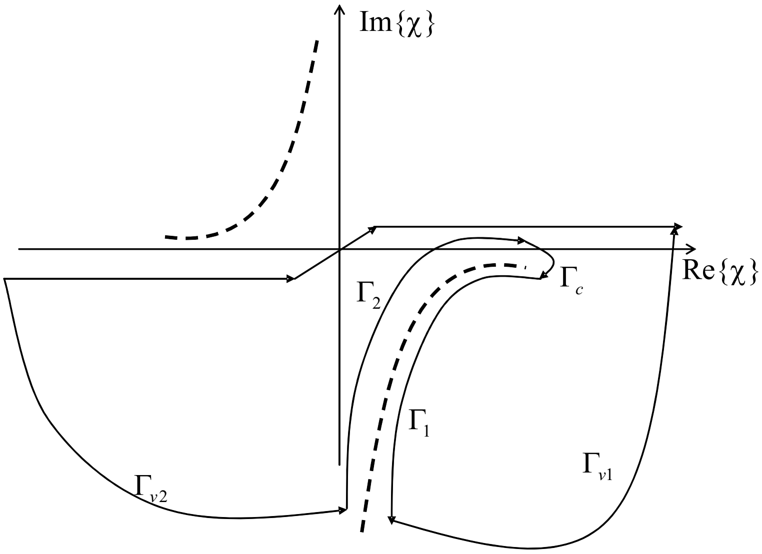

Figure 10.13: Deformation of the integration path

(10.35), for a LCX whose geometrical and electric characteristics are: inner conductor radius $\rho_1 = 3.4$ mm, outer conductor radius $\rho_2 = 8.8$ mm, slot width $s = 3$ mm, frequency $f = 1$ GHz, dielectric permittivity $\varepsilon_{r1} = 1.26$. The values of A, B and C have been estimated by a minimum least square routine on the integral values for $n \in [40, 50]$. There is a very good agreement between the two curves and the relative error (Fig. 10.16 (right)) is less than 1%. Let us now consider the elements related to A_{uv}:

$$\int_{-\infty}^{+\infty} Y_{uv}^{tot}(\chi, n)\tilde{g}_c(\chi)\, \tilde{f}_r^*(\chi) d\chi \tag{10.36}$$

In this case, it can be shown that the asymptotic behavior of the total admittance is (see Section 2.7):

$$Y_{uv}^{tot}(\chi, n) \approx \begin{cases} \dfrac{j\chi}{\mu\omega\, a} \displaystyle\sum_{q=1}^{\infty} \dfrac{C_q}{n^{q-1}} & \text{when } |\tau\, \rho_2| \ll n \\ \\ \dfrac{j\, n}{\chi\omega\, b} & \text{when } |\tau\, \rho_2| \gg n \end{cases} \tag{10.37}$$

where C_q are constants whose expression is quite complicate. Then one can suppose that the general behavior of (10.36) is:

$$\int_{-\infty}^{+\infty} d\chi \approx \sum_{q=-1}^{\infty} \frac{d_q}{n^{q-1}} \tag{10.38}$$

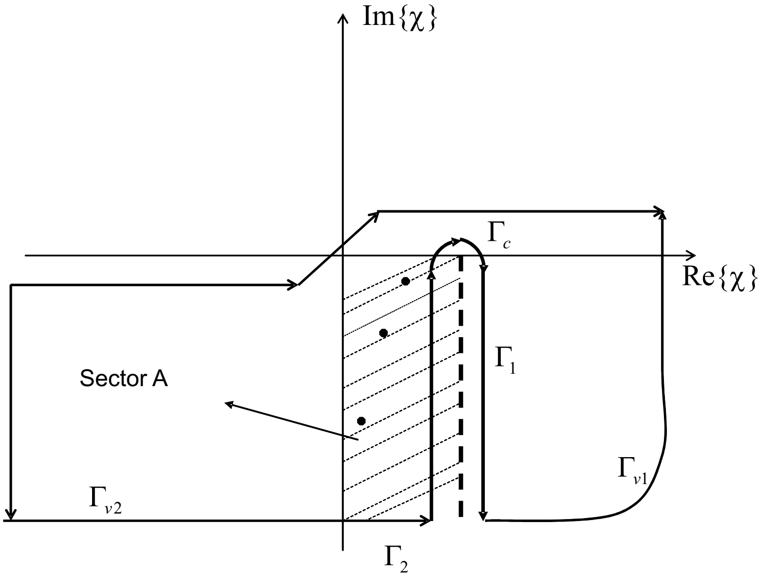

Figure 10.14: New integration path around the modified branch cut

where the coefficients d_q can be computed using the least square method. Usually, the series in (10.38) can be truncated with three term. The exact integrals (10.36) and their approximations (10.38) are shown in Figure 10.17 (left) for LCX whose geometrical and electric characteristics are the same as before. The values of $\{d_q\}$ have been computed on the basis of the values for $n \in [40, 50]$. The agreement is very good and the relative error (reported in Figure 10.17 (right)) is less than 2%. Identical considerations hold for the element vu. Finally, let us consider the elements related to A_{vv}:

$$\int_{-\infty}^{+\infty} Y_{vv}^{tot}(\chi, n)\tilde{g}_c(\chi)\,\tilde{g}_r^*(\chi)d\chi \tag{10.39}$$

The asymptotic behavior of the integrand is (see section 2.7):

$$Y_{vv}^{tot}(\chi, n) \approx \begin{cases} \dfrac{j\,b\tau^2}{\mu\omega\,n} & \text{when } |\tau\,\rho_2| \ll n \\[2ex] \dfrac{\tau}{\omega\,\mu} & \text{when } |\tau\,\rho_2| \gg n \end{cases} \tag{10.40}$$

Then, one can suppose that the general behavior of (10.39) is:

$$\int_{-\infty}^{+\infty} d\chi \approx A + \frac{B}{n} \tag{10.41}$$

where A and B are two constants to be computed using the least square method. The integrals (10.39) and their approximations (10.41) are shown in Figure 10.39 for the same LCX as before.

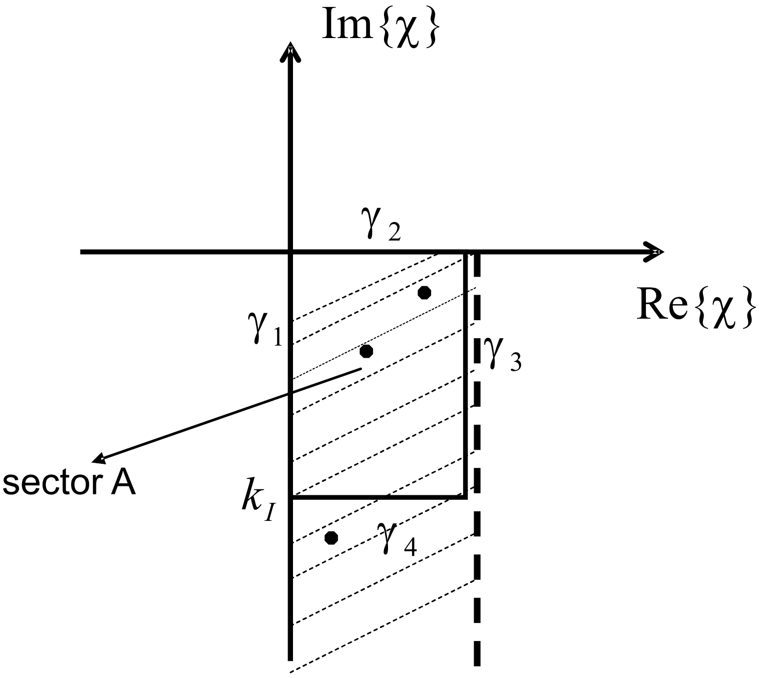

Figure 10.15: Modification of the integration path, to avoid the computation of leaky waves in the case of dielectric covered cable

The values of A, and B have been computed by a least square routine on the basis of the values for $n \in [40, 50]$. The agreement is again very good and the relative error (reported in Figure 10.18 (right)) is less than 1%. It has to be remarked that the use of a least square method in order to compute the constants of the asymptotic expression is necessary since the equations (10.35), (10.38) and (10.41) are to be interpreted as a tool for a qualitative confirmation of an intensive numerical investigation. However they can be employed to prove that the series are convergent. In fact, if one combines, for example, (10.35) and the asymptotic expression, for large argument of the expansion functions, the asymptotic behavior of the elements of the series is:

$$\frac{A + B\,n + C\,n^2}{n^3} \cos\left(n\alpha/2 - \pi/4 - r\pi/2\right) \cos\left(n\alpha/2 - \pi/4 - c\pi/2\right) \tag{10.42}$$

and it is well known that a series with such general term is convergent.

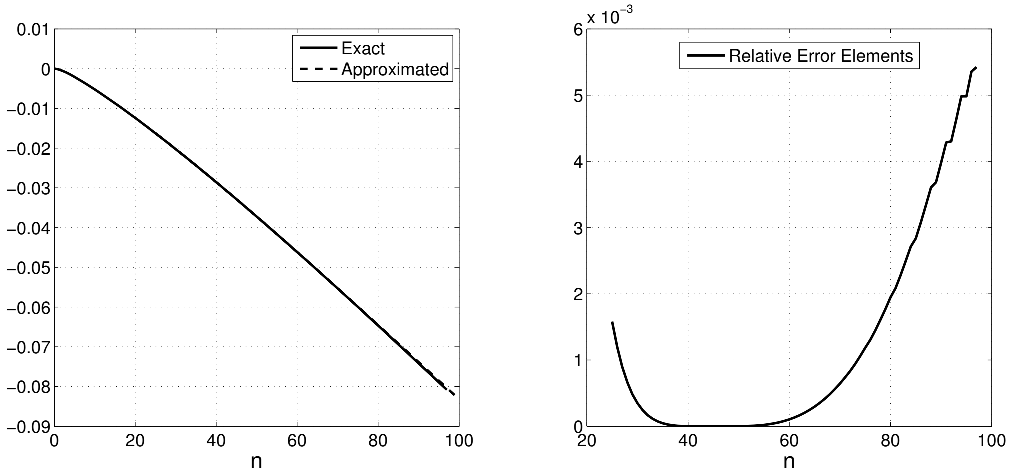

Figure 10.16: Left: comparison between the exact elements A_{uu} and their approximation (10.35): the two curves are superimposed; Right: Relative error of the approximation of A_{uu}

10.5 Discretization of the slot scattering operator

The discretization of the scattering operator requires the computation of many integrals of functions with integrable singularities in $\tau = 0$ and $\tau = k_0$. Since two different sets of basis functions, with different integration domain, have been employed for the discretization of the above and below cut-off portion of the spectrum, it is convenient to consider separately the corresponding integrals.

Before starting to show the technique, it is useful to recall the small argument asymptotic behavior of the Hankel function $H_q^{(1)}(x)$:

$$H_q^{(1)}(x) \propto \begin{cases} \log x & \text{for } q = 0 \\ \\ \dfrac{1}{x^q} & \text{for } q > 0 \end{cases} \tag{10.43}$$

Since the complete expressions of the integrand function are quite complicated, we will focus our attention only on the divergent part.

The integrals related to a generic TM spectral composite mode, in the above cut off portion of the spectrum, have an integrand function containing the factor:

$$\frac{1}{(k_0 - \tau)^{1/2}\, \tau^{1/2} H_m^{(1)}(\rho_2 \tau)} \tag{10.44}$$

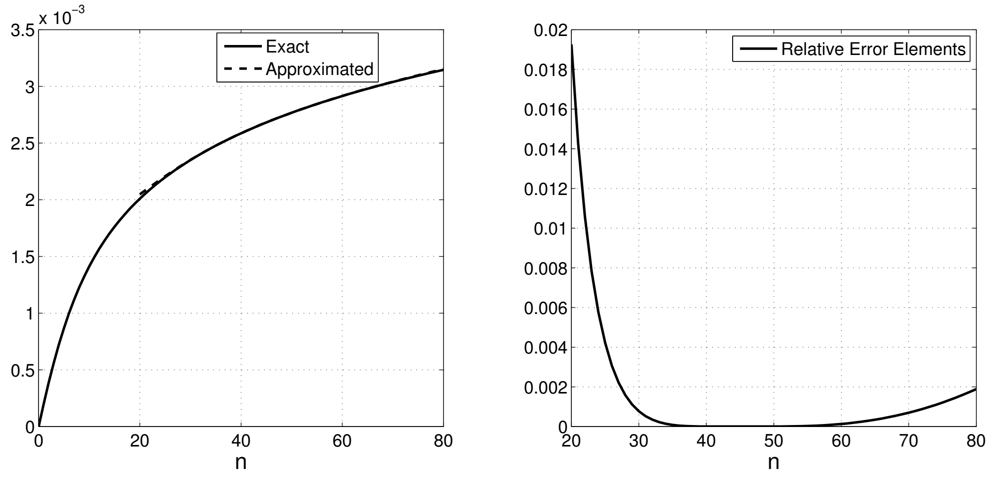

Figure 10.17: Left: comparison between the exact elements A_{uv} and their approximation (10.38): the two curves are superimposed; Right: Relative error of the approximation of A_{uv}

where m is the azimuthal mode index. In this case the integration domain is $\tau \in [0, k_0]$, then combining (10.43) and (10.44) we see that the integrand function is singular in $\tau = 0$ only if $m = 0$ (i.e. for the $TM_{0,\tau}$ modes), while it has a square root singularity for any value of m in $\tau = k_0$. Employing the theory of the improper integrals, we can assert that the integrals exists for any value of m. In order to compute these integrals it is useful to exploit the following numerical scheme. First, the integration domain is split in two parts:

$$\int_0^{k_0} d\tau = \int_0^{k_0/2} d\tau + \int_{k_0/2}^{k_0} d\tau \tag{10.45}$$

The first integral can be easily computed using the variable transformation $\tau = x^R$. In the new variable (10.44) becomes:

$$\frac{R\, x^{R/2-1}}{(k_0 - x^R)^{1/2}\, H_m^{(1)}(\rho_2\, x^R)} \tag{10.46}$$

with integration limits 0 and $(k_0/2)^{1/R}$. From the (10.46) it is evident that if $R > 2$ the integrand is no longer singular.

Analogously, for the second integral we employ the variable transformation $x = k_0 - x^M$ and obtain:

$$-\frac{M\, x^{M/2-1}}{\sqrt{k_0 - x^M}\, H_m^{(1)}(b\,(k_0 - x^M))} \tag{10.47}$$

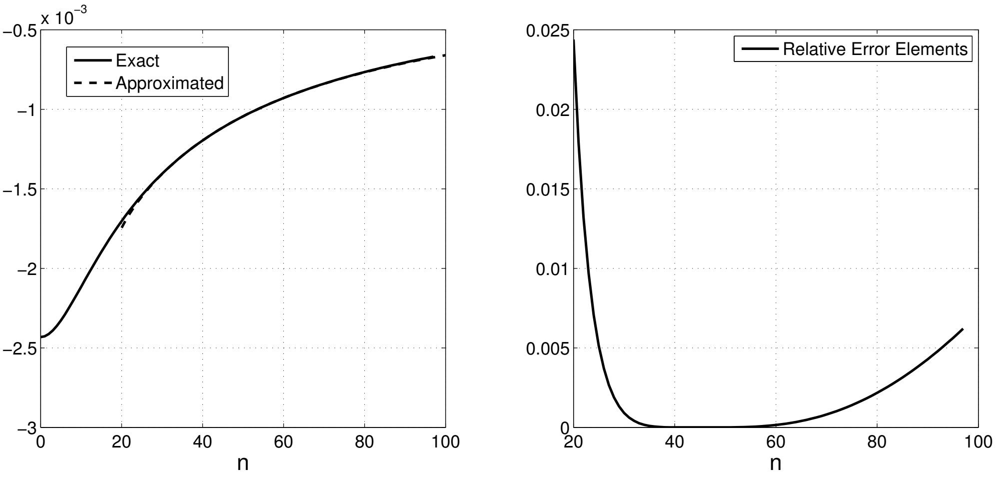

Figure 10.18: Left: comparison between the exact elements A_{vv} and their approximation (10.38): the two curves are superimposed; Right: Relative error of the approximation of A_{vv}

with integration limits 0 and $(k_0/2)^{1/M}$. Again if $M > 2$, (10.47) is no longer singular along the integration path.
After the change of variable both integrals can be computed by a gaussian Legendre quadrature scheme since the other singularities have been moved far away from the integration path. Moreover, selecting $M = R$, the same nodes and weights can be used for the computation of the two integrals. A fast convergence can be obtained for values of R not too large. On the other hand, the number of nodes has to be chosen in relation with the order of the Chebyshev polynomials used for the discretization of the scattering operator since the number of its oscillations has to be taken into account. After an extensive numerical investigation, we decided to use $R = 4$ with the number of nodes equal to $4N_\tau$, where N_τ is the number of basis functions used for the discretization of the scattering operator.

Let us now consider in detail the contribution to spectral TM composite modes from the below cut-off portion of the spectrum (i.e. $\tau \in [k_0, \infty)$. The relevant part of the integrand function is:

$$\frac{\mathrm{e}^{-L_d\tau/2}}{\sqrt{k_0 - \tau}} \tag{10.48}$$

then the only singularity is represented by the square root divergent behavior in $\tau = k_0$. As before, it is useful to subdivide the integration domain in two parts:

$$\int_{k_0}^{\infty} d\tau = \int_{k_0}^{3k_0/2} d\tau + \int_{3k_0/2}^{\infty} d\tau \tag{10.49}$$

The first integral can be computed as before using the variable transformation $\tau = k_0 + x^R$. In this way one can employ the same quadrature formula employed in the preceding case. In fact, the upper limit (i.e. $3/2k_0$) has been chosen in order to use the same nodes and weights. The second part of (10.49) can be evaluated by a gaussian Laguerre scheme after the variable transformation $\tau = 3\,k_0/2 + 2v/L_d$. Since the effect of the below cut off composite modes is quite low, it has been numerically shown that 32 modes guarantee a satisfactory accuracy.
Let us now briefly consider the integrals involved in the TE composite modes. The only difference is that the integrand function is no longer singular in $\tau = 0$ and $\tau = k_0$ since for TE modes the azimuthal index m is different from zero and the admittance $Y_\infty = \frac{\sqrt{k_0^2-\tau^2}}{\omega\mu}$ compensates the square root singularity in $\tau = k_0$.

Let us now consider the integrals for the reconstruction of the radiated electromagnetic field according to the method presented in Section 4.7. Again, it is useful to distinguish the two cases of above- and below-cut-off continuous spectrum modes. It can be shown that the singular portions of the integrands are

$$\begin{cases} 1/(\tau^{3/4} H_n^{(2)}(\tau\,\rho_2)\sqrt{k_0 - \tau}) & \text{for TM modes} \\ 1/\sqrt{k_0 - \tau} & \text{for TE modes} \end{cases}$$

for $0 < \tau < k_0$ and

$$\begin{cases} \mathrm{e}^{-\tau\,L_d}/\sqrt{k_0 - \tau} & \text{for TM modes} \\ \mathrm{e}^{-\tau\,L_d}/(\tau^{3/4} H_n^{(2)}(\tau\,\rho_2)) & \text{for TE modes} \end{cases}$$

for $\tau > k_0$. From the preceding expressions it is evident that the same method shown for the discretization of the scattering matrix can be successfully employed also for the computation of the electromagnetic field. Moreover the same nodes and weights can be used if R is chosen equal to 4.

10.6 Computation of the projection integrals for the ring cavity filter

In this section the numerical evaluation of the moment matrix of the ring cavity filter will be discussed.

Under the assumption that only the TE_{11} mode is above cut-off, the only singularities along the integration path in the complex χ plane are the two poles

$$\chi_p = \pm k_{z11} = \pm\sqrt{k_0^2\varepsilon_r - \left(\frac{\chi'_{11}}{\rho_1}\right)^2}$$

which correspond to the progressive and regressive waves of this mode. χ'_{11} is the first zero of the derivative of the Bessel function $J_1(x)$. In the case of ring cavity filters, there are four types of integrand functions, related to the various components uu, uv, vu, vv. The generic integral has the form:

$$\int_{\Re} Y(\chi,n)\tilde{u}_r^*(\chi,n)\tilde{u}_c(\chi,n)d\chi \tag{10.50}$$

Since the uu and vv admittance components are even and the uv and vu are odd and the Fourier Transforms of the basis functions are either even or odd, several integrals are zero and for the remaining ones

$$\int_{-\infty}^{\infty} \tilde{u}_r^*(\chi,n)\,Y(\chi,n)\,\tilde{u}_c(\chi,n)\,d\chi = 2\int_0^{\infty} \tilde{u}_r^*(\chi,n)\,Y(\chi,n)\,\tilde{u}_c(\chi,n)\,d\chi \tag{10.51}$$

Finally, the evaluation of each integral has been done subdividing the integration domain in two parts:

$$\int_0^{\infty} d\chi = \int_0^{2k_1} d\chi + \int_{2k_1}^{\infty} d\chi \tag{10.52}$$

where $k_1 = k_0\sqrt{\varepsilon_r}$.

The first integral has been computed by extracting the asymptotic expression for $\chi \approx \chi_p$ as in Section 10.3, while the second integral has been evaluated employing the double exponential technique.

The asymptotic expressions of the admittances for $\chi \approx \chi_p$ are:

$$Y_{uu}(\chi \approx \chi_p) = \frac{j\chi_p}{\omega\mu\,\rho_1\chi_p^2}\frac{J_1(\chi'_{11})}{(\chi-\chi_p)J_1''(\chi'_{11})} \tag{10.53}$$

$$Y_{uv}(\chi \approx \chi_p) = Y_{vu}(\chi \approx \chi_p) = \frac{j}{\omega\mu\,\rho_1^2}\frac{J_1(\chi'_{11})}{(\chi-\chi_p)J_1''(\chi'_{11})} \tag{10.54}$$

$$Y_{vv}(\chi \approx \chi_p) = \frac{j\chi'_{11}}{\omega\mu\,\rho_1^3\chi_p}\frac{J_1(\chi'_{11})}{(\chi-\chi_p)J_1''(\chi'_{11})} \tag{10.55}$$

Hence, the first term of (10.52) can be computed as:

$$\int_0^{2k_1} \tilde{u}_r^*(\chi,n)\,Y_{uu}(\chi)\,\tilde{u}_c(\chi,n)d\chi =$$

$$= \left(-j\pi + \log\left(\frac{2k_1 - \chi'_{11}}{\chi'_{11}}\right)\right) \frac{j\chi_p}{\omega\mu\,\rho_1\chi'^2_{11}} \frac{J_1(\chi'_{11})}{J''_1(\chi'_{11})} \tilde{u}_c(\chi_p, n)\tilde{u}^*_r(\chi_p) + \int_0^{2k_1} \Delta F^{uu}_{r,c}(\chi) d\chi$$

$$\int_0^{2k_1} \tilde{u}^*_r(\chi, n)\, Y_{vv}(\chi)\, \tilde{u}_c(\chi, n) d\chi =$$

$$= \left(-j\pi + \log\left(\frac{2k_1 - \chi'_{11}}{\chi'_{11}}\right)\right) \frac{j\chi'^2_{11}}{\omega\mu\rho_1^3\chi_p} \frac{J_1(\chi'_{11})}{J''_1(\chi'_{11})} \tilde{u}_c(\chi_p, n)\tilde{u}^*_r(\chi_p) + \int_0^{2k_1} \Delta F^{vv}_{r,c}(\chi) d\chi$$

$$\int_0^{2k_1} \tilde{u}^*_r(\chi, n)\, Y_{uv}(\chi)\, \tilde{u}_c(\chi, n) d\chi =$$

$$= \left(-j\pi + \log\left(\frac{2k_1 - \chi'_{11}}{\chi'_{11}}\right)\right) \frac{j}{\omega\mu\,\rho_1^2} \frac{J_1(\chi'_{11})}{J''_1(\chi'_{11})} \tilde{u}_c(\chi_p, n)\tilde{u}^*_r(\chi_p, n) + \int_0^{2k_1} \Delta F^{uv}_{r,c}(\chi) d\chi$$

$$\int_0^{2k_1} \tilde{u}^*_r(\chi, n)\, Y_{vu}(\chi)\, \tilde{u}_c(\chi, n) d\chi =$$

$$= \left(-j\pi + \log\left(\frac{2k_1 - \chi'_{11}}{\chi'_{11}}\right)\right) \frac{j}{\omega\mu\,\rho_1^2} \frac{J_1(\chi'_{11})}{J''_1(\chi'_{11})} \tilde{u}_c(\chi_p, n)\tilde{u}^*_r(\chi_p, n) + \int_0^{2k_1} \Delta F^{vu}_{r,c}(\chi) d\chi$$

where the elements $\Delta\, F^{xx}_{r,c}(\chi)$ are the difference between the exact integrand functions and their asymptotic expressions. Note that the application of a gaussian quadrature technique does not assure a rapid convergence since the effect of the extracted pole plagues that technique. For this reason, these integrals have been computed using a trapezoidal scheme.

10.7 Behavior of the longitudinal series for the ring cavity filter

The series (9.39) can be accelerated employing the Kummer Method. For this purpose we need to consider the large argument asymptotic expressions of the admittance $Y_{cc}(\chi, \pm 1)$ and of the Fourier transforms of the basis functions $\tilde{\phi}(\chi)$ and $\tilde{\zeta}(\chi)$. In particular, we retain the first two terms of the asymptotic expansions. With some algebra, we have shown that the elements of the series are asymptotically proportional to a combination of terms which decay as $m^{-7/3}$, $m^{-10/3}$, $m^{-13/3}$, $m^{-16/3}$ and $m^{-19/3}$. This fact implies that the asymptotic series can be computed analytically in terms of the Zeta Riemann function. The difference series is easily evaluated by a direct summation, since its elements converge to zero extremely fast.
As an example, let us consider the computation of the element

$$A^{conn}_{uu}|_{11} = \sum_m \underline{\acute{u}}^*_1(m, \pm 1) \cdot \underline{\underline{B}}^T \cdot \underline{\underline{Y}}_{cc}|_{11}(m, \pm 1) \cdot \underline{\underline{B}} \cdot \underline{\acute{u}}_1(m, \pm 1) \tag{10.56}$$

The n summation contains only the indicated two terms, since the slot is complete and the incident field is TE$_{11}$. The geometrical and electric characteristics of the structure are circular waveguide radius $a = 5.3$ mm, ring cavity inner radius $b = 8.8$ mm, slot width $s = 2$ mm , frequency $f = 20$ GHz. Figure 10.19 (left) shows a plot of the absolute values of the elements of the series while the elements of the difference series are shown in Figure 10.19 (right). Note that after the 25th element the difference can be considered of the same order as double precision round-off error, so that it can be neglected.

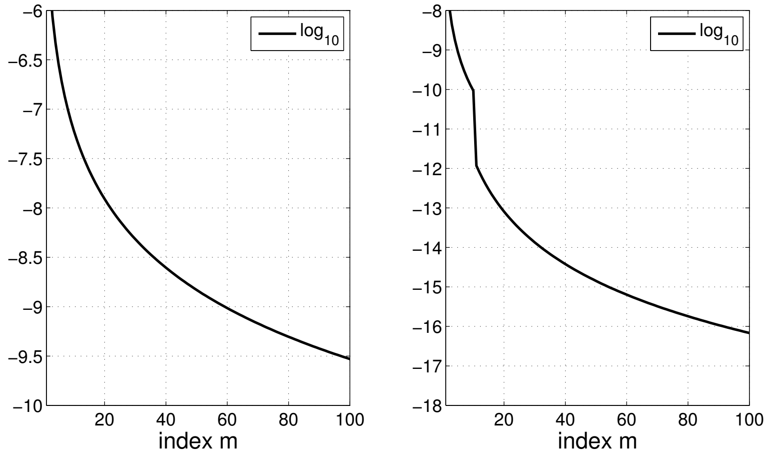

Figure 10.19: $\log_{10}$ of the absolute values of the elements of the series (left) and of the difference series (right)

Chapter 11

Conclusions and Recommendations

The main theme in this thesis has been the use of circuit theory in the solution of guided wave scattering problems. The term “guided wave” is actually to be interpreted, since also free space can be viewed as a (peculiar) waveguide.
Propagation in usual rectilinear waveguides is often phrased in the language of transmission line theory. It has been remarked that the theory of equivalent transmission lines is a way to give physical insight into the mathematical method of separation of variables. This opens the way to the use of non conventional equivalent transmission lines, such as the radial ones or the angular ones.

In this thesis we focused on the concept of radial waveguide, a structure which has the radial direction $\hat{\rho}$ as propagation direction and is possibly bounded by metal plates parallel to the coordinate planes. It is not possible in the present case to introduce vector mode functions as in conventional waveguides, but the transmission line concept is introduced on a component basis. From the conceptual point of view, it was useful to adopt a vector setting, so that TE and TM wavefield components (with respect to $\hat{z}$) are treated at the same time.
Radial lines are peculiar, because they have an absolute origin and are neither shift invariant nor reflection invariant. Nevertheless the usual circuit theory concepts can be applied, with appropriate definition of impedances, propagators, scattering matrices, etc. As soon as we have transmission line theory at our disposal, we can use it to solve scattering problems.

We have addressed two problems, the first concerning slotted coaxial cables, the second circular waveguide filters, comprising ring cavities. They may seem very different at first sight, but have been attacked by the same method, *i.e* magnetic field integral equation. The kernel of that is the Green's function of the structure and the radial transmission line theory has been very helpful in its construction. Actually, it is a spectral representation of the Green's function which is directly computed and it is convenient to carry out the numerical solution of the HFIE, by the method of moments, directly in the spectral domain.

The advantage of this approach to the study of slotted coaxial cables is that not only does it allow the computation of the radiated field, but also of the input reflection coefficient. The drawback is that the numerical effort increases with the number of slots. Even if a very efficient code has been developed, so that the simulation of cables with several hundreds of slots is feasible,it was judged necessary to explore two other approaches.
The first one is strictly related to the periodic slot configuration of uniform LCX. Indeed, it is well known that, in the study of periodic structures, the Bloch wave technique is the most appropriate one. The difficulty here is that the outside of the cable is an open waveguide, characterized by a continuous spectrum, so that the application of standard theory is not possible. In this work we developed a method to discretize the continuous spectrum, based on the introduction of basis functions for the expansion of the modal amplitudes. The results have been very satisfactory, since beyond the numerical advantage in the case of large arrays, a conceptual framework was obtained, which yielded design guidelines.
The third technique we have developed in this work is the extension to the cylindrical geometry of the eigencurrent approach, originally introduced for in the analysis of large planar arrays. This method is based on the computation of the approximate eigenvalues and eigenvectors of the moment matrix of the entire array as a linear concatenation of the eigencurrents of a subarray of the entire antenna. In this way it is possible to obtain the electromagnetic solution avoiding the storage and inversion of large moment matrix.

As for the design, it is clear that the use of identical slots in a cable is not convenient since an inevitable tapering of the radiated power appears. A design procedure has been developed that allows the design of the slots in such a way that the radiated power level is quite uniform, despite the cable radiation and ohmic losses.

Concerning the waveguide filter application, a particular type of coaxial cavity has been studied. In the transverse setting, the coupling of the cavity to the main circular waveguide takes place via a thick iris. This structure is characterized by a response with a transmission and a reflection zero, whose positions can be adjusted by acting on the geometrical parameters of the cavity. In this way, it was possible to design stop band filters working in double polarization.

It is to be stressed that the application of the integral equation technique to the solution of scattering problems is fairly simple from a conceptual point of view, but its numerical implementation in an efficient code is far from trivial and has required a major effort. In particular, the computation of the elements of the moment matrix requires the evaluation of series of infinite domain integrals. The integrands have singularities, oscillatory behavior and slow decay at infinity. The use of complex function theory and of specially developed integration schemes was essential for the construction of a fast and reliable code.

Recommendations

We would like to conclude with some recommendations for the use of the analysis techniques developed in this work and some indication of further work.
The transverse approach is the most convenient method when the slots are all different or resonant in both directions. However, its limitation is clearly related to the number of slots of the array.
The longitudinal technique (*i.e.* the Bloch wave approach) is convenient when the slots are equal and equally spaced and for the determination of the considerable parameters for the design of LCX.
Finally the eigencurrent approach becomes particularly useful when the array is composed by slots with irregular shapes and sub domain basis functions (as, for instance, RWG) are applied. In this case the cpu time reduction is remarkable. On the other hand it is not so convenient when the shape is regular and full domain basis functions can be used.

Ohmic losses in the cable have been described by means of an equivalent loss tangent, taking approximately into account both dielectric and copper losses. A more accurate approach is that of computing the copper losses by the method of [40]. In this way, also the power dissipated by the reactive fields excited in the neighborhood of the discontinuities is accurately evaluated.

Another investigation deals with the reduction of the computation time. The array consists of a multitude of slots, acting as scattering centers. A classical technique in this case is that of evaluating the response of the system in the form of a multiple-scattering series representation. In general, this approach can be impracticable, but we have shown that in the case of slotted cables, the scattering of each slot is not so large. This leads us to expect that this method could be convenient.

We have shown that it is possible to design a non-uniformly slotted cable such that the radiated power is fairly uniform along its length. In this case, Bloch wave theory, as it has been developed in this thesis, is not applicable since the structure is not, strictly speaking, periodic. However, the change in the slot size may be so small that it could be convenient to regard the array as a slightly non uniform periodic structure and try to apply some sort of coupled mode theory to the "local" Bloch waves. This extension could be very interesting in order to evaluate the sensitivity of the structure to manufacturing tolerances.

Radial transmission line theory finds application also in other fields, such as that of conformal arrays, both of slots and of patches, or in the construction of the complete spectrum (both discrete, guided modes, and continuous, radiated modes) of layered optical fibres. The extension of the eigencurrent approach to these $2-$D and $3-$D problems could be particularly useful but a deep analysis on the eigenvalues behavior of the array increasing the number of elements is strongly necessary and decisive.

As for the design of dual polarized ring loaded filters, it would be interesting to ascertain whether and in which way the eigencurrent approach can be applied and how the eigencurrents are related to the electromagnetic response of the single stub.

At the very end it is to be remarked that transmission line theory is by no means limited to electromagnetic problems. These techniques have been used also in the study of elastic wave propagation and the use of circuit concepts has been very helpful in the formulation of the solution method and in the interpretation of the results.

Bibliography

[1] E. Weber and F. Nebeker, *The Evolution of Electrical Engineering*, IEEE Press, Piscataway, New Jersey USA, 1994

[2] W. Thomson, "On the theory of the electric telegraph", *Mathematical and Physical Papers*, Vol.2, 1854, p.61

[3] O. Heaviside, "Electromagnetic induction and its propagation", *The Electrician*, Vol. 23,1885

[4] J. C. Maxwell, *A treatise on electricity and magnetism*, Clarendon Press, Oxford, 1873

[5] A.A. Oliner,"Historical perspectives on microwave field theory", *IEEE Trans. Microw. Theory Tech.*, Vol. MTT-32, pp.1022-1045, September 1984.

[6] N. Marcuvitz and J. Schwinger, "On the representation of electric and magnetic fields producedby currents and discontinuities in waveguides", *J. Appl. Phys.*, Vol. 22, pp. 806-819, June 1951.

[7] N. Marcuvitz, *Waveguide Handbook* Peter Peregrinus, copyr. 1986

[8] L. Felsen and N. Marcuvitz, *Radiation and scattering of waves*, Englewood Cliffs (NJ), Prentice-Hall, 1951.

[9] Gantmacher F.R. , "The theory of matrices", New York : Chelsea,copyr. 1960

[10] M. Abramowitz , *Handbook of mathematical functions*, Dover publications Inc., New York, 1965.

[11] Bastiaan P. de Hon and Marianne Bingle "A modal impedance-angle formalism: Schemes for accurate draded-index bent slab calculations and optical fiber mode counting", *Radio Science* Vol. 38, No. 2, 8012, 2003

[12] R.E. Collin, *Foundations for Microwave Engineering*, New York:McGraw-Hill, 1992, Ch.s 5 and 8.

[13] P.P. Delogne, L.Deryck, “Underground Use of a Coaxial Cable with Leaky Sections”,*IEEE Trans. Antennas Propagat.*, Vol. 28, n.6, pp. 875-883, April 1980.

[14] D.A. Hill, J.R. Wait, “Electromagnetic Characteristics of a Coaxial Cable with Periodic Slots”,*IEEE Trans. on Electromagnetic Compatibility*, Vol. EMC-22, n.4, pp. 303-307, November 1980.

[15] E.E. Hassan, “Field Solution and propagation characteristic of monofilar-bifilar modes of axially slotted coaxial bable”,*IEEE Trans. Microwave Theory and Technology*, Vol. MTT-37, n.4, pp. 553-557, March 1989.

[16] J.H. Richmond, N.N. Wang and H.B. Tran “Porpagation of surface waves on a buried coaxial cable with period slots”,*IEEE Trans. Electromagn. Compat.*, vol. EMC-22, pp.303-307, Nov.1980.

[17] S. Kim, G.Yun, H.Park, “Numerical Analysis of the Propagation Characteristics of Multiangle Multislot Coaxial Cable Using Moment Method”,*IEEE Trans. Microwave Theory Tech.*, Vol. 46, n.3, pp. 269-278, March 1998.

[18] P.P.Delogne and A.A.Laloux, “Theory of slotted coaxial cable”,*IEEE Trans. Microwave Theory and Technology*, Vol. MTT-28, n.4, pp. 1102-1107, October 1980.

[19] R.F. Harrington, *Time harmonic electromagnetic fields* , McGraw-Hill, New York,1961.

[20] J.Meixner, “The behavior of electromagnetic fields at edges”,*IEEE Trans. Antennas Propagat.*, vol. AP-20, pp.442-446, 1972.

[21] J.M.B. Kroot, S.J.L.van Eijndhoven, A.A.F. van de Ven, “Eddy currents in a gradient coil, modeled as circular loops of strips”,*J.Eng.Math* (2007) n.57, pp.333-350, January 2007

[22] A.F. Peterson, R.E. Wilton, Jorgenson,“Variational nature of Galerkin and non-Galerkin moment method solutions”, *IEEE Trans. Antennas Propagat.*, Vol. AP-44, pp. 500-503, April 1966.

[23] D. G. Dudley, “Comments on “Variational nature of Galerkin and non-Galerkin moment method solutions””, *IEEE Trans. Antennas Propagat.*, Vol.AP-45, pp.1062-1063, June 1997.

[24] Mittra R. and Lee S.W., *Analytical Techniques in the Theory of Guided Waves*, The MacMillan Company, New York, 1971.

[25] G. Addamo, R.Orta, D. Trinchero, R. Tascone and G. Gianola , “Slotted Coaxial Cables for wireless communications”, *Loughborough Antennas & Propagation Conference 2005*, Lougborough, Great Britain.

[26] R.E. Collin, *Field Theory of Guided Waves*, IEEE, New York, 1991.

[27] T.E. Rozzi,“ Network analysis of strongly coupled transverse apertures in waveguide”,*Int. J. Circuit Theory Appl.,* vol. 1, 1973, pp. 161-178

[28] H. Shigesawa, M. Tsuji,“A new equivalent network method for analyzing discontinuity properties of open dielectric waveguides”, *IEEE Trans. Microwave Theory Tech.*, Vol. 37, n.1, pp. 3-14, January 1989.

[29] Borsboom P. and H.J. Frankena, “Field analysis of two-dimensional integrated optical gratings”, *Journal Optical Society Am. A*, Vol 12, n.5, pp. 1134-1141, May 1995.

[30] R.E. Collin, F. J. Zucker, *Antenna theory*, McGraw-Hill, New York,1969.

[31] D.J. Bekers, *Finite Antenna Arrays: An Eigencurrent Approach*, Ph.D. Thesis, Eindhoven University of Technology, The Netherlands, 2004.

[32] L.N. Trefethen, “Pseudospectra of linear operators”. Siam Review, 39(3):383-406, September 1997

[33] S.Kouachi, “Eigenvalues and Eigenvectors of Tridiagonal Matrice” , Electronic Journal of Linear Algebra, 15, pp.115-133, April 2006

[34] A.Papoulis, *Signal analysis*, McGraw- Hill, Auckland, 1977

[35] G. H. Knittel, A. Hessel, A. A. Oliner, “Element pattern nulls in phased arrays and their relation to guided waves”, *Proc. IEEE*, Vol. 56, No. 11, Nov. 1968, pp. 1822-1836.

[36] Kirilenko, et al, “Harmonic Rejection Filters for the dominant and higher waveguide modes based on slotted strips”, *IEEE MTT-S Digest*, 2002, pag. 373-376.

[37] I. Erdelyi, *Operator theory and functional analysis*, Pitman, San Francisco, 1979.

[38] R.J. Pogorzelski, “Quadratic phase integration using a Chebyshev expansion”, *IEEE Trans. Antennas Propagat.*, vol AP-33, pp. 563-566, May 1985.

[39] H. Takahasi and M. Mori, “Double exponential formulas for numerical Integration”, *Publ. Res. Inst Math. Sci.*, 9 (1974) 721-741.

[40] R. Orta, P. Savi, R. Tascone, “The effect of finite conductivity on frequency selective surface behaviour”, *Electromagnetics*, Vol.10, pp.213-227, 1990

[41] G. Addamo, R.Orta, D. Trinchero, R. Tascone and G. Gianola , “Analysis and Characterization of Leaky Coaxial Cables”, *ICEAA 2005* , Italy, Turin, September 2005.

[42] G. Arfken, *Mathematical Methods for Physicists*, Harcourt Academic Press, Amsterdam, 2001.

[43] C. E. Baum, “Emerging technology for transient and broadband analysis and synthesis of antennas and scatterers”, *Proc. IEEE*, vol.64, 1976, no. 11, pp. 1598-1616.

[44] Hsi-Tseng Chou and Hsien-Kwei Ho, “A generalized forward-backward method for the efficient analysis of large array problems”, *IEEE Trans. Antennas Propagat.*, vol. AP-52, no. 2, February 2004, pp. 388-396.

[45] P. Geren, “An FFT Approach to Large Array Analysis”, *IEEE Antennas Propagat. Symposium*, APS-4-9, pp. 135-138, 1985.

[46] S. Kim, G.Yun, H.Park, “New design technique for 22mm ultra-wideband LCX”,*Proc.Asia Pacific Microwave Conf.*, 1995, pp. 514-516.

[47] T. Ooura and M. Mori, “The double exponential formula for oscillatory functions over the half infinite interval”, *J. Comput. Appl. Math*, vol.38, 1991, pp. 353-360. s

[48] A.G. Ramm, “Theoretical and practical aspects of singularity and eigenmode expansion method”, *IEEE Trans. Antennas Propagat.*, vol. AP-28, no. 6, 1980, pp. 897-901.

[49] S. Rampalli and H.R. Nudd, “Recent advances in the designs of radiating (leaky) coaxial cables”,*Proc. 40th Int. Wire Cable Symp. Conf.*, 1991, pp. 67-77.

[50] A.J. Roscoe and R.A. Perrott , “Large Finite Array Analysis Using Infinite Array Data”, *IEEE Trans. Antennas Propagat.* vol. AP-42, no. 7, July 1994, pp. 983-992.

[51] J.H. Wang, K.K. Mei, “Theory and Analysis of Leaky Coaxial Cables With Periodic Slots”,*IEEE Trans. Antennas Propagat.*, Vol. 49, n.12, pp. 1723-1732, December 2001.

Summary

The motivation for developing the computational electromagnetic methods presented in this thesis is to model the radiation of leaky slotted coaxial cables (LCXs), which are used as distributed antennas in environments that are not readily accessible via conventional antenna substations, and to model ring cavities that act as circular waveguide filters. We employ circuit-based electromagnetic wave theory in the solution of guided-wave scattering problems. Here the term "guided wave" is actually to be interpreted loosely, since even free space can be viewed as a waveguide.

Propagation in usual rectilinear waveguides is often phrased in literature in the language of transmission line theory. The theory of equivalent transmission lines has been contrived as a way to give physical insight into the mathematical method of separation of variables. This opens the way to the use of unconventional equivalent transmission lines, such as radial or angular ones.

In this thesis we have focused on the concept of radial waveguide, a structure that has the radial direction as the direction of propagation, and that is possibly bounded by metal plates parallel to the coordinate surfaces. Unlike the traditional vector mode functions encountered in conventional waveguides, the radial transmission line concept is introduced in a component basis. Radial lines are peculiar, because they have an absolute origin and hence is not shift invariant. Nevertheless, using a suitable vector formalism, the usual circuit theory concepts can be still applied, including the definition of voltages and currents, impedances, propagators, scattering matrices, etc.

The LCXs are standard coaxial cables from which, on the outer conductor, slots are cut in order to induce energy exchange between the interior of the cable and the surrounding external domain. These kinds of antennas are usually employed for indoor communications in places where the traditional antenna systems fail or their application and installation are problematic, such as in

subways and tunnels. They are also used for security reasons, e.g., in outstations and airports, in order to confine the communications inside specific places. In particular, nowadays, there is an increasing interest in the application of this technology in the GSM and UMTS frequency bands.

LCXs have been studied by several researchers in the past. The analysis techniques employed in these studies produce solutions, to a varying degree of accuracy, for the particular problem of the infinite periodically slotted cable. The problem of junctions between closed and slotted cables has so far not been addressed. The periodically slotted LCXs considered in the literature suffers from poor efficiency in terms of percentage of incident power used for the radiation. Indeed, since the decay of the power inside the cable is exponential and the radiated field decays along the cable length with the same law, the standard periodically slotted LCX requires a compromise between an almost constant level of power along the slotted cable length and minimum power at the end of the cable that is not employed for radiation. In the present thesis we have developed accurate and efficient modeling techniques, enabling us to analyze both periodic and aperiodic LCXs, as well as transitions between open and closed cables.

The second type of devices of interest is a particular category of stop-band filters commonly used in antenna systems to isolate receivers from the signals produced by transmitters, internal or external to the system, and operating in adjacent frequency bands. The structure that we have analyzed presents advantages in terms of the radial and longitudinal dimensions, which allows for the high level of integration that is often essential for space applications. Due to the resonance behavior of the device, the commercial numerical codes require long computational times before sufficiently accurate field solutions are obtained. Our dedicated modeling method is much more efficient in attaining the required results, which has made it possible to produce several design examples.

Our modeling techniques are based on the magnetic field integral equation. The associated kernel is the Green's function of the structure, which is been computed in the spectral domain, using radial transmission line theory. The solution of the corresponding integral equation is obtained, for both problems, by the method of moments in the Galerkin form, using a suitable set of basis functions. The computation of the moments requires particular care. We have developed dedicated numerical techniques by which the numerical convergence is improved and the computation of the integrals is accelerated considerably.

For LCXs, we have developed a design procedure based on tapering the geometrical dimensions of the slots in order to obtain an uniform radiation and to maximize the radiated power. Since a typical LCX consists of thousands of slots, one approaches practical limitations of integral equation techniques, as the dimension of the linear system resulting from the discretization of the integral equation increases with the number of slots. For this reason, we have augmented our approach to analyze LCXs in two alternative directions. One is based on the application of the Bloch wave approach, the other comprises an extension, for the electromagnetic problem under consideration, of the so-called eigencurrent approach, that was originally developed for linear arrays of patches.

First, the Bloch wave approach is not standard in this case since the structure consists of two different regions, one is closed (the interior of the coaxial cable) the other is open (the unbounded exterior domain). We have employed a particular mathematical formalism to overcome this problem, viz., we have solved the junction problem between an closed cable and a slotted one using the mode matching technique. In the Bloch wave approach a LCX with any number of slots, all equal and equally spaced, can efficiently be analyzed.

Second, the eigencurrent approach is a versatile two-step technique for modelling large compound structures. The first step is to evaluate the eigenvalues and current eigenfunctions of the integral operator associated with a single slot. Subsequently, the pertaining eigencurrents act as global-domain basis functions for the slotted array. In the resulting equivalent linear system, the interaction between the slots is adequately described in terms of very few of these eigencurrents. We have applied this method for LCXs with slots of different geometric dimensions, and have observed a substantial reduction of computation times.

For a LCX with a large but finite number of identical slots, it turns out that the dominant Bloch wave is the same as the one excited in the semi-infinite case. When this so-called Forward wave reaches the junction between the slotted and unslotted cable, it gives rise to several reflected Bloch waves that, upon scattering at the first junction, couple only with the Forward wave. Further, we have observed that all the regressive Bloch waves have globally a negligible effect on the magnetic currents on the slots. Hence the field propagating in the slotted region of the finite slotted cable is essentially a progressive wave.

As regards the radiation properties of an infinite LCX, a paradox arises. In practical LCX applications the receiver is always in the near-field region of the array, but in the far-field region of the majority of the slots. This is related to the infinite length of a LCX. Application of the Poisson sum formula to the expression for the radiated field emanating from a LCX converts that expression into a linear superposition of spatial harmonics, in line with the Bloch-wave description. As a consequence, cables with different slot spacings are perfectly explained in terms of the various modes of operation resulting from the Bloch-wave description, i.e., surface-wave, mono-radiation and multi-radiation operation.

About the Author

Giuseppe Addamo was born on October 23rd, 1979 in Messina, Italy. In July 1998, he graduated from high school at the institute "G. Sequenza" of Messina. From September 1998 until July 2003 he studied electronic engineering at the Politecnico di Torino, Italy. He completed his studies with an MSc thesis on the analysis and design of a corrugated horn at the Applied Electromagnetic Group of IEIIT-CNR (an institute of the Italian National Research Council) of Turin. From January 2004 until December 2006, he was a PhD student in Applied Electromagnetics at Politecnico di Torino under the supervision of Prof. R. Orta. Since 2004 he has assisted in a course on Electromagnetic field theory and Mathematical Analysis at the Politecnico di Torino. In 2005 he received the Graduate Fellowship Award by the MTT-Society for his PhD research project on the analysis and design of leaky coaxial cables. From January 2006 to July 2006 he worked, under the supervision of Prof A.G. Tijhuis, at the Technische Universiteit Eindhoven (TU/e) on the application of the eigencurrent expansion for the analysis of slotted cable. In January 2007 he joined the Applied Electromagnetic Group of IEIIT-CNR, directed by Prof R. Tascone, where he is currently involved in the analysis and design of dielectric radomes and high power microwave devices for satellite communications systems.